Development of Resonance Tracking and Optical Readout Methods for MEMS Sensor Arrays

by

Arif Mustafazade

A Thesis Submitted to the
Graduate School of Sciences and Engineering
in Partial Fulfillment of the Requirements for the Degree of

Doctorate of Philosophy
in
Electrical and Electronics Engineering

Koç University

2016

Koc University

Graduate School of Sciences and Engineering

This is to certify that I have examined this copy of a Ph.D. thesis by

Arif Mustafazade

and have found that it is complete and satisfactory in all respects,
and that any and all revisions required by the final
examining committee have been made.

Committee Members:

_____

Prof. Dr. Hakan Urey (Advisor)

_____

Associate Prof. B. Erdem Alaca

_____

Assistant Prof. Şükrü Ekin Kocabaş

_____

Associate Prof. Göksen G. Yaralıoğlu

_____

Associate Prof. Arda D. Yalçınkaya

Date: _____

ABSTRACT

In this thesis work, we developed various resonance tracking and optical readout methods for magnetically actuated MEMS sensor arrays. For magnetic actuation, we designed an electro-coil and a closed-loop high-current driver operating at nominal current of 1 A_{p-p}, frequency range of DC – 100 kHz with maximum phase error of less than 2°, and total harmonic distortion of less than 1%. Using this broadband actuator we demonstrated simultaneous monitoring of multiple MEMS sensors in gases using an interferometric readout method with a single photodiode operating in closed-loop self-sustained actuation (SSA) mode.

SSA method is suitable for high-quality factor resonators where most of the noise and harmonic distortions are filtered out in the resonator. As a more robust closed-loop method for low-quality factor resonators, we developed a broadband resonance tracking system that is based on CMOS digital PLLs. It provides a fixed-amplitude and frequency-independent +90° phase-shifted sinewave output for exciting resonant systems at their resonance frequency without any initial tuning or calibration process. We achieved a maximum of ±2.5° phase error over the whole operating frequency range of 5 – 50 kHz.

The PLL system we have developed shows extremely stable results with standard resonators, we have however experienced large frequency drifts originating from phase-detection errors in the interferometric optical readout. For solving this problem, we developed a novel dual-edge detecting dual-PLL system. This method suppresses all the phase-detection errors arising from the asymmetrical waveform of the feedback signal as well as the dc-offset drifts in the front-end electronics. We demonstrate a viscosity measurement system for measuring the viscosity of blood plasma using the developed dual-PLL system.

Since PLL systems could only lock into a single resonator at a time, for parallel measurements a time-multiplexing mechanism must be employed. As an alternative method providing real-time simultaneous measurements, we developed a novel optical fiber-based readout method with phase-based resonance monitoring. For high-precision phase measurements, we implemented a custom multi-channel lock-in amplifier in software. To our knowledge this is the first demonstration of simultaneous parallel optical monitoring of dynamic mode micro-cantilever sensors in liquid environment.

ÖZET

Bu tez çalışmasında, MEMS sıra algılayıcılar için çeşitli *tınlaşım frekansı*[1] takibi ayrıca farklı optik okuma yöntemleri geliştirilmiştir. *Manyetik eyleyici*[2] olarak, bir bobin ve yüksek akımlı bir bobin sürücüsü geliştirilmiştir. Anma akımı 1 A_{p-p} olan bu sürücü ile DC – 100 kHz frekans aralığında, en fazla 2° faz hatası ve %1'in altında toplam armonik distorsyon elde edilmiştir. Geliştirilen bu geniş bantılı manyetik eyleyiciyi kullanılarak, interferometrik optik okuma ve kapalı devre *kendi kendine uyarma*[3] (SSA) yöntemi ile tek foto diyot kullanılarak, gaz ortamında MEMS mikroçubukların çoklu tınlaşım frekanslarının okuması gerçekleştirilmiştir.

SSA yöntemi genellikle yüksek kalite faktörü olan rezonatorlerde uygun performans sergilerken, düşük kalite faktorlü sistemlerde büyük ölçüde gürültü ve bozulmalara yol açmaktıadır. Bu problemlere çözüm olarak, sayısal *faz kilitli halka*[4] (PLL) tabanlı ve analog sinüs dalga üreten bir tınlaşım frekans takip sistemi geliştirilmiştir. Geliştirilen bu sistemle, 5-50 kHz frekans aralığına, +90° (±2.5°) faz tepkisi elde edilmiştir.

Geliştirilen PLL tabanlı sistem, yaygın rezonatorler ile yüksek karalılık sergilerken, interferometrik okuma yönteminin doğrusal olmayan optik dönüşüm fonksiyonunda meydana gelen faz algılama hatalarından, büyük olçüde frekans kaymaları gözetlenmiştir. Faz algılama hatalarını çözmek için, çift PLL'li bir yöntem geliştirilmiştir. Geliştirilen bu çift PLL'li sistem, kan plazmasının viskozite ölçümü deneylerinde kullanılmıştır.

PLL sistemleri aynı anda sadece tek bir frekansa kilitlenebilir olmalarından, çok kanallı uygulamalar için zaman bölüşümlü yöntemler kullanılmalıdır. Eşzamanlı çoklu okuma sağlayan alternatif yöntem olarak, optik fiber tabanlı çok kanallı bir optik okuma yöntemi geliştirilmiştir. Diğer yöntemlerden farklı olarak, bu yöntemde tınlaşım frekansı okuması, faz ölçümü yapılarak gerçekleştirilmiştir. Yüksek hassasiyetli çok kanallı faz ölçümleri için, yazılım tabanlı bir kilitlemeli yükselteç[5] geliştirilmiştir. Literatürde sıvı ortamında MEMS çubukların tınlaşım frekansı takibi çalışmalarının bulunmasına karşın, bu çalışmada ilk kez sıvı ortamında eş zamanlı çok kanallı tınlaşım frekansı okuması gerçekleştirilmiştir.

---

[1] Resonance Frequency
[2] Magnetic Actuator
[3] Self-Sustained Actuation
[4] Phase-Locked Loop
[5] Lock-in Amplifier

ACKNOWLEDGEMENTS

I would like to thank my advisor Prof. Dr. Hakan Ürey and Assoc. Prof. Göksenin Yaralıoğlu for their continuous support, my brother Prof. Dr. Ali Mostafazadeh for his help in dealing with various mathematical problems, our biosensor research group members Dr. Onur Çakmak and Erhan Ermek for their support in experiments, Assoc. Prof. Dr. B. Erdem Alaca, Assist. Prof. Şükrü Ekin Kocabaş, Assoc. Prof. Arda D. Yalçınkaya, Adnan Kurt and, Assoc. Dr. Alper Erdoğan for valuable discussions.

I would also like to express my gratitude to the Graduate School of Sciences and Engineering of Koç University, for providing me with the opportunity to realize my dream of engaging in scientific research, and particularly the founders and the administration of Koç University for creating and maintaining such an ideal center of excellence.

Finally, and most importantly, I would like to thank my wife, Merve Çerçi Mustafazade for her support, encouragement, patience, and standing beside me throughout my career and writing this thesis.

TABLE OF CONTENTS

LIST OF TABLES

LIST OF FIGURES

NOMENCLATURE

B	*magnetic field intensity*
b	*damping factor*
C	*capacitance*
D	*duty cycle*
d	*laser spot diameter*
f	*frequency*
f_0	*natural frequency*
G	*voltage gain*
g_m	*transconductance gain*
I	*optical intensity*
i	*electrical current*
k	*spring constant*
L	*inductance*
m	*mass*
N	*number of turns*
n	*refractive index*
P	*optical power*
P_{diss}	*dissipated power*
Q	*quality factor*
q	*electron mass*
r	*coil radius*
R	*resistance*

S	*sensitivity*
SR	*slew rate limit*
T	*temperature*
T	*period*
V	*electrical potential*
z	*distance in z-axis direction*
Z	*impedance*
θ_{ca}	*thermal resistance from case to ambiance*
θ_{jc}	*thermal resistance from junction to case*
θ_m	*mechanical angle*
θ_{opt}	*optical angle*
λ	*optical wavelength*
σ	*standard deviation*
τ	*time constant*
Φ	*phase angle*
φ	*optical phase angle*
ω	*angular frequency*
ω_0	*natural angular frequency*

1 Introduction

1.1 Literature Review

MEMS cantilevers were introduced as sensing elements due to their high sensitivity. Volatile chemical detection in air has been demonstrated in resonant mode [1,2]. The high sensitivity stems from the fact that one can make cantilevers with very small dimensions decreasing the mass of the sensitive element. Bio-agent detection in liquid environment have also been demonstrated using micro cantilevers in static mode [3,4] where the spring constant of the cantilevers was made very small to detect atomic forces. Later, to increase the specificity of the sensor and to reduce the test time cantilever arrays have been introduced. The detection of multiple cantilevers in an array has increased the complexity of the measurement setups. A common technique used in dynamic non-contact and tapping mode AFMs and in resonant Microcantilever-based biological and chemical sensors is to frequency sweep an external AC signal for observing the resonance frequency and/or quality factor change as a result of the detected target [5–7]. It is also reported that frequency can be monitored real-time using self-sustained actuation (SSA) without requiring signal generators and complicated electronics [8–10]. Previously, our group developed SSA method to monitor the changes in resonant frequency of Microcantilever due to accreted biological mass in liquid media and demonstrated sensing with 0.1 ng/ml sensitivity and high selectivity for Hepatitis applications [11,12].

The MEMS cantilevers used in the experiments, were magnetically actuated using a remote electro-coil. This method is used in most of the magnetically actuated MEMS systems [13–18]. For driving the electro-coil with a fixed current over the desired operating frequency, a broadband high-current coil driver was designed. Design procedure of this closed-loop coil driver was discussed in detail. The coil driver was characterized and compared to the previously used coil driver.

The vibration of the MEMS cantilevers was read out optically. For simultaneous optical readout of cantilever arrays in Gaseous medium, an interferometric method using a single photodiode was demonstrated and discussed in chapter 3. For resonance tracking,

simultaneous SSA operation of microcantilever array was demonstrated in the air using the interferometric readout.

SSA method are generally suitable for high quality factor resonators where the most of the noise and distortions are filtered out in the resonator. Because of the closed-loop nature of SSA operation, it could be very noisy and generate distorted signals with low quality factor resonators, such as MEMS sensors operating in liquids.

For a more robust resonance tracking, a PLL-based method was introduced and developed in chapter 4. In this method, a type-II digital PLL was used to lock into the input signal from the cantilever and an analog sinewave generating method was employed for actuating the cantilevers. The proposed method maintain a constant +90° phase shifted sinewave to keep the system operating at its undamped resonance frequency. The advantages of this method over the conventional PLL methods was discussed and demonstrated using simulations. The frequency stability of the proposed method was analyzed and simulated in presence of the input noise. Though, the developed method is intended for sensing applications, but generally could be used for actuation proposes also. The performance of the developed system was demonstrated on an RLC resonator and a Quartz tuning fork crystal.

Beside of the complexity of the available PLL methods, Analog PLLs, with multiplexer phase detectors, does not provide frequency-independent phase tracking and broadband frequency range[19–21]. The frequency dependent phase response of these PLLs, introduces additional phase error in the loop which will cause error in the locked frequency. Digital PLLs with Phase/Frequency Detectors (PFD) have frequency independent phase response and are suitable for wideband operation but they generate square waves and could not be directly used for applications where sinewave excitation is required. Output filtering was demonstrated with square wave VCOs but the distorted output waveform will not be suitable for high precision applications [21]. Although PLLs with PFDs lock to zero-phase angle, they could be used for the resonant systems where resonance occurs in zero phase shift between the actuation and feedback signals [22–25]. Otherwise one must employ analog phase-shifters for manual phase tuning [26]. Modern DSP PLLs with special frequency tracking algorithms can provide both wide operating

frequency range and sinewave output signal. However, their applications are limited to research purposes and high-end products due to their high cost and complexity [27–29].

In the method we propose, the frequency-independent and wide operating frequency range of digital PLLs with PFDs are combined with an analog wave generation method to provide both broadband operating frequency range and frequency-independent +90° phase shifted sinewave output. Frequency-independent operation is a highly desired property for broadband actuators and driving high-dynamic-range sensors such as those used for viscosity and density measurement applications in liquids [30–34].

Proposed closed-loop resonance tracking method locks and drives a resonator at its natural frequency without any initial tuning process. For sensor applications, the drive frequency will be the natural frequency of the sensor and could be measured easily using a frequency counter. For resonant actuators this method will drive and keep the actuator always in its natural frequency delivering maximum performance out of the actuator. This is very important issue for most of the resonant actuators where the resonance frequency drifts with temperature or other environmental parameters. In the case of a fixed-frequency-drive system, the amplitude of the resonator can be reduced with drifts in its natural frequency. In our method the drive frequency will change automatically to match the natural frequency of the actuator, keeping the actuation in its maximum amplitude.

The PLL system we have developed shows extremely stable results with standard resonators, we have however experienced large frequency drifts originating from phase-detection errors in the interferometric optical readout. As a solution for interferometric optical readout problems with PLL-based resonance tracking, we developed a novel dual-edge detection method using two cascaded PLL stages. This method, shows extremely high immunity to drifts and asymmetry of the feedback signal as well as DC-offset drifts in front-end electronics. This method was used in a high sensitivity viscosity measurement system for measuring the viscosity of human blood plasma. In general case, this dual-edge phase detection method could be implemented in many digital PLL applications having asymmetrically distorted feedback signals.

Since PLL systems could only lock into a single resonator at a time, for parallel measurements a time-multiplexing mechanism must be employed. Simultaneous monitoring of cantilevers in an array has been demonstrated for atomic force microscopy

operating in air. Those systems used electrical readout using fabricated piezo sensors [35,36], diffraction gratings with integrated photodiode array [37]. In these methods all cantilever deflections are read at the same time using a dedicated electronics. This increases the number of electrical connections to the sensors and complicates the operation under water due to passivation requirements. It is also possible to employ time multiplexing, which reads one cantilever at a time using a single position sensitive detector (PSD), for static and dynamic mode measurements [38–42]. However, time multiplexing methods cannot provide real-time noise cancellation. The frequency-multiplexing methods are not suitable for cantilevers in fluids where the quality factors are low, resulting in large overlap in the frequency responses of the cantilevers. For liquid operation, electrical readout methods are challenging due to required electrical connections. Applying optical lever readout method for array of cantilevers in parallel for simultaneous measurements requires complicated multiple PSD or quad detector fabrication with exact pitch of the cantilevers.

As an alternative method providing real-time simultaneous measurements, we developed a novel optical fiber-based readout method with phase-based resonance monitoring. In this method, we designed a multi-spot laser engine to illuminate the cantilevers. For optical readout, we constructed a fiber array readout head to capture the reflected laser beams from the cantilevers. Identical cantilevers were actuated with a fixed frequency and the phase of each cantilever was measured with respect to the actuation signal. For simultaneous phase measurements, we developed a multi-channel high-precision software lock-in amplifier. We analyzed the phase stability of the developed system in presence of input noise. And finally, we demonstrated a two channel viscosity measurement experiment and a four channel stability measurement in DI-water.

In the appendices, we discussed practical issues of the electro-coil design, design of an analog temperature controller and an advanced Lorentzian function fit model. In this fit model, effect of non-flat frequency response of the photo detector amplifier and background noises was added to the model. This function showed perfect fit results on experimental frequency sweep results of our cantilevers. One could use this fit model for estimating precise values of the natural frequency and quality factor of the cantilever sensors.

1.2 Contribution of Thesis

Bio or chemical sensor systems utilizing MEMS cantilevers are often used in dynamic mode. In such systems, an actuator, a sensor, and control electronics to detect the dynamic changes are used. We mainly focused on remote actuation using electromagnetic coil, remote sensing using optics, and resonant tracking based controller. Fig. 1-1 shows a general block diagram illustrating the key parts of the system and Fig. 1-2 shows four different systems we developed during the thesis.

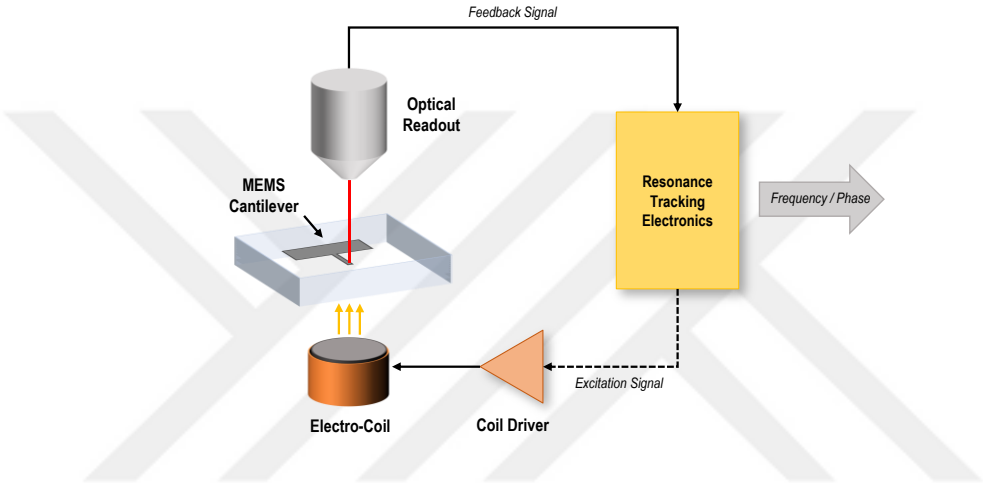

Figure 1-1 - General block diagram of the MEMS sensor system

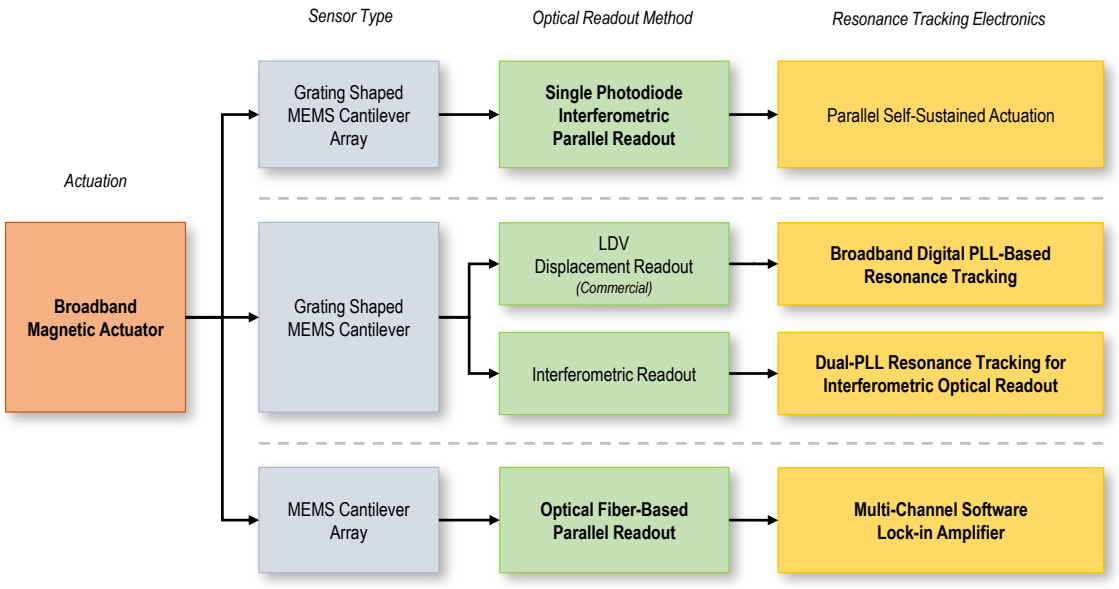

Figure 1-2 – Four different systems developed during this thesis

In this thesis work, we developed a broadband magnetic actuator consisting of an electro-coil and a closed-loop current amplifier. This actuator have been used in all of the experimental setups with magnetically actuated sensors in our group [31,33,43,44]. Using this broadband actuator, simultaneous self-sustained actuation (SSA) of multiple MEMS cantilever sensors was demonstrated in air. This work was published in [43].

As a more precision and robust resonance tracking system, we developed a novel broadband PLL-based resonance tracking method with analog sinewave generation, equipped with all required front-end electronics and phase compensation analog filters. This work was submitted to *Sensors and Actuator A: Physical* journal [45]. A more sophisticated dual-PLL method is also developed to eliminate for asymmetric distortions in the optical interferometric readout method and also for minimizing the DC-offset drifts and low-frequency interference issues. This method was used in resonance tracking of a MEMS-based viscosity sensor system for serum and blood plasma measurements and was published in [31]. A paper describing the details of the electronics will be submitted to *Sensors and Actuator A: Physical* journal [46].

For minimizing the temperature drifts, we also designed an analog temperature controller. This temperature controller was used in [31,33,44].

Since the PLL systems are limited to lock into a single resonator at a time, for real-time simultaneous resonance tracking of MEMS cantilevers in liquids, we developed a novel optical fiber-based readout method. For parallel phase-based measurements I also developed a high-precision multi-channel software lock-in amplifier implemented in LabVIEW. To our knowledge, this is the first demonstration of parallel resonance monitoring of MEMS cantilevers in the liquids in dynamic mode and was published in [34].

2 Broadband Coil Driver Design for Magnetic Actuation

2.1 Introduction

The magnetic actuator consists of an electromagnetic coil and its driver, is the engine of the magnetically actuated MEMS systems [13–18]. For experimental purposes and especially for development of resonant MEMS systems which expected to work in both the gaseous and in the liquid environments, makes it a necessary to have a broadband magnetic actuator.

For a broadband magnetic actuation, both the coil and the driver must have linear behaviors over the expected frequency range and for this aim all of the non-linear and unwanted effects have to be minimized. As there are many parameters in analog circuits that must be took into account, having a broadband frequency response is a challenging task. In this chapter, all of the design constraints and practical parameters will be discussed. Details of the coil design is described in Appendix I. For a broadband coil driver design, we first define the model of the coil driver and then discuss about open-loop and closed-loop coil driver architectures. The advantages of the closed-loop topology and its design criteria was discussed. And finally, the step by step design procedure of high-current broadband DC to 100 kHz with 1 $A_{p\text{-}p}$ output current described in detail.

2.2 Ideal Coil Driver

As the generated magnetic field directly related to the current passing through the coil, for a broadband coil driver with fixed magnetic field over the operating frequency, we need a driver to supply a fixed current into the coil independent of the operating frequency.

In an ideal coil (without parasitic effects), impedance of the coil as shown in equation 2.15, linearly increases with the frequency.

$$Z_L(j\omega) = j\omega L \,, \tag{2.15}$$

and the current passing through the coil will be

$$i_L(j\omega) = \frac{v_L}{j\omega L} \,. \tag{2.16}$$

For an amplifier stage as shown in the Fig. 2-11, the transfer function could be written as

$$G(j\omega) = \frac{v_L(j\omega)}{v_{in}(j\omega)} \,. \tag{2.17}$$

Here v_{in} is the input drive signal and G is the driver's transfer function. The drive signal is a pure sinewave signal with fixed amplitude and variable frequency (called as excitation frequency).

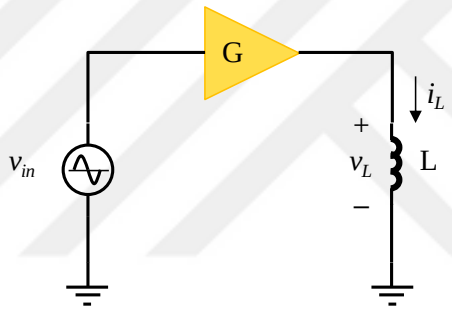

Figure 2-1 - Coil driver as an amplifier

Rewriting the coil current equation using equation 2.15, 2.16 and 2.17, we have

$$i_L(j\omega) = \frac{v_{in}(j\omega)G(j\omega)}{j\omega L} \,. \tag{2.18}$$

The driver's gain will be

$$G(j\omega) = j\omega L \frac{i_L(j\omega)}{v_{in}(j\omega)} \,. \tag{2.19}$$

Considering g_m as transconductance gain coefficient,

$$g_m = \frac{i_L(j\omega)}{v_{in}(j\omega)}, \tag{2.20}$$

the transfer function of the ideal coil driver could be written in general form as

$$G(j\omega) = j\omega L\, g_m. \tag{2.21}$$

The magnitude and phase of the driver also could be written as

$$\left|G(j\omega)\right| = \omega L\, g_m, \tag{2.22}$$

$$\angle G(jw) = +90°. \tag{2.23}$$

As seen in equation 2.22, for a fixed amplitude current operation over the operating frequency range, the voltage gain of the driver must increase linearly with frequency. In addition, as seen in the equation 2.23, in phase sensitive applications in ideal case it is important to have a fixed +90° phase response over the whole operating frequency range which is not an easy task in practical circuits.

2.3 Open-Loop Coil Driver

The main purpose of the coil drive is to maintain a fixed amplitude current passing through the coil independent of the frequency (in desired operating frequency range). Based on the preferred control method, there are two implementation topologies, open-loop and closed-loop. Closed-loop systems instead of their complexity and higher cost, generally have more advantageous over open-loop systems [17,18]. Fig. 2-2 shows an open-loop topology. In this system, an RC network increasing the gain of the voltage amplifier by increasing frequency.

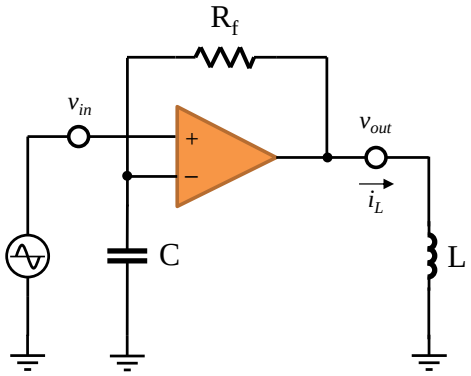

Figure 2-2 - Open-loop coil driver topology

The voltage gain of the system could be written as:

$$G(j\omega) = 1 + \frac{R_f}{Z_C} = 1 + j\omega C R_f \quad (2.24)$$

.

And for the current gain or the transconductance we have:

$$g_m = \frac{i_L(j\omega)}{v_{in}(j\omega)} = \frac{1 + j\omega C R_f}{j\omega L} \quad (2.25)$$

,

Assuming the fact that the impedances are much higher than one, then the equation 2.14 could be simplified as follows:

$$g_m = \frac{C R_f}{L} \quad (2.26)$$

.

Now for a fixed current amplitude this gain must be remain unchanged in the desired frequency range. Selecting a proper feedback resistor value, the capacitor value will be:

$$C = g_m \frac{L}{R_f} \quad (2.27)$$

.

With proper R_f and C values theoretically one could maintain a fixed current amplitude over the desired frequency range, but practically there are few important disadvantaged in this topology which made this method unsuitable for most of the applications specially for precision applications.

First of all the current gain of the system depends on the load inductance. This means that for a fixed input voltage, the output current amplitude will be changed with

the coil inductance. This is very important issue, where mass production was thought. Using this method will require tuning and calibration of each circuit.

Linear behavior of the components also is very important in this topology, because the constant current gain characteristic of the driver completely lies on the matched decrease of the capacitor's impedance versus increase of the coil's impedance, in the frequency domain. But in real components, evidence of parasitic effects causes deviations from the ideal behavior. Because of this effect, the open-loop only could be used for a limited frequency range where the mismatched impedance changes remain in a certain tolerance.

In our project, where PPM level stabilities were intended to be achieved, this method was not suitable at all and more sophisticated closed-loop topology was developed.

2.4 Closed-Loop Coil Driver

Like all of the close-loop control systems, in this topology we need a current feedback and a gain control mechanism to maintain a fixed amplitude at the output. Fig. 2-3 shows the basic form of the closed-loop coil driver topology.

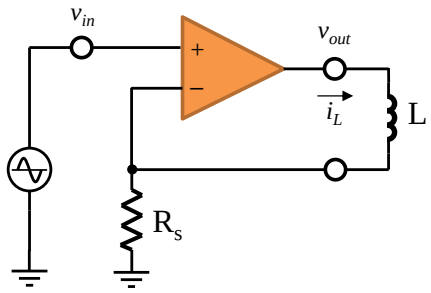

Figure 2-3 - Closed-loop coil driver topology

Here we used a series resistor with the coil as the current monitoring device. The voltage on the resistor is the feedback of the current passing through the coil. The Op-Amp in the circuit will try to equate the feedback signal from the coil current and the input signal both in the amplitude and phase. In this interesting topology, beside of the fixed amplitude of the output current, the phase of the current also will be matched with

the input signal. The zero-phase native of this topology is an important property especially for phase sensitive applications.

Equating the voltages of the inverting and non-inverting input ports of the op-amp, one could write the equations for the output current signal as follows:

$$i_L = \frac{1}{R_s} v_{in} \quad . \tag{2.28}$$

And the current gain or transconductance of the circuit will be:

$$g_m = \frac{1}{R_s} \quad . \tag{2.29}$$

As seen in the equation 2.18, the transconductance gain of the system is only depends on the series feedback resistance (R_s) and there is no load-dependent behavior.

It means that for a range of output coil's inductance where the output of the signal remains in the safe voltage and current limits, independent of its inductance and other parameters, current gain of the system remains fixed. And with a fixed amplitude input voltage signal we will have a fixed amplitude current signal at the output.

Rewriting the output voltage, we have:

$$v_{out} = i_L \left(j\omega L + R_s \right) . \tag{2.30}$$

Assuming $R_s << j\omega L$, the voltage gain of the system will be:

$$G(j\omega) = \frac{(j\omega L) i_L}{v_{in}} = j\omega L \, g_m \quad . \tag{2.31}$$

And based on the fact that in this topology the current gain g_m is a real number, the magnitude and phase of the voltage gain will be

$$\left| G(j\omega) \right| = \omega L \, g_m \, , \tag{2.32}$$

$$\angle G(jw) = +90°. \tag{2.33}$$

Comparing the equations 2.32 and 2.33 with 2.22 and 2.23 shows that the closed-loop topology is an exact implementation of the ideal coil driver.

2.5 Practical Implementation

Practically, the implementation of the closed-loop topology is a challenging task especially where high output power and wide operating frequency are needed. In our research project, fabricated MEMS cantilevers mainly have resonance frequencies up to 100 kHz in gases and up to 50 kHz in liquids. Therefore, we consider the upper bandwidth requirement of the driver to 100 kHz.

Returning to coil design topic, as discussed before, we need to minimize the inductance of the coil to reduce the power supply voltage requirement. Using higher supply voltages also will result in higher power dissipations in the output stage of the driver.

As the output stage, I preferred to use a high-voltage, high-current operational amplifiers where their maximum operating voltages and output currents meet our requirements such as OPA544T [47]. The OPA544T with $4A_{p\text{-}p}$ ($2A_{rms}$) maximum output current and 70V (±35V) of maximum supply voltage is a good choice for our voltage and current requirements.

2.6 Practical Parameters of the Coils

Considering the maximum output current of 2 $A_{p\text{-}p}$, and maximum 10°K heating in the coil, based on maximum allowable current tables and on-line wire heating calculators[1], I find the minimum wire cross section area around 0.05 mm^2 or 0.25 mm in diameter. Taking 25 µm insulation thickness into the account, a 0.3 mm diameter wire will be sufficient for our coil design.

Minimizing the inductance and maximizing the turn number (as the electromagnetic force is related to $\boldsymbol{N \cdot i}$) and keeping the parasitic capacitances negligible in the operating frequency range are the main coil design criteria. In the driver side also

[11] http://www.axon-cable.com/en/06_customerArea/03_toolbox/04_intensity/index.aspx

gain-bandwidth limit, slew-rate limit and the dissipated power values also must be taken into the account for the final design specifications.

From the MEMS die dimensions we have already set a coil diameter of 14 mm for our coil design. For finding the frequency range where the parasitic capacitances are negligible, I made different handmade single-layer coils with turn numbers of 20, 40, 60 and 80 and also two-layer versions of 20×2, 30×2, 40×2 and 60×2 turns. The phase and impedance response of these coils were measured with the experiment setup discussed in Appendix I (See Fig. 9-5).

As the final result, we found the 40 turn single-layer coil as the optimum coil design for high-frequency ranges up to 100 kHz. Allowing some parasitic capacitances in two-layer designs, the 40×2 (80-turn, two-layer) coil showed the optimum results for applications under 50 kHz frequency range (In-Liquid experiments). Fig. 2-4 shows the measured and calculated frequency response for the 40 × 2 (80-turn, two-layer) coil. The coil's resistance measured around 2.8 Ω and its inductance based on the frequency response calculated around 70 µH. The theoretical value for inductance calculated as 67.5 µH. As seen in the graphs, measured values are in a very good agreement with theoretical values.

The effect of the parasitic capacitances is become observable after 10 kHz and increase to a few degrees at around 70 kHz. For high frequency applications where this level of parasitic effect may affect the system, the single layer coils could be preferred.

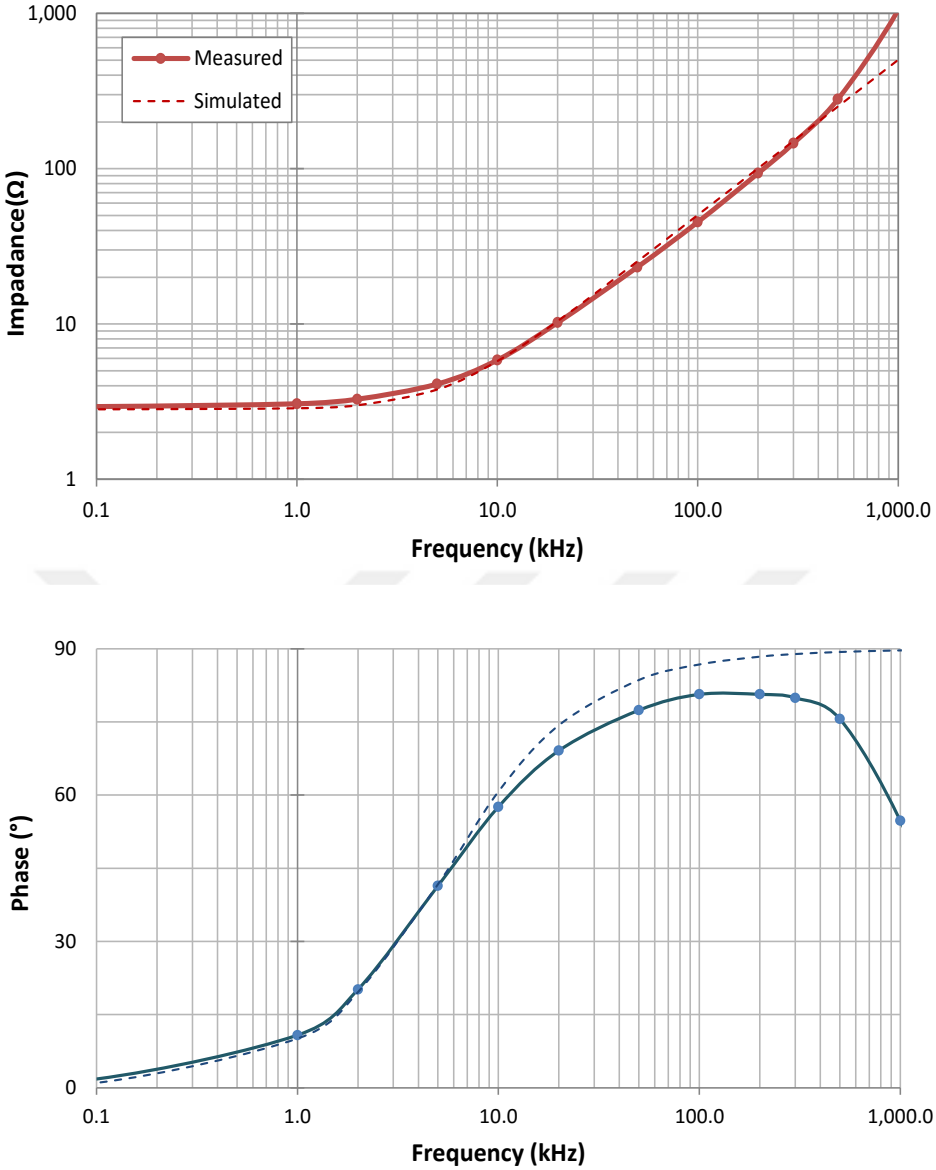

Figure 2-4 - Frequency response of the two layer 80-turn coils

2.7 Generated Magnetic Field

For verifying the amount of the generated magnetic field, an experiment was setup and the AC magnetic field was measured versus the passing current through the coil using a commercial Tesla meter. As the bandwidth of the Tesla meter was limited to 10 kHz, the experiment done at 10 kHz. Taking the thickness of the Tesla meter's head and small air gap between the coil, into the account,

For calculating the theoretical values, the effect of the Tesla meter's bandwidth and also the distance of the Tesla-meters head to the coil were taken into the account. Fig. 2-5, shows the measured and theoretical values.

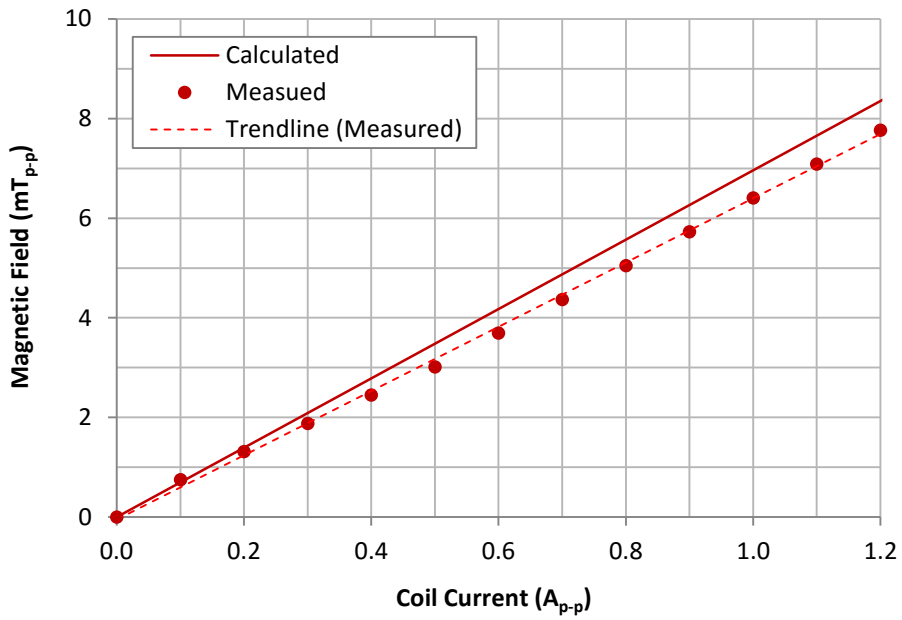

Figure 2-5 - Generated AC magnetic field vs. coil current

2.8 Maximum Output Voltage

Based on the inductance and impedance of the optimum coil, and the design constrains of 1 $A_{p\text{-}p}$ output current up to 100 kHz, the required maximum ratings of the power stage could be calculated. For the simple coil model with a series current shunt resistor R_S the output voltage is:

$$v_{out} = i_L (j\omega L + R_L + R_S), \tag{2.34}$$

and the maximum output voltage will be:

$$v_{out,\max} = i_{L,\max} \left| j\omega_{\max} L + R_L + R_S \right|. \tag{2.35}$$

Theoretically, for minimizing the resistive losses in the series feedback resistor *Rs*, its resistance must be minimized. In the other side, as the amplitude of the current feedback signal is directly related to resistance of the R_s. Low feedback voltages force the power stage to operate at higher gain values and this will increase distortions and noise in output waveform.

In practical applications, a range of 100 mΩ up to few ohms are suitable values for our nominal current of 1 $A_{p\text{-}p}$. For optimum shunt resistance value, different resistances were tested practically on the closed-loop circuit and the best result in terms of output waveform distortion and output noise level achieved with 2 Ω resistor.

The resistance of the coils was measured about 1.4 Ω and 2.8 Ω and impedance values of 11.7 Ω and 42.4 Ω, at maximum operating frequency of 100 kHz respectively for single-layer 40 turns and double-layer 2×40 turns coils. Taking the resistance values of the shunt resistor, for 1 $A_{p\text{-}p}$ coil current, the maximum output voltage will be around 46 $V_{p\text{-}p}$ with double-layer coil. This value could achieve with OPA544T with ±25V supply voltage. Maximum output voltage with OPA544T at its maximum supply voltage is around 62 $V_{p\text{-}p}$. Lowering the supply voltage will reduce the dissipated power in the output stage. This topic will be discussed in detail in 2.6.6. Fig. 2-6 shows the simulated output voltage vs. operating frequency with 2 Ω shunt resistor.

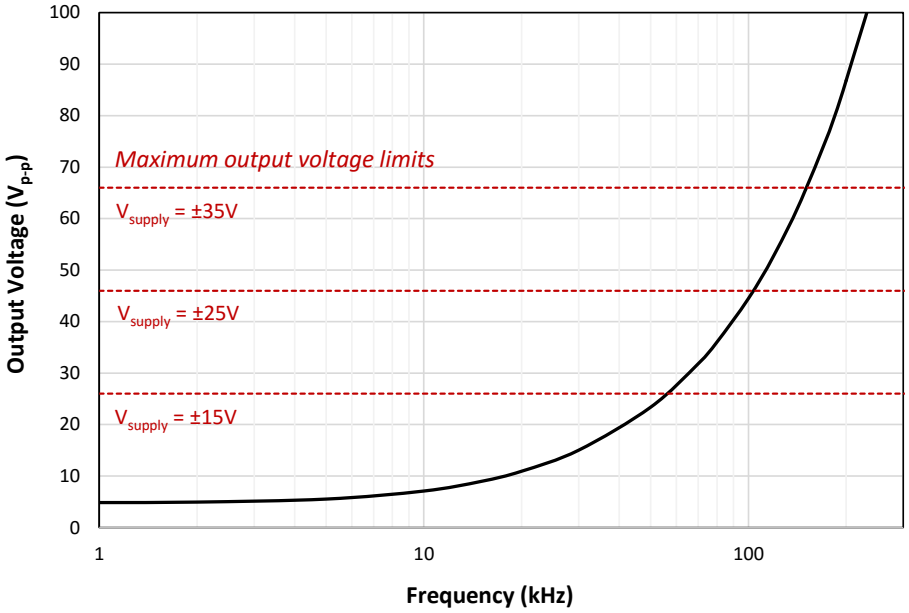

Figure 2-6 - Output Voltage vs. Frequency

Based on the maximum output voltage of the OPA544T working at maximum allowable supply voltage of ±35 V and for 1 A_{p-p} coil current, the maximum operating frequency based on the supply voltage limit will be around 130 kHz.

2.9 Gain Bandwidth Product Limit

One of the most important specifications of the operational amplifiers is their Gain-Bandwidth product parameter (designated as GBWP, GBW, GBP or GB). Gain-Bandwidth product of the OPA544T is 1.4 MHz.

In the closed-loop coil driver the input signal of the op-amp is a fixed amplitude sine wave (excitation signal), but the output voltage and therefore the gain of the op-amp depends on the operating frequency. For safe operation of the op-amp, the gain of the system must remain below its gain bandwidth product limit. Fig. 2-7 shows the gain and the gain-bandwidth product limit for OPA544T in our closed-loop drive circuit with double-layer coil.

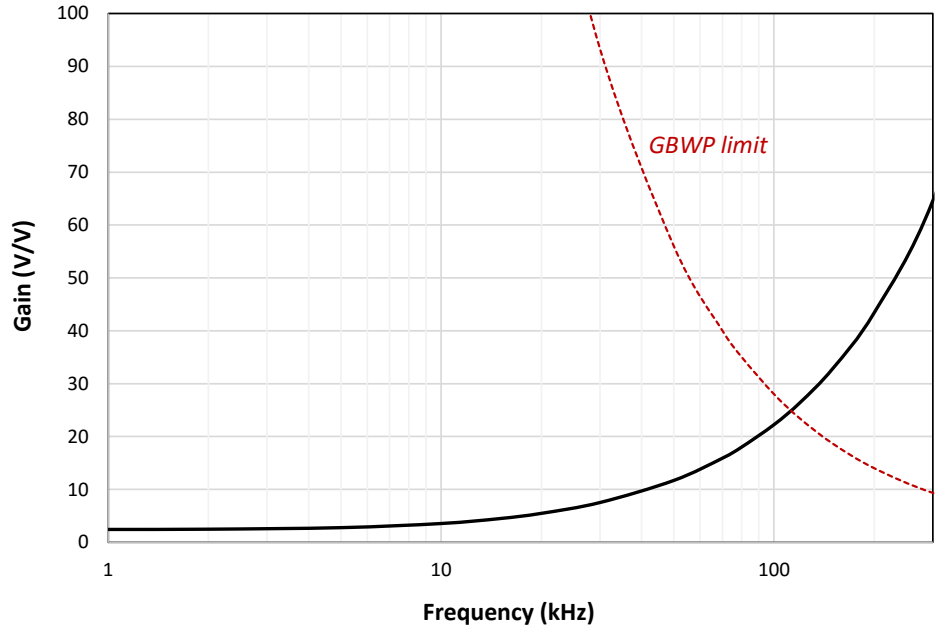

Figure 2-7 – Required gain and Gain-Bandwidth product (GBWP) limit

As seen in the Fig. 2-7, the maximum achievable gain in our closed-loop circuit with 1 $A_{p\text{-}p}$ coil current a 2 Ω shunt resistor, is around 110 kHz.

2.10 Slew-Rate Limit

Another design parameter in Op-Amp circuits is the slew rate limit. Slew rate is defined as the maximum rate of change of output voltage per unit of time and is electronic circuit expressed as V/μs as follow:

$$SR = \max\left(\left|\frac{dv_{out}(t)}{dt}\right|\right), \tag{2.36}$$

and for an amplifier in all points this condition must be satisfied. This parameter is 8 V/μs for OPA544T [47].

For a sinusoidal waveform with amplitude V_p,

$$v_{out}(t) = V_p \sin(2\pi f t), \tag{2.37}$$

slop of the output voltage is the derivative:

$$\frac{dv_{out}(t)}{dt} = V_p(2\pi f)\cos(2\pi f t) \quad , \tag{2.38}$$

The highest slop occurs at the zero-crossing (t=0) where the cosine is one. Therefore, for a sine wave with amplitude of V_p, the slew rate condition will be:

$$2\pi f V_p < SR \quad , \tag{2.39}$$

Fig. 2-8 shows the slew rate and the slew rate limit of our circuit using OPA544T with 40 turn coil.

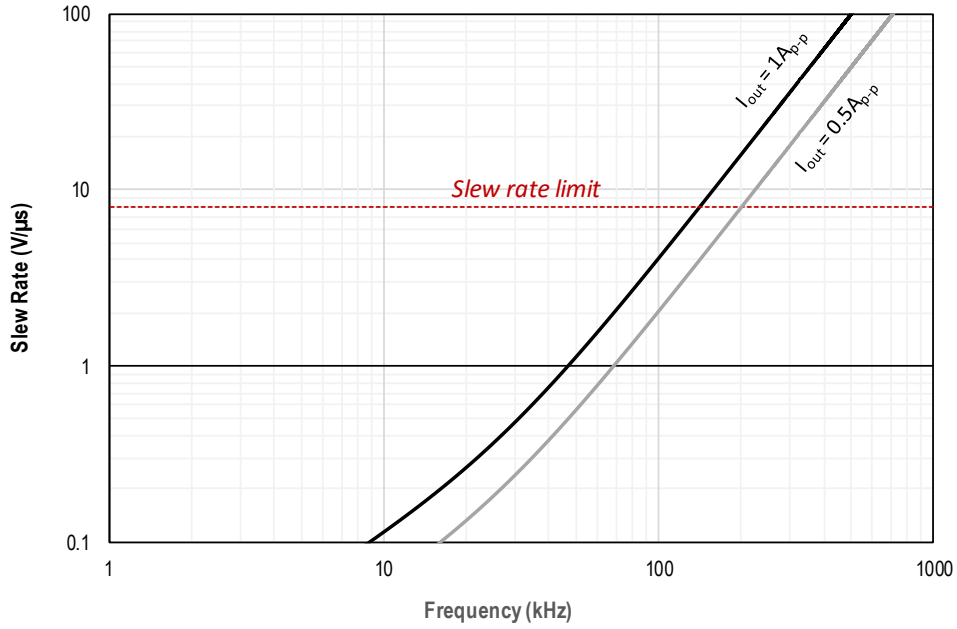

Figure 2-8 - Slew rate and SR limit for output current of 1 A_{p-p} and 0.5 A_{p-p}

As shown in Fig. 2-8, slew rate limit of the OPA544T is sufficient for operating up to 130 kHz at nominal current of 1 A_{p-p} and up t0 200 kHz with 0.5 A_{p-p} of coil current.

2.11 Dissipated Power

Calculation of dissipated power and heat management in power electronics components is one the most important design stages. Minimizing the dissipated heat is also important because of the energy saving issues and also to reduce heat induced noises which are more important in precision and noise sensitive applications.

The dissipated power in output stage is equal to voltage drop at the output stage multiplies by the current passing through. In inductive loads, maximum output current occurs when the output voltage is near zero and full supply voltage will drop at the output stage. Dissipated power could be simulated using the instantaneous values of current and voltage drop across the power op-amp. Fig. 2-9, shows the simulation results with different supply voltages at 1 A_{p-p} coil current.

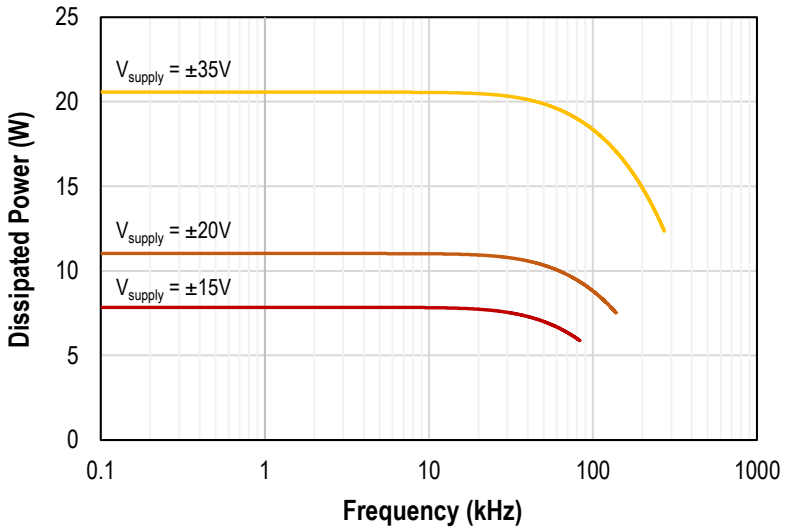

Figure 2-9 - Dissipated power in output stage for different supply voltages

As discussed before, ±20 V supply voltage will be sufficient to maintain 1 A_{p-p} in the coil up to 100 kHz. At lower operation frequencies for minimizing the dissipated power, the supply voltage could be reduced. Based on the dissipated power levels, for cooling of the output stage, a heat sink must be used. Temperature of the heat sink could be calculated as follows:

$$T = (\theta_{jc} + \theta_{ca})P_{diss} + T_a \quad (2.41)$$

Here θ_{jc} and θ_{ca} are the junction to case and case to ambient thermal resistances respectively and T_a is the ambient temperature.

With 2.7°K/W thermal resistance (θ_{jc}) of the OPA544T, assuming maximum 12 W of dissipated power (±25V supply voltage) and ambient temperature of 25°C, using a forced air cooled small Aluminum heat sink with thermal resistance of 0.3°K/W, resulting heat sink temperature will be around 60°C.

2.12 Design Optimization

Since the design parameters for the coil and driver are dependent to each other, it will be very useful to have a tool to combine all the design parameters and see the effect of each parameter in the overall design. For this aim an Excel code was developed. This code, uses all of the coil and Op-Amp parameters and also design constrains and generates all of frequency related circuit parameters described in previous sections as result. For visualizing the limiting factors, all of them were calculated based on the output voltage to show on a single graph and finally the bandwidth of system in terms of generated magnetic field were shown. Fig. 2-10 shows a screen shot of this code.

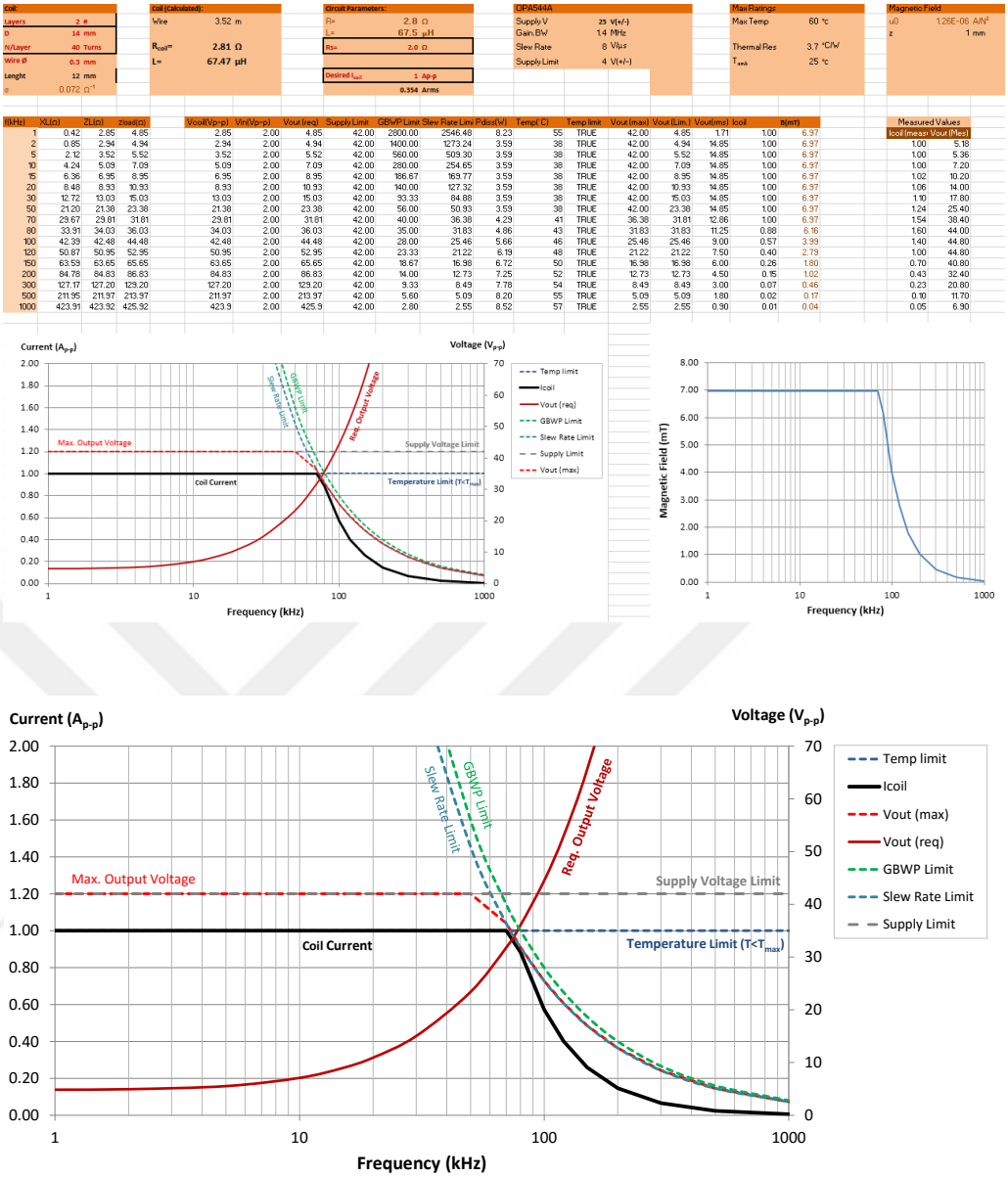

Figure 2-10 - Design optimization tool showing all design parameters

2.13 Simulation and Experimental Results

Fig. 2-11 shows the implemented closed-loop coil driver circuit.

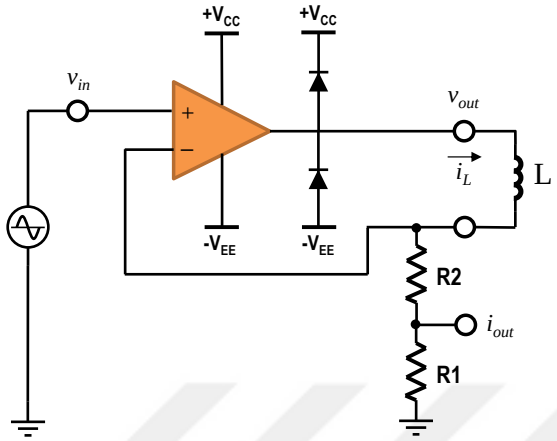

Figure 2-11 - Closed-loop coil drivers circuit with current monitoring output

For measuring the current passing the coil, the series shunt resistor was divided to two 1 Ω resistors. The voltage across the *R1*, named as i_{out} will be equal to the coil's current. The silicon diodes are also added for protection of the Op-Amp from the potential induced high voltages in the coil.

The frequency response of the circuit, with exact component models was simulated using NI MultiSim and compared with experimental results. The frequency response was measured experimentally using a sweep generator as a sinewave source and a spectrum analyzer connected to current monitoring output. Fig. 2-12 shows the simulation and experimental results.

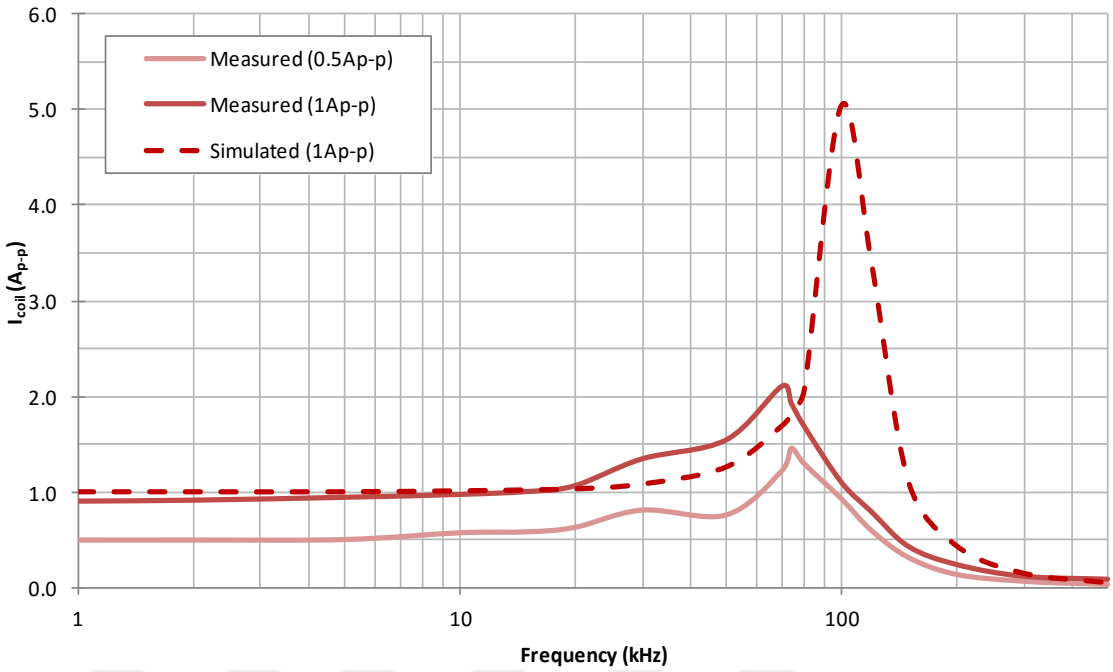

Figure 2-12 - Simulation and measured frequency response of the coil driver

As shown in the Fig. 2-12, a gain peaking occurs at frequencies around 100 kHz. This effect arises from the input and output capacitances of the Op-Amp and could not be cancelled completely, but could be minimized using some compensation methods. In this experiment, for reducing the dissipated power, the circuit was driven with ±15 V power supply and the current breakdown occurs at around 70 kHz as discussed before in 2.6.1. Since the frequency response simulations done in AC mode, the DC supply parameters are not took into the account and the current breakdown doesn't occur in the simulations.

Based on the frequency response experiment, the circuit showed a nearly flat current response from DC up to 20 kHz, but for frequencies higher than 20 kHz distortions appears in the current wave form. Fig. 2-13, shows the current wave for different frequencies from 1 to 100 kHz at 1 A_{p-p} coil current with single layer coil.

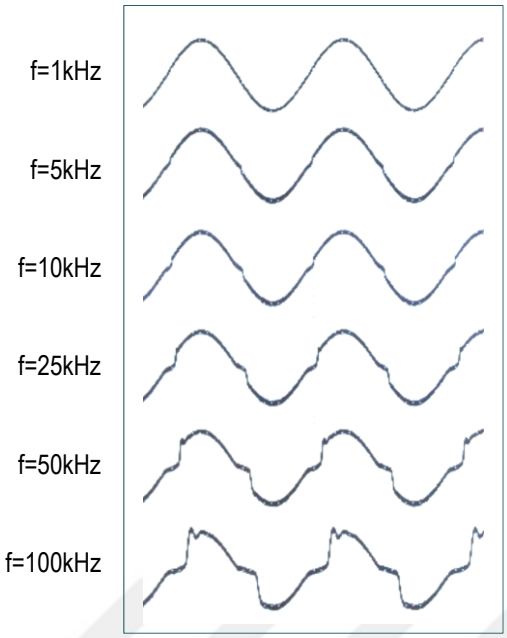

Figure 2-13 – Coil current waveform for different operating frequencies

As shown in the Fig. 2-13, the distortions occur at the zero-crossings and results in harmonic generations in the coil current. In our MEMS resonance tracking project, evidence of high harmonic is problematic because of higher mode excitation of the MEMS cantilevers.

For solving this problem, we developed to a dual stage architecture for closed-loop coil driver using two Op-Amps. The first one as the error amplifier and the second one as the high current buffer for output stage. In this architecture, the output stage works in unity gain mode and the error amplifier which could be a faster and smaller Op-Amp provides the required gain. Implementing this circuit, resulted in a very clean current waveform and also lower gain peaking and wider bandwidth. We used TL071 general purpose JFET-input op-amp [48] as the first stage but for higher supply voltage requirements we used OPA552 high-voltage op-amp [49] in final design. Fig. 2-14 shows the dual stage architecture.

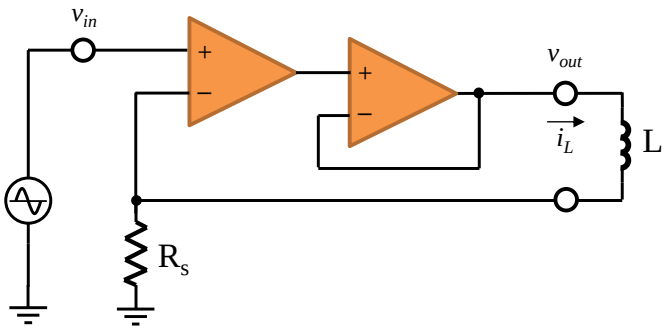

Figure 2-14 - Dual stage closed-loop coil driver architecture

The main problem that observed in this architecture, was the instability of the system which caused oscillations in the absence of input signal. The system was simulated and analyzed using exact component models and the oscillations is also appeared in transient mode analysis. Fig. 2-15, shows the transient response of the system without input signal.

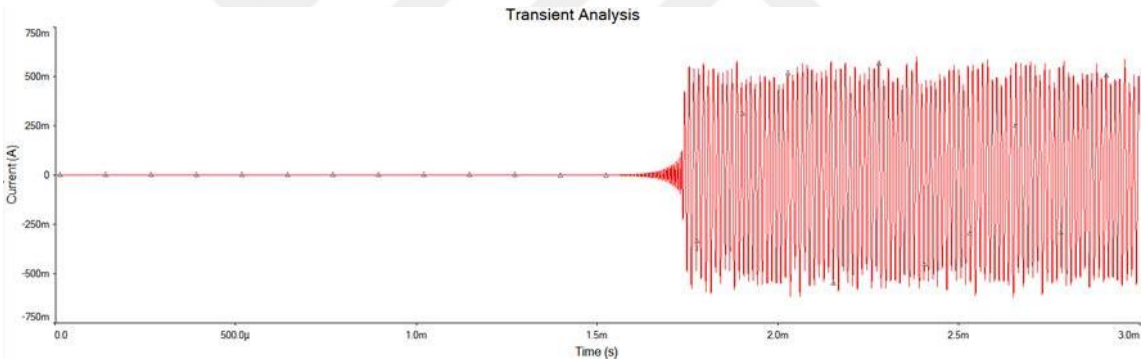

Figure 2-15 – Simulation result of oscillations in dual stage coil driver

2.14 Compensator Design for Stabilizing

For solving the stability problem, a compensating phase-lead filter was employed in between dual stages. The filter compensates for phase delays of the system. Fig. 2-16, shows the architecture of the compensated method.

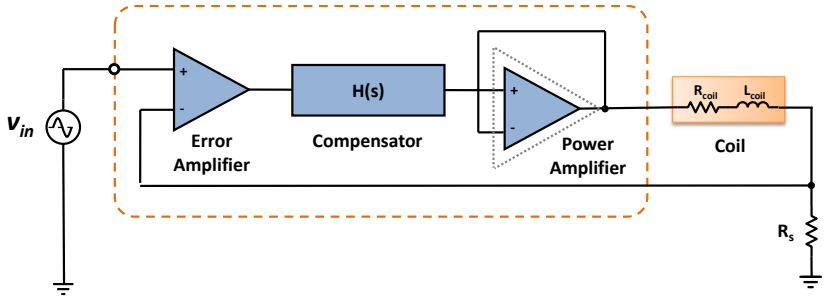

Figure 2-16 - Overall architecture of the dual stage coil driver with compensating filter

For optimizing the lead compensator parameters, a Simulink model was developed. Fig. 2-17 shows the developed model.

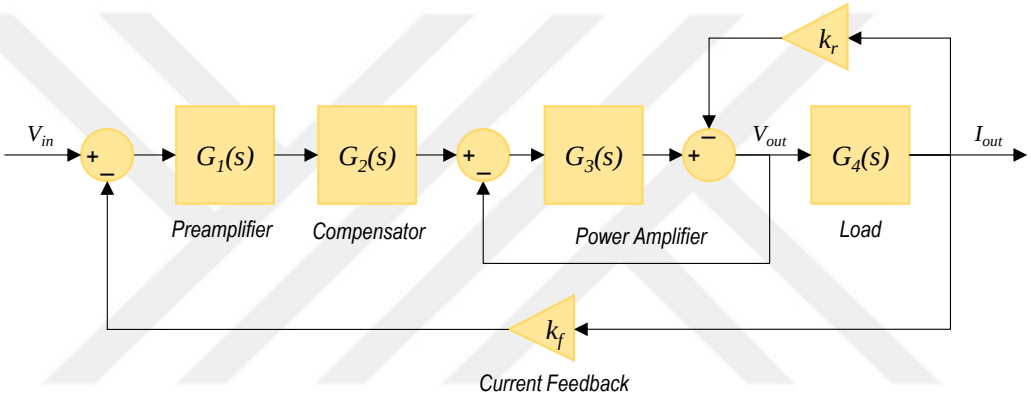

Figure 2-17 - Control model of the compensated dual stage coil driver

Transfer function of the amplifier stages was built using band limited op-amp model with non-linear saturation and rate limiter blocks for simulating the supply voltage limit and slew rate limit, respectively. Effect of the output impedance was neglected for the first op-amp, but for the power stage op-amp was included in the model. Simulation results showed excellent agreement with experimental measurements. Transfer function of the lead compensator in general form could be expressed as

$$G_2(s) = \frac{1}{\alpha}\left(\frac{1+\alpha\tau s}{1+\tau s}\right) \tag{2.42}$$

Where α and τ are attenuation and time constants, respectively as follows:

$$\alpha = \frac{R_1 + R_2}{R_1} \tag{2.43}$$

$$\tau = \frac{R_1 R_2}{R_1 + R_2} C \tag{2.44}$$

For calculating the optimum component values, parametric simulations were done using NI MultiSim and optimum values was found as α = 0.6 and τ = 160 ns. Fig. 2-18 shows the pole-zero analysis of the compensated and uncompensated system. The instability of the uncompensated circuit appeared as right hand poles in the s-plane.

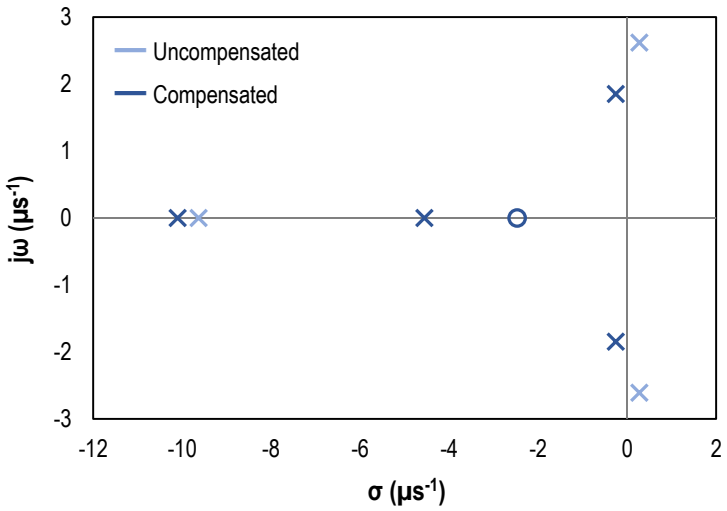

Figure 2-18 - Pole-zero analysis of the compensated and uncompensated dual stage driver circuit

Developed control model was used to compare the single and dual stage circuits. Fig. 2-19 shows bode plot simulation results.

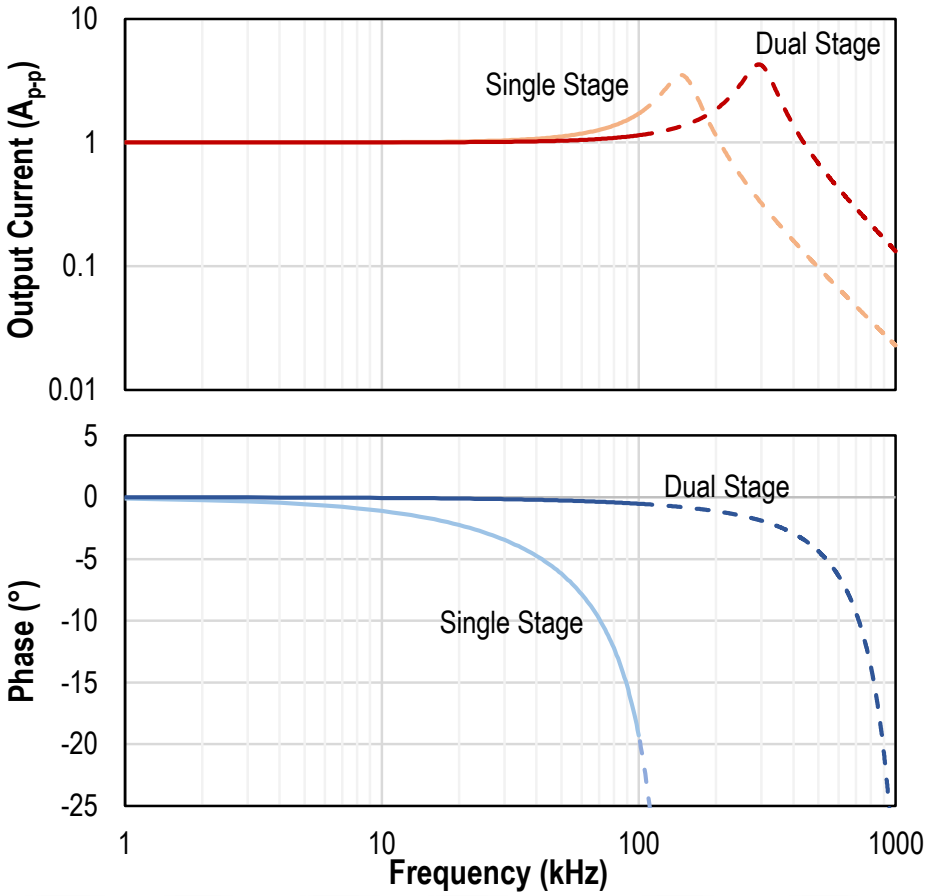

Figure 2-19 - Bode plot simulations of the single and dual stage coil driver

Simulation results shows improvement in frequency response of the system especially in the phase response. For more clear analysis, step responses of the single and dual stage compensated architecture were simulated and also measured experimentally. Fig. 2-20 shows the square wave (step) response simulation results comparing the real captured waveforms.

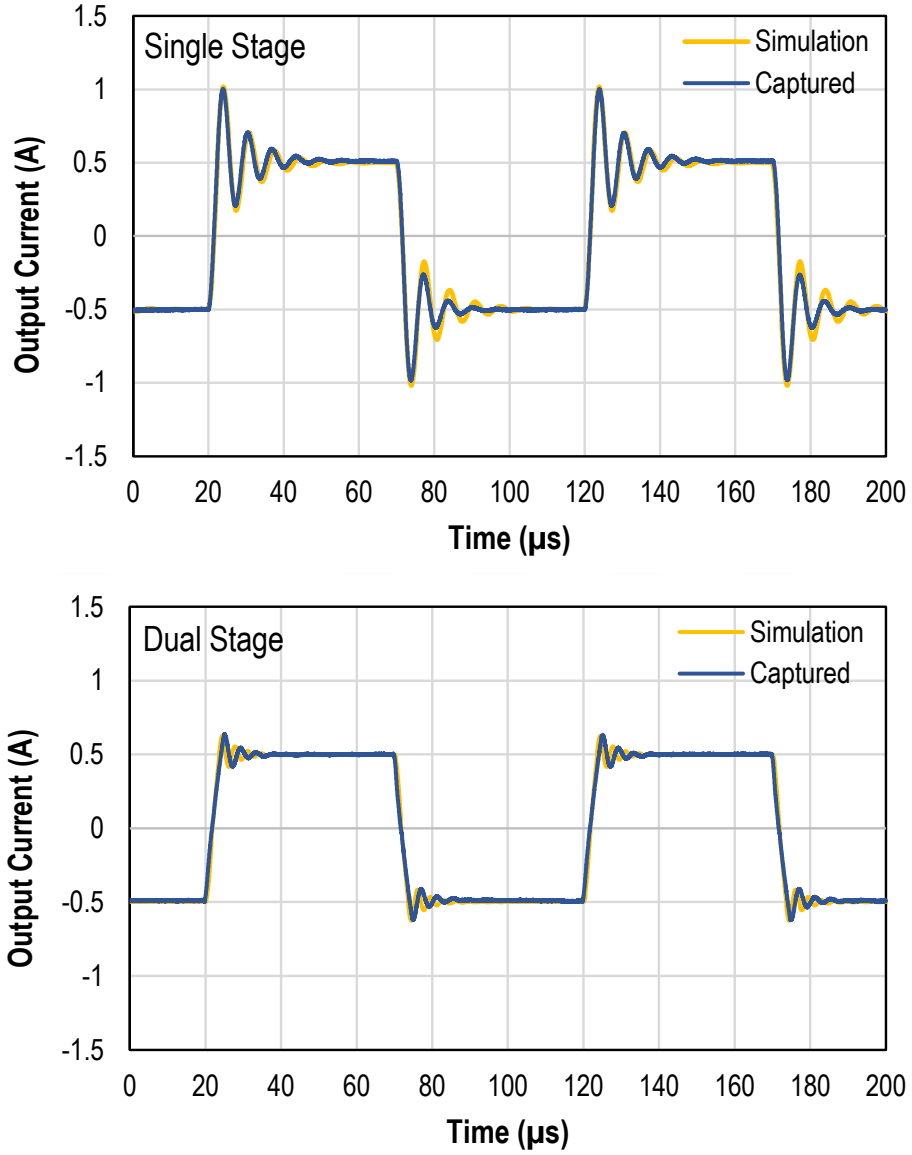

Figure 2-20 - Simulation and measured square wave response of the single and dual stage coil driver circuits

Fig. 2-21 shows the output current waveform captured at 1 $A_{p\text{-}p}$ and frequency of 100 kHz.

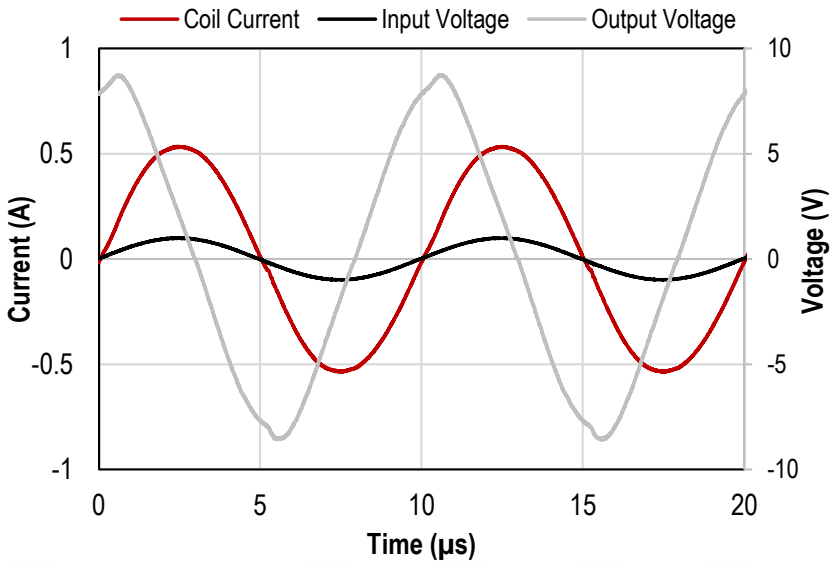

Figure 2-21 - Waveforms of dual stage coil driver at nominal current and maximum operating frequency

Comparing to the output waveform of the single stage circuit, proposed dual stage configuration dramatically reduced the distortions in the output current. Maximum total harmonic distortion of 0.96% was measured with 1 A_{p-p} output current at frequency of 100 kHz. Fig. 2-22 plots the measured total harmonic distortion of single and dual stage configurations versus the frequency.

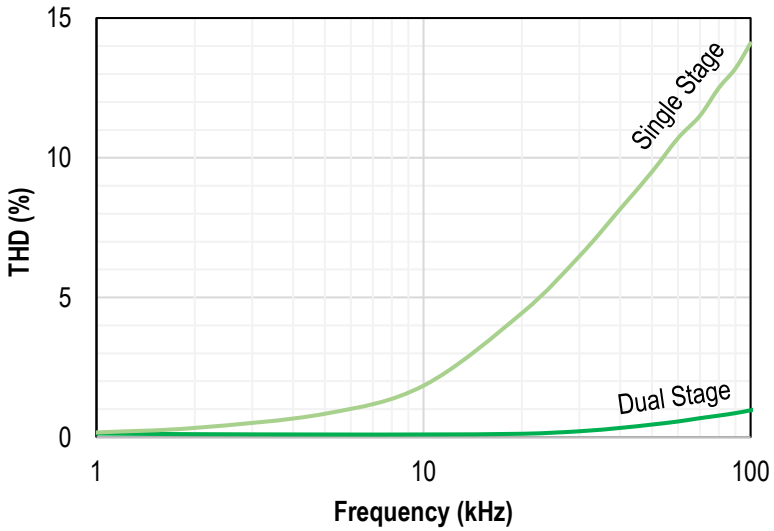

Figure 2-22 - Total harmonic distortions of the current wave form

In terms of phase delay, dual stage configuration showed significant reduction in phase delay with respect to single stage configuration. Maximum phase delay of about 2° was measured with dual stage driver at 100 kHz where this value reaches 22° with single stage driver. Fig. 2-23 shows the phase response for single and dual stage configurations.

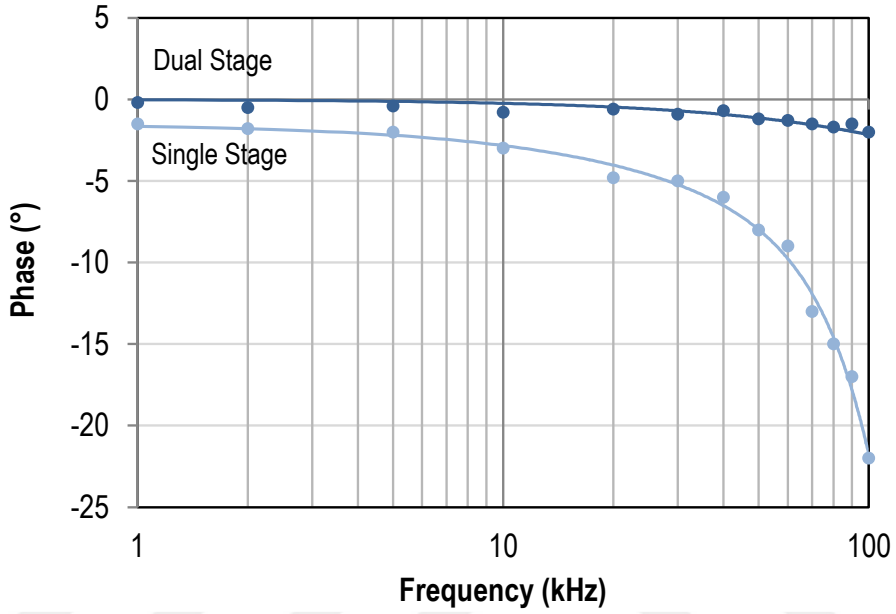

Figure 2-23 - Phase response of single and dual stage drivers at 1 A_{p-p} coil current

Fig. 2-24 shows the bandwidth of the dual stage driver as the coil current vs. the frequency at different coil current amplitudes. Bandwidth of the system increases up to 180 kHz at 0.5 A_{p-p} and up to 250 kHz in lower coil current of 100 mA_{p-p}. Small gain peaking in order of few percent occurs at the higher end of the frequency response due to the parasitic capacitance effect.

An input potentiometer is used for gain adjust, two series protection at the input are employed for protection of the circuit from high input voltages and also high output current. Two diodes at the output is also are protecting diodes for eliminating induced voltages in the coil. Fig. 2-25 shows the final circuit of the compensated dual stage driver.

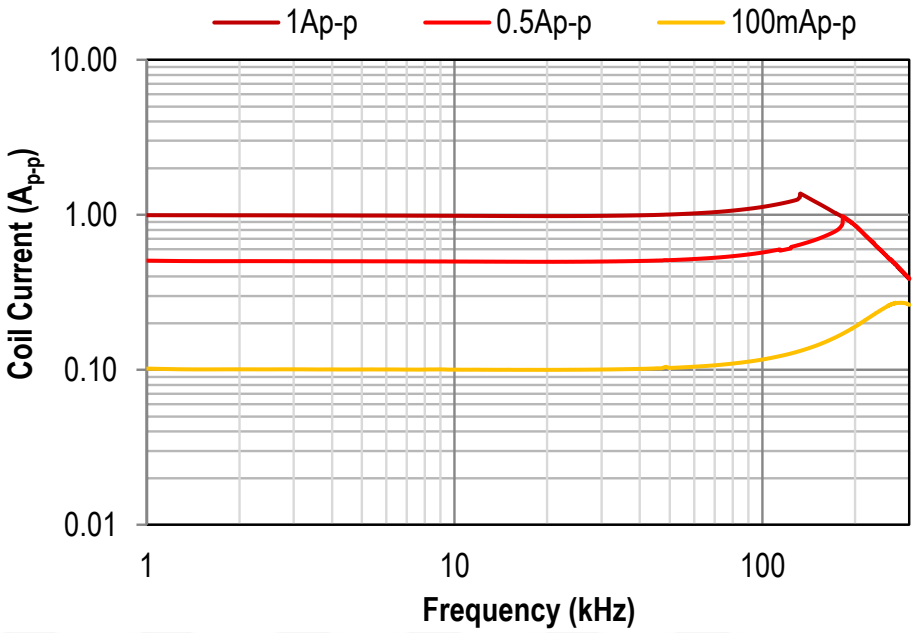

Figure 2-24 - Frequency response of the dual stage driver

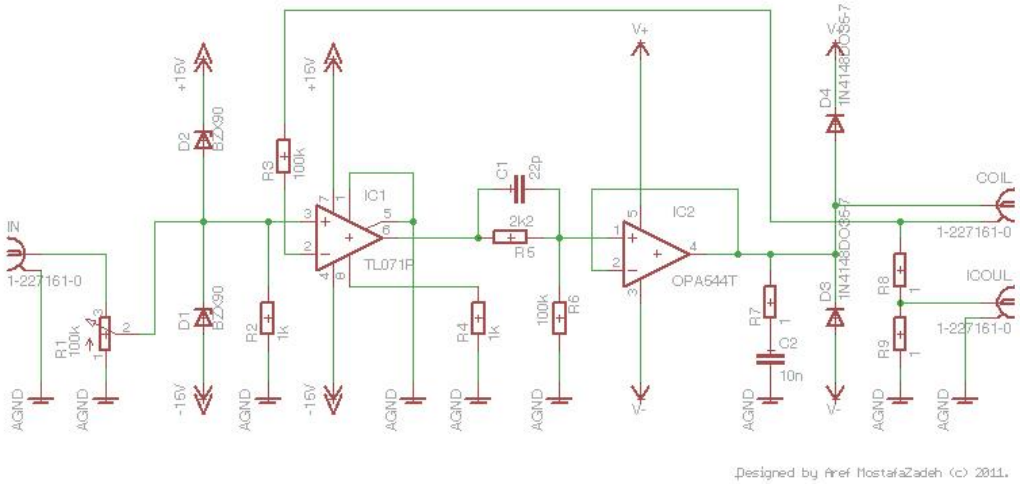

Figure 2-25 - Compensated two-stage closed-loop coil driver

2.15 PCB Design

After the finalizing the circuit parameters, a PCB designed for the coil driver. An additional reverse voltage and over current protection and also a fan power supply was added to drive the cooling fan at a fixed voltage independent of the supply voltage. Fig. 2-26 and 2-27 shows the designed PCB and the constructed final board.

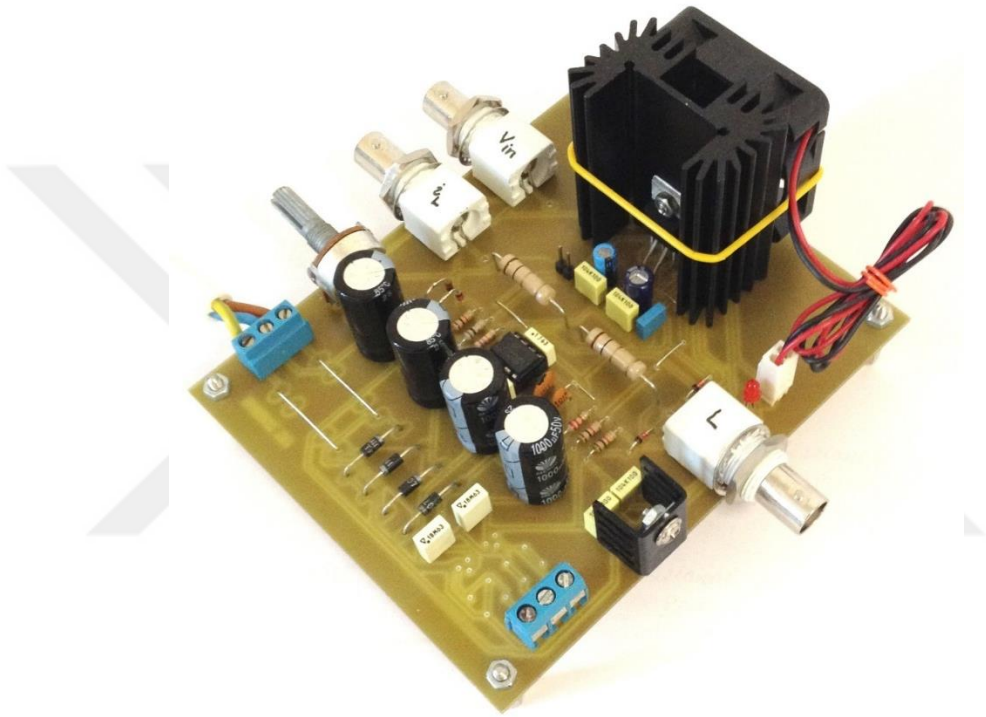

Figure 2-26 – Assembled PCB of the closed-loop dual stage coil driver

Board has a voltage input labeled as V_{in}, and a symmetric supply voltage input of ±15V up to ±35V (Blue terminal at left side). The BNC output labeled i_L is the current monitor output and the BNC labeled L is the output to the coil.

2.16 Characterization and Comparing with the Previous Driver

For characterization and comparing the developed closed-loop driver with the previous open-loop coil driver with 640-turn multilayer coil, we setup a couple of

experiments on both coil drivers. Fig. 2-28 to Fig. 2-31 shows the comparison results, the left side graphs are the old (open-loop) driver's results.

Because of the heavy distortions in the current wave form of the open loop driver, the current values are measured and presented as RMS values. The supply voltage of the open-loop driver is also set to its maximum value of ±18 V.

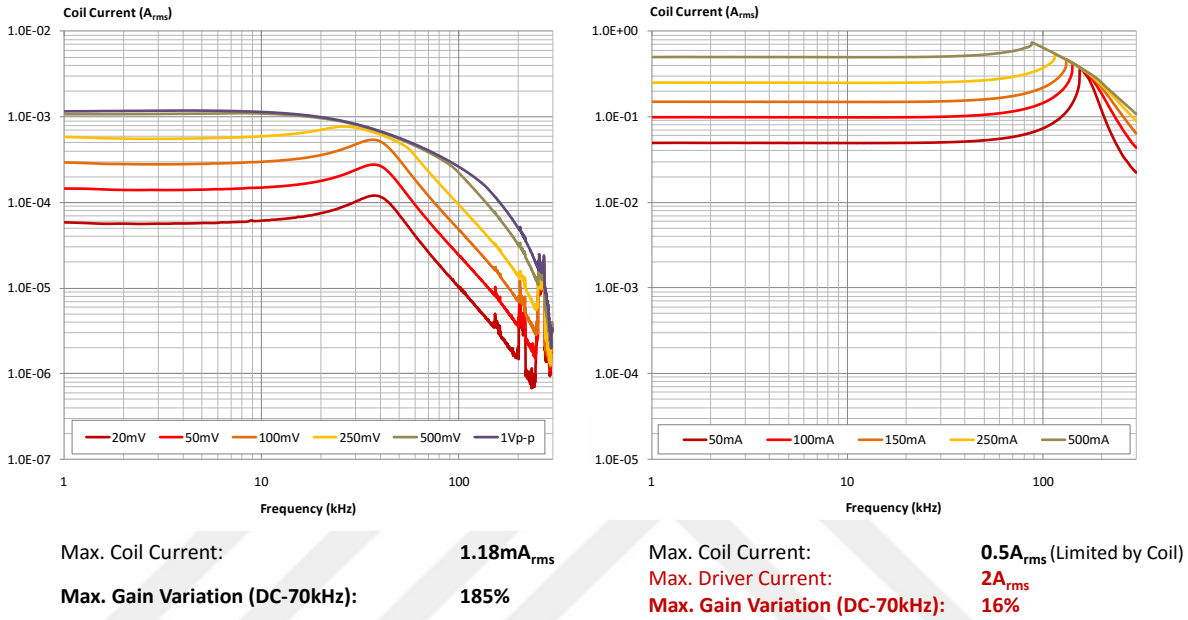

Figure 2-27 - Frequency response comparison for the open-loop and closed-loop driver

The maximum coil current was measured as 1.18 mA_{rms} with 185% gain peaking on its non-saturated region in the DC-70 kHz frequency range, while with the new closed-loop driver a nominal current of 0.5 A_{rms} with maximum of 16% gain peaking was demonstrated completely in linear region without any saturations.

Harmonic distortions are measured around 24% and 8% respectively for 2^{nd} and 3^{rd} order harmonics in the old open-loop driver with overall 49 dB (1/300) SNR ratio. Same parameters are 0.08% and 0.016% for 2^{nd} and 3^{rd} harmonics and >100 dB (1/160,000) for the closed-loop coil driver. Harmonic components was measured with frequency sweeping on a spectrum analyzer.

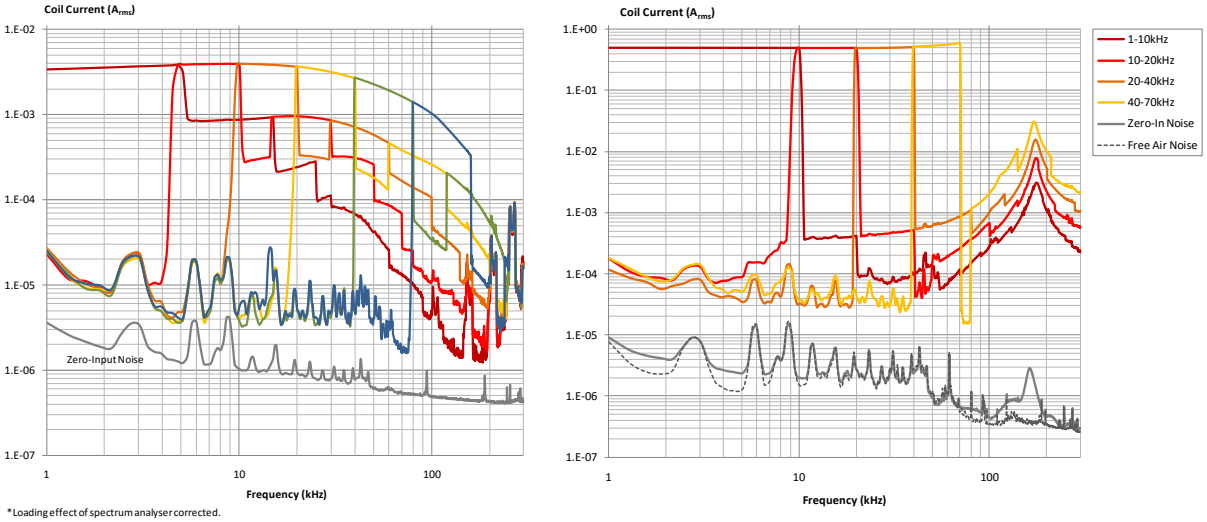

2nd. Harmonic (@20kHz):	**24%**	**2nd. Harmonic (@20kHz):**	**0.08%**
3rd. Harmonic (@20kHz):	**8%**	**3rd. Harmonic (@20kHz):**	**0.016%**
SNR (@50kHz):	**49dB (1/300)**	**SNR (@50kHz):**	**>100dB (1/160000)**

Figure 2-28 - Harmonic distortion and noise comparison of open-loop and closed-loop driver

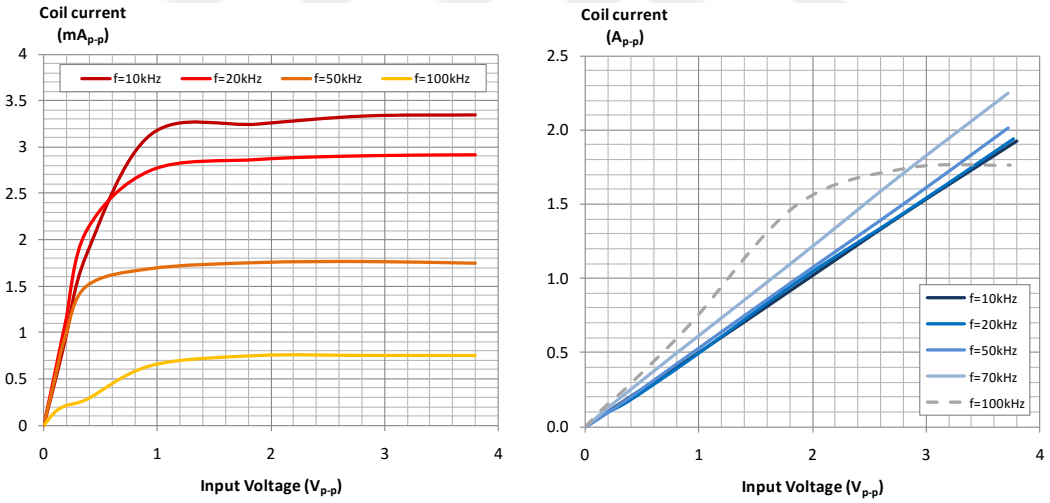

Figure 2-29 - Linearity comparison of open-loop and closed-loop driver

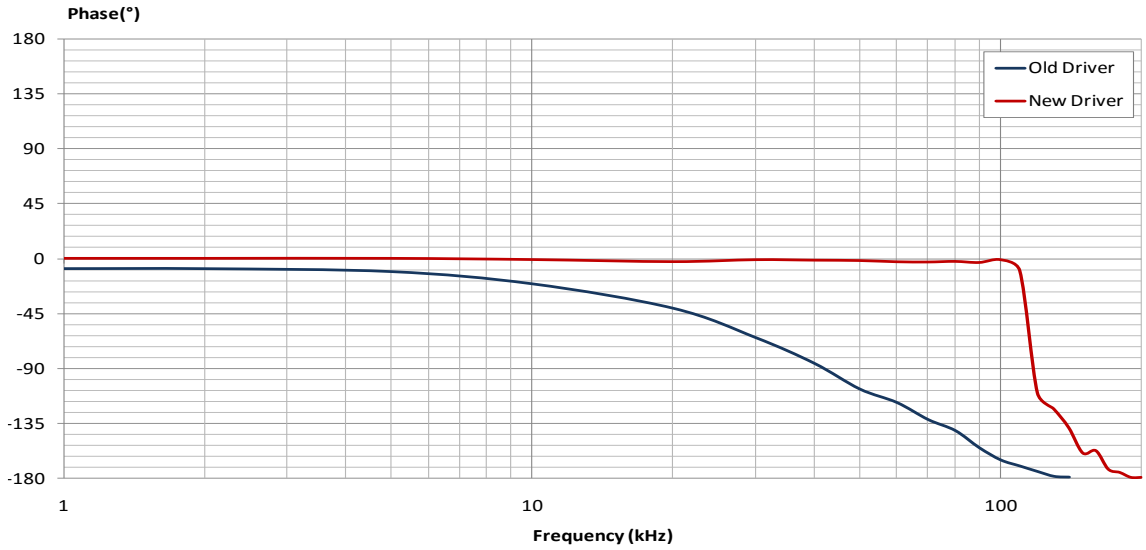

Figure 2-30 - Phase response comparison of the open-loop and closed-loop driver

The phase response of the open-loop driver shows a fixed phase drop of around 10° at low frequencies and drops to -165° at 70 kHz, while with closed-loop driver maximum phase delay was measured less than -2° at whole operation frequency range from DC to 100 kHz. Table 2.1 shows a summary of comparison results.

Table 2-1 - Summery of comparison results for open-loop and closed-loop driver

Driver	**Open-loop**	**Closed-loop**	
Coil	N=640 (Multi-layer)	N=40 (Single Layer)	N=80 (Two Layer)
Linear Bandwidth	20 kHz	100 kHz @ 1Ap-p	70 kHz @ 1Ap-p
Harmonic Distortion	30 %	< 1 %	
Linear Current Range (@ f = 50 kHz)	Up to 1.2 mAp-p	Up to 2 Ap-p	
Phase Error (@ f = 100kHz)	165°	2°	

2.17 Conclusion

In this chapter, the magnetic actuation, coil design, open-loop and closed-loop coil driver topologies was discussed. Complete design procedure of the proposed broadband high current closed-loop coil driver and practical problems and the generated solution was described in detail.

A dual stage closed-loop topology with a passive lead compensator is introduced for minimizing the phase delays and waveform distortions. Practical design criteria and design procedure was discussed in detail. Control model of the driver was developed to optimize the compensator network. Experimentally, 1 A_{p-p} output current with DC-100 kHz bandwidth was demonstrated driving a single-layer air-core 40 turns solenoid coil with inductance of 18 µH. Maximum phase delay of 2° with total harmonic distortion of less than 1% was measured with 1 A_{p-p} output current at 100 kHz.

3 Simultaneous Self-Sustained Actuation of MEMS Cantilevers

3.1 Introduction

Resonant Microcantilever have been widely used for sensing and imaging applications [8,50]. A common technique used in dynamic non-contact and tapping mode AFM's and in resonant Microcantilever based biological and chemical sensors is to frequency sweep an external AC signal for observing the resonance frequency and/or quality factor change as a result of the detected target [5–7]. It is also reported that frequency can be monitored real-time using self-sustained actuation (SSA) without requiring signal generators and complicated electronics [8–10]. SSA can be obtained by amplifying the thermal noise peak and then feeding it back as the actuator signal after applying a certain amount of phase shift. This technique is also used for self-sustained actuation of AFM Microcantilever and known as auto-tapping mode of operation [51]. Previously, our group developed SSA method to monitor the changes in resonant frequency of Microcantilever due to accreted biological mass in liquid media and demonstrated sensing with 0.1 ng/ml sensitivity and high selectivity for Hepatitis applications [11,12].

While SSA and other methods work well for a single cantilever, parallel array operation has not been demonstrated before. This is the first report of a sensor system to simultaneously monitor an array of cantilevers using one actuator and one detector. The method allows readout and analysis of dense array of sensors on a small chip. Therefore, it can open up new horizons for parallel and real time sensing and imaging applications such as multiplexed diagnostics with small sample volumes or parallel AFM.

Fabrication of the Microcantilever array is explained briefly in the next section. Afterwards, operation principle of the closed-loop SSA system is explained in detail including the experimental setup, which contains optical, electrical and mechanical components. The optical interferometric readout and its inherent nonlinearity play a key role in the oscillator operation and explained in the subsequent section. Finally, experimental results are presented that show parallel monitoring of the multi-cantilever

array: Brownian noise peaks obtained without any actuation, broadband white noise actuated spectrum, sine wave sweep spectrum and the resonance frequency peaks of simultaneous SSA of a Microcantilever array.

3.2 Microfabrication

Cantilevers are fabricated using single mask process, ~1 µm thick Nickel was electroplated on a thin Gold layer followed by wet etching for releasing [10,12]. Silicon and Nickel surface quality is not very critical as the measurements are made in dynamic mode, which can reject large bias signals. Figure 3-1 shows different tail length cantilevers with 2-3 µm wide grating slits at the tip of the cantilevers to facilitate interferometric readout. The cantilevers are made with different tail lengths to have different stiffness values, leading to different resonant frequencies. Whereas, the cantilever tips are designed to be on a straight line for simultaneous illumination with a 1D focused laser line.

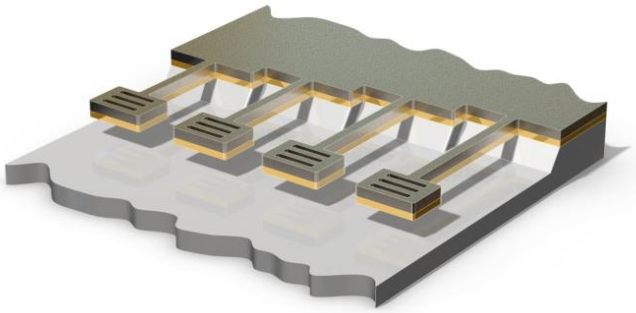

Figure 3-1 - Concept drawing of electroplated Nickel cantilevers with Gold seed layer on Silicon substrate.

Fabricated Microcantilever are shown on a MEMS die in Figure 3-2. The die (10 mm×10 mm) contains hundreds of Microcantilever. Adjacent eight cantilevers in the same row are selected and illuminated with a laser line for parallel SSA oscillation.

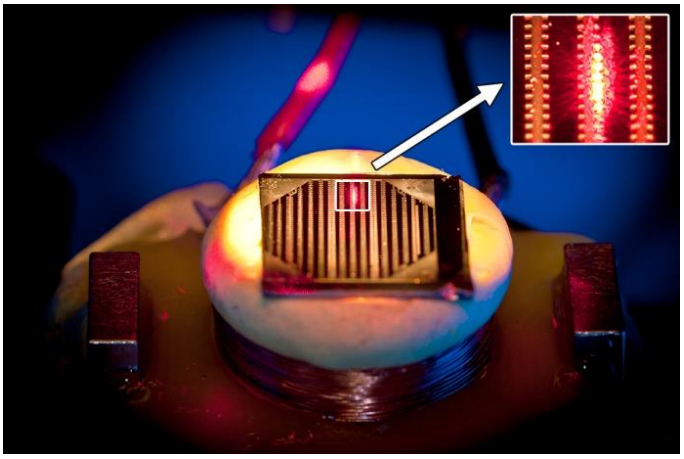

Figure 3-2 - Laser line illuminating the cantilever array on the chip. The magnetic actuation coil underneath and magnets on both sides are visible around the chip.

3.3 Operation Principle

The overall system schematically is shown in Figure 3-3. The system includes a MEMS chip containing the Microcantilever array, a coil for actuation, interferometric optical readout setup (detailed in the next section) and closed-loop control electronics. CCD camera and white light source are not essential and for monitoring purposes only. Spectrum analyzer is used to monitor the spectrum.

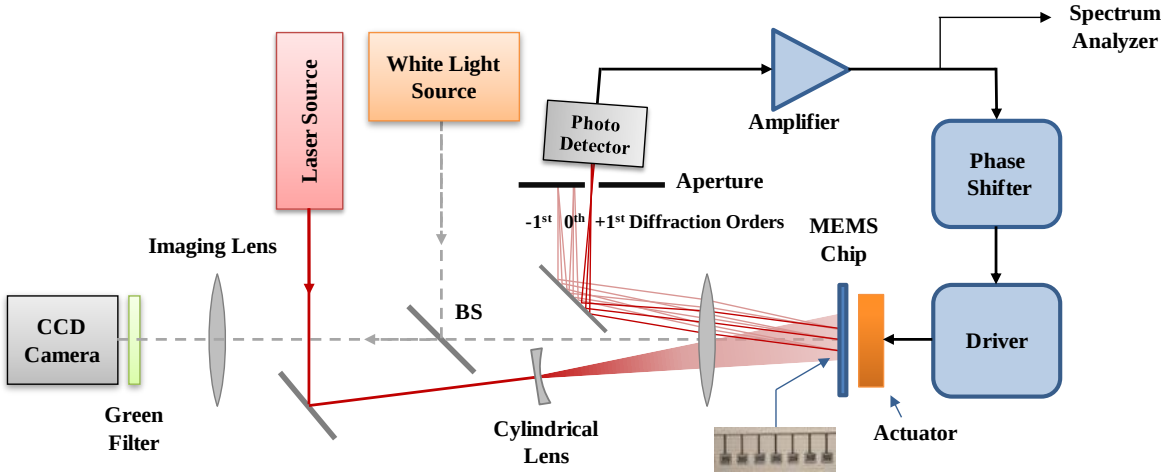

Figure 3-3 - Schematic diagram of the system.

The microcantilever array contains eight microcantilevers with increasing resonance frequency in the 60-130 kHz frequency range. The microcantilevers are above the coil, which is placed in between two magnets for magnetizing the cantilevers in the direction perpendicular to the anchor, thus leading to an enhanced magnetic force sensed by the cantilevers. The details of the optimized magnetic actuator were discussed in chapter 2. In the feedback loop, the photodetector output is amplified and phase shifted by a variable gain amplifier and a variable phase shifter and fed back to the actuation coil driver. The amplifier and the phase shifter need to be broadband in order to support a range of distinct resonant frequencies within the cantilever array. One advantage of the proposed method is that magnetic actuation and an optical readout provide a non-contact/remote actuation and sensing.

Oscillations start with Brownian motion and amplified with a gain of G and +90° phase shifted by the feedback control system to lock at the resonant frequency of each cantilever, which can be precisely monitored simultaneously using a spectrum analyzer. For a single cantilever case, assuming sinusoidal oscillation characteristics at steady-state, the equation of motion of the system can be written as follows:

$$m\ddot{x} + b\dot{x} + kx = F_{in} \tag{3.1}$$

where m, b, and k are the effective mass, total damping, spring constant and x is the deflection of the cantilever, which can be expressed as:

$$x = A\, e^{j\omega t} \tag{3.2}$$

For self-oscillating system the input is given as jGx and equation 3.1 becomes:

$$-m\,\omega^2 x + jb\omega x + kx = jGx \tag{3.3}$$

where ω is the oscillation frequency of the cantilever. At resonance, for zero effective damping, critical gain is calculated as $G_c = \omega_o b$, with:

$$\omega_0 = \sqrt{\frac{k}{m}} \tag{3.4}$$

In theory, by making G=G_C, one can obtain SSA and oscillations grow without bound if there is no nonlinearity that limit the response. In practice, G is taken as a little above G_C and oscillation amplitude reaches to a saturation value due to a required nonlinearity in the system and stabilizes. This saturation mechanism forces the SSA

oscillation to stabilize at specific amplitude and therefore determines the amplitude of oscillation [52].

SSA is also reported as self-excitation, a method to virtually cancel out the damping in the system and results in sustained oscillation [53]. For the multi-cantilever case one gain stage is used in the electronic feedback circuit, which can provide necessary gain even for the highest resonance frequency cantilever.

3.4 Coil Driver, Phase Shifter and Photodiode Amplifier

Coil driver design used in this experiment was described in detail in previous chapter. For phase shifting an elementary op-amp based circuit was designed in previous works. Fig. 3-4 shows the mentioned circuit. Since design of a frequency independent analog phase shifter working simultaneously in different frequencies is impossible practically. The same op-amp circuit is used in these experiments also. Circuit has a frequency dependent phase response starting from 0° at DC up to -180° at the end of its frequency response. Using a variable resistor R_2 the phase response of the circuit could be tuned to maintain desired phase shift at certain frequency.

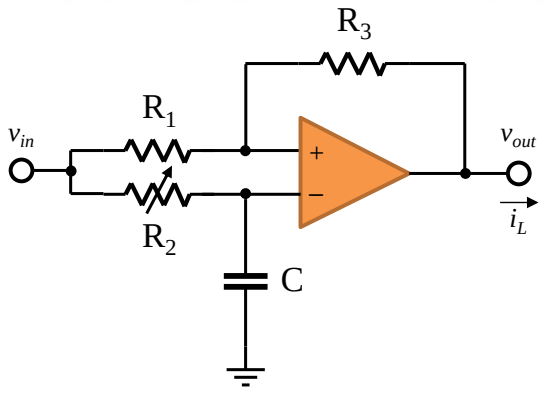

Figure 3-4 - Phase Shifter Circuit

The value of the components could be calculated to give a 90° phase shifter at the center of the frequency range of all the cantilevers. In our experiment, the value of all the resistors is 5 kΩ and the capacitor is 3.9 nF.

A commercial lab pre amplifier SR560 by Stanford Research Systems, is used for amplifying the photodiode signal.

3.5 Interferometric Readout

Reflected laser light from the substrate and the sensor surface interfere and create diffraction orders. The photodiode is aligned on the Fourier plane and on the 1st order spot's location. A single photodetector is sufficient to detect the 1st order light from multiple cantilevers. In addition, responsivity of each cantilever depends on the gap underneath each cantilever but the frequency of oscillation is not affected by the gap, variations due to microfabrication, refractive index variations, or environmental vibrations, making the sensor readout robust.

The laser source used for the optical readout is a low power single mode He-Ne Laser. The Gaussian beam shape of the laser is turned into an elongated elliptic shape using a cylindrical lens and then focused on the cantilever tips. The focused laser line is constructed long enough to keep eight cantilevers in the middle of the beam to illuminate the microcantilevers as uniform as possible. Reflected light from the microcantilever surface and substrate interfere and create diffraction orders for each microcantilever. At the Fourier plane, the reflected laser beam separated into its diffraction orders and at this plane it is possible to select the 1st order beams of all the microcantilevers, focused at a point, By aligning the photodetector at this location.1st diffraction order beam is selected for the readout to avoid large bias in the 0th order direct reflection beam, and also for its higher power compared to the higher diffraction orders.

For alignment and monitoring the microcantilevers a CCD camera, a white light source, a beam splitter and an additional imaging lens is used. The front imaging lens is employed also as the focusing lens for the monitoring optics.

The interferometric readout is based on the Optical Phase Difference in between the reflected light from the microcantilever surface and from the substrate, which can be approximated as twice the gap underneath the microcantilevers. Sinusoidal shaped interference characteristic depends on the wavelength of the readout laser beam and the gap underneath the microcantilever. The normalized intensity at the photodetector can be written as follows:

$$I_{PD} = sin^2(\pi \frac{2}{\lambda} d) = \frac{1}{2} - \frac{1}{2} cos(2\pi \frac{2}{\lambda} d) \quad (3.5)$$

where λ is the wavelength of the readout laser beam and d is the gap underneath the microcantilever. d can be expressed as:

$$d = g_0 + A\, sin(\omega_0 t) \quad (3.6)$$

where g_0 is the initial gap, A is the deflection amplitude, and w_0 is the oscillation frequency. Fig. 3-5 illustrates I_{PD} assuming λ=635nm for different g_0 values, which determine the bias point. In the figure, assuming 20 nm sinusoidal deflection, two intensity signals are plotted for two different initial gaps at $n\lambda/2 + \lambda/8$ (marked with red star) and $n\lambda/2+3\lambda/8$ (marked with blue square), where n is a nonnegative integer. Even though interferometric readout does not change the oscillation frequency, optical nonlinearity adds higher harmonics to the system, which will be mechanically filtered by the microcantilevers.

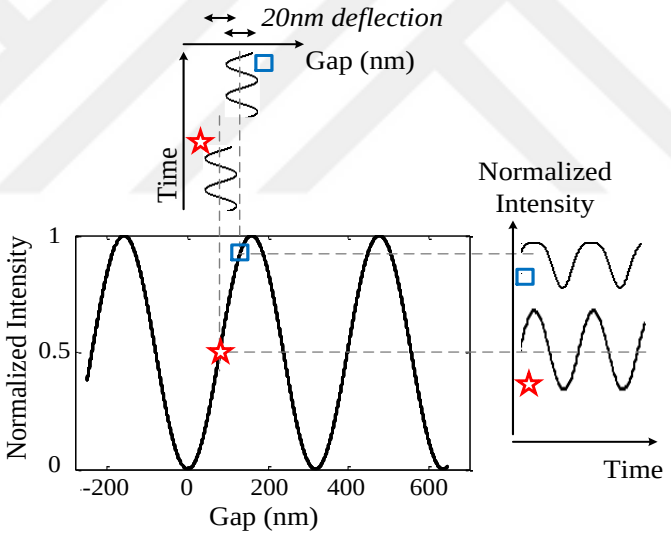

Figure 3-5 - Interferometric readout photodetector normalized intensity characteristic assuming 635nm wavelength and 20nm deflection for two different nominal gap positions.

3.6 Experimental Results

Multi-cantilever simultaneous SSA and parallel readout concept is experimentally proved by using the system shown in Fig. 3-3. In order to verify the operation of the

optical setup and to detect the resonance frequency and quality factors of the microcantilevers, a cantilever array containing eight cantilevers were illuminated via a line shaped laser without any actuation in the open loop mode, i.e. by breaking the loop just before the actuator driver. The photodetector signal was observed via a spectrum analyzer. In Fig. 3-6, the thermal noise peaks of eight different cantilevers are clearly visible. The resonance frequencies and quality factor of the cantilevers are measured with the help of this data. Open loop frequency sweep and driving the system with broadband noise also gave consistent results with the thermal noise response as illustrated in the figure.

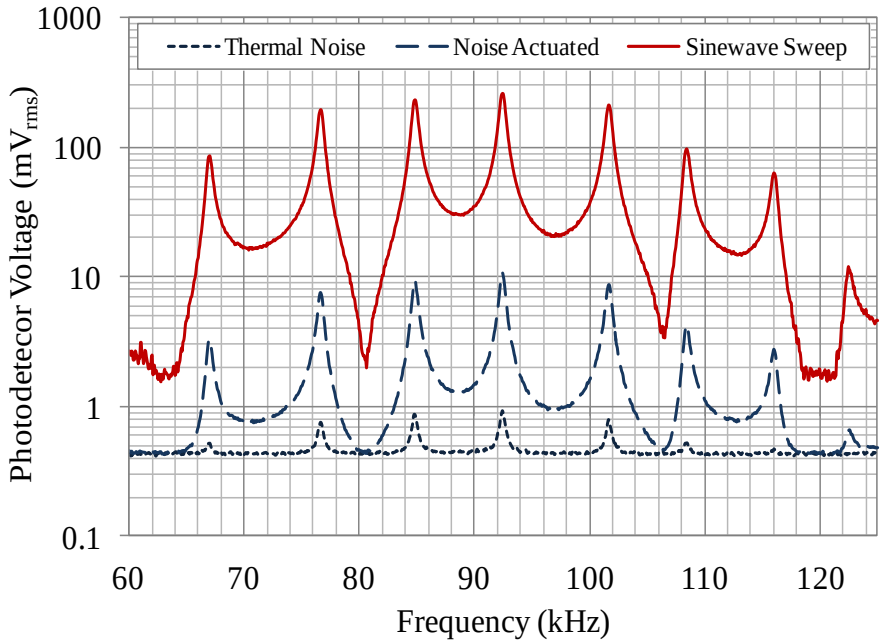

Figure 3-6 - Photodetector signal frequency spectrum that shows thermal noise data (no actuation), white noise driven response and frequency sweep response by coil.

In order to obtain simultaneous SSA, the loop is closed, and in milliseconds the saturation of oscillations was observed and separated SSA oscillations were obtained as very narrow frequency peaks in the frequency spectrum. In Fig. 3-7, simultaneous SSA oscillations of microcantilevers are illustrated. The bandwidth of the oscillation peaks are solely limited by the measurement bandwidth of the spectrum analyzer. Fig. 3-8 shows the zoomed-in view of the peak at 92.765 kHz with a measurement bandwidth of 1 Hz.

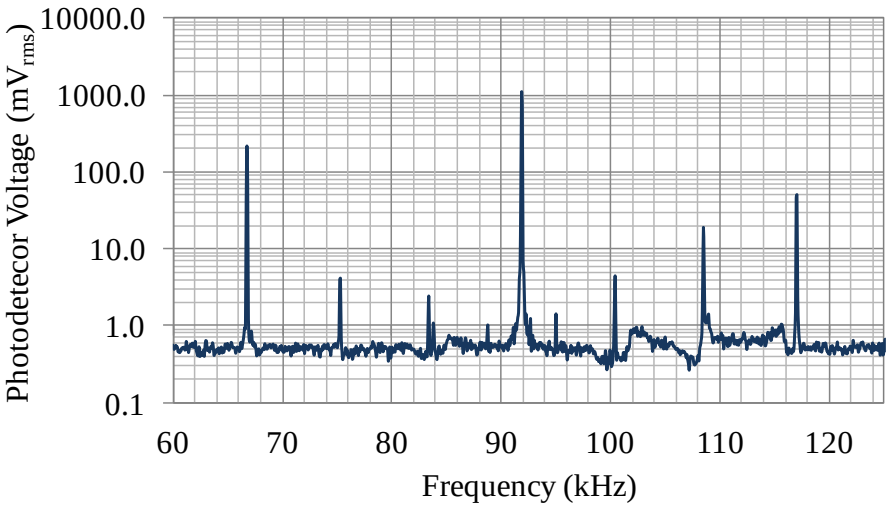

Figure 3-7 - Photodetector signal frequency spectrum that shows simultaneous SSA of MEMS cantilever array.

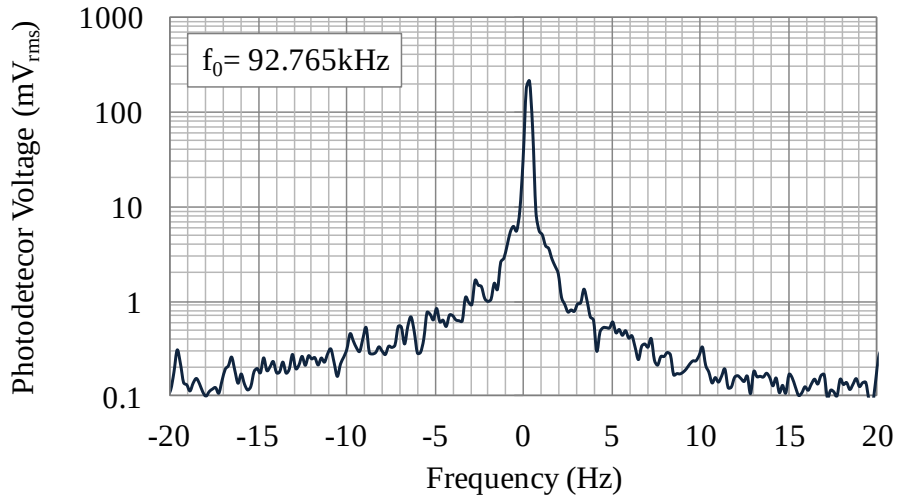

Figure 3-8 - Zoomed spectrum of one of the cantilevers. (This is closed-loop operation, bandwidth is related to measurement and control electronics and not indicative of the mechanical quality factor)

3.7 Simulation

Parallel readout of the microcantilevers as a unit system could be modeled as parallel connected second order resonators. All of them has the same input, since they

excite with the same signal and the output will be super position of the output of all resonators. Fig. 3-9 shows the model for parallel excited cantilevers.

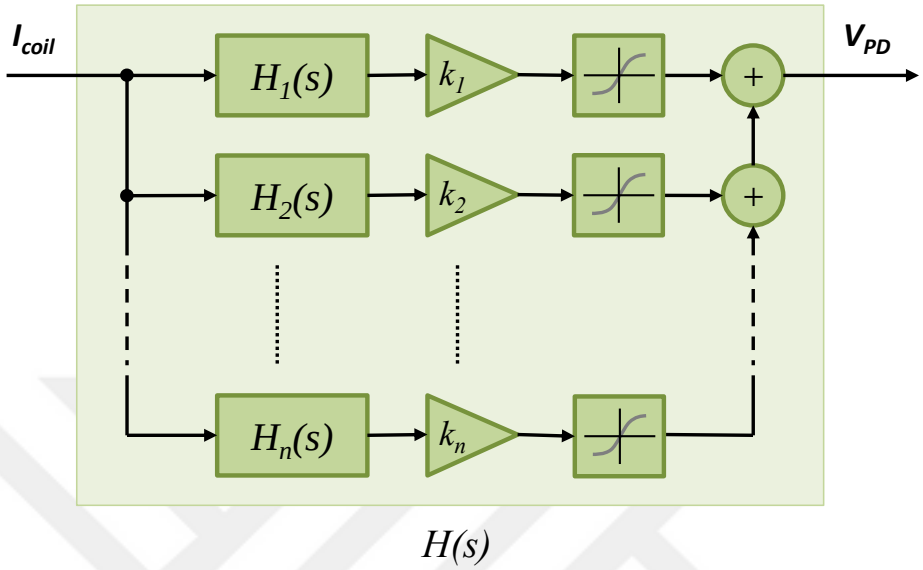

Figure 3-9 - Model of parallel excited MEMS cantilevers

Here, $H_n(s)$ and k_n are transfer function and gain value of the nth cantilever, respectively. Transfer function of the whole model could be written as follows:

$$H(s) = \sum_{n=1}^{8} k_n \frac{\omega_{o,n}^2}{s^2 + \frac{\omega_{o,n}}{Q_n} s + \omega_{o,n}^2} H_L(s), \tag{3.7}$$

where ω_n and Q_n are the natural frequency and quality factor of the nth cantilever respectively. And $H_L(s)$ is the transfer function for optical non-linearity limiter. Fig. 3-10 shows the SSA system schematics used for simulations.

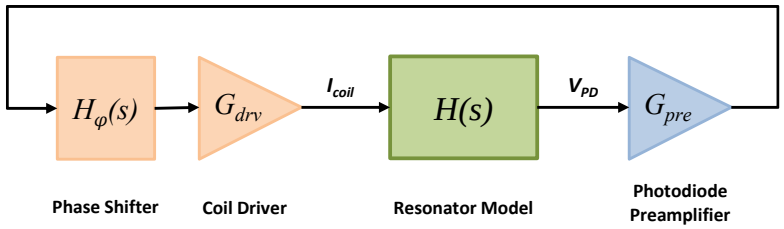

Figure 3-10 - SSA system model schematics

The system model is constructed in NI MultiSim® software. For phase shifter and Coil Driver, detailed spice model of each component was used. The rest of the system was modeled using transfer function, gain and limiter blocks.

Fig. 3-11 shows the single channel resonator block model implemented in MultiSim. For insulating the cantilevers from each other and also preventing any loading effect between the coil driver and cantilevers, a voltage follower buffer block (B1) using an ideal op-amp employed for each cantilever.

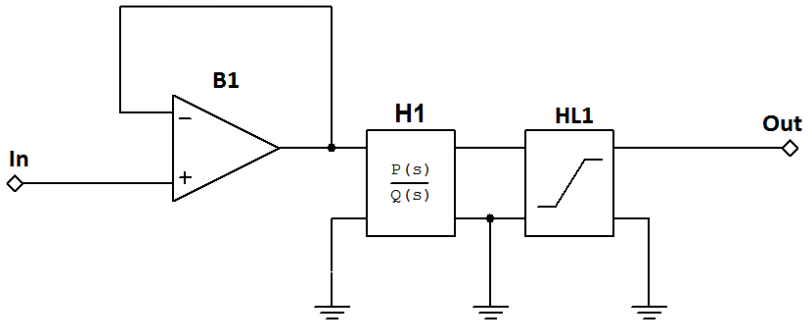

Figure 3-11 - Implemented model of each cantilever in MultiSim® software

A gain block converts the coil current to excitation force for cantilevers. For collecting the signals from all of the cantilevers adder blocks are used. Fig. 3-12 shows the implemented 8-channel resonator model.

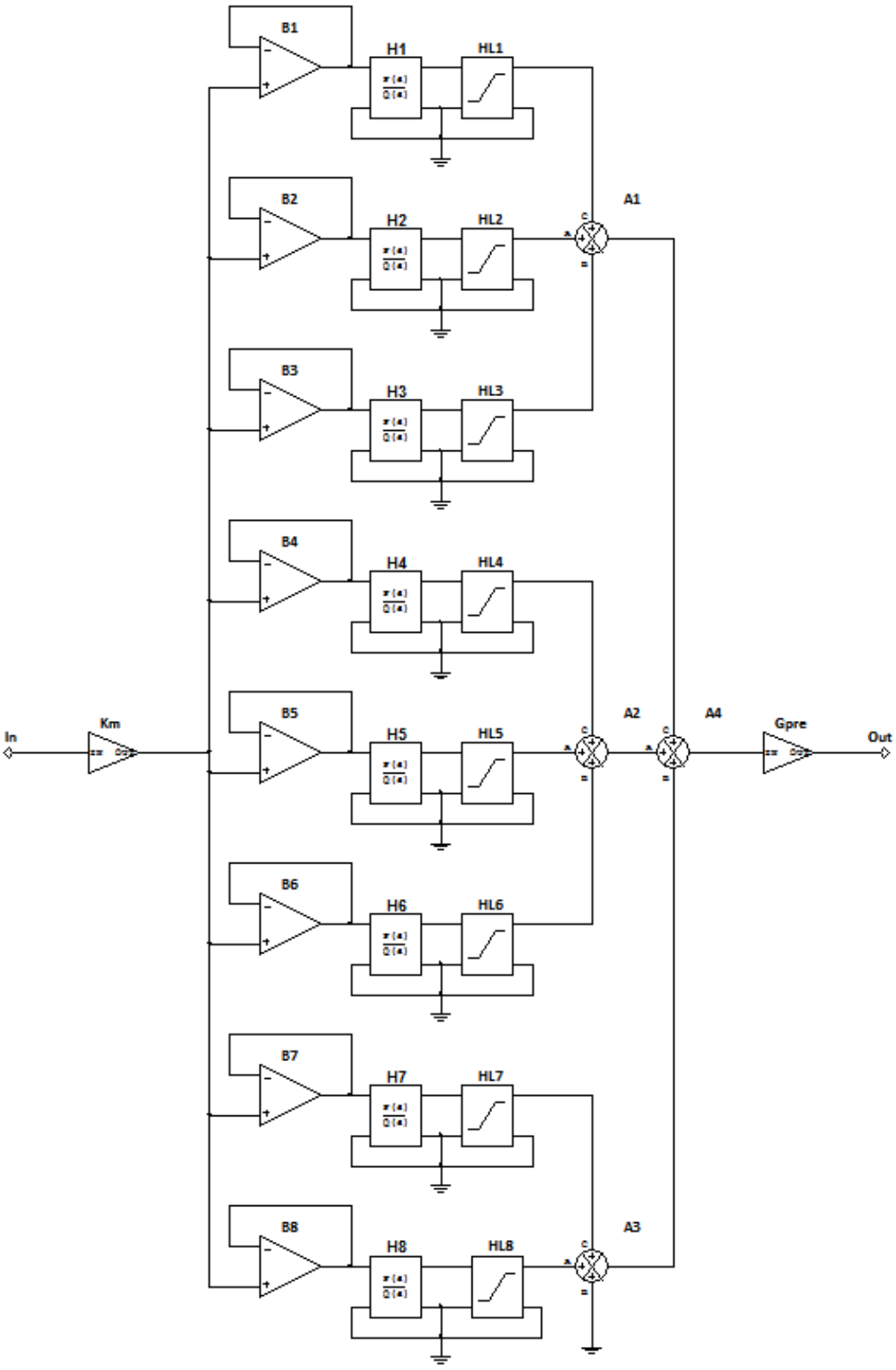

Figure 3-12 - 8-channel resonator model

Based on the experimental frequency sweet results, one could calculate the natural frequencies, gain values and other coefficients of the system. Open-loop frequency sweep experiment simulated to confirm the model parameters. Fig. 3-13 shows the experimental and simulated frequency sweep data.

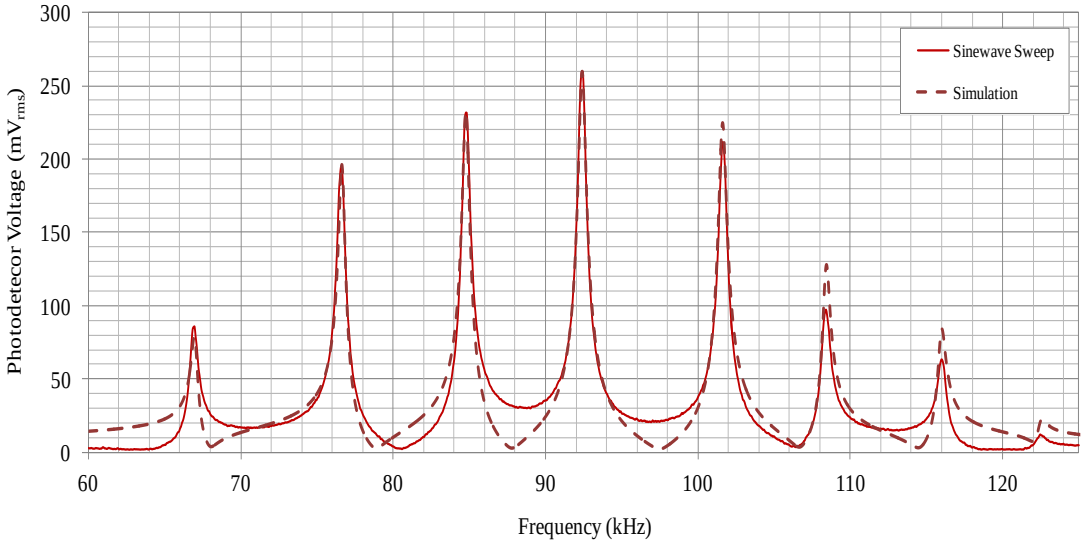

Figure 3-13 - Experimental and simulated open-loop frequency sweep results

After verifying the resonator model parameters, a single cantilever model simulated in closed-loop SSA mode. Fig. 3-14 shows transient and steady state waveform of the system. Transient simulation shows how the system start to oscillate and settles at a certain amplitude.

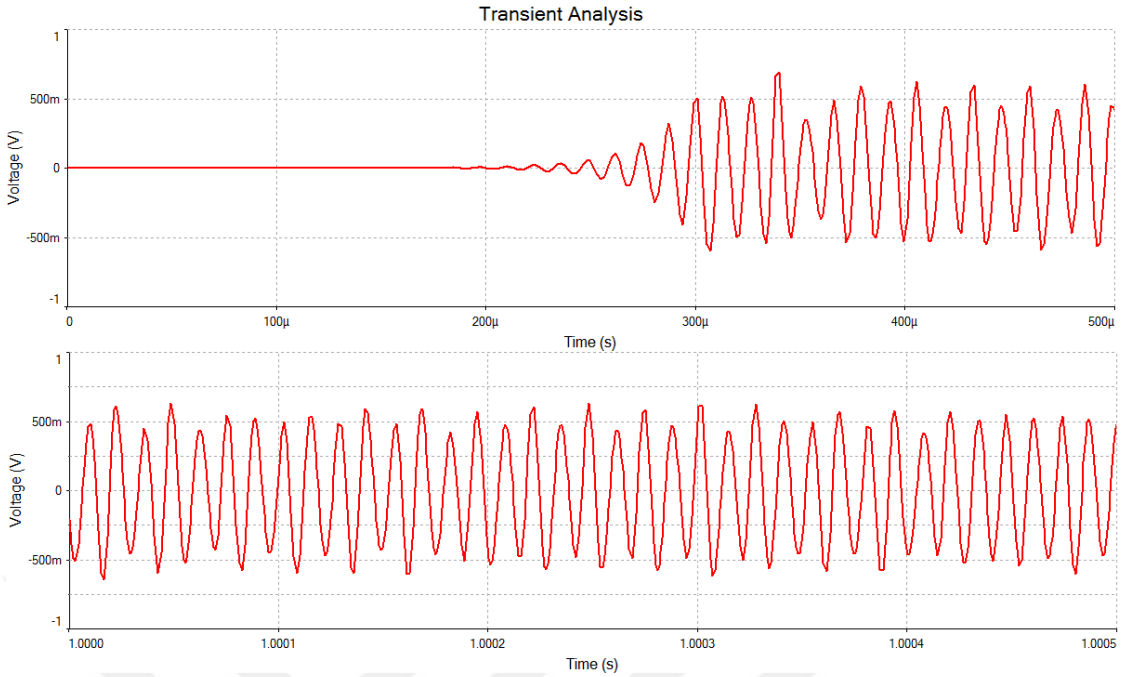

Figure 3-14 - Transient and steady state SSA simulation result for a single cantilever system

For simulating the multi-channel SSA operation, a four-channel model was used, because of very long simulation time. Fig. 3-15 shows the simulation results overlapped with open-loop sweep results. In the simulation, frequency of the resonating peaks are near the experimental results. The amplitudes of the oscillation peaks are around 1.5 V_{p-p}, but in the experimental results, only one of the cantilevers oscillates at the same amplitude. Since the amplitude of the oscillations depends on the limiting function of the implemented optical readout method, such differences in the amplitudes may be directly related to different working point of each cantilever on the optical transfer function curve.

Fig. 3-16 shows a close-up view of the frequency response for one of the cantilevers in 4-channel SSA model overlapped with open-loop sweep frequency response. The measured and simulated frequency of the SSA operation is around 100 Hz and 120 Hz lower than open-loop peak of the cantilever, respectively. The phase delay of the used photo diode pre amplifier may be the main cause of this frequency shift.

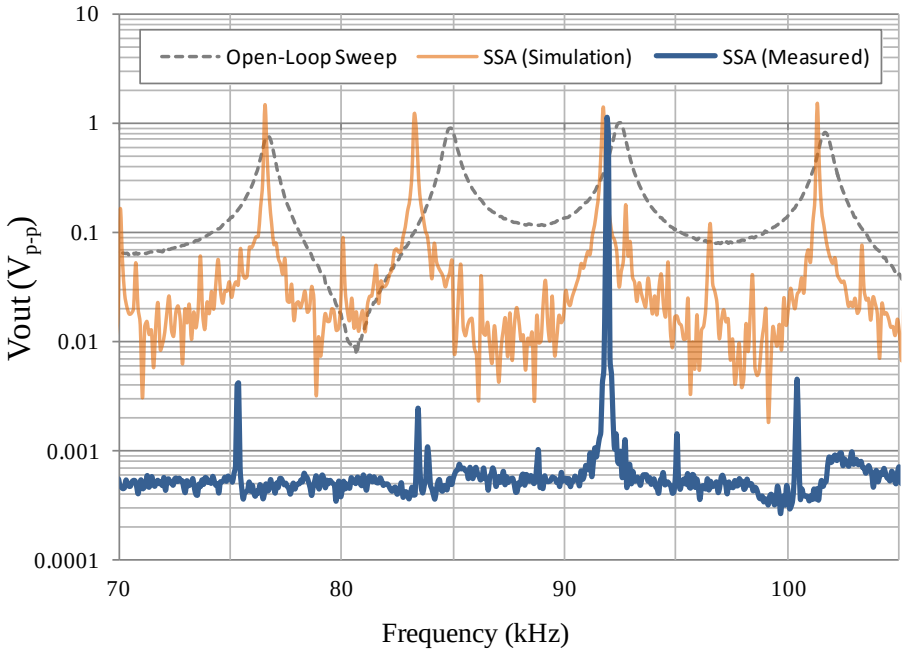

Figure 3-15 - Simulation result for 4-channel SSA operation.

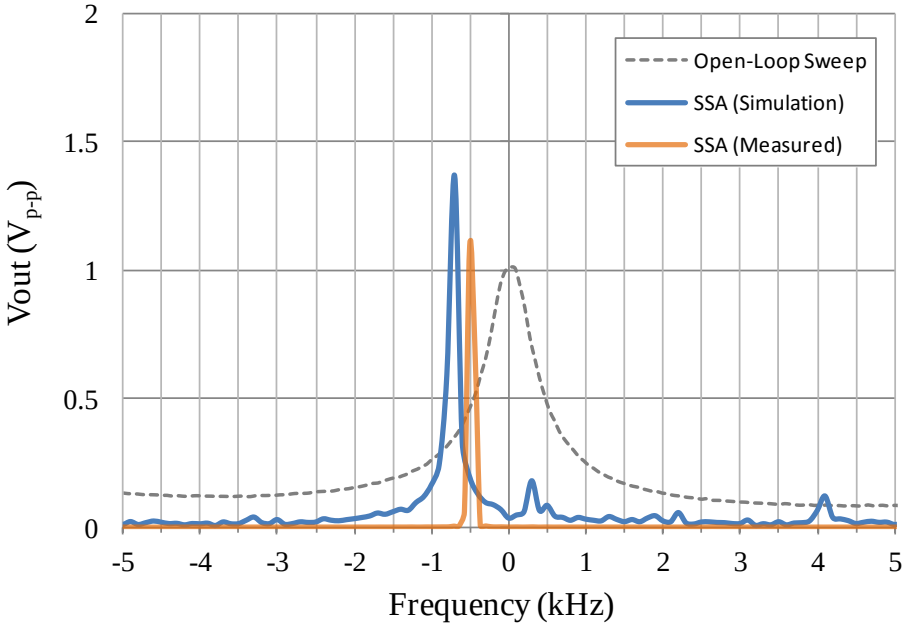

Figure 3-16 - Comparison of the simulation and experimental result for one of the cantilevers in the 4-channel model.

3.8 Conclusion

A MEMS cantilever array operated with parallel SSA oscillations is reported in this work. A broadband driver circuit and a single driver coil are employed for simultaneous magnetic actuation. Microcantilevers are designed with different resonance frequencies and microfabrication was a simple one mask process. In order to perform parallel readout of the simultaneous oscillations, interferometric readout of 8 cantilevers through a single detector and a single electro-coil are used. One set of discrete feedback electronics is utilized to phase shift and amplify the photodetector signal and close the loop.

Without any actuation, Brownian motion of the microcantilever array is observed clearly using a single photodetector and the interferometric setup. SSA oscillations are performed for seven microcantilevers with changing resonance frequencies in the 60-130 kHz range. Measurements are performed in air environment.

Implementation of parallel SSA by using a single actuator and single photodetector opens up new horizons for multiplexed biosensing. The method is suitable for low-cost multiplexed portable biosensor platform with its easy to process sensor array and non-contact actuation and readout mechanism. This work was presented in IEEE MEMS conference held in Paris [43].

4 Digital PLL-Based Broad-Band Resonance Tracking for MEMS Sensors and Actuators

4.1 Introduction

Resonance frequency tracking is an important issue in both resonant sensors and actuators, and PLLs are widely used for various applications such as ultrasonic motors and actuators [22,54], induction heating [27], resonant power converters [23,24], wireless power transmission [25], MEMS Gyro and mirror actuators [26,28,55], MEMS sensors [21,29,56], dynamic force microscopy [20], and capacitance measurement [19]. Beside of the complexity of the available PLL methods, Analog PLLs, with multiplexer phase detectors, does not provide frequency-independent phase tracking and broadband frequency range[19–21]. The frequency dependent phase response of these PLLs, introduces additional phase error in the loop which will cause error in the locked frequency. Digital PLLs with Phase/Frequency Detectors (PFD) have frequency independent phase response and are suitable for wideband operation but they generate square waves and could not be directly used for applications where sinewave excitation is required. Output filtering was demonstrated with square wave VCOs but the distorted output waveform will not be suitable for high precision applications [21]. Although, PLLs with PFDs naturally can only lock to zero-phase angle, they could be used directly for resonant systems where resonance occurs in zero phase shift between the actuation and feedback signals [22–25] or manual phase tuning using analog phase-shifters will be required [26]. For power actuation applications a PWM sinewave generation method is also reported [25]. Modern DSP PLLs, with special frequency tracking algorithms, could provide both the wide operating frequency range with sinewave output signal, but due to their high cost, their applications are limited to research purposes and high-end products [27–29].

In the proposed method, the frequency-independent and wide operating frequency range of digital PLLs with PFDs was combined with an analog wave generation method to provide both broadband operating frequency range and frequency-independent +90° phase shifted sinewave output. Frequency independent operation is highly intended

property for driving high dynamic range sensors and actuators with wide operating frequency range such as viscosity and density measurement applications in liquids [31–34,44].

Proposed closed-loop resonance tracking method, locks and drives a resonator at its natural frequency without any initial tuning process. For sensor applications, the drive frequency will be the natural frequency of the sensor and could be measured easily using a frequency counter. For resonant actuators, this method will drive and keep the actuator always in its natural frequency delivering maximum performance out of the actuator. This is very important issue for most of the resonant actuators where the resonance frequency drifts with temperature or other environmental parameters. In the case of a fixed frequency drive system, the amplitude of the resonator could be reduced with drifts in its natural frequency. In the proposed method, the drive frequency will be chnage automatically to match the natural frequency of the actuator, keeping the actuation in its maximum amplitude.

For sinewave generation, we first construct a triangular wave by combining the ramp waveforms and output square wave of the VCO and then we use a logarithmic wave shaper circuit to convert the constructed triangular waveform to sinewave. 90° phase shifting property comes from the triangular waveform generation which acts like an integrator. The implemented architecture with ideal components has no frequency dependent phase delay but because of the non-zero propagation delays in all stages of the system except for the PLL circuit, there will be an increasing phase delay proportional to the operating frequency in practical circuit. For compensating to these phase delays, was implemented a 2^{nd} order passive phase-lead filter at the input resulting maximum of ±2.5° phase error over the whole operating frequency range.

4.2 Theoretical Background

Consider a resonant system, driven with a resonance tracking system, as an oscillator. Based on the Barkhausen oscillation criterion [57], The system will sustain steady-state oscillations only at frequencies for which:

1. The loop gain is equal to unity in absolute magnitude,
2. The phase shift around the loop is zero or an integer multiple of 2π.

In resonant systems, the phase of the output signal with respect to the actuation signal is -90° at natural or undamped resonance frequency. Thus, for a resonance tracking system, it required to have +90° phase shift with a controlled amplitude to maintain a unity gain over the loop. This method is called as Self-Sustained Oscillation (SSA) and could be implemented using a cascaded amplifier and a phase-shifter with an amplitude limiting mechanism. This method, because of the limitations in analog phase-shifters could not be used for wide frequency ranges. Amplitude instability and distortions due to the saturation in the exciting waveforms are also other problems in SSA method which makes this method unusable for high precision applications.

To overcome the instability and distortions of the SSA method, a resonance tracking system with an embedded sinewave oscillator could be a perfect solution. For such a system, as shown in Fig. 5-1, we need a sinewave oscillator, whose frequency could be adjusted automatically in such a way, that a -90° phase shift observed at the output of the resonator. This method could be implemented using Phase-Lock Loop (PLL) circuits.

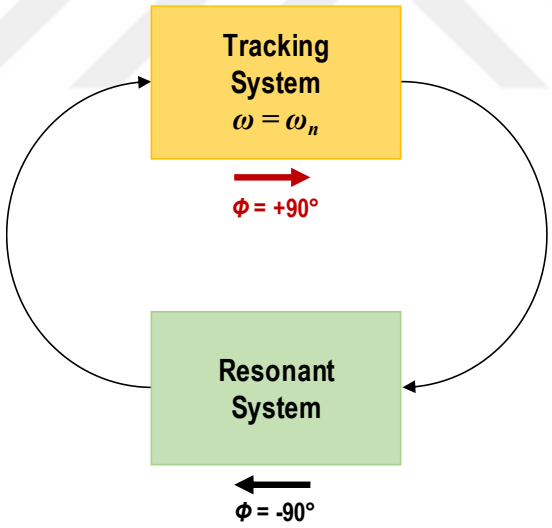

Figure 4-1 - A resonant system driven by an ideal resonance tracking system

4.3 Phase-Locked Loops

Phase Locked Loops (PLLs) are closed-loop control systems to generate a signal with equal frequency and a fixed phase to a reference signal. The reference signal may be a noisy signal, where the output signal will be a clean undistorted signal, generated locally with exactly the same frequency of the reference signal and a fixed or zero phase delay with respect to the reference signal. All phase-locked loops consist of three main blocks [58]:

1. Phase Detector
2. Loop Filter
3. Controlled Local Oscillator (mainly a voltage controlled oscillator (VCO))

Fig. 4-2, shows the block diagram of a PLL system.

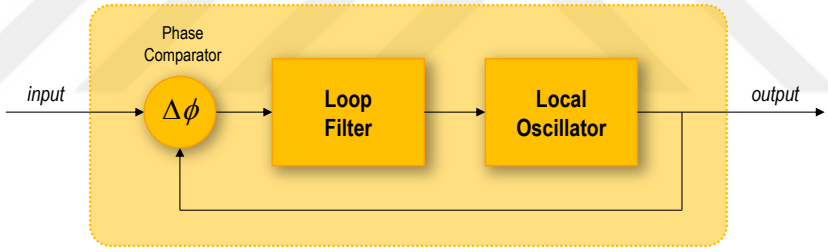

Figure 4-2 - Block diagram of a PLL system

For a certain input frequency, the phase comparator or phase detector, compares the phase of the local oscillators signal with input signal and generates an error signal. The loop filter mostly a low-pass filter integrates the phase error signal. A positive phase error signal increases the voltage at output of the low-pass filter (integrating capacitor) and the control voltage of the VCO, initiating increase of the output frequency to compensate the phase errors. This mechanism automatically changes the output frequency to minimize the phase error to keep it at zero or at a minimum level. This is called locking to the input frequency.

Since the VCO input signal is stabilized at the loop filter, rapid changes in the phase of the input signal will be rejected in the loop filter. The noise immunity nature of the PLLs is based on this behavior of the loop filter.

PLLs could also be used as FM demodulators, because the input signal of the VCO will be the demodulated signal of the input. In this case, the bandwidth of the loop filter must be equal to the bandwidth of the communication system for proper demodulation.

From this point of view, the PLL-based resonance frequency tracking is also a kind of demodulation. Changes in the resonance frequency will be reflected into changes in the control voltage of the VCO. But since the frequency measurement with high precision is easier than voltage measurement, we prefer to measure the output frequency of the PLL as the demodulated output signal.

4.4 Classification of PLLs

Based on the used phase detecting methods and implementation of the loop filter and the local oscillator, the PLLs could be classified into four main groups [59]:

1. Analog or Linear PLLs (APPL)
2. Digital or Mixed-Signal PLLs (DPLL)
3. All-Digital PLLs (ADPLL)
4. Software PLLs (SPLL)

In analog PLLs, analog mixers are used as phase detector, cascaded with an analog filter and an analog sinewave VCO. In mixed signal PLLs, the phase detectors are designed using logical circuits, an Exclusive-OR gate or a phase/frequency detector circuit (PFD). The loop filter is an analog filter and the local oscillator is a square wave VCO.

Unlike the digital PLLs where are actually semi-analog systems, the all-digital PLLs were designed with pure digital circuits and all the signals inside the PLL are digital words. The loop filter is also implemented digitally and the VCO is replaced with a digitally controlled oscillator (DCO).

In software PLLs, all the blocks were implemented inside a microcontroller or a digital signal processor (DSP) chip. The input signal was digitalized using an ADC and the output signal is generated using a DAC (all could be implemented in a modern single DSP chip). Software PLLs are the most advanced of all methods, but for high precision or high frequency applications they need extremely high speed DSP chips and needs huge processing power.

4.5 Mixer Phase Detectors

In analog or linear PLLs, a mixer is used as the phase detector. This phase detector also called as Type-I phase detector, has frequency dependent phase responses. In the PLL's with this type of detectors, the phase of locked signal depends on the VCO's frequency range. At VCO's center frequency the phase will be +90° with respect to the input signal. For simplicity of the equations and the fact that the locked frequency generally is near the center frequency of the VCO, the VCO output signal was written as a cosine function. In this case the phase error at VCO's center frequency will be 0° corresponding to +90° phase shift. The input signal and the phase detector output for input signal and VCO's output as a cosine function could be written as follows:

$$v_1(t) = A_1\, sin(\omega_1 t + \phi_1), \tag{4.1}$$

$$v_2(t) = A_2\, cos(\omega_2 t + \phi_2), \tag{4.2}$$

$$v_d(t) = v_1(t)v_2(t). \tag{4.3}$$

In the locked state where $\omega_1 = \omega_2$ the phase detector output will be as follows:

$$v_d(t) = \frac{A_1 A_2}{2}\,[sin(2\omega_1 t) + sin(\phi_1 - \phi_2)]. \tag{4.4}$$

Since the bandwidth of the loop filter is always lower than the operation frequency, the $2\omega_1$ frequency component will be filtered out in the loop filter.

If we define the phase error as:

$$\phi_e = \phi_1 - \phi_2, \tag{4.5}$$

the averaged phase error signal will be:

$$\overline{v_d(t)} = k_d \sin(\phi_e(t)), \tag{4.6}$$

and could be approximated for small phase errors as:

$$\overline{v_d(t)} \cong k_d \phi_e(t), \tag{4.6}$$

where k_{pd} is the gain of phase detector:

$$k_d = \frac{A_1 A_2}{2}. \tag{4.7}$$

Fig. 4-3, shows the waveforms of the input signals and the phase detector output for a fixed phase difference of 45°. The dashed line is the corresponding to DC level passing through the loop filter. For an increasing phase difference, the DC level of the phase error passing through the filter will be variable. Fig. 4-4, shows the phase detector output for an increasing phase difference.

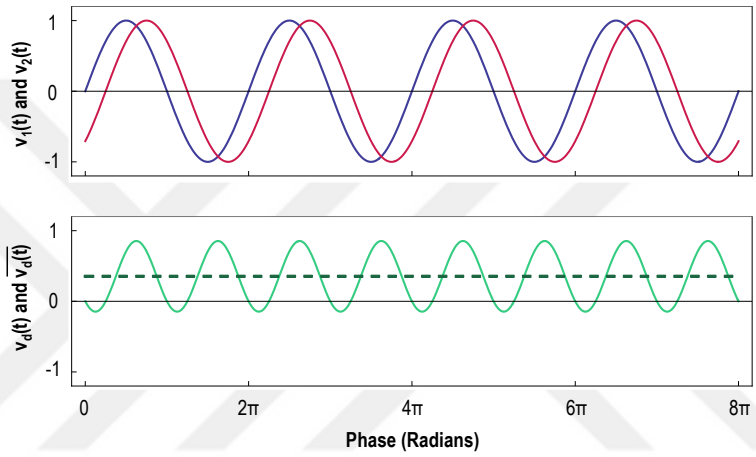

Figure 4-3 - Waveforms of the input signals and the phase error signals for a fixed phase difference

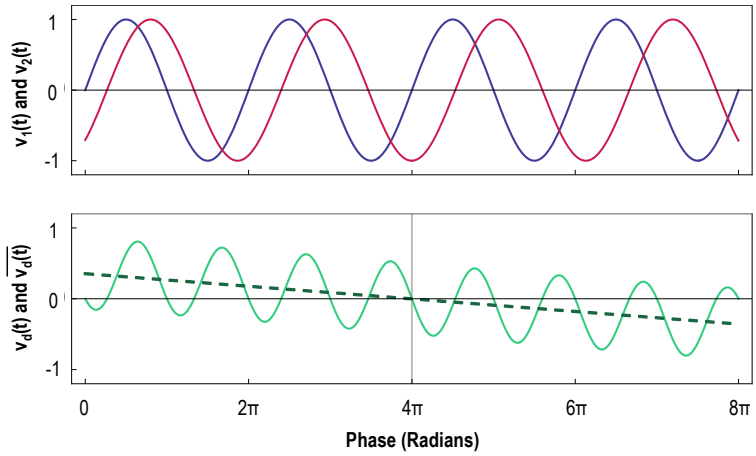

Figure 4-4 - Waveforms of the input signals and phase detector output for an increasing phase difference

Fig. 4-5, shows the plot of $\overline{v_d}$ with respect to the input phase difference. In linear PLLs, gain of the detector is related to the amplitude of the input signals, but in the case of digital PLLs, where amplitudes are fixed values, the gain value will be constant. For unity gain sine wave inputs, the phase detectors gain for small phase errors will be 0.5.

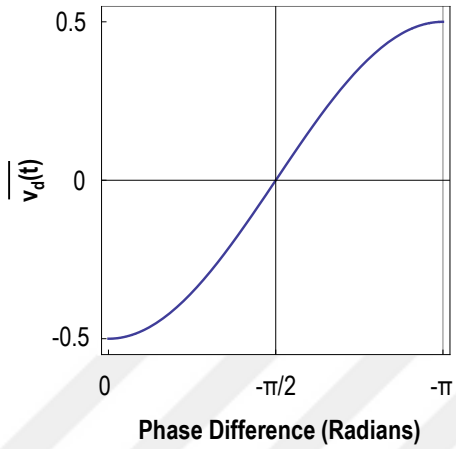

Figure 4-5 - Phase response of the multiplier phase detector for unity gain sine wave inputs

4.6 Exclusive-OR Digital Phase Detector

The digital counterpart of this phase detection in mixed signal PLLs is an Exclusive-OR gate. In the case of symmetrical square wave inputs, similarly the equations for the phase detector could be written as:

$$\overline{v_d(t)} = k_d \phi_e(t), \tag{4.8}$$

Practically, for the gain value of the XOR phase detector, since the voltage in logic circuits are in between the zero (GND) and the power supply voltage ($+V_{CC}$), the averaged output of the phase detector also will be in this range and the mentioned relation could be shifted by $+0.5V_{CC}$.

Thus, the gain of the phase detector will be:

$$k_d = \frac{V_{CC}}{\pi}. \tag{4.7}$$

Fig. 4-6 and Fig. 4-7, shows the waveforms of the XOR phase detector in the case of a fixed and increasing phase differences. The phase response was shown in Fig. 4-8.

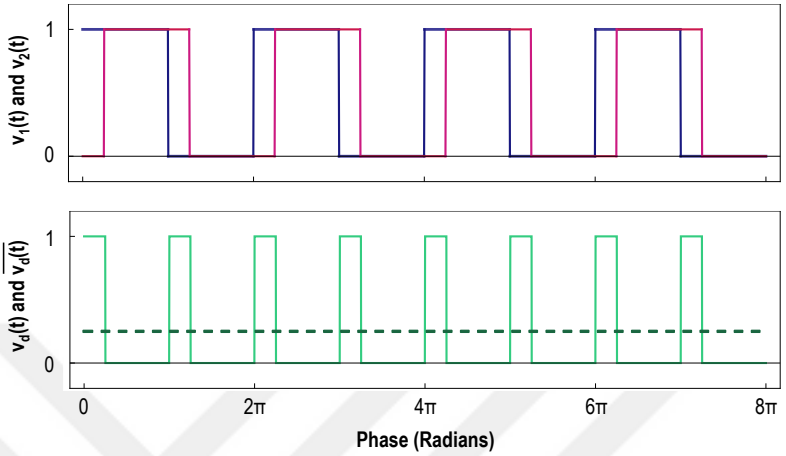

Figure 4-6 - Waveforms of the input signals and phase detector output for a fixed phase difference in Exclusive-OR gate phase detector.

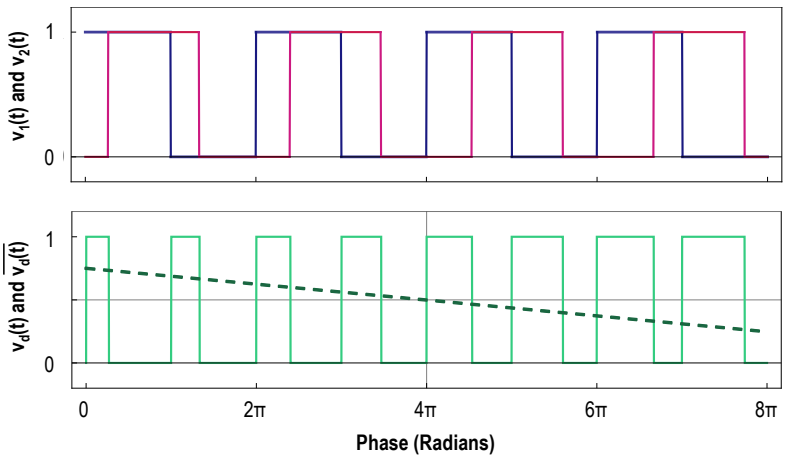

Figure 4-7 - Waveforms of the input signals and phase detector output for an increasing phase difference in Exclusive-OR gate phase detector.

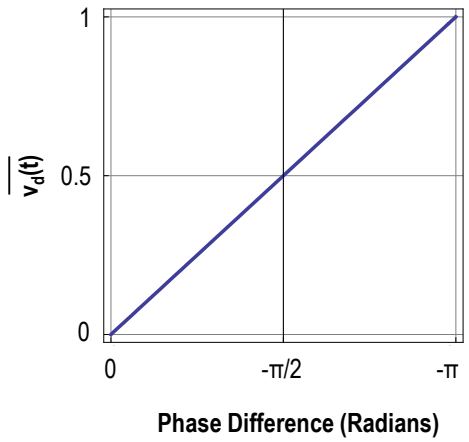

Figure 4-8 - Phase response of the XOR phase detector for square wave inputs

4.7 Digital Phase/Frequency Detectors

In the proposed resonance tracking method, I developed a digital PLL with Phase/Frequency Detecting (PFD) phase comparator. This type of the phase detection also called as Type-II phase detectors is widely used method in mixed signal PLLs. The most important advantage of PFD, is its zero phase locking property. The zero phase locking is essential for resonance tracking applications, where we want to drive the system in a fixed phase, independent of the operating frequency. Type-I phase detectors as described before will introduce a frequency dependent phase shift into the loop.

The other important property of the PFD, is its capability for broadband locking frequency range and also preventing to lock into the harmonics of the reference signal. This is important for high dynamic range sensor applications where the resonance frequency could change in large scales. In the case of type-I phase detectors, the lock range is limited and PLL could be locked into the harmonics also, but this is prevented with PFDs. Fig. 4-9, shows a basic schematics of a voltage source PFD.

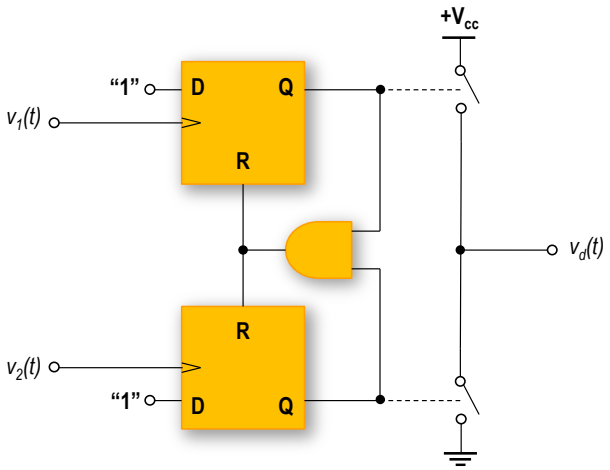

Figure 4-9 - Basic schematic of a voltage source PFD phase detector

As shows in the Fig. 4-9, PFDs consists of two D-type flip-flops. The upper flip-flop will go to high state with a rising edge on the $v_1(t)$ signal and similarly the lower the flip-flop for $v_2(t)$. The AND gate prevent both flip-flops to be in high state at the same time by resetting both flip-flops. Fig. 4-10, shows the waveforms of a PLL with PFD.

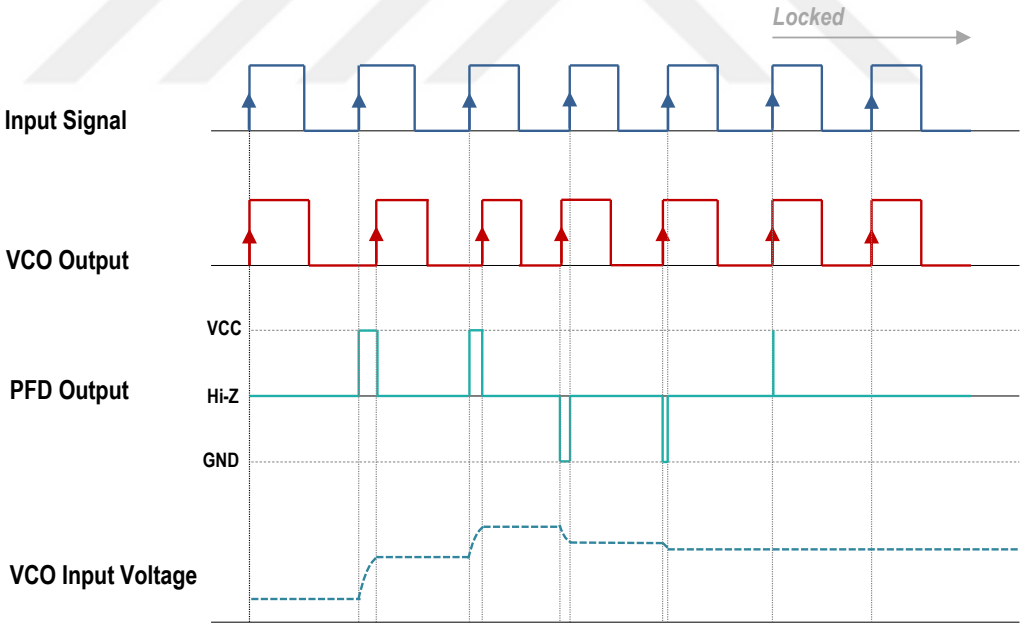

Figure 4-10 - Waveforms of a mixed-signal PLL with Phase/Frequency Detector (PFD)

Since the PFDs are edge trigger, the phase error is restricted to -2π and 2π and the phase transfer function will be

$$k_d = \frac{V_{CC}}{4\pi}. \tag{4.8}$$

Fig. 4-11, shows simulation results of a PLL with PFD. For better representation of the PFD output waveform, a combined signal was constructed and its duty cycle was shown. This signal shows the state of the flip-flops as "1" for upper flip-flop's high state, "-1" for lower flip-flop's high state and "0" for both in low state or Hi-Z state. The reference frequency was set to 1 kHz at t = 0 and then 800 Hz at t = 2s.

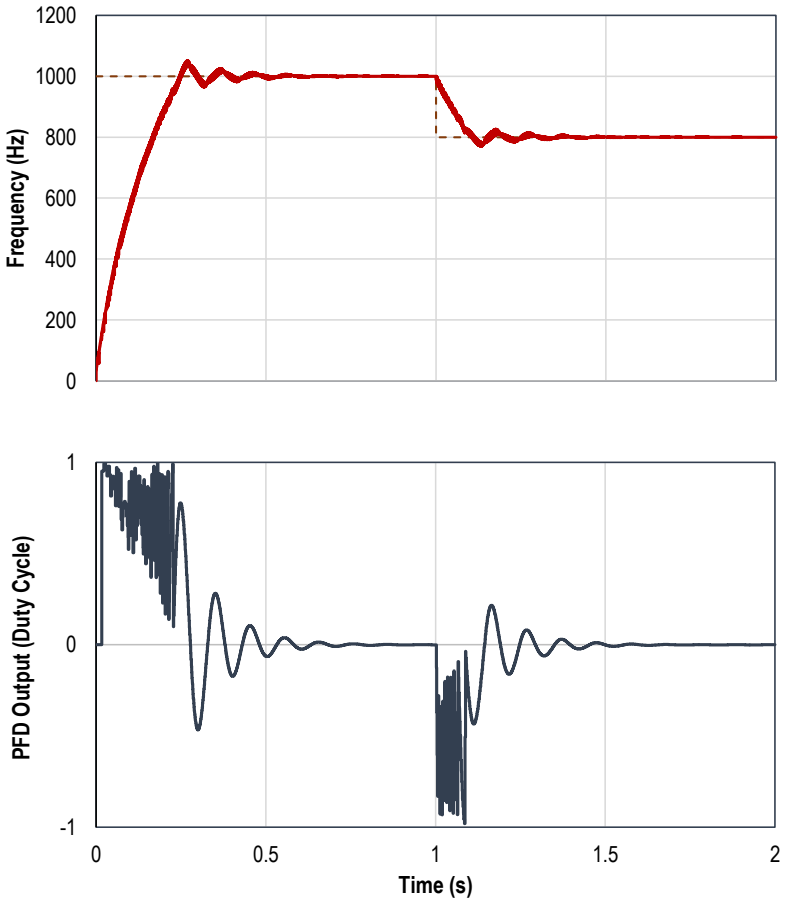

Figure 4-11 - Simulated output frequency and PFD output duty cycle

4.8 Loop Filters

After the phase detector, the loop filter is the second fundamental block of any PLL system. As discussed before, since the output of phase detector has high harmonic components and we need only the DC component of it, the loop filter must be a low-pass filter. Loop filters could be implemented in many different forms. In linear and mixed-signal PLLs passive and active filters of first order or higher orders could be used. In all-digital and software PLLs, digital filters must be implemented. The simplest form of passive loop filters is the first order lead-lag filter. Fig. 4-12, shows the first order lead-lag filter design.

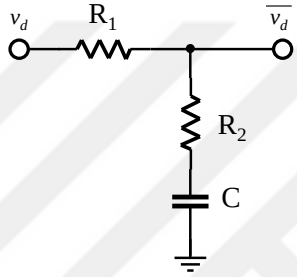

Figure 4-12 - First order lead-lag filter design

This filter is a combination of phase-leading and phase-lagging networks. The transfer function of the filter could be as follows:

$$H_f(s) = \frac{1 + s\tau_1}{1 + s(\tau_1 + \tau_2)}. \tag{4.9}$$

The phase-leading part comes from its zero and the phase-lagging part from its pole. The time constant will be:

$$\tau_1 = R_1 C, \tag{4.10}$$

$$\tau_2 = R_2 C. \tag{4.11}$$

The time constants of the lead-lag filter determine most of PLLs critical performance such as lock speed, frequency stability and phase noise. These parameters could be defined in combination with VCO parameters and the operating frequency parameters of the PLL. In our system, for design flexibility I used multi-turn potentiometers for tuning the time constants to optimum values for desired specifications.

Although active lead-lag filters or higher order filter could be implemented but due to the instabilities and additional drifts in active circuits, I preferred to use passive lead-lag filter in the proposed system.

4.9 Noise Rejecting Property of PLLs

PLL's because of their loop filters, are noise rejecting systems by nature. Fast transitions in the phase of the input signal will be filtered in the loop filter. This property makes the PLL a very useful method for phase noise rejection and recovering noisy signals. The fixed amplitude of the VCO is also another big advantage in signal recovery where the signal amplitude attenuation and fluctuation problems completely will be suppressed.

Phase noise and stability of a PLL depends on the performance and properties of all its units but mainly depends on the loop filters design. For a well-defined signal conditions, detailed procedures are available for loop-filter design for desired PLL properties. In this thesis work, I focused on the demonstration of the proposed method as a resonance tracking method. But further detailed work could be done on the deep analysis of the noise and stability of this method.

For demonstrating the noise rejection capability of a PLL, I simulated a PLL with a noisy input signal. The level of the additional noise was calculated to be equal to the noise level in our experimental system. Fig. 4-13, shows the block diagram of the simulated system.

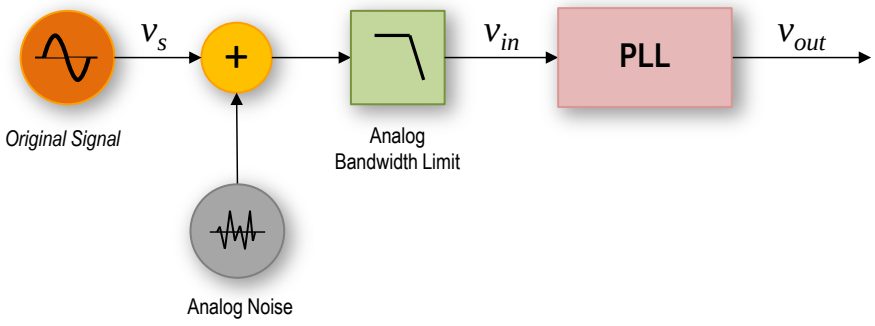

Figure 4-13 - Block diagram of PLL noise simulations

Here, v_s is a pure sinewave signal at f_s = 20 kHz. v_{in} is the PLL's input signal, superposition of the original signal with a bandlimited noise, imitating the experimental noise. The analog bandwidth block is a first-order low-pass filter modeling the analog bandwidth of the sensor's readout circuitry (the photodiode amplifier in the experimental setup).

The PLL block is a mixed signal PLL with PFD and a lead-lag filter. For simplicity the time constant of the filter is considered as the loop filter specification. The time constant is 100ms in this simulation.

As system stability indicator, the difference between the frequency of the original signal and the PLL output was shown as the frequency error. The instability and fluctuations in the phase of the input signal was shown by the phase difference between the original signal and the input signal as the input phase in degrees. Similarly, the phase between the original signal and PLL's output was shown as the output phase. Fig. 4-14, shows the simulation results.

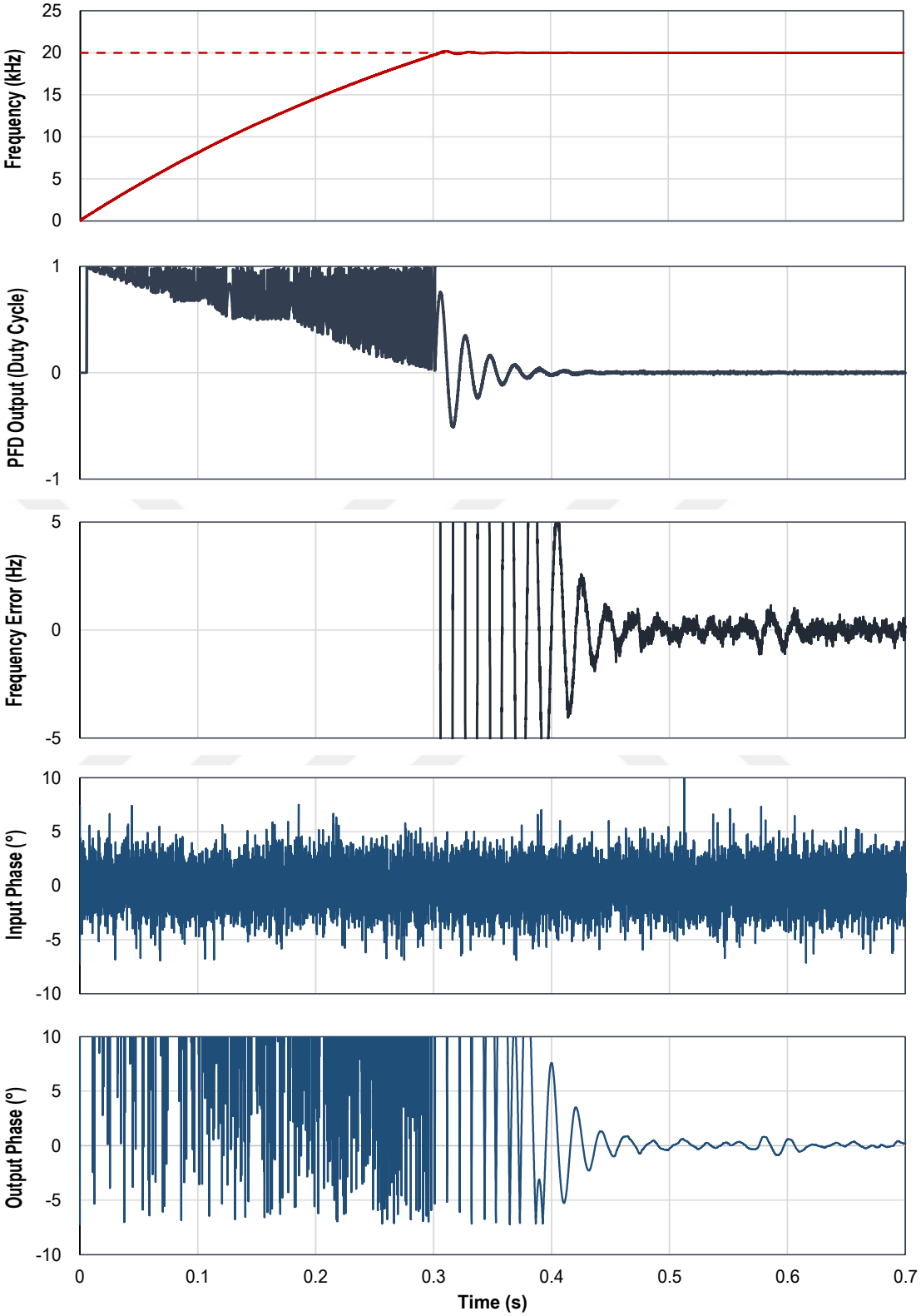

Figure 4-14 - PLL noise rejection simulation results

4.10 Resonance Frequency Tracking using Digital PLLs

For a resonator driven at the resonance frequency, the output phase will be -90° with respect to the drive signal. As described before in chapter 3, in the self-sustained oscillation using a +90° phase shifting and amplifying the signal from the resonator, the system automatically will lock on the resonance frequency. Similar mechanism could be implemented using PLLs as well.

Using PLLs for resonance tracking will improve the stability of the system by two ways:

1. Phase noise rejection property of the PLL will directly reject fast jumps in the frequency of the system by low-pass filtering phase noise in the PLL loop filter.
2. Driving the resonator with a fixed amplitude will improve the stability of the drive and readout stages by minimizing the amplitude dependent drifts in the analog circuits.
3. Driving with a pure sinewave will block all the potential harmonic oscillations and feeding back these parasitic harmonics into the resonator.

Beside the general advantages of PLLs for resonance tracking applications, type-II PLLs because of their wide frequency range and preventing lock to harmonics made them attractive solution for this kind of systems.

4.11 Advantages of Type-II over Type-I PLLs for Resonance Tracking

As mentioned earlier, the Type-I systems with frequency dependent phase response will introduce frequency and phase errors at frequencies different than VCO's center frequency. For studying and comparing the behavior of the Type-I systems with the proposed method using Type-II PLL, a Simulink model was developed and simulated. Fig. 4-15. shows the block diagrams of Type-I and Type-II PLL based resonance tracking systems.

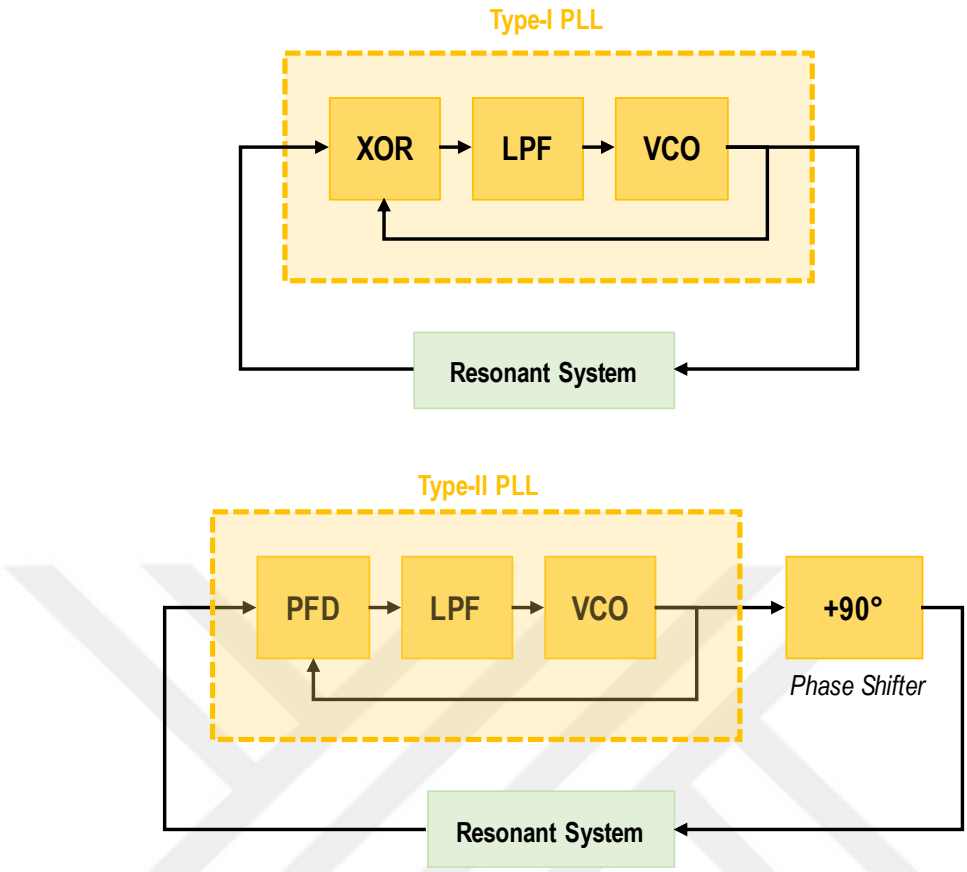

Figure 4-15 - Block diagrams of Type-I and Type-II PLL resonance tracking systems

Performance of two methods was simulated on two different resonators with quality factors of 5 and 10. The VCO range for both systems was set to 15 to 25 kHz. The natural frequency of the resonator was changed from 16 to 24 kHz with 2 kHz steps and the frequency tracking performance of both methods was simulated in terms of the locked frequency, phase angle and, the amplitude of the resonator. The output of the VCO was set to $1V_{p\text{-}p}$ and the amplitude of the resonator was normalized to the amplitude at natural frequency. For phase-shifting in Type-II system, a secondary oscillator operating at the same frequency of the VCO with +90° phase shift (Quadrature Oscillator) was used in the simulation model. Details of the simulation model discussed on 4.15. Fig. 4-16 shows the simulation results.

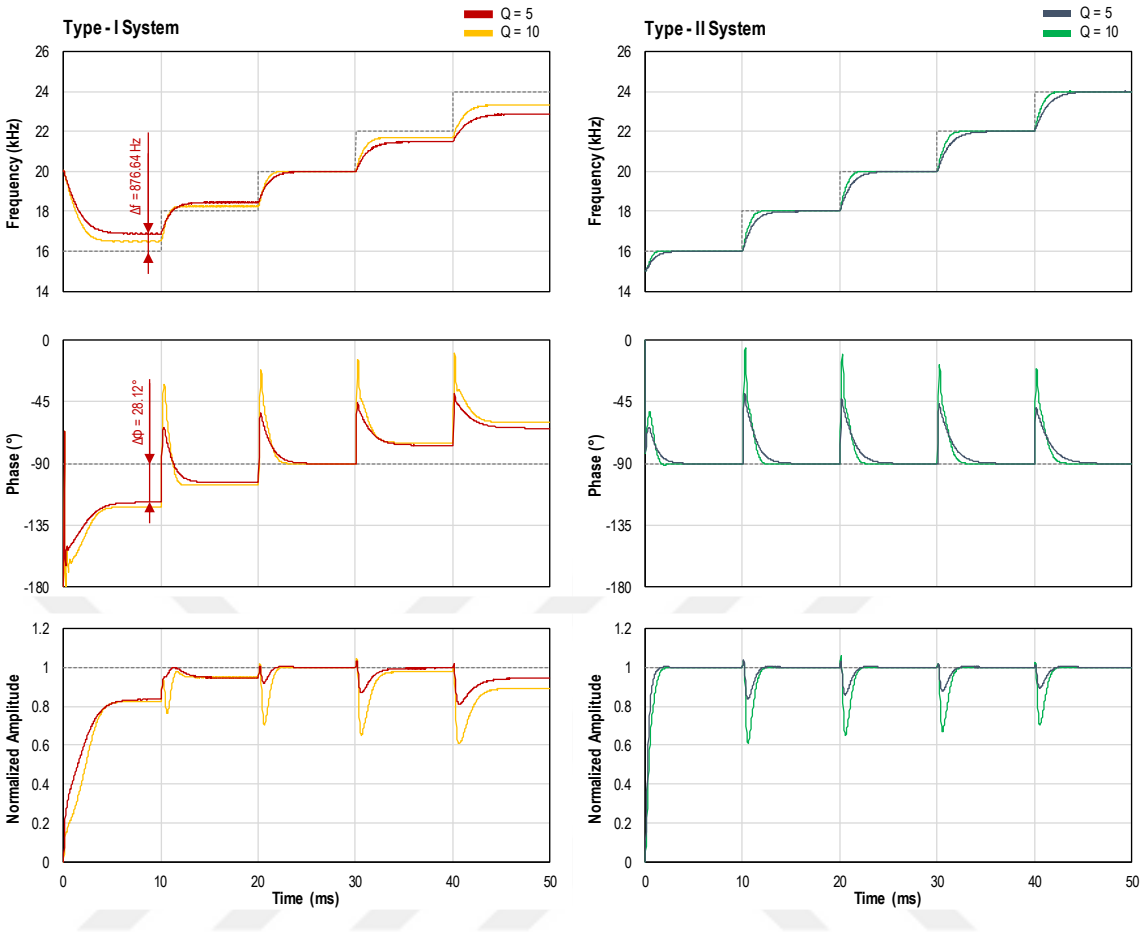

Figure 4-16 - Frequency tracking performance of both Type-I and Type-II PLL with two resonators with quality factors of 5 and 10.

As shown in simulation results, Type-II system clearly shows better tracking performance with zero frequency and phase error for all frequencies in the operating range and also maintaining a fixed amplitude at resonator.

The resonators in ideal case must be driven with a sine wave, and the readout signal is also sinusoidal. But digital PLLs with PFDs, work with square waves. For implementing a resonance tracking system using Type-II digital PLLs we will need to solve these fundamental units:

1. Analog front-end stage for converting the sinewave input to square wave
2. Broadband sinewave VCO
3. Broadband +90° analog phase-shifter

The first block could be implemented using a voltage comparator op-amp. For the sinewave VCO and the +90° phase shifter there is no general solution.

4.12 Sinewave Phase Detection in Digital PLLs

For converting the analog sinewave input signal to a digital signal an ideal zero crossing detection circuit could be implemented at the input of the PLL block. The simplest design is an op-amp configured as a comparator. Fig. 4-17, shows the voltage comparator design.

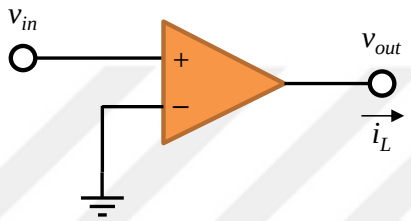

Figure 4-17 - Zero crossing detection circuit

The analog sinewave signal will be convert to a square wave at the output of the op-amp and the analog noise will be appeared as phase instability called as Jitter. Fig. 4-18, shows the waveforms for input and output of the circuit in presence of noise.

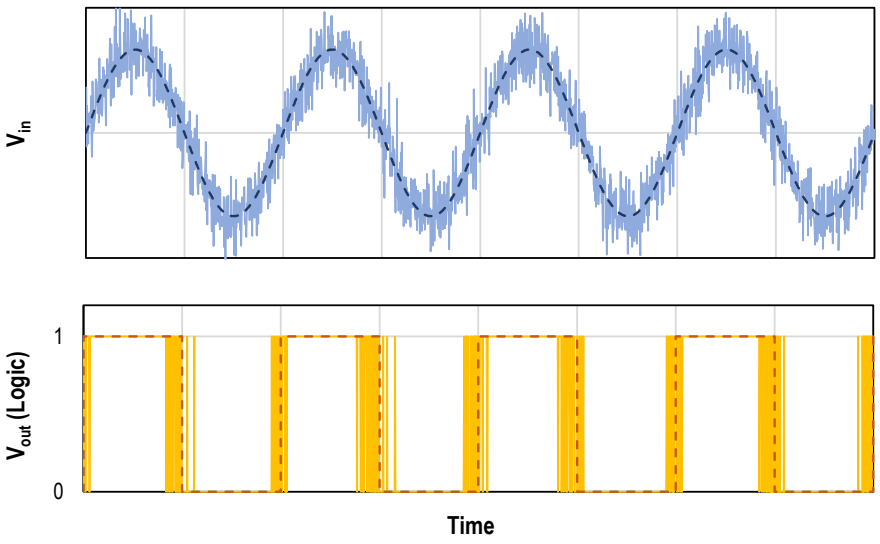

Figure 4-18 - Input noise and jitter in the zero-crossing detection

The timing phase jitter at the output of the zero crossing circuits depends on the SNR and the slope of the input signal near the switching point. For a sinusoidal input signal it could be shown that the slope in proximity of zero is

$$\frac{\Delta v}{\Delta t} = 2\pi f A. \tag{4.12}$$

A is the amplitude of the sinusoidal input signal and *f* is the frequency. For an instantaneous noise voltage of $v_n(t)$ corresponding timing jitter will be

$$\Delta T(t) = \frac{\Delta v}{\Delta t} v_n(t) = 2\pi f A\, v_n(t), \tag{4.13}$$

and in terms of phase it could be written as

$$\Delta\phi(t) = \frac{2\pi}{T}\left(2\pi f A\, v_n(t)\right) = 4\pi^2 f^2 A\, v_n(t). \tag{4.14}$$

T is the period of the sinusoidal signal.

4.13 Sinewave Generation with Digital PLLs

For sinewave generation basically a sinewave VCO could be implemented instead of square wave VCO of the Digital PLL. For phase detection of the sinewave VCO, its output must be converted to square wave using a zero-crossing detection circuit as described before. For sinewave VCO there are various design topologies but mostly have limited frequency range.

On the other side we need also a broadband +90° analog phase shifter. This is also impossible with simple analog electronics. For +90° phase shifted VCO, A quadrature oscillator could be a good choice but like the sinewave VCO techniques, their narrow frequency range will limit the operation frequency of the system for wide band applications.

As an easy solution for this problem, I proposed an old sinewave generation method called as logarithmic sinewave shaping using differential pair with active load [60]. I used this method many years ago in analog function generator designs. This method has a very wide operating range without any time constants in the circuit, keeping phase delay in minimum possible values.

Combining this method with a triangular wave generator coupled to the square-wave VCO of the Digital PLL results in a broad-band sinewave VCO with exact +90° phase shift on its whole operating frequency range.

In this method, the sinewave is generated by deforming a triangular waveform using logarithmic current relation of the differential pair transistors. The generated sine wave will not be pure sinewave but with carefully tuning of the circuit to its optimum conditions a good enough approximation of sinewave with THD level of <0.3% could be achieved [60]. Fig. 4-19, shows the core of the triangular to sine wave converter circuit.

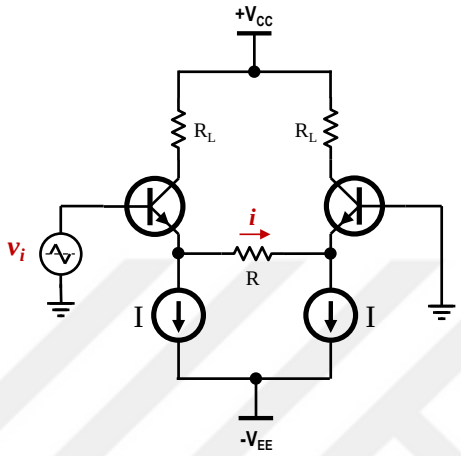

Figure 4-19 - Triangular to sine wave converter circuit

Fig. 4-20, shows the waveform transfer function of the circuit at the optimum input amplitude.

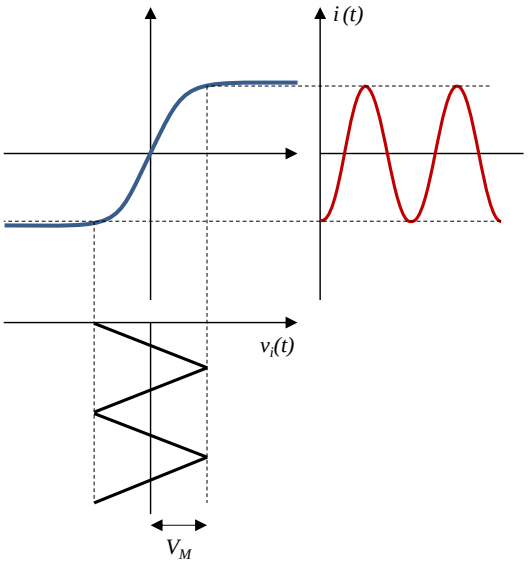

Figure 4-20 - Waveform conversion signals and at optimum input amplitude

In this circuit, the purity of the output sinewave highly depends on the amplitude of input triangular wave. The optimum operation point of the circuit for minimum possible distortion analytically could be determined using power series expansion of the output signal. Simulated results reported in [60] shows the lowest harmonic distortions at at V_i/V_T of 6.6. This gives the optimum triangular amplitude of 170 mV for V_T = 25.7 mV at room temperature to T = 25°C.

For a voltage output circuit, it is possible to convert the current through the R using an op-amp to amplify the voltage across the R. Alternatively a simpler equivalent circuit could be implemented as shown in Fig. 4-21 [61].

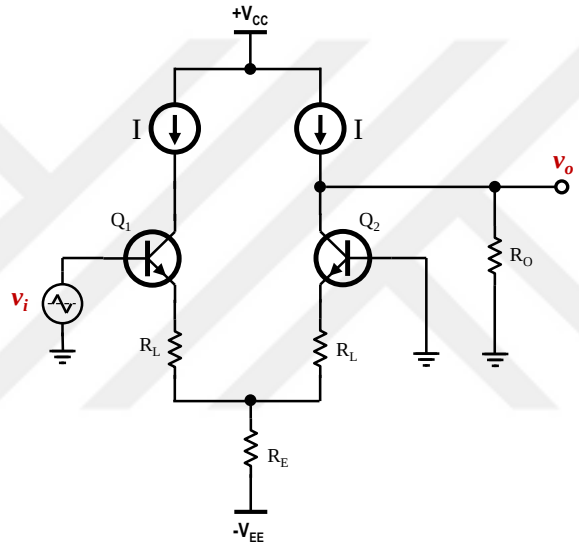

Figure 4-21 - Triangular to sine wave converter with voltage output

In this design, the differential current signal of the transistors will be reflected through the R providing a ground referred signal of v_o. Since,

$$i_o(t) = I_{C1} - I_{C2} \tag{4.15}$$

the output voltage will be

$$v_o(t) = (I_{C1} - I_{C2})R_O \tag{4.16}$$

For practical construction of the design shown in Fig. 4-21, the identical current sources could be implemented using current mirror circuit as shown in Fig. 4-22.

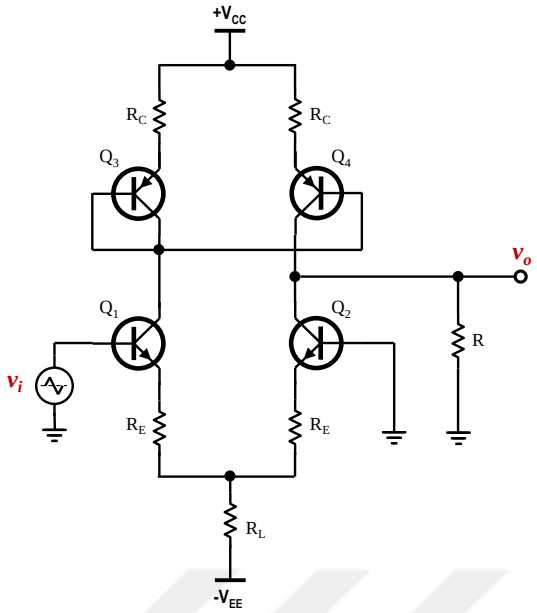

Figure 4-22 - Triangular to sine wave converter with current source circuit

4.14 Current Mismatch in Differential Pair Sine Wave Shaping

For the proper operation of the circuit, it is very important to equate the DC currents in left and right branches of the circuit. In the case of non-equal currents, the resulting output waveform will be asymmetric. For discarding this non-equalities, several different methods could be used. One method is to add a small DC current to the input voltage [61]. This approach is shown in Fig. 4-23.

Use of matched pair transistors for Q1-Q2 and Q3-Q4 pairs are also recommended for the optimum waveform generation with lowest possible harmonic distortion.

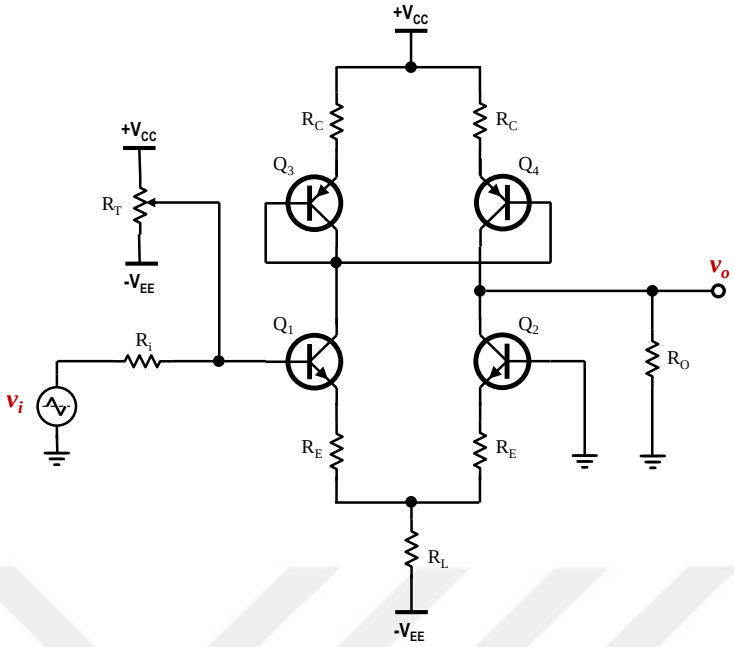

Figure 4-23 - Matching the circuit symmetry by additional DC voltage offset

Another method is to adjust for the matched R_E resistors in the circuit. This method was shown in Fig. 4-24.

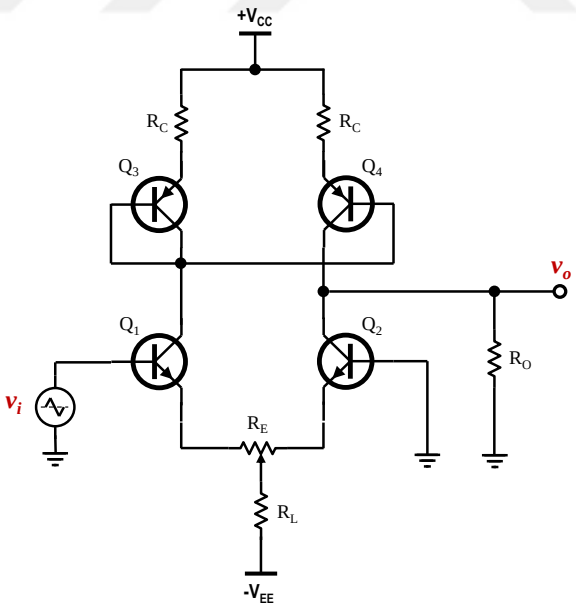

Figure 4-24 - Matching the circuit symmetry by adjustable emitter couple resistor

4.15 Experimental Implementation of the Sine Wave Shaper

For the circuit in Fig. 4-24, with recommended values of R_C = 10 kΩ, R_E = 47 Ω, R_L = 15 kΩ and R_O = 100 Ω, maintains a DC current about 1 mA in current mirror transistors. Fig. 4-25 and 4-26 show the measured waveforms of the circuit and frequency spectrum of the output sine wave, operating at its minimum distortion point, respectively. The minimum distortion conditions is in a good agreement with experimental results where the lowest distortion achieved around 150 mV of peak amplitude for the input triangular wave. The total harmonic distortion of < 0.35% was achieved.

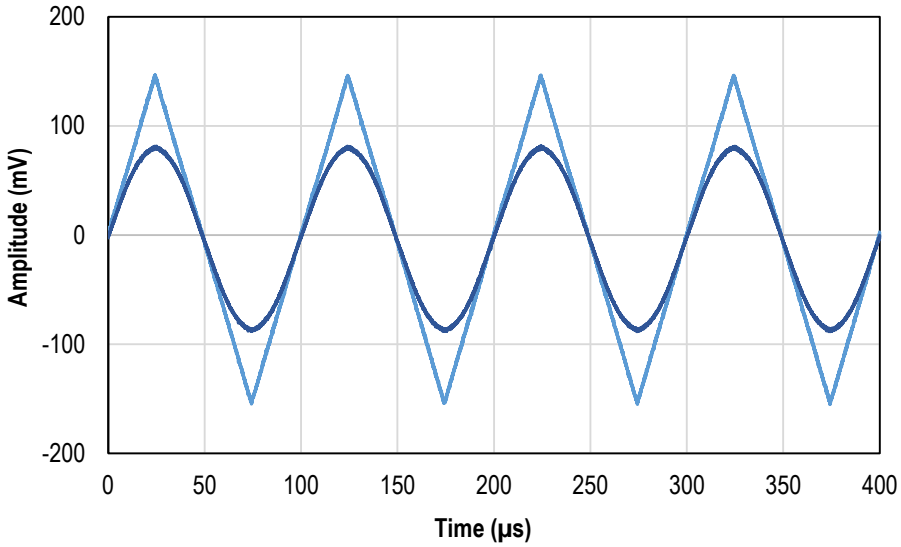

Figure 4-25 - Measured waveforms of the practical implemeted triangular to sine wave converter

For measuring distortions of the output sinewave, a LabVIEW based signal analyzer was developed. Fig. 4-26, shows the measured distortion of the circuit was in desired frequency range of 1 to 100 kHz in terms of THD.

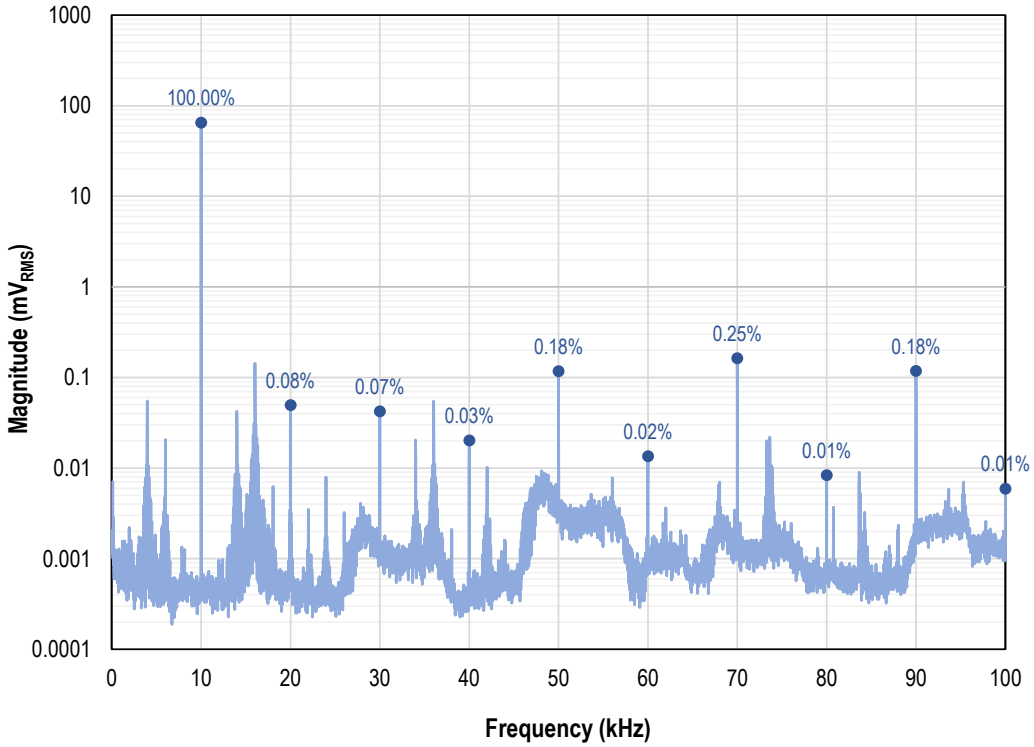

Figure 4-26 - Frequency spectrum of the generated sinewave

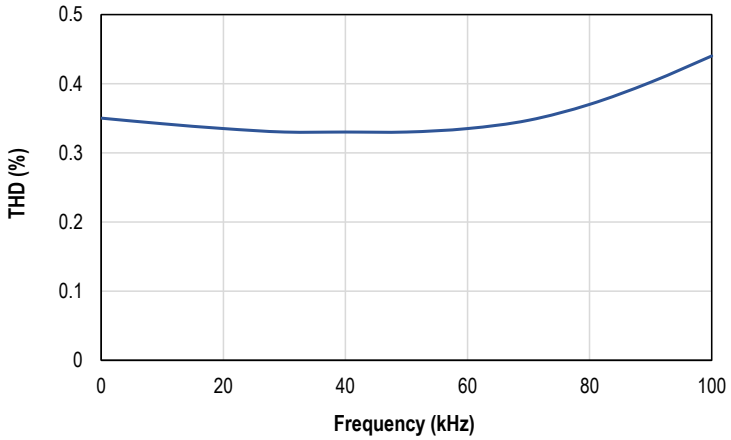

Figure 4-27 - Distortion of the output sinewave vs. operating frequency

4.16 Broadband +90° Phase Shifting

The +90° phase shifting property comes from the square wave to triangular wave converter circuit. In the case of square wave VCO's usually used in Digital PLLs, the triangular waveform could be extracted directly from the waveforms already are present in the square wave VCOs [62].

4.17 Square Wave VCOs

Mixed-signal PLLs use monolithic square wave VCOs. In these VCOs an integrator capacitor is charged by current sources whose the current depends on the input voltage of the VCO [63]. The voltage across the capacitor will be a linear ramp because of the fixed charging current provided by the current source. When capacitor voltage reaches to a certain threshold voltage usually $V_{DD}/2$. The logic changes the current direction in opposite direction. The changing logic state of the VCO logic circuit, provided a square wave whose frequency depends on the input voltage of the VCO. Fig. 4-28, shows the simplified charging network of VCO's capacitor is square wave VCOs.

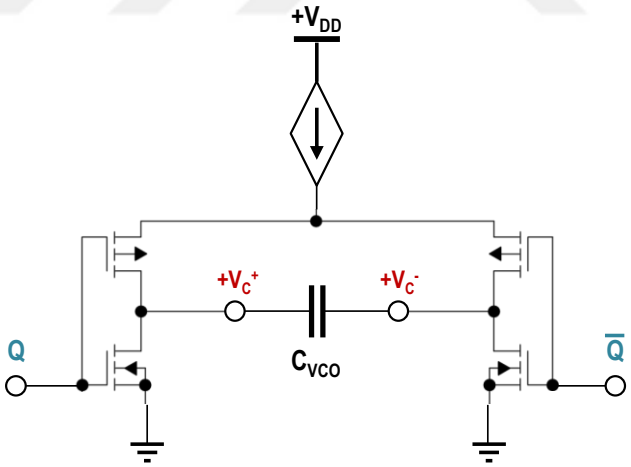

Figure 4-28 - Simplified charging network of VCO's capacitor is square wave VCOs

4.18 Triangular Waveform Construction

Using the voltage of the VCO's capacitor, triangular or sawtooth waveforms could be constructed. Fig. 4-29 shows the output and capacitor waveforms in a square wave VCO operating at 20 kHz.

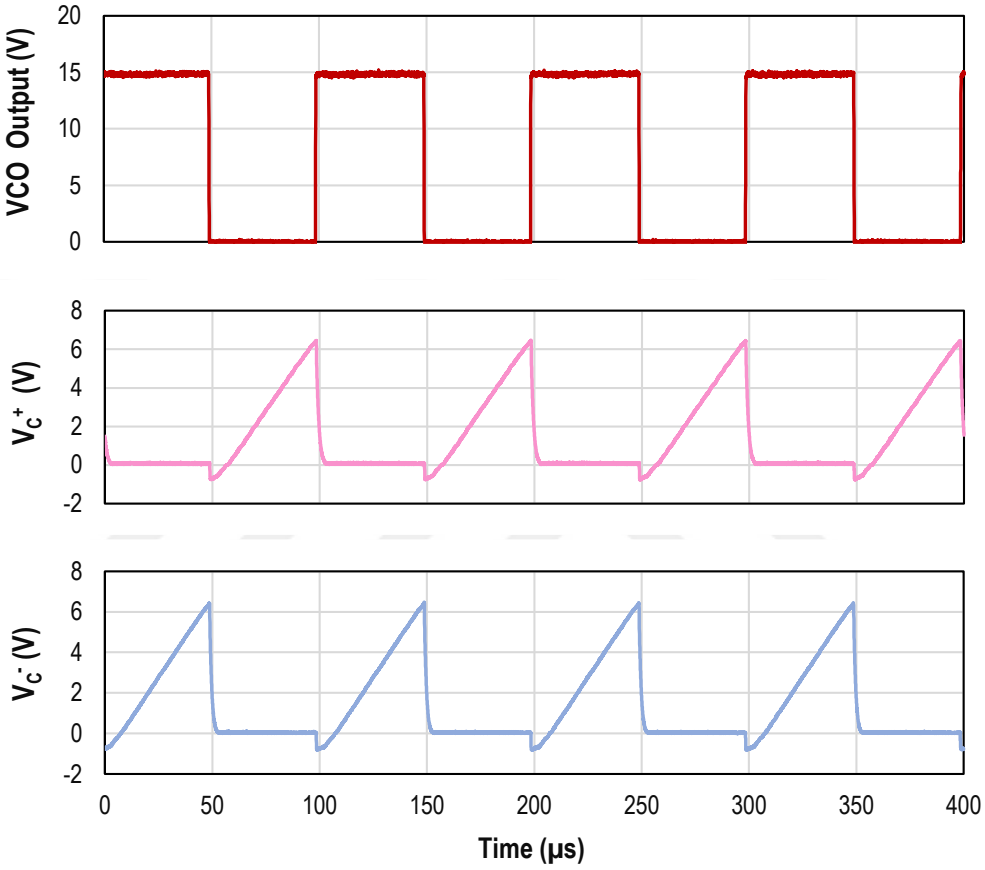

Figure 4-29 - Output and capacitor voltage waveforms in square wave VCO

The V_c^+ waveform contains the rising ramp for constructing a triangular waveform but inverting the V_c^- could not be directly used as the falling ramp because of the DC offset at its first half cycle. This DC offset could be cancelled by adding a fraction of the VCO output to the inverted V_C^- waveform. Finally, a DC voltage must be added for nulling the remaining DC offset on the triangular wave. The proposed method for constructing a triangular waveform was shown in Fig. 4-30.

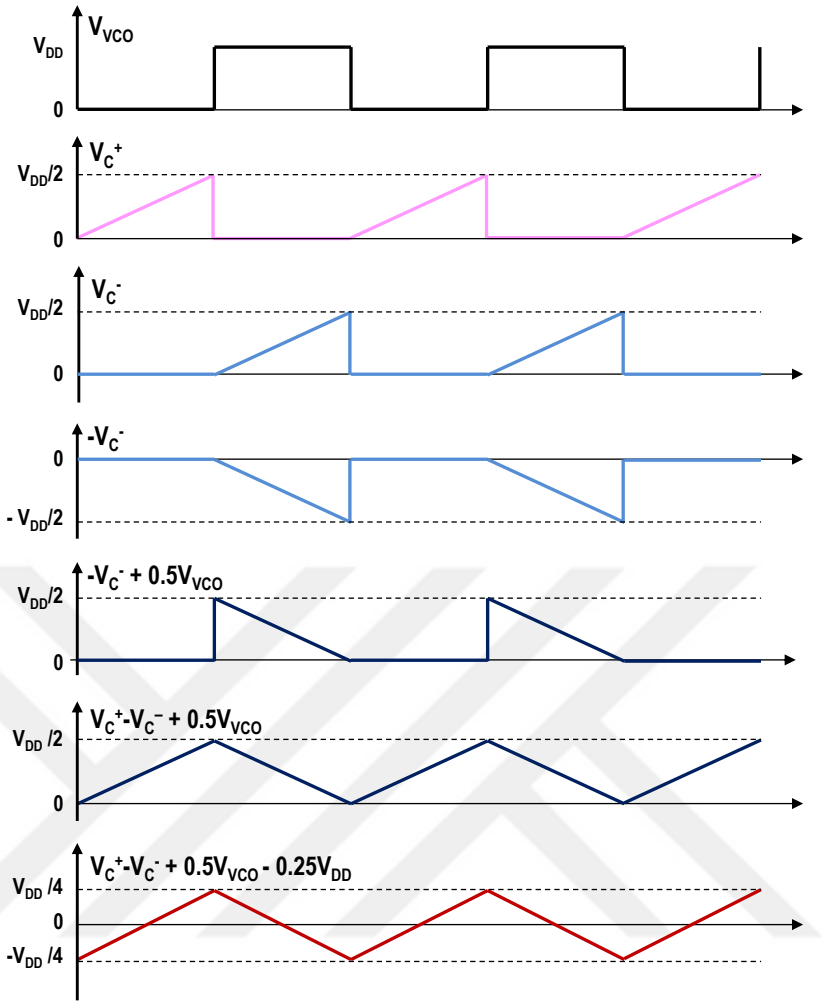

Figure 4-30 - Waveforms in square wave VCO and constructing of triangular waveform

Assuming identical waveform parameters for the VCO capacitor waveforms, the general equation for generating a triangular waveform as a function of the V_C^+, V_C^-, VCO output and V_{DD} voltage could be expressed as follows:

$$v_{tri}(t) = \alpha(V_C^+(t) - V_C^-(t) + \beta_1 V_{VCO}(t) + \beta_2 V_{DD}) \tag{4.17}$$

In this equation, α is the gain coefficient for adjusting the output amplitude of the triangular wave, β_1 and β_2 are coefficients for the VCO output signal and the supply voltage of VDD, respectively. Fig. 4-31, shows a simple analog adder circuit for implementing the proposed method.

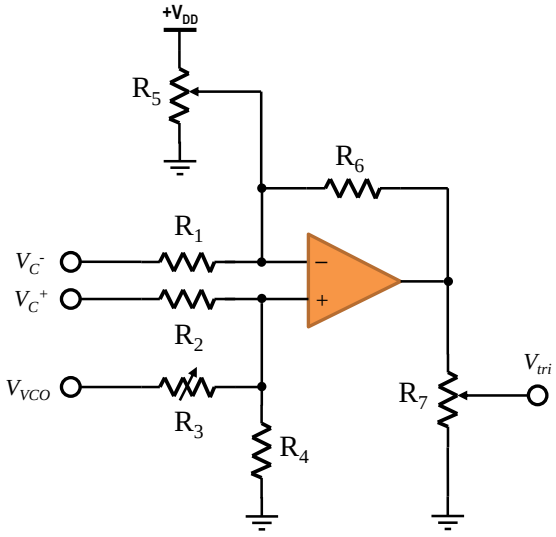

Figure 4-31 - Adder circuit for constructing the triangular waveform

In the adder circuit, R3 and R4 network adjusts β_1 coefficient and R5 adjusts the β_2. In the ideal case the values of β_1 and β_2 are 0.5 and -0.25 as shown in Fig. 4-30. The gain of the adder op-amp could be near unity. The voltage dividing network of R7 were used to adjust the α coefficient to set the amplitude of the triangular wave to its optimum amplitude. For eliminating the loading effect of the adder circuit on the VCO, buffer op-amps must be used at the capacitor pins.

4.19 Experimental Implementation of the Triangular Waveform Generator

For generating a symmetric triangular waveform, the coefficients of the adder circuit must be calculated properly based on the measured signal levels on the experimental circuit. Fig. 4-32 shows the experimentally generated triangular waveform.

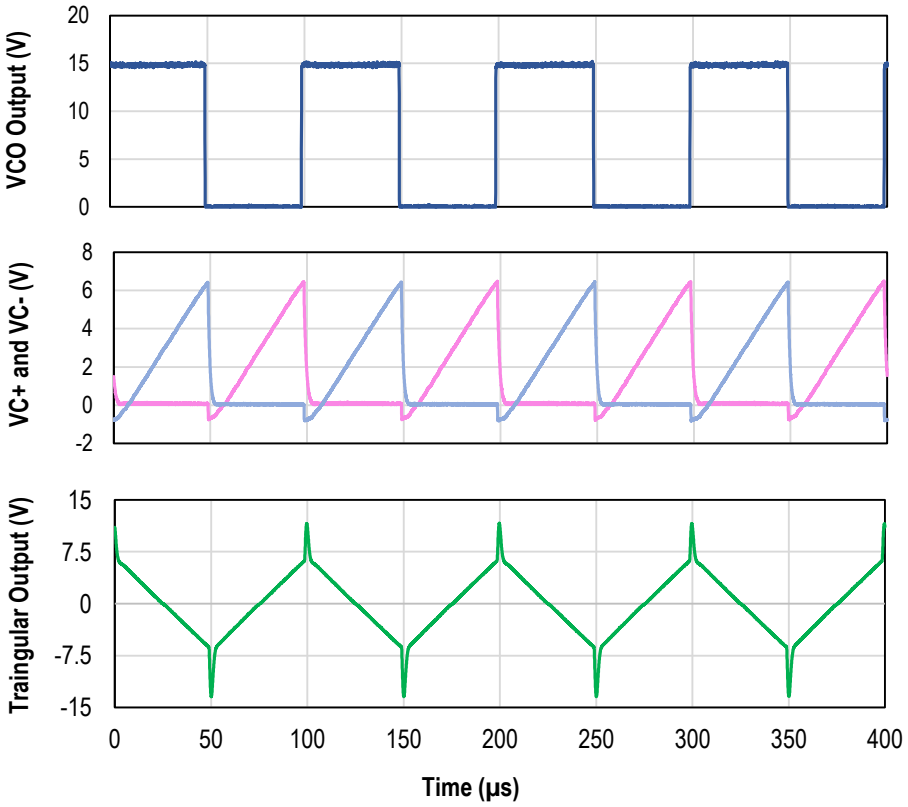

Figure 4-32 - VCO and triangular output waveforms

The spikes on the triangular wave comes from the rise and fall time duration of the VCO's H-bridge network and could not be eliminated. But in our sinewave shaping circuit, because of its saturation region at the peaks of the sinewave, these spikes will be clipped. For a near unity gain adder circuit, the output amplitude of the triangular output waveform was around 8 $V_{p\text{-}p}$. For the optimum triangular waveform of 150 $mV_{p\text{-}p}$, the α coefficient will be 0.033.

4.20 Sinewave Generation

Combining the sinewave shaper circuit discussed in chapter 4.12 with the triangular wave generator will be the targeted 90° phase shifted sinewave VCO. As a cascaded design, the quality of the generated sinewave highly depends on the quality of the generated triangular waveform also. For the optimum possible results, the whole design must be tuned for lowest distortion at the output. Fig. 4-33, shows the output

waveform of the sine shaper circuit using the generated triangular waveform. A variable gain amplifier was implemented to adjust the output amplitude at desired value. The output amplitude was set to $1V_{p-p}$.

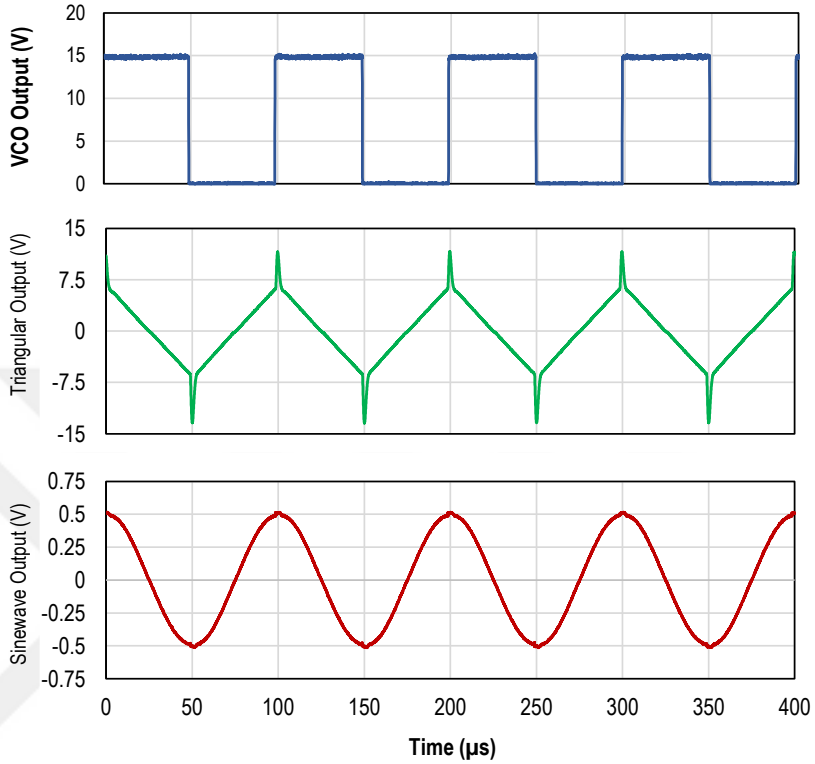

Figure 4-33 - Sine output waveform using the generated triangular waveform

For measuring the quality of the output sinewave, the frequency spectrum and distortion of the output signal were also measured. Fig. 4-34 shows the frequency spectrum of the generated sinewave results. The lowest total harmonic distortion of <1% was achieved at frequency range of 10 to 20 kHz. For our experimental purposes the achieved distortion level is sufficient but for further increase of the purity high precision op-amps could be used. Fig. 4-35, shows the distortion level versus frequency.

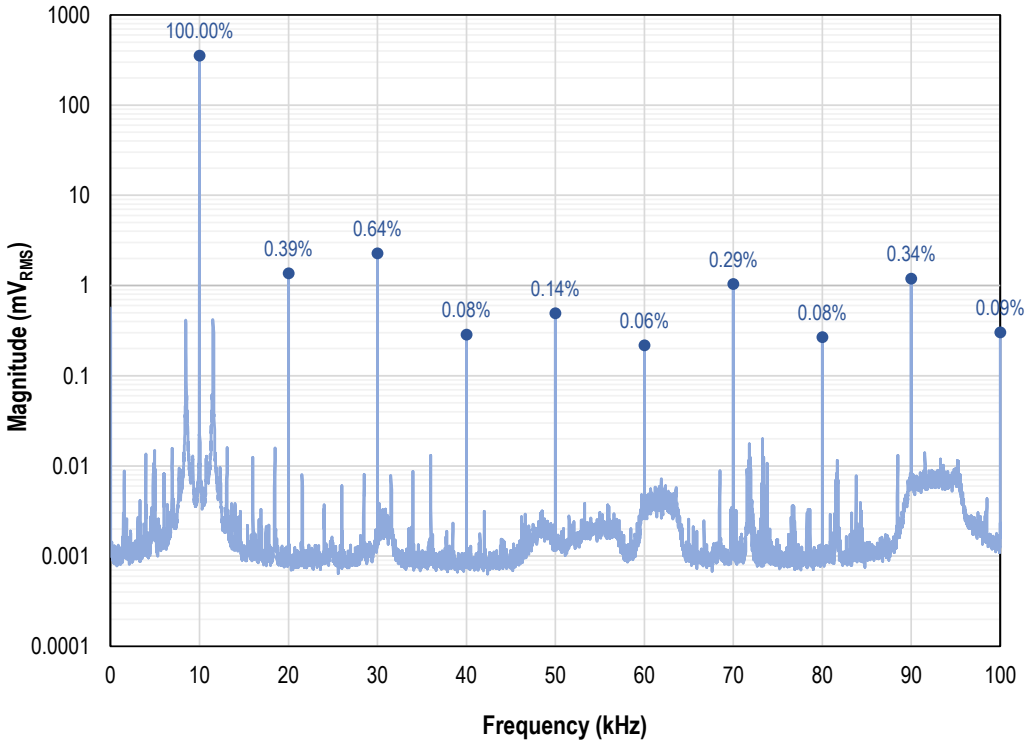

Figure 4-34 - Frequency spectrum of the generated sine wave

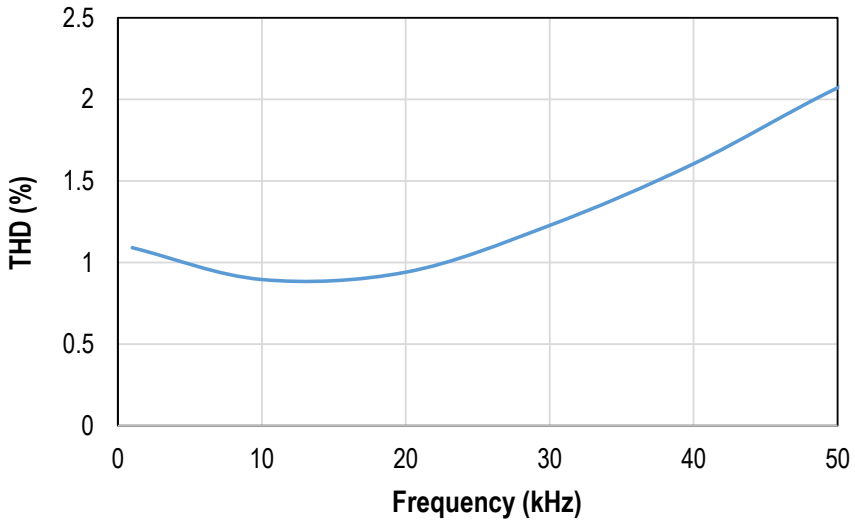

Figure 4-35 - Distortions of the generated sine wave versus operating frequency

4.21 Modeling and Simulation

Because of the highly non-linear behavior of the PLL system, simulations are wide used in design and development of PLL-based systems [59]. For the proposed method of resonance tracking a simulation model was developed using Simulink. Fig. 4-36, shows the block diagram of the developed model.

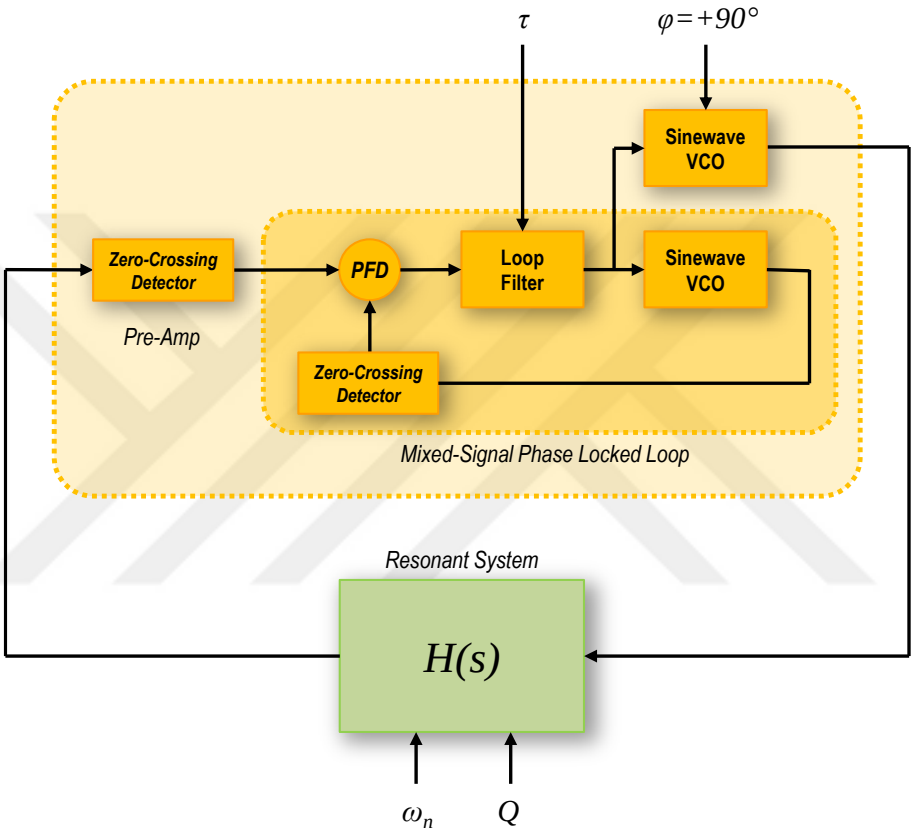

Figure 4-36 - Block diagram of the simulation model

PFD and loop filter ware modeled exactly using their logic and analog circuits. The VCO was modeled using an ideal sinewave with +90° shift. The in-phase output was connected to PFD and the quadrature output was used to drive the resonator. A resonator model with variable resonance frequency was also developed.

Fig. 4-37 shows the transient response of the system from startup. In this simulation a resonator with natural frequency of 20 kHz and quality factor of 5 was modeled. The time constant of the PLL's loop filter was set to 100 ms.

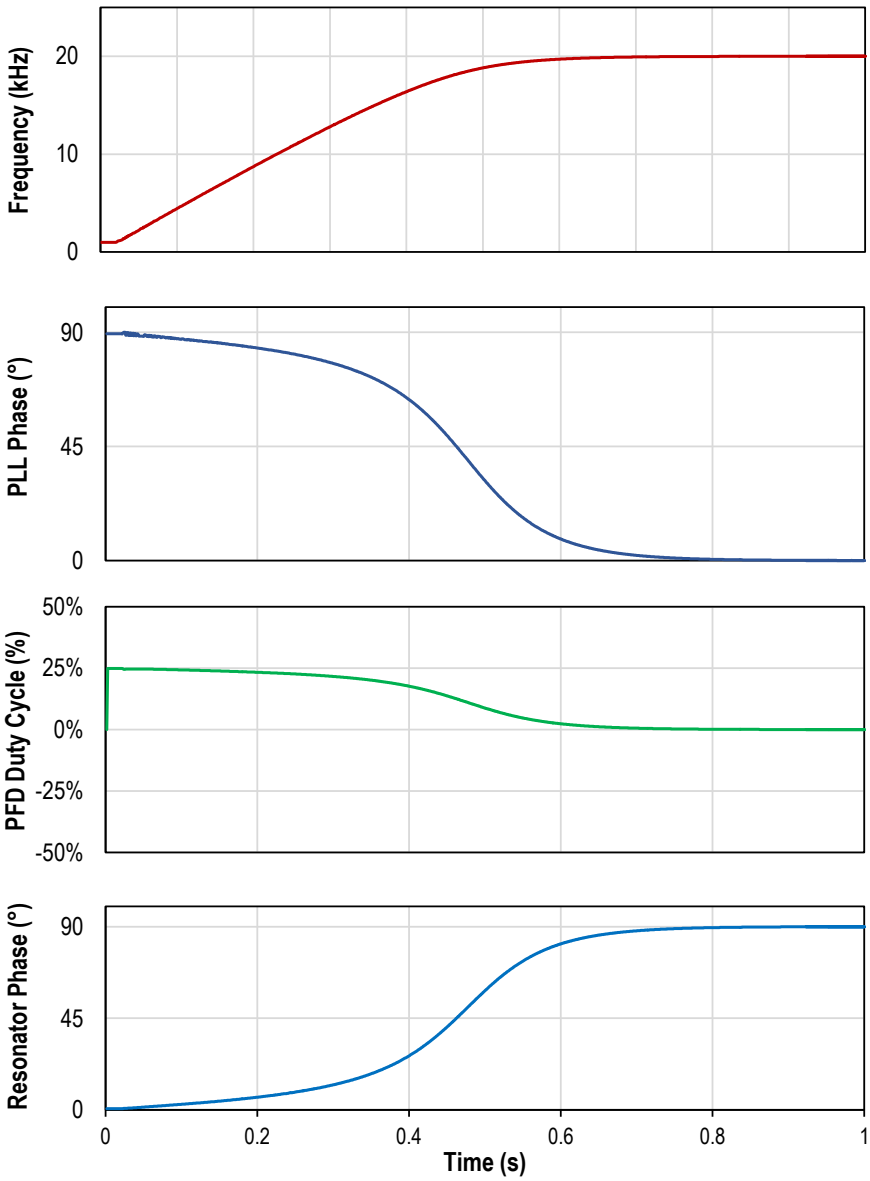

Figure 4-37 – Simulation results for transient response of the system locking to the natural frequency of the resonator.

The simulation results completely agree with theoretical expectations of the system. The VCO starts from its minimum free-running frequency of 1 kHz. The phase difference in the resonator is around zero degrees at this frequency. Since the resonator was driven with +90° phase shifted sinewave the output of the resonator or the input of the PLL is 90° leading with respect to its VCO input. This phase difference causes a positive phase error signal at the output of the PFD and increase the output of loop-filter

and subsequently increasing the VCO output frequency. This sequence repeats until the frequency reaches to the natural frequency of the resonator.

At natural frequency, the resonators phase reaches to -90° and eliminates the +90° phase of the phase-shifted VCO causing a total phase shift of zero in the resonator feedback loop. In this case, the phase difference between the PLL's VCO and output of the resonator will be zero and the PLL will be settled at lock state.

4.22 Step Response to Natural Frequency Shifts

If the natural frequency of the resonator shifts at the lock state. The phase of the resonator loop will be changed, causing a phase error in the PFD. This error signal passing through the loop-filter will change the VCO output frequency in such a way to compensate the natural frequency shift until nulling the total phase at resonator loop to zero degrees.

Fig. 4-38 shows the response of the system to changes in the natural frequency of the resonator. In this simulations the natural frequency of the resonator changes in 1 Hz and 2 Hz steps at the lock state. The initial natural frequency of the resonator is 20 kHz with quality factor of 5 and the time constant of the PLL is 10 ms.

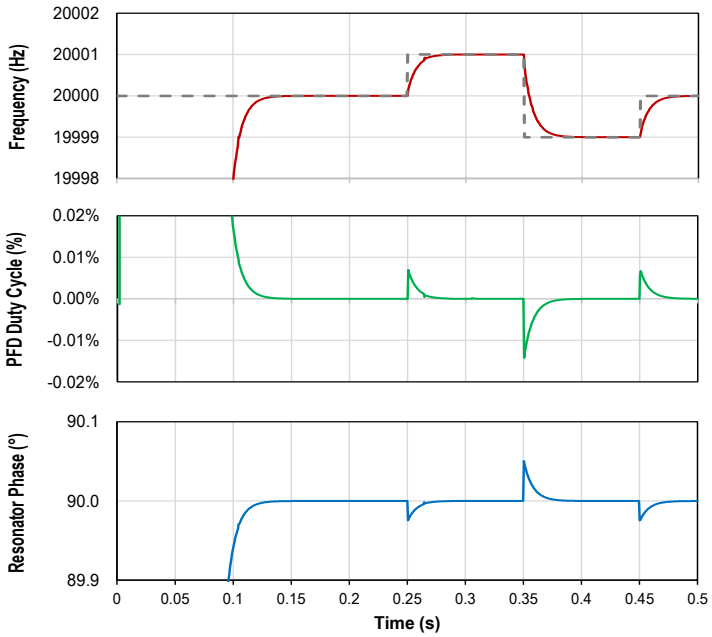

Figure 4-38 - Response of the system to changes in the natural frequency of the resonator

4.23 Locking Performance

Using the developed model, it is possible to simulate the performance of the proposed resonance tracking system in different conditions to study its key performance parameters such as the locking speed, stability and noise immunity. The stability of the output frequency in the presence of input noise is the most important parameters for sensor applications.

The performance of the system depends on the resonators parameters also. In this part, the transient response of the system was simulated as a function of key system parameters of both the PLL and the resonator.

4.24 PLL Time Constant

Loop filter time-constant is the most important parameter in the transient response of PLLs. As described before increasing the time constant will slow down the response of the system but will increase the stability of the output frequency. For slow sensor applications where the best possible stability is aimed, larger time constants must be preferred. On the contrary, a faster response time must be required for actuator applications. For observing the effect of the time constant on the transient response of the system, developed model was simulated in different time constant values from 10, 20, 50 and 100 ms for a resonator with natural frequency of 20 kHz and quality factor of 5. The VCO operating frequency range was set to 1 to 25 kHz in these simulations. Fig. 4-39 shows the simulation results.

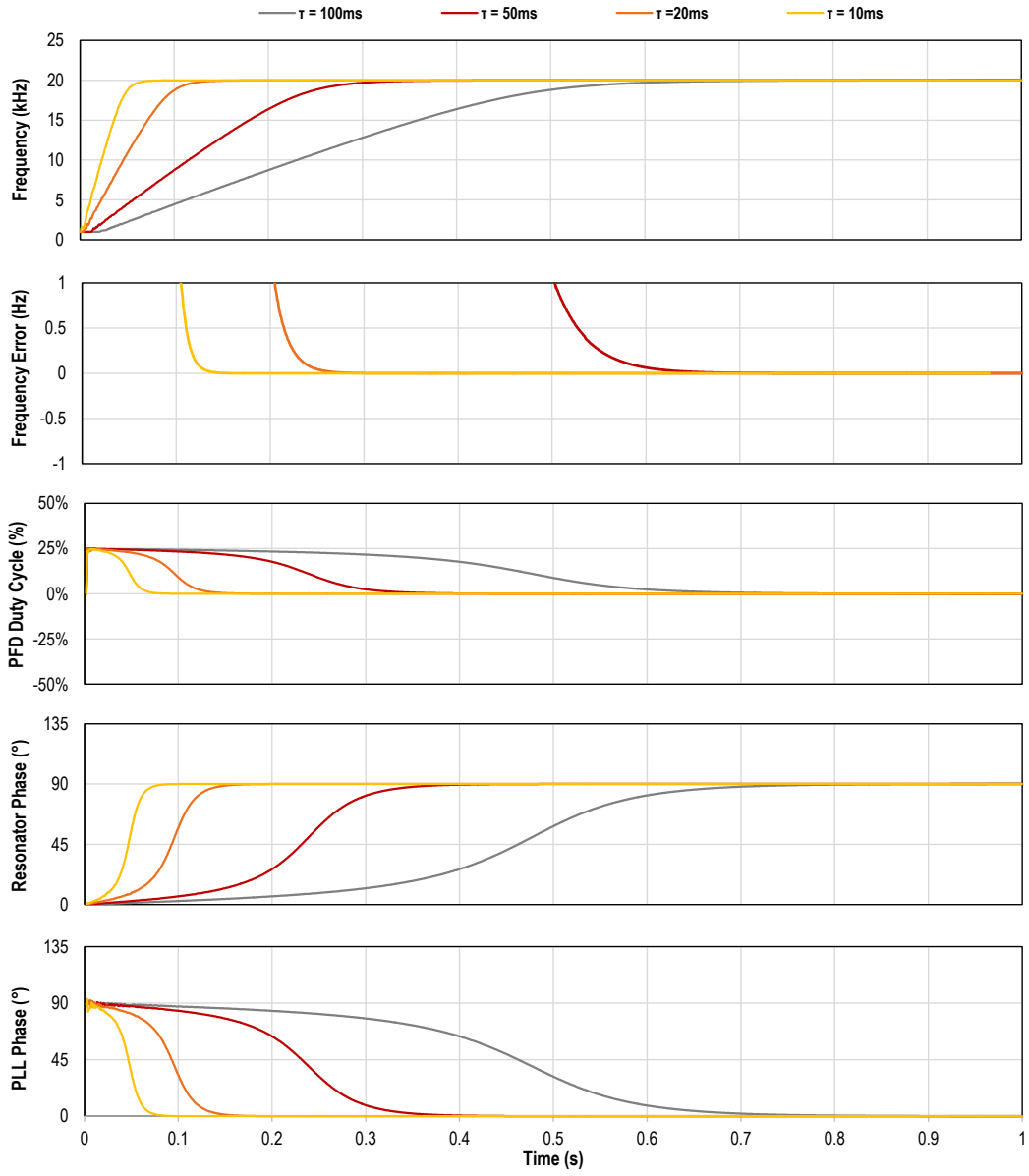

Figure 4-39 - Transient response of the system versus PLL's time constant

4.25 Resonator's Quality Factor

Since the phase difference in the resonator depends on the quality factor, the resulting phase error in the PLL input will be a function of the resonators quality factor. Fig. 4-40, shows the simulation results for different quality factors of 1, 2, 5 and 10. Time constant of the PLL was set to 100 ms in these simulations.

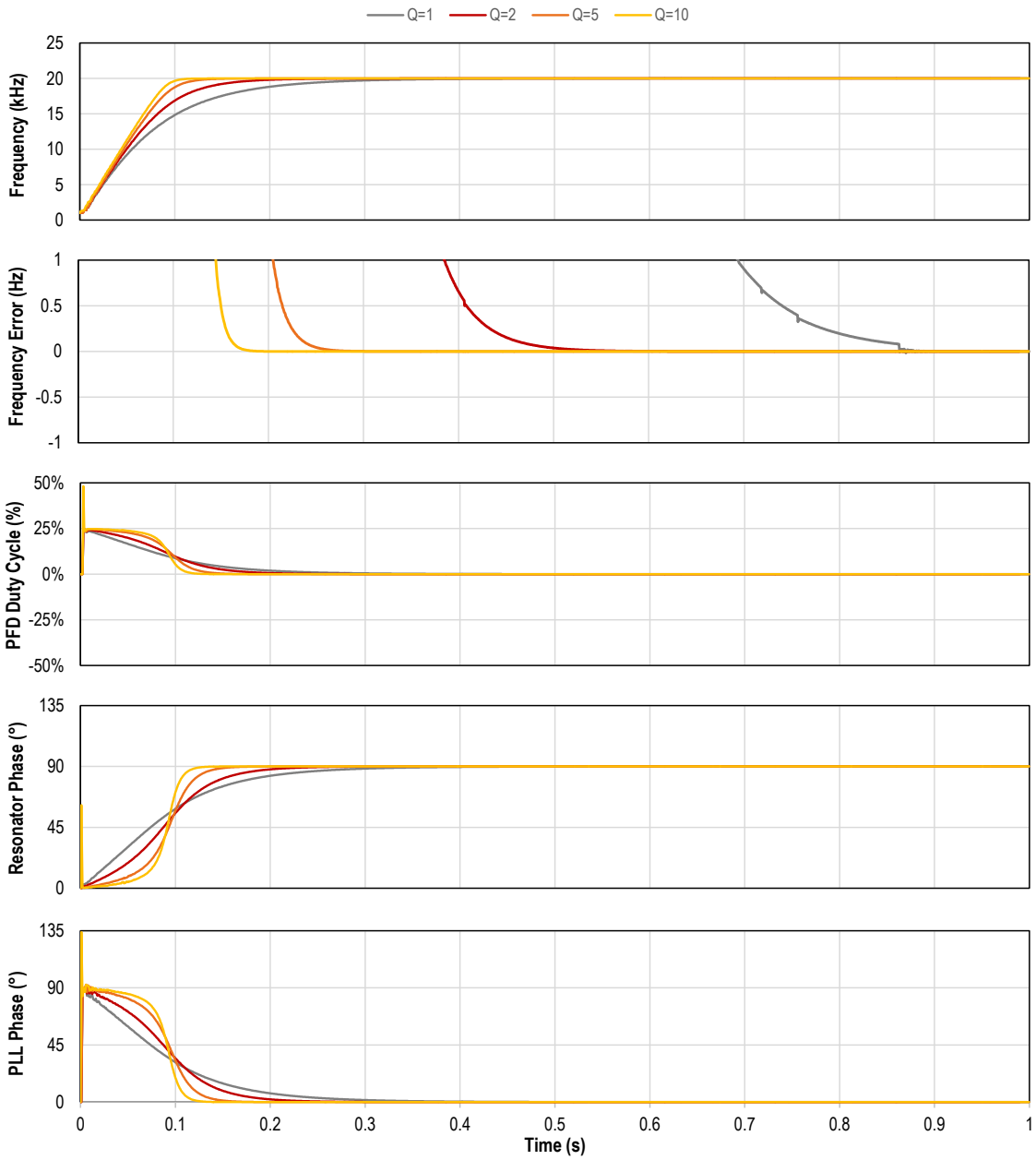

Figure 4-40 - Transient Response of the System versus Resonator's Quality Factor

4.26 Phase Compensation

Because of the propagation delays in each stage, a frequency dependent phase error will be introduced in practice. Using high-speed components could improve these phase error in a large scale, but for a low-cost solution using general purpose components, we implemented a passive 2nd order phase-lead filter at the input stage. Fig. 4-41, shows the implemented filter network.

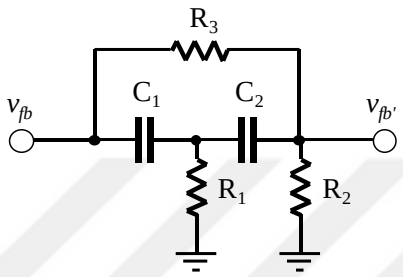

Figure 4-41 - 2nd order passive phase-lead filter network

The filter was designed based on the measured phase response of the system in order to maintain a fixed +90° phase shift. Filter parameters was determined with iterative parametric simulations as follows R1 = 22 kΩ, R2 = 10 kΩ, R3 = 39 kΩ, C1 = 100 pF, and C2 = 220 pF. Fig. 4-42 shows the measured phase response of the system with and without the compensating filter.

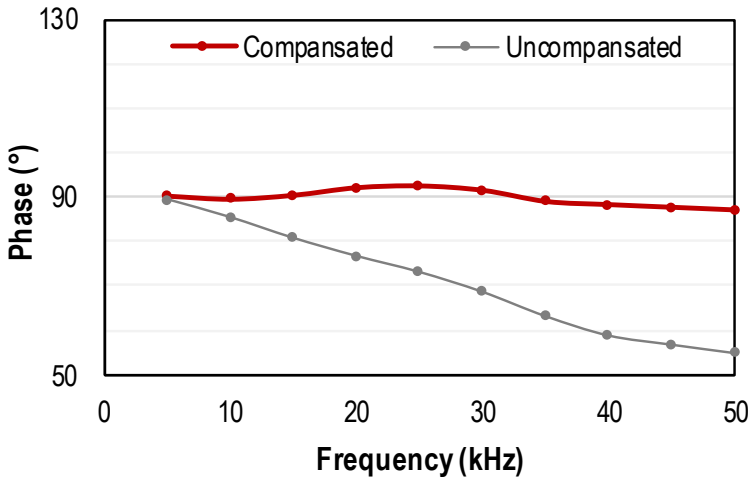

Figure 4-42 - Phase response of the system with and without compensating filter

4.27 Practical Implementation

Fig. 4-43, shows the overall block diagram of the proposed system.

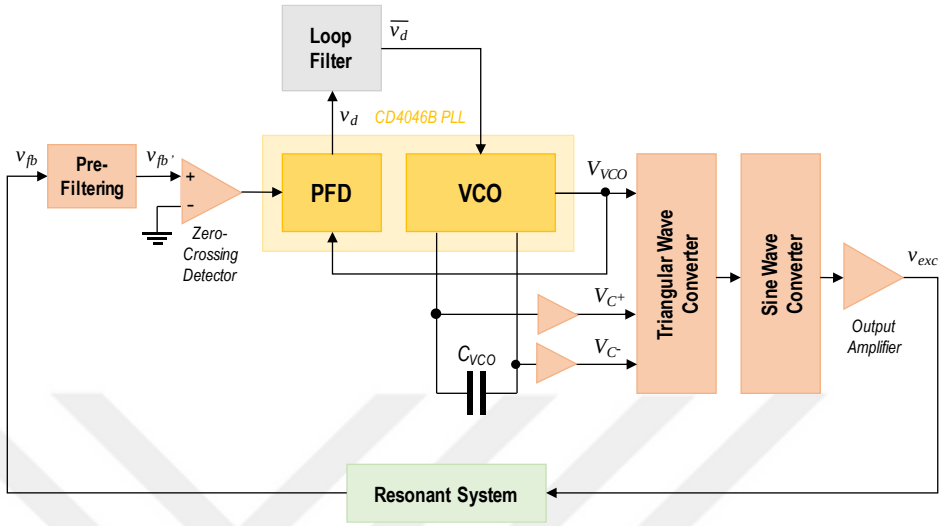

Figure 4-43 - Block diagram of the resonance tracking system

4.28 PCB Design

Fig. 4-44, shows the PCB design of the whole system on a 50×58 mm (2.0×2.3") two-layer FR-4 PCB. Five potentiometers were used for output waveform calibration and one potentiometer for adjusting the output amplitude. A high-current op-amp was used as output amplifier and could deliver up to 10 $V_{p\text{-}p}$ at ±15 V supply.

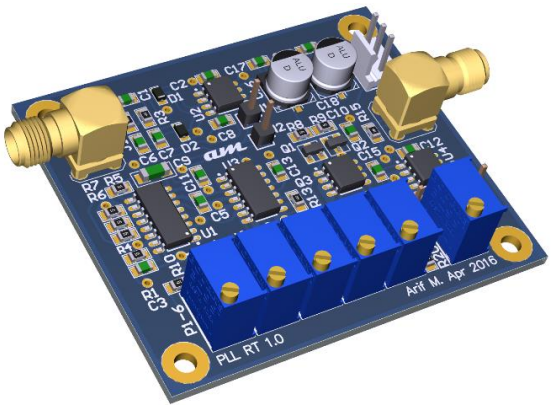

Figure 4-44 - PCB design of the PLL resonance tracking system (50×58 mm^2)

4.29 Experimental Results

The lock-time of the system was measured in open-loop configuration, using an external modulated signal applied into the input of the system. The signal generator was programmed to switch between 5 and 50 kHz with a half period of 10 ms. Fig. 4-45 shows the VCO input voltage with the modulated input signal. The lock time of < 5 ms was measured.

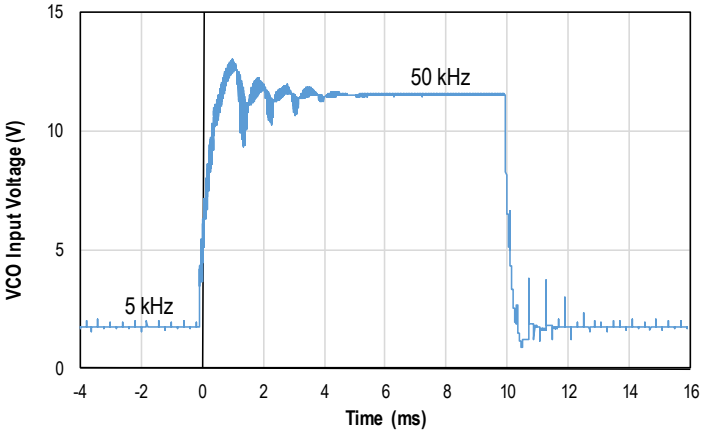

Figure 4-45 - Lock-time measurement result using external modulated input signal

The stability of the system highly depends on the frequency range of the VCO, for high sensitivity applications where very small changes are considered, the VCO operating range could be reduced.

4.29.1 RLC Resonator

The resonance tracking performance of the system was tested using a series RLC circuit shown in Fig. 4-46. For a resonator with natural frequency of 20 kHz and quality factor of 5 the values of equivalent circuit calculated as L = 100 mH, C = 1 µF and R = 62 Ω. Practical implementation of the series RLC circuit on the proposed resonance tracking system showed very good agreement with theoretical expectations. The system automatically locked on the resonance frequency of the resonator.

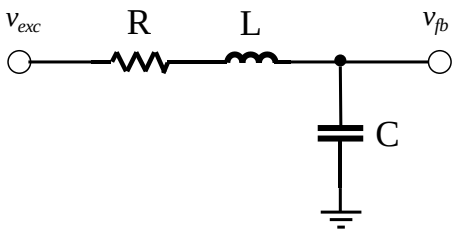

Figure 4-46 - Series RLC resonator circuit

Fig. 4-47 shows the stability of the system at closed-loop operation with series RLC resonator, centered at 20140.50 Hz. The phase of the system was measured as +92.2°. The standard deviation of the measured frequency was calculated as 0.77 Hz. For frequency measurements, a 16-bit DAQ card with sampling rate of 2 MSps was used with a simple LabVIEW code. The time resolution of the frequency measurement is 20 ms. The detection limit of the system in terms of the resonator capacity was estimated around 10 fF.

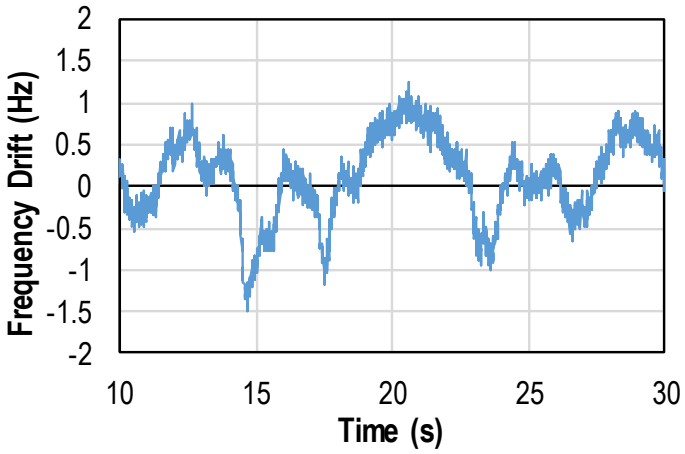

Figure 4-47 - Frequency stability of the system with RLC resonator locked at 20140.50 Hz.

4.29.2 Quartz Tuning Fork Crystal

As a high-quality resonant system application, we used a 32.768 kHz Quartz tuning fork at series resonance mode. Fig. 4-48 and 4-49 shows the implemented circuit and the open-loop frequency response of the circuit. From the data sheet parameters of the Quartz tuning fork parallel capacitor were selected as C1 = C2 = 12 pF and resistors

are R1 = 330 kΩ and R2 = 10 MΩ. Driving the tuning fork circuit with the resonance tracking circuit, locked at 32767.16 Hz at phase angle of +89.9° and the overall closed-loop frequency stability was calculated as 0.19 mHz. Fig. 4-50 shows the stability of the system at closed-loop mode.

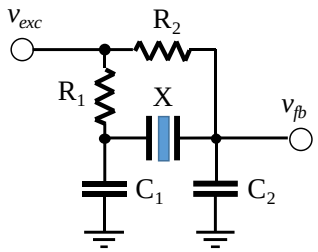

Figure 4-48 - Quartz tuning fork circuit

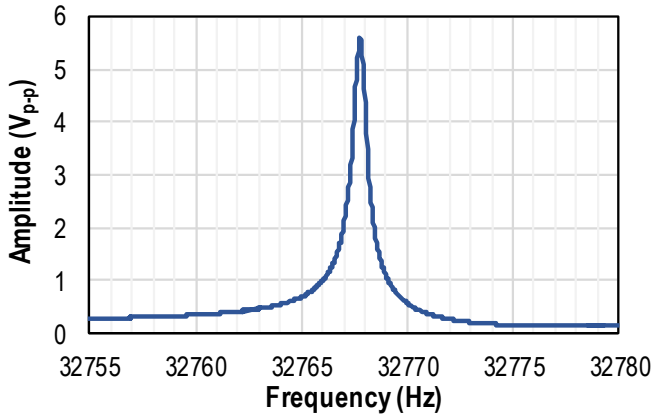

Figure 4-49 - Frequency response of the Quartz tuning fork circuit.

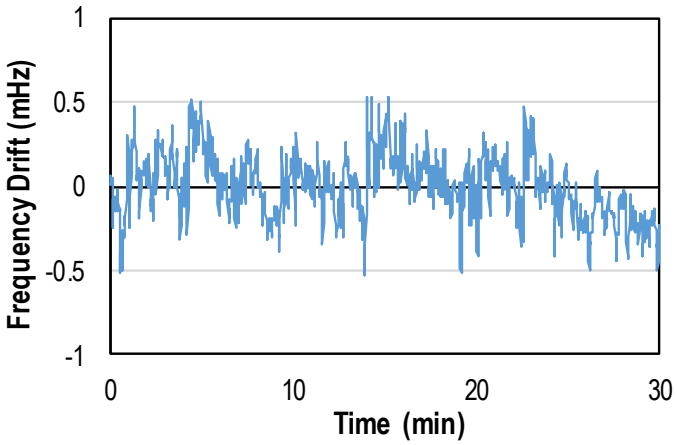

Figure 4-50 - Frequency stability of the system with Quartz tuning fork circuit

4.30 Conclusion

In this chapter, we present a low-cost broad-band resonance tracking system that makes use of a simple digital PLL with analog sine-wave generation. The method we propose provides a fixed-amplitude and frequency-independent +90° phase-shifted sinewave output for exciting resonant systems at their undamped resonance frequency that does not involve any initial tuning or calibration process. We employ an analog sinewave generation method with an acceptable THD of less than 2% and implement a passive second-order phase-lead filter in the input stage for compensating the propagation delays and achieving a maximum phase error of ±2.5° on the whole operating frequency range of 5 – 50 kHz. We discuss the advantages of this method over the conventional PLLs that use mixer-type phase detectors with limited frequency ranges and frequency-dependent phase errors. We demonstrate the resonance tracking performance of the proposed system on a low-quality-factor series RLC resonator and also a high-quality-factor Quartz tuning fork crystal. We measure a long-term stability of 0.77 Hz with the RLC resonator locked at 20140.5 Hz and 0.19 mHz with a 32.768 kHz Quartz tuning fork with locking time of < 5 ms. With the demonstrated RLC resonator, we achieve a capacitance detection limit of 10 fF in room temperature. We have designed the proposed system on a 50×58 mm^2 (2.0×2.3 in^2) two-layer PCB. The achieved performance of the system is comparable with the state of the art DSP resonance tracking systems that are used in high-end applications. Wide operating frequency range, fast locking time, and tuningless operation of our system can make it into an attractive solution for driving MEMS sensors in integrated CMOS-MEMS designs and also parallel resonance tracking of MEMS sensor arrays in time multiplexed operation [34,40,43].

5 Dual-PLL Resonance Tracking Method for Systems with Distorted Feedback Signals

5.1 Introduction

In interferometric readout method, residual bending of the cantilevers introduces non-linear optical transfer function in the readout signal. This non-linearity appears as asymmetric output signal waveform. This asymmetry introduces phase detection errors in the Phase/Frequency detector of the PLL-based resonance tracking system introduced in chapter 4. For overcoming this problem, we developed a novel dual-edge detection method using two cascaded PLL blocks. This method, automatically cancels out all phase errors due to the asymmetry of input signal and also other drift related phase errors in the input stage of the system.

5.2 Optical Non-Linearity in Interferometric Readout

For the interferometric readout, grating shaped MEMS cantilevers was discussed in chapter 3. In this cantilevers, as discussed before, the readout signal is the interference of the reflected Laser beams from the cantilever and the substrate.

For a linear optical transfer function of the interferometric readout, distance of the cantilevers must be exactly in the ideal locations corresponding to the zero-crossings of the optical transfer function. In these ideal discrete distances, the phase of the optical transfer function is zero and since the amplitude of the vibrations is very low, it could be easily assumed that the $sin(\varphi) = \varphi$. Any shifts from these ideal locations will introduce asymmetry in the feedback signal which will reflects as phase detections errors in the PFD. The main source of these shifts in our sensors are residual bending of the cantilevers and temperature dependent bending during the experiments. Fig. 5-1 shows the distortions in the readout signal due to the bending of the cantilevers. Non-linear transfer function of the interferometric readout method was shown previously in chapter 3.5, (See Fig. 3-5).

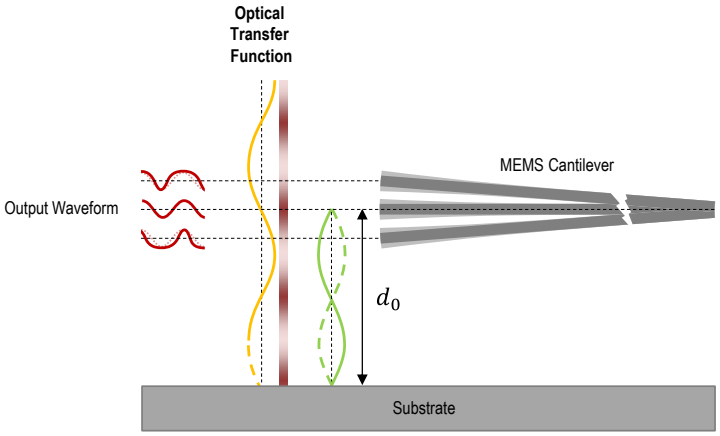

Figure 5-1 - Nonlinear optical transfer function of bended cantilevers

In the diffraction grating shaped cantilevers of our experimental setup, the reflected beam is a combination of the reflected beam from the substrate and partially reflected beam from the cantilever surface.

For the distance *d* between cantilever and the substrate, the optical phase difference between the reflected beams from the cantilever and the substrate will be

$$\varphi = \frac{4\pi n}{\lambda} d + \varphi_0 \tag{5.1}$$

And the intensity of the reflected beam could be written as

$$I_r = I_1 I_2 + 2\sqrt{I_1 I_2}\cos\left(\frac{4\pi n}{\lambda} d + \varphi_0\right) \tag{5.2}$$

Where I_1 and I_2 are the intensity of the reflected beams from the substrate and cantilever respectively, d is the distance of the cantilever from the substrate, λ is the wavelength of the readout Laser and *n* is the refractive index of the medium [64].

Extracting the DC signal and transforming $\varphi'0 = \varphi_0 - \pi/2$, we have

$$i_r = \alpha \sin\left(\frac{4\pi n}{\lambda} d + \varphi_0'\right) \tag{5.3}$$

Here, α is a constant representing the amplitude of the optical transfer function. This equation shows the periodic optical transfer function of the readout system which have a period of 4πnd/λ and for ideal non-linear response it is necessary that the phase component be small enough around zero degrees. From the coefficient of the d in the equation 5.3, it could be shown that the ideal distance for the cantilever will be

$$d_0 = \frac{N\,\lambda}{2\,n} \tag{5.4}$$

Where, d_0 is the ideal distance of the cantilever and N is an integer number. Any deviation from these ideal locations will introduce distortions in the readout signal.

For investigating the effect of the deviations from the ideal distance, I defined an error distance d_e, as follows:

$$d = d_0 + d_e \tag{5.5}$$

Taking the vibration of the cantilever into the account, the total distance of the cantilever will be

$$d_v(t) = A\sin(2\pi f t) + \mathrm{d} \tag{5.6}$$

Here, A is the amplitude of the cantilevers vibration, d is the static distance of the cantilever and f is the frequency of the vibrations. Substituting equations 5.6 into 5.3 we have

$$i_r = \alpha \sin\left(\frac{4\pi n}{\lambda}(A\sin(2\pi f t) + \mathrm{d}) + \varphi_0'\right) \tag{5.7}$$

From the periodic property of the sine function, equation 5.3 could be simplified as:

$$i_r = \alpha \sin\left(\frac{4\pi n}{\lambda}(A\sin(2\pi f t) + d_e)\right) \tag{5.8}$$

Using the equation 5.8 the distortion of the output readout signal could be simulated for our experimental setup. From equation 5.4, for optical wavelength of 532nm, assuming refractive index of 1.33 for DI-water, ideal distance of the cantilever will be integer multiples of 200nm. Fig. 5-2 shows the optical readout signal for various distance error values. In this simulations, the amplitude of vibrations is 5 nm and frequency is 20 kHz. The output amplitude is normalized to the output amplitude at ideal distance.

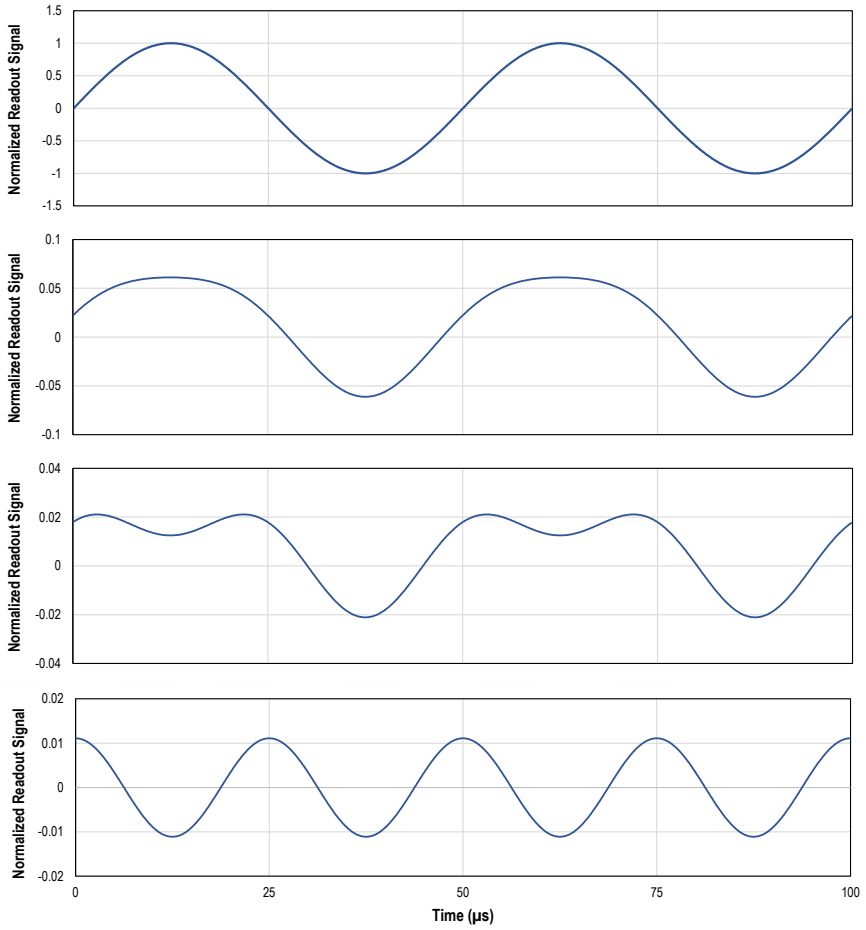

Figure 5-2 - Distortions in the readout signal versus error distance

As shows in the Fig. 5-2, the distortions increase exponentially near the half optical cycle of the readout system. And exactly at the half optical cycle, the output signal is a symmetrical sinewave with twice of the vibration frequency. The phase error in this case rises to 45°.

In the PLL-based resonance tracking system discussed in chapter 4, these distortions will reflect directly as phase errors in the input signal. For calculating the amount of phase error in the edge-triggered PFD phase detector, it could be more convenient to define the distortions in terms of the produced phase error in readout signal.

The phase error could be defined as the phase difference between the vibration signal and the readout signal. For out mixed-signal PLLs it is more convenient to define the phase error based on the logical signals. Since the output readout signal at ideal distance is in phase with the vibration signal, the phase error could be calculated between

the phase in the ideal distance and phase in the desired error distance. Thus, the introduced phase error could be expressed as

$$\varphi_e = \frac{1}{T}\int_0^T (I_0 \otimes I_{de})\,\mathrm{dt} \tag{5.9}$$

I_0 and I_{de} are the logical phase signal of the ideal signal and the distorted signal and T is the period of the vibration. $\otimes$ is the logical exclusive-OR operator acts as a Type-I phase detector, discussed in chapter 4. Fig. 5-3, shows the distorted signal and corresponding logical phase signals.

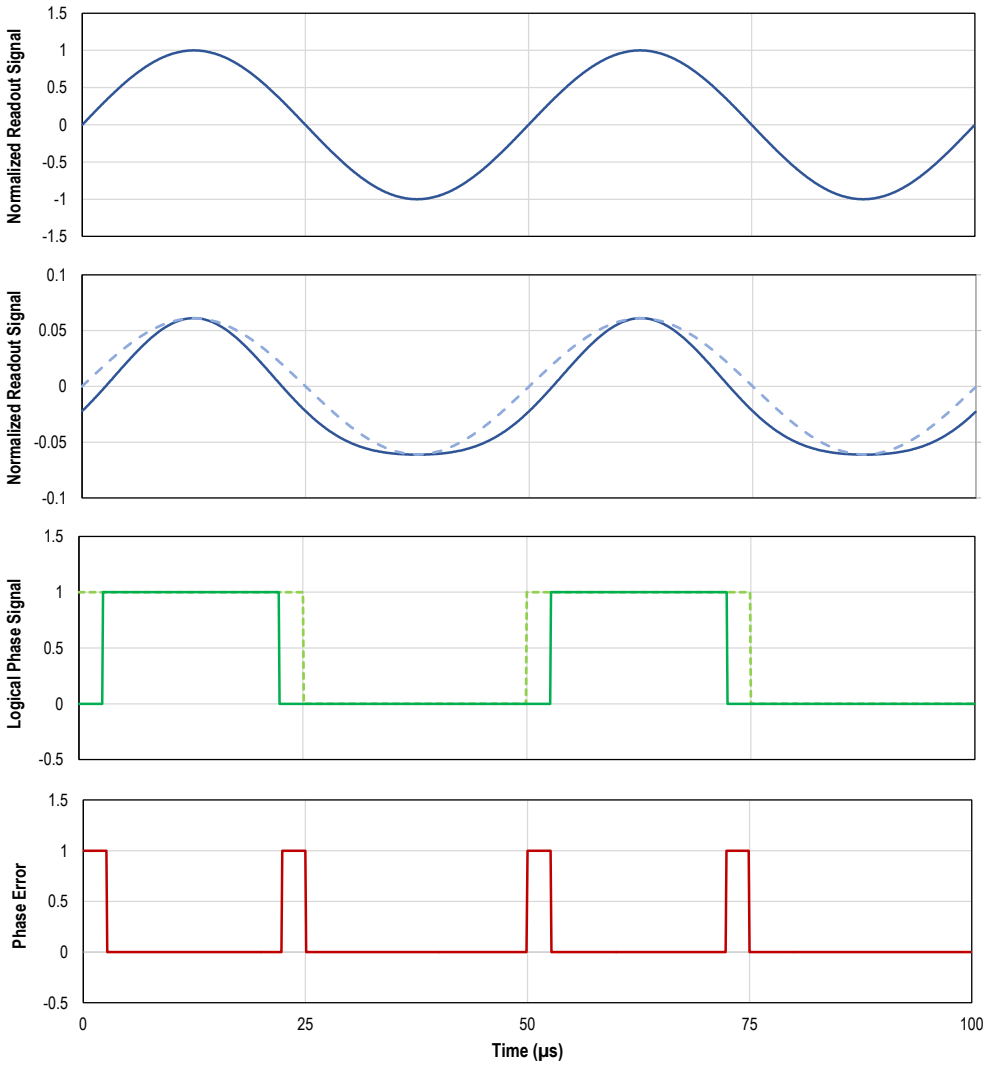

Figure 5-3 - Distorted readout signal and corresponding logical phase signals

Plotting the amplitude and phase error of the readout signal with respect to the distance error will actually shows the optical transfer function of this optical readout method. Fig. 5-4, shows the simulation results.

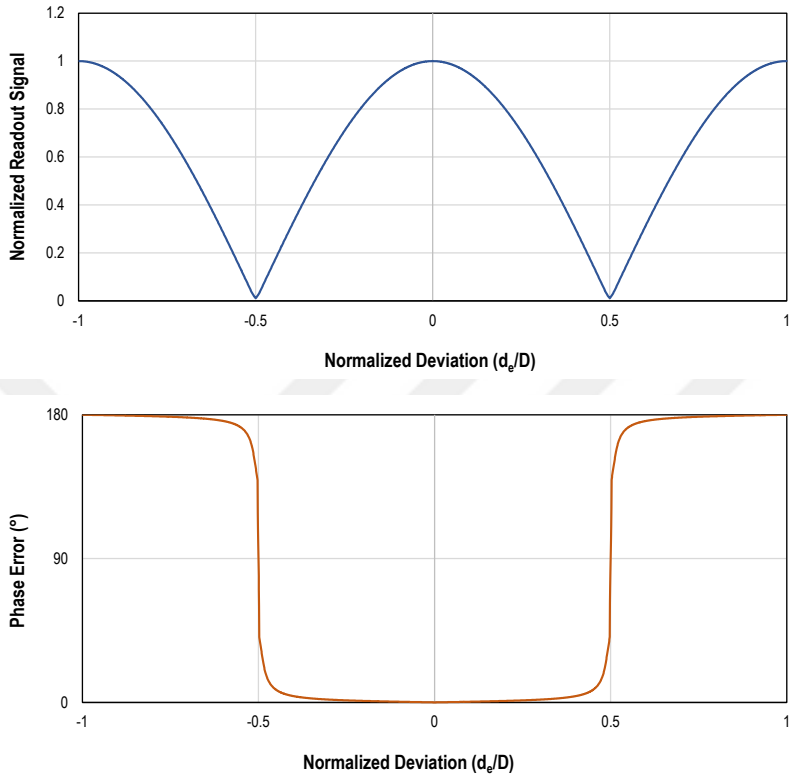

Figure 5-4 - Optical transfer function of interferometric readout method vs. distance

In this simulation, the amplitude and phase of the readout signal was plotted versus the normalized distance to optical cycles. Distance between the ideal locations was called as optical cycle, corresponding to integer multiples of half optical wavelength. The amplitude is normalized to its maximum level where occurs at ideal distances from the substrate. Output amplitude reaches to its minimum at half optical cycle. The output phase reverses at one optical cycle.

These simulations show a very high phase and amplitude dependency to the cantilevers distance. High temperature dependences of the Bi-layer cantilever design, makes robust readout with these cantilevers difficult because of temperature dependent bending of the cantilevers. This phenomenon is the source of continues reshaping of the readout signal and even phase reversals during the experiments.

In terms of phase readout error, a more precision plot shows the sensitivity of this method to distance drifts. Fig. 5-5, shows the phase error versus distance error for our experimental setup.

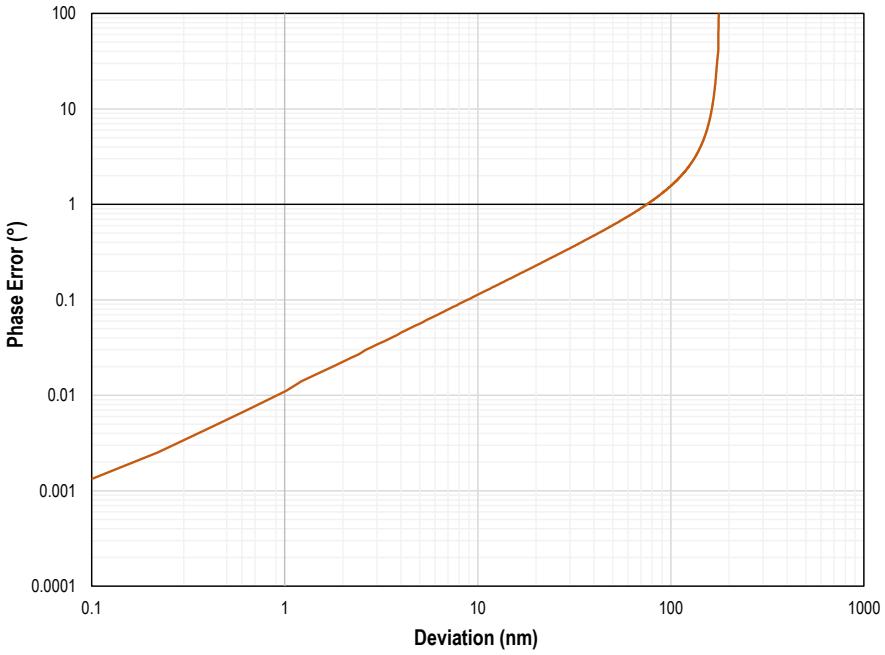

Figure 5-5 - Phase error versus distance errors

Based on this simulation, for a 1 m° phase stability, less than 0.1 nm distance stability is required. But even with a perfect stability, since the cantilevers have different bending levels due to residual stresses, the readout signal will have a fixed phase error with respect to the cantilevers deviation from the ideal distances. For solving this problem, I developed a novel dual edge detecting PLL method, using two cascaded mixed-signal PLLs for suppressing these phase errors.

5.3 Dual Edge Detection

As described before, the interferometric readout method in our cantilevers has a big phase and amplitude fluctuation due to the residual bending and also thermal depending bending during the experiments.

For the proposed mixed-signal PLL based resonance tracking method in chapter 4, the asymmetry of the input signal directly appears as phase error in the input because of the drifts in the zero-crossing detection circuit. And since the PFD looks on the rising edge of the input pulses the asymmetry directly reflects on the detected phase.

Based on the periodicity of the input signal, it could be shown that the drifts of the zero-crossings in the rising edges are equal to drifts in zero-crossings of the falling edges in the case of asymmetric signals.

Developing a method for adding up the resulting phase errors in both of the rising and falling edges will be a solution to suppressing the phase errors in the asymmetric input signals. Fig. 5-6, shows the phase errors for rising and falling edges of the asymmetric input signal.

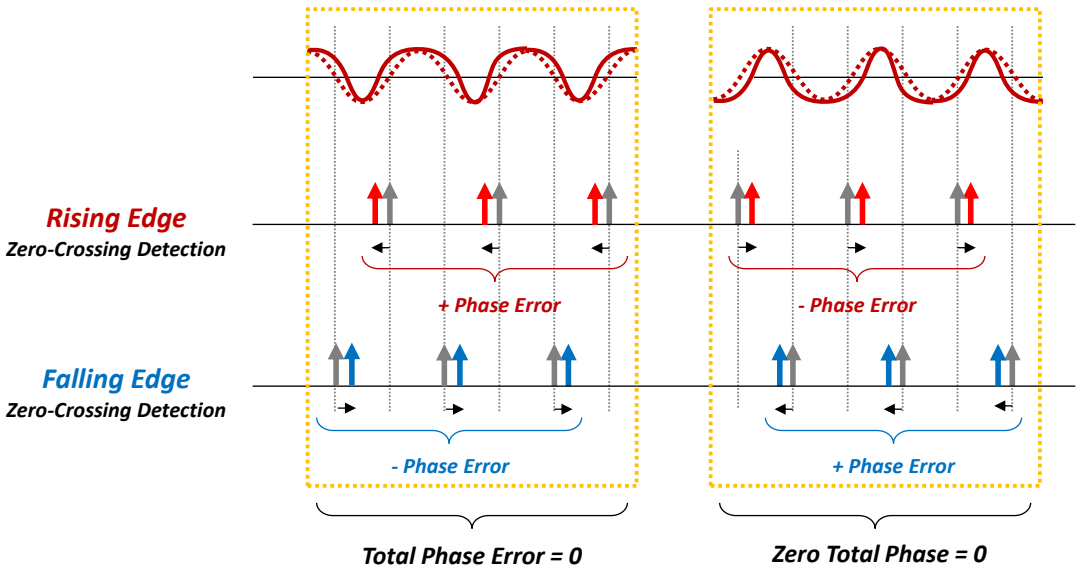

Figure 5-6 - Phase errors for rising and falling edges of the asymmetric input signal

Adding the phase errors on both edges of the input signal could improve the input phase detection in case of low-frequency modulated signals and also dc offset problems in input stages. Fig. 5-7 and 5-8, shows the phase error compensation in these situations for the dual-edge phase detection method.

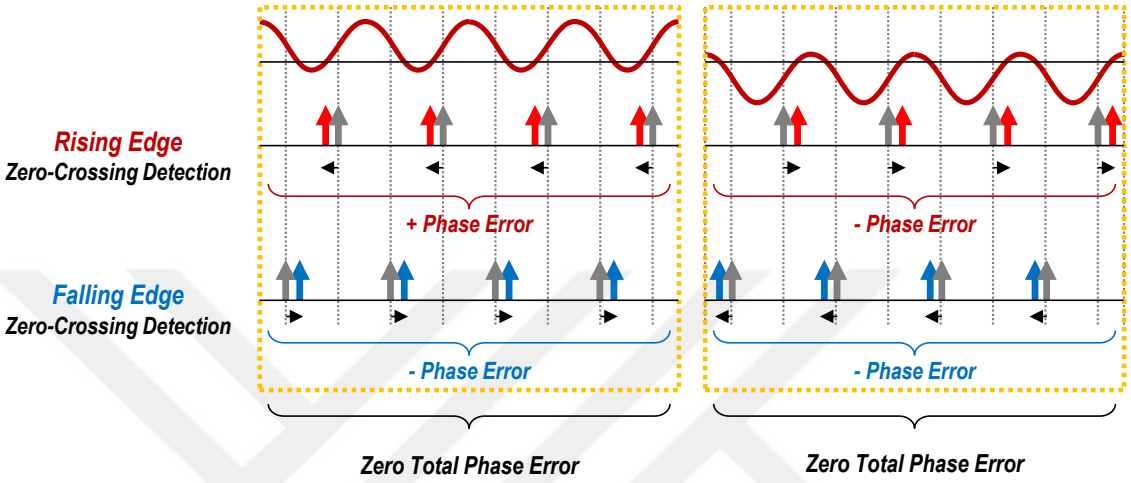

Figure 5-7 - Phase error compensation in presence of DC offset

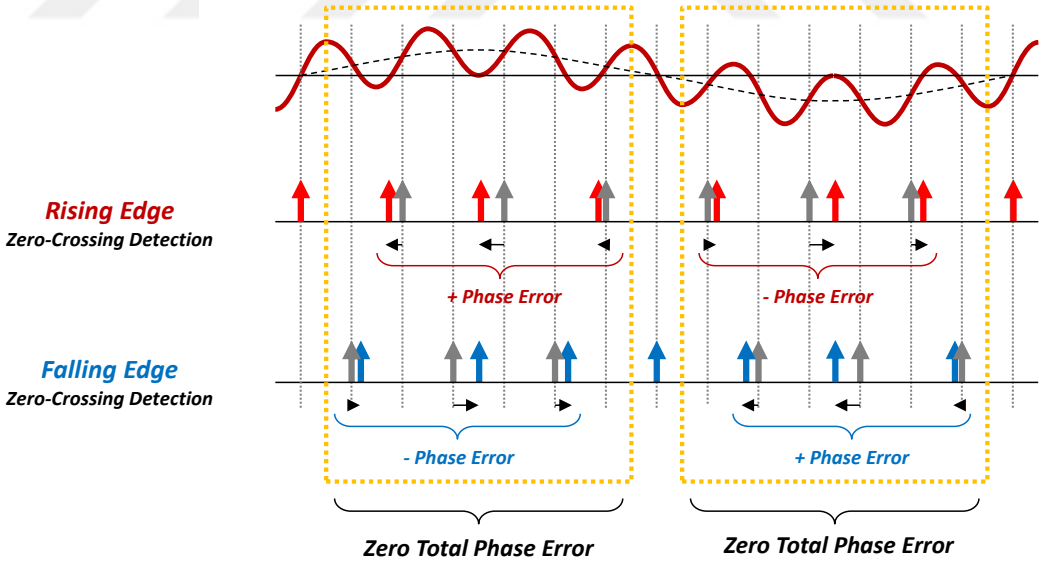

Figure 5-8 - Phase error compensation for low-frequency modulated signals

For practical implementation of the proposed method using logical circuits, we need a mechanism to accumulate for phase errors on both edges to a signal with an averaged phase. This could be realized using an additional PLL, whose phase detector initiate on both rising and falling edges and a divide by two circuit. This primary PLL, will generate a reference signal with an averaged phase of both rising and falling edges at twice of the input signal frequency. Using a logical divide by two circuit, a reference signal at the input frequency could be generated with average phase of both edges. Fig. 5-9, shows the signal waveforms for the proposed method.

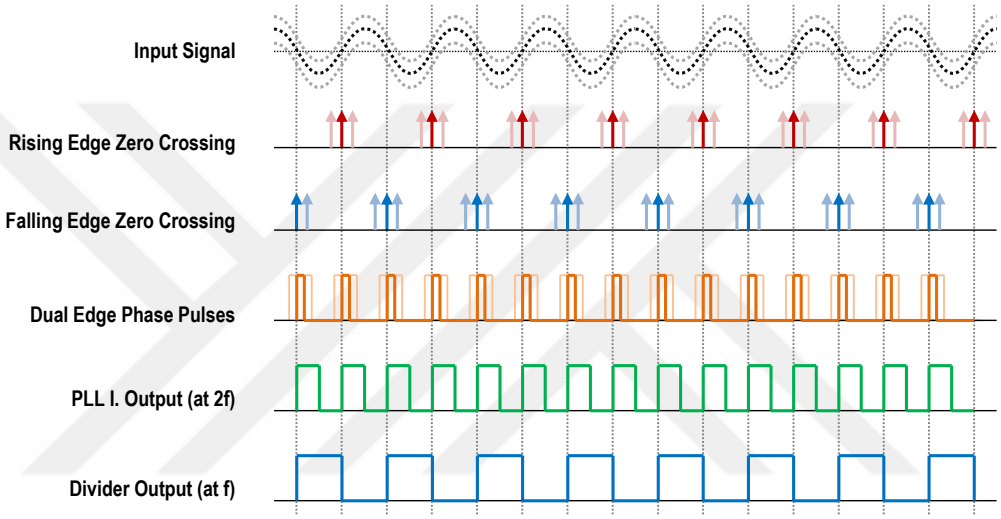

Figure 5-9 - Signal waveforms for the dual edge phase error compensation method.

The divider output is the phase error compensated signal at f, and could be cascaded with the PLL resonance tracking system. The primary PLL adds an additional phase jitter filtering to the system and increases the order of the system by one in the phase domain.

5.4 Simulation and Analysis

All the mentioned problems in the readout signal, eventually cause an asymmetry in the square wave input of the mixed-signal PLL. In general case, the influence of these effects could be studied in terms of the PFD input signal's duty cycle.

Duty cycle is the duration of a digital signal at high-state divide by its period:

$$D = \frac{T_h}{T} \tag{5.10}$$

where, D is the duty cycle, T_h is the duration at high-state and T is the period of the signal.

For a mixed-signal PLL with an edge-triggered PFD, resulting edge delays due to the asymmetry of the input signal was shown in Fig. 5-10.

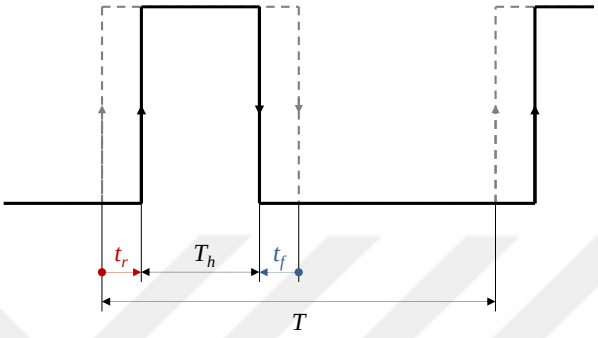

Figure 5-10 - Edge delay in asymmetric square wave

Here t_r and t_f are the delays in the rising and falling edges respectively. Resulting delay in the rising edge will be

$$t_r = \frac{\frac{T}{2} - T_h}{2} \tag{5.11}$$

Substituting 5.10 in 5.11 we have

$$t_r = T\left(0.25 - \frac{D}{2}\right) \tag{5.12}$$

And finally, the resulting phase delay could be expressed as follows

$$\varphi_r = \pi(0.5 - D) \tag{5.13}$$

φ_r is the phase delay of rising edge in radians. Fig. 5-11, shows the plot of the phase delay with respect to the duty cycle.

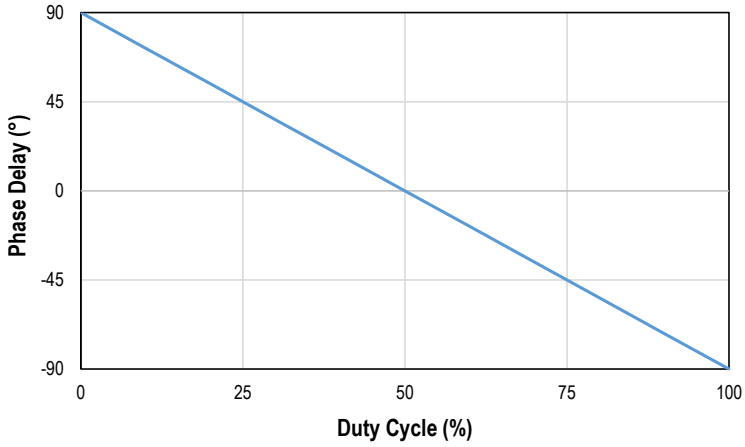

Figure 5-11 - Phase delay with respect to the duty cycle

As shown in Fig. 5-11, the introduced phase delay is proportional to the duty cycle of the input signal. For the proposed dual-edge detection method, since the phase delays for rising edge and falling edges in an asymmetric signal are inverse of each other, the resulting absolute phase error will be zero independent of the duty cycle.

In the meantime, asymmetry of the input signal in the dual-edge detection will introduce an additional duty cycle dependent phase jitter at primary PLL's input. Fig. 5-12, shows the phase jitters in the primary PLL's input.

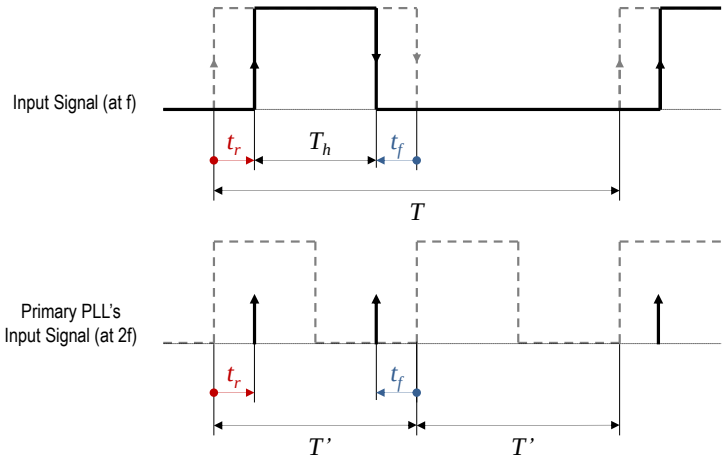

Figure 5-12 - Phase jitter at the input of primary PLL

Here, *T'* is the period of the primary PLL's output, where will be half of the period of the input signal. The amount of the time jitter will be equal to the edge delays, but in

terms of phase, the phase jitter will be twice of the phase delay calculated for the rising or falling edges.

$$\varphi_{r\prime} = 2\pi(0.5 - D) \tag{5.14}$$

Since the occurrence of these jitters are periodic, at frequency of twice of the input signal, they could be easily filtered out at primary PLL's loop filter. For the PFD of the primary PLL at locked state, the amplitude of the phase error signal at its output will be

$$v_{pd} = k_{pd}\varphi_{r\prime} \tag{5.15}$$

Substituting the PFD's phase transfer function, the amplitude of the phase error signal due to the asymmetry of the input signal will be

$$v_{pd} = \frac{1}{4\pi}\big(2\pi(0.5 - D)\big) = 0.25 - 0.5D \tag{5.16}$$

Theoretically, one could calculate the amplitude of the phase ripple passing through the loop filter for estimating the output phase jitter. But for a detailed study, simulation of whole system will give more precise results.

Simulating the dual-edge detection method showed incredible locking performance for input signals with duty cycles as low as 1% and up to 99% with almost zero frequency and phase error. With normal mixed-signal PLL with PFD, 1% duty cycle will result 88.2° phase error at the output.

Fig. 5-13 shows the simulation results for input signal with 1% duty cycle. In this simulation an asymmetric square wave was used as the input signal. The loop filter of both PLLs are identical with time constant of 10 ms. The input signal frequency is 20 kHz.

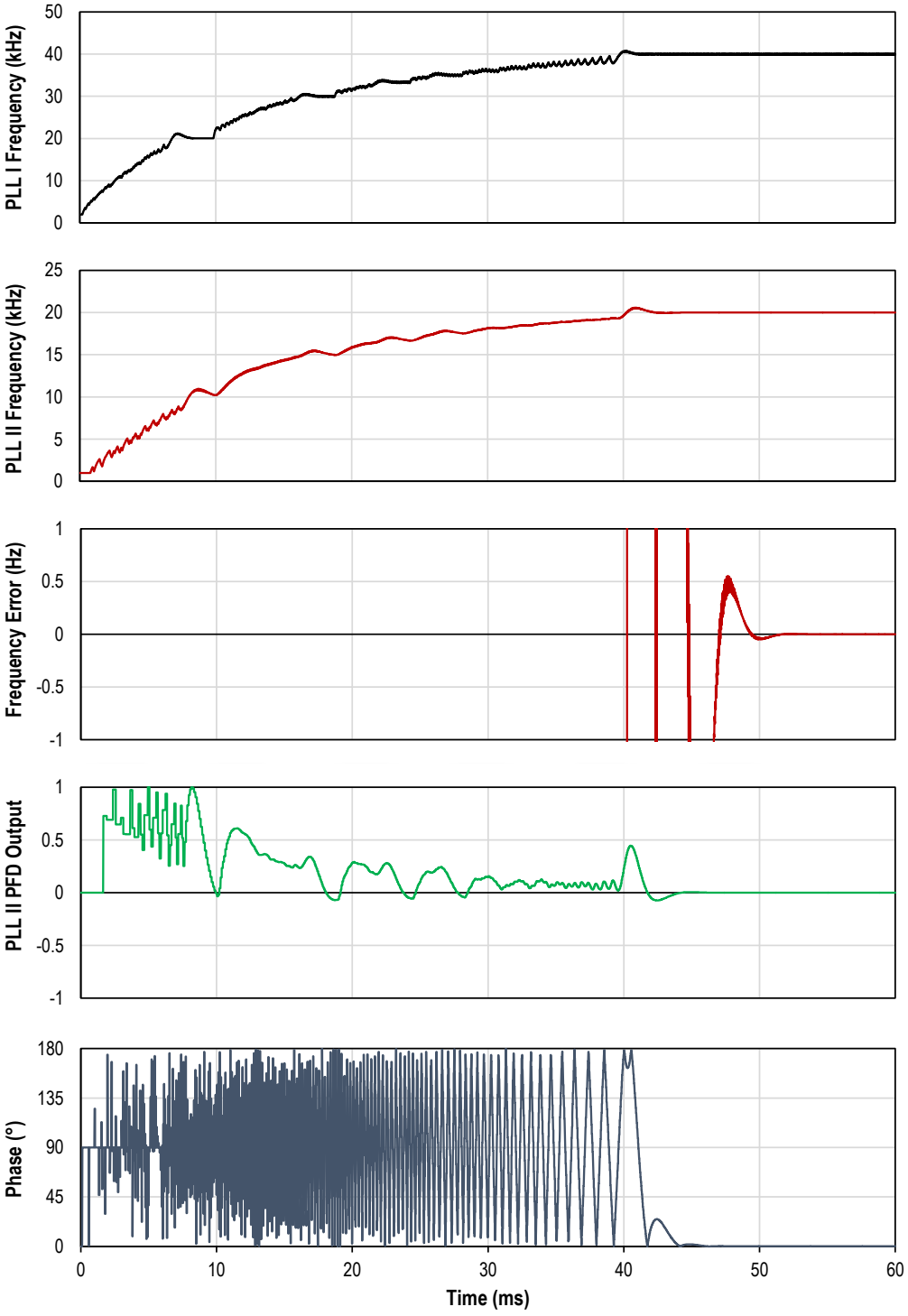

Figure 5-13 - Dual-edge detection PLL performance with 1% duty-cycle input signal.

Fig. 5-14, shows the waveforms in the dual-edge detection method, simulated for input signal with 10% duty cycle.

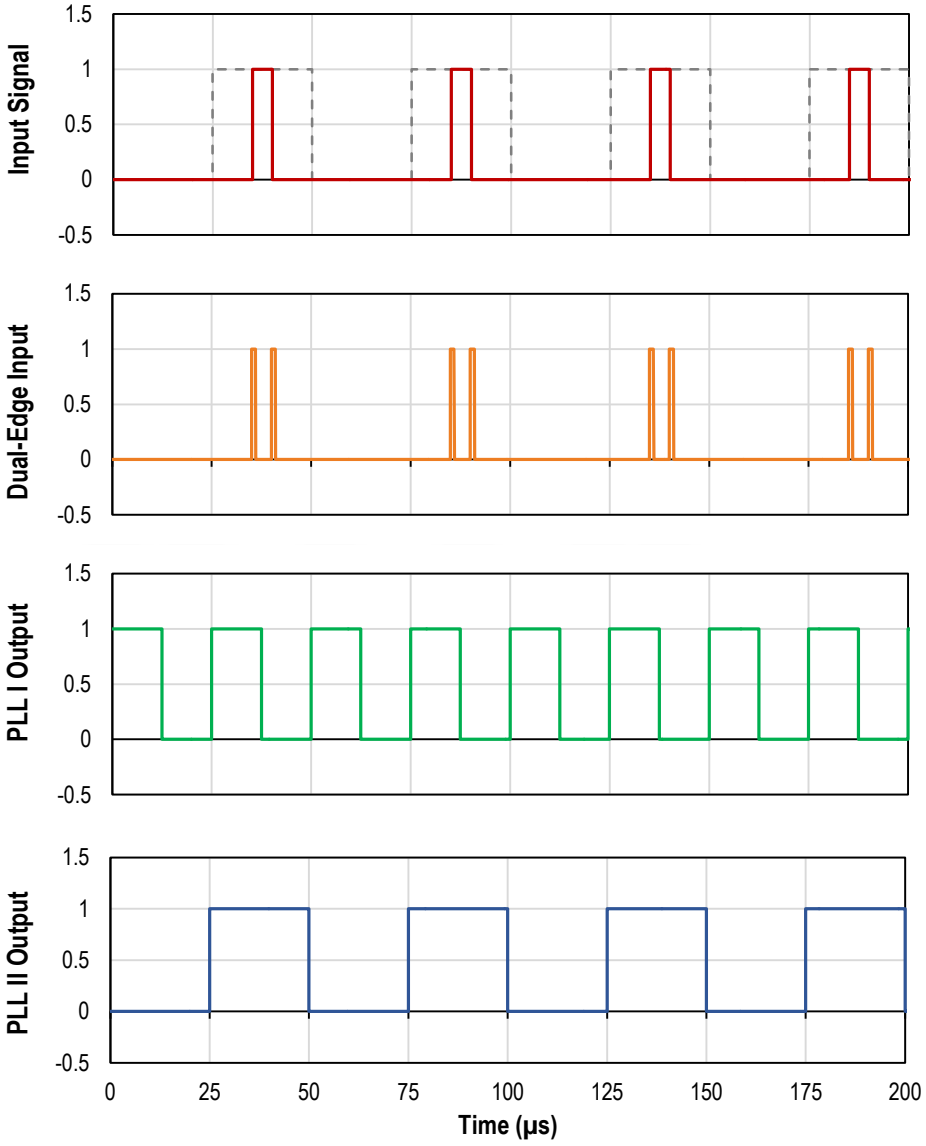

Figure 5-14 - Waveforms of dual-edge detection method with asymmetric input signal

5.5 Practical Implementation

For a dual edge phase detection, we need rising edges for both the rising and falling edges of the input signal. Two parallel zero-crossing detector cascaded with a mono-stable vibrator will gave the desired signal. Fig. 5-15, shows the block diagram of the dual edge zero crossing detector.

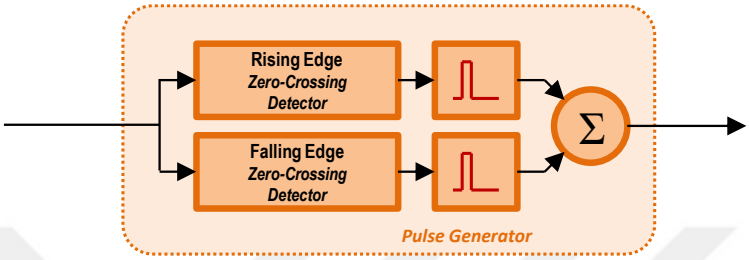

Figure 5-15 - Block diagram of dual-edge zero crossing detector

Practically, the proposed block diagram could be implemented using two voltage comparator op-amps cascaded with a logic mono-stable vibrator stage as shown on Fig. 5-16.

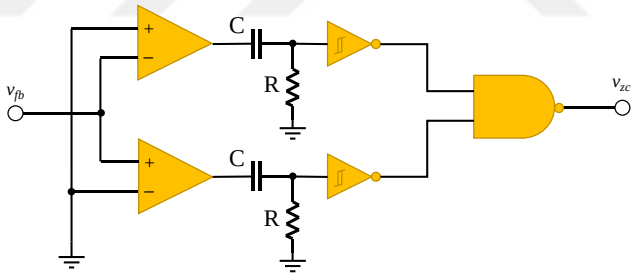

Figure 5-16 - Dual edge zero-crossing detection circuit

Two parallel complementary voltage comparator op-amps converts the input signal to inverse square wave logic outputs. The high-pass RC filter and the Schmitt-trigger inverting buffing generate negative pulses on every rising edge of the comparators. And finally a NAND gate adds up two negative pulses as positive pulses at the output. The values for R and C sets the duration of the pulses at since the PFDs are edge sensitive the pulse duration has no effect on the operation of the system but must be set to

reasonable values with respect to operation frequency range of the system for proper pulse generation.

This circuit could be simplified using a single comparator and XOR gate as follows. In this circuit, the RC circuit forms a low-pass filter and sets the duration of the pulses. Fig. 5-17, shows the simplified circuit.

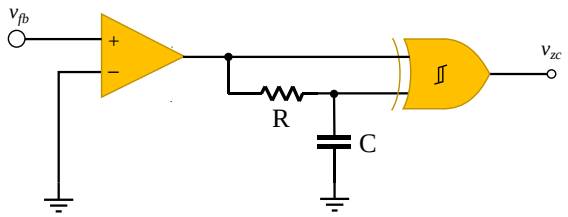

Figure 5-17 - Simplified dual edge zero-crossing detection circuit

In this circuit, the introduced delay in the filtered input of the XOR gate, cause inequality in the XOR gate inputs which generates a positive pulse in each level change.

5.6 Inverse-Phase Correction Circuit

Locking to the inverse phase of the input signal is a problem in dual-edge phase detection method. Since the primary PLL observes rising edges on both of the rising and falling zero-crossings of the input signal. The divider circuit output could be locked to the inverse phase (180° phase shifted) of the input signal. For preventing this situation an additional phase correction circuit was developed.

The inverse phase condition could be detected comparing the phase of actuation and readout signals. Since the phase of the readout signal must have a delay with respect to the actuation signal (-90° phase delay at natural frequency), the readout signal must be always in phase-lagging condition. If the readout signal is phase leading, it means an inverse phase condition. Using a phase reversing circuit, the phase could be inverted back to its non-inverted phase.

As a second advantage, this circuit will also solve the phase inversion problem in the interferometric readout, where phase reversal may occur because of the bending of the cantilevers.

The proposed circuit, could be realized using a D-flip-flop as phase comparator and an exclusive-OR gate for phase inverting. Fig. 5-18, shows the logical circuit diagram of the inverse phase correction unit.

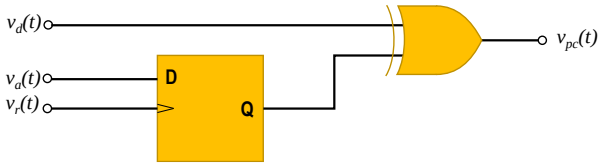

Figure 5-18 - Logical circuit diagram of the inverse phase correction unit

In this circuit, the v_a is the logical feedback signal from the actuating signal, v_r is the logical readout signal, v_d is the divider unit output and v_{pc} is the phase corrected output signal. This circuit looks at the readout signal at every rising edge on the actuation signal, in the case of phase-leading, the output of the flip-flop will go to high-state and the exclusive-OR gate will invert the signal from the divider unit.

Combining the dual-edge phase detection method with the 90° phase shifting sine wave generation method shaped a new resonance tracking system. Thanks to the duty-cycle independent property of the developed dual-edge detection, all the optical non-linearity and analog front-end drift problems was suppressed. The phase reversal problem also was automatically corrected using the automatic phase correction circuit in the dual-edge method.

Fig. 5-19, shows the waveform of the input, dual-edge phase detector, primary PLL's output and sinewave output signal waveforms respectively.

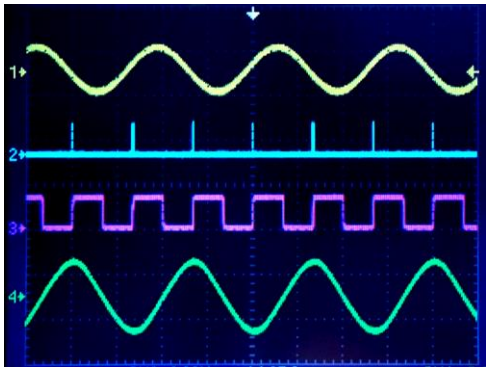

Figure 5-19 - Waveform of dual-edge detecting resonance tracking system

The overall block diagram of the system and PCB design of the whole system ares shown in Fig. 5-20 and 5-21, respectively.

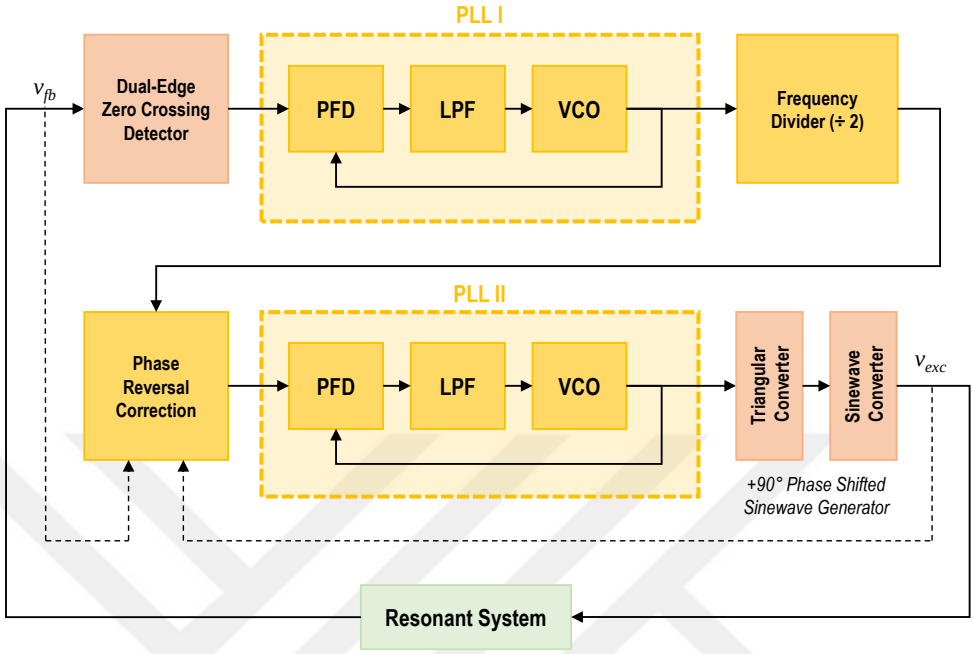

Figure 5-20 - Block diagram of the dual-PLL resonance tracking system

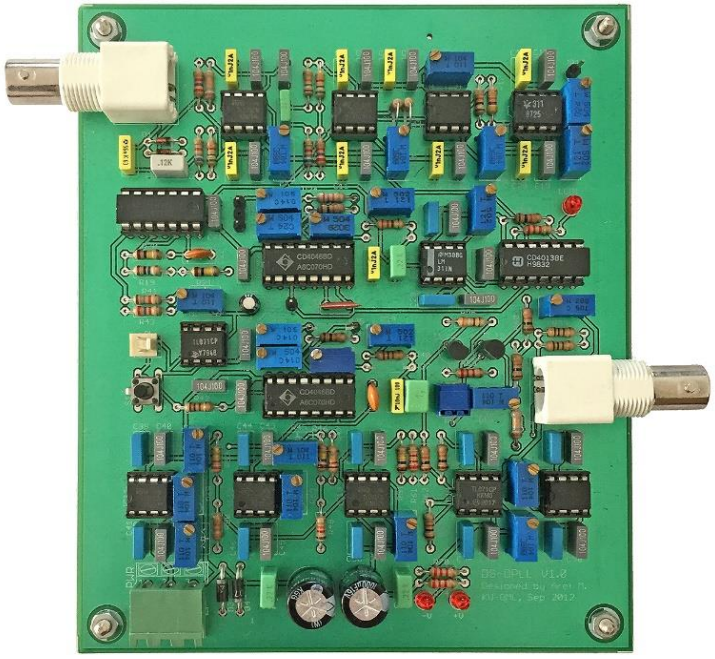

Figure 5-21 - PCB design of the dual-PLL resonance tracking system including a two stage front-end preamplifier and filter stage (120×145 mm^2)

5.7 Experimental Results

5.7.1 RLC Resonator

Using the equivalent RLC resonator circuit discussed in 4.29.1 with a very low quality factor of 1 and resonance frequency of 19.355 kHz, sub-PPM frequency stability was achieved with the proposed system in room temperature. Similar to our experiments on MEMS cantilevers the integration time for frequency averaging was set to 10 s. Fig. 5-22, is the screenshot of the LabVIEW based developed measurement software showing the frequency stability experiment results

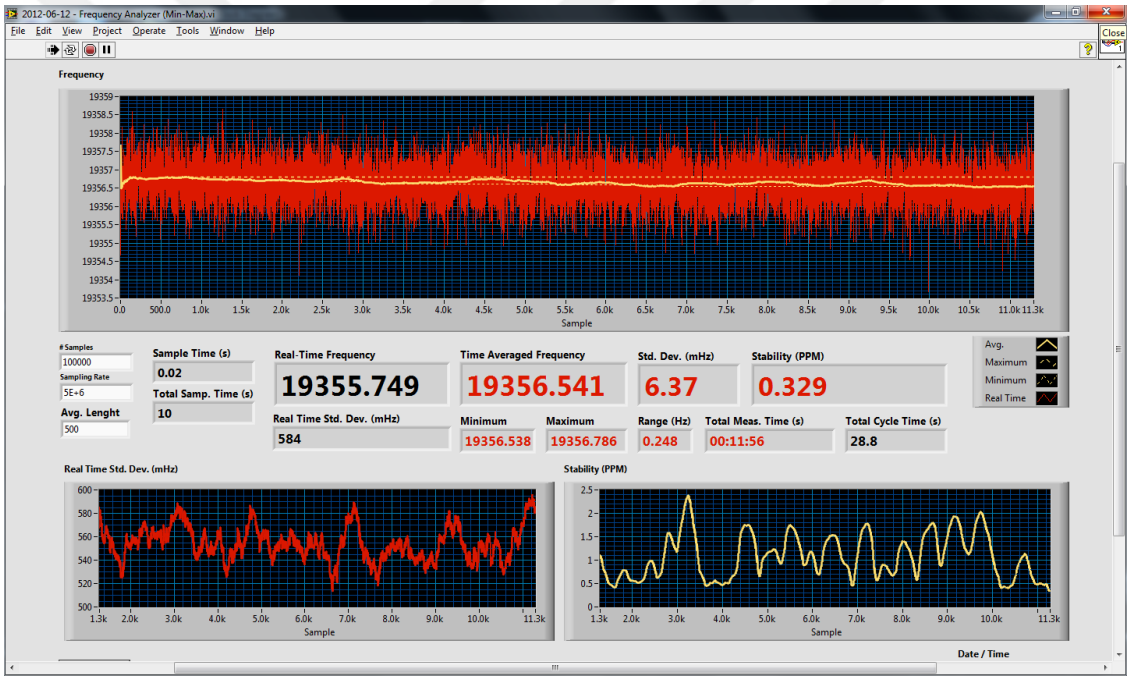

Figure 5-22 - Experimental frequency stability result on equivalent RLC resonator

5.7.2 MEMS Cantilevers

Proposed dual-PLL resonance tracking system was used to track the resonance frequency of micro-cantilevers with grating shaped tips mentioned before at chapter 3 for in-liquid experiments. The resonance frequency of the cantilever in this experiment was around 13.5 kHz with very low quality factor of around 1.6 in DI-water. Fig. 5-23, shows the achieved stability with these cantilever in DI-water. A commercial frequency meter was used to measure the PLL output frequency with 1 s sampling duration. Standard deviation of < 2 Hz was achieved. The equivalent achieved phase stability of this system was calculated as less than 25 m°. (See chapter 7)

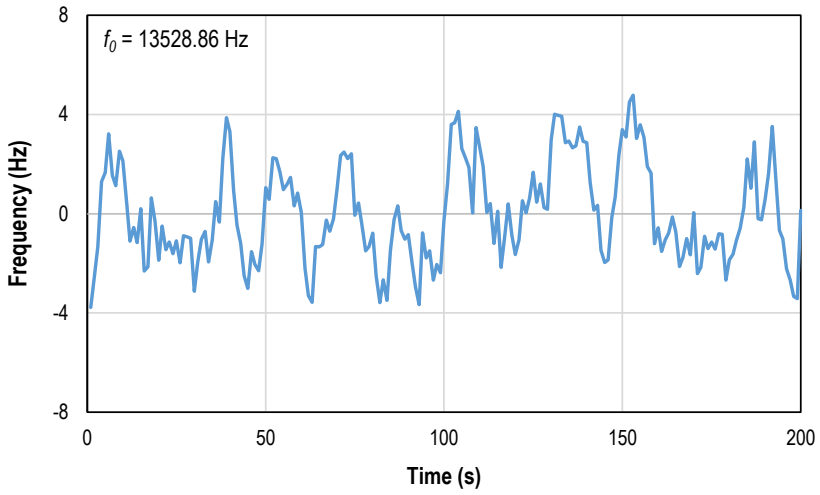

Figure 5-23 - Frequency stability of double-edge detection method in DI-water

An analog temperature controller was designed to stabilize the temperature of the cartridge within ±0.05°C during the experiments. Designed controller was discussed in appendix III. For blood plasma experiments, the temperature was set to 35.0 °C.

In this viscosity measurement system, the percentage of the resonance frequency change is the calculations. For viscosity reference measurements, Glycerol solutions in DI-water with weight percentage of 5 to 40% is used. Maximum 23% shift in the resonance frequency (~3 kHz) observed at 3.02 cP viscosity. Based on the measured stability data, a sensitivity of 0.04 cP was achieved in the range of 0.86 up to 3.02 cP which covers the viscosity range of the human blood plasma.

The resonance frequency shift in this experiments, is a result of changes in both viscosity and density [31]. Viscosity of the liquids used in this experiment, changes from 0.95 cP for DI-water up to 3.02 cP for 40% Glycerol solution (measured using Anton Paar AMVn commercial viscometer at room temperature of 23°C), and the density change from 1.00 to 1.0983 kg/m^3. The relative impact of viscosity and density on the frequency shift depends of the cantilever geometry as well as other parameters [33], The resulting frequency shifts in our experiments are mainly due to the viscosity changes, and the impact of the density change is small.

5.8 Conclusion

In this chapter, we presented a novel dual-PLL resonance tracking system for solving the optical non-linear transfer function induced phase-errors. Proposed system, detects both of the rising and falling edges of the input signal. A primary PLL, locks into a pulse train generated by the dual-edge zero-crossing detector circuit. The locking frequency is twice of the input signals frequency. Then a divide by 2 circuit cascaded with a reverse phase detection circuit provides a square wave with a rising edge located exactly at the middle of the rising and falling edges of the input signal. The proposed method, not only solves the phase errors due to the asymmetry of the input signal, but also solves for dc offset and low-frequency interferences on the input signal.

We demonstrated the performance of this method on a series RLC resonator and MEMS cantilever sensors. With RLC resonator, sub PPM stability was achieved in long time experiments. This system was used to measure the viscosity of human blood plasma using MEMS cantilevers. Viscosity measurement sensitivity of 0.04 cP was achieved between 0.86 to 3.02 cP. [31]

6 Multi-Channel Optical Fiber-Based Readout

6.1 Introduction

Diffraction grating shaped MEMS cantilevers because of very high damping ratios in the liquids, temperature dependent and un-symmetric readout signals are not suitable for in-liquid applications. As an alternative sensor system, we focused on more convenient straight cantilevers with reflection mode optical readout.

In this chapter we discuss development of a novel method for simultaneous resonance monitoring of MEMS cantilevers using phase based dynamic measurements. To our knowledge this is the first demonstration of simultaneous parallel optical monitoring of dynamic mode micro-cantilever array in liquid environment. Illumination is generated using a laser source and a diffractive pattern generator, which provides 500 µW laser power per channel. A compact fiber array based pick-up was built for optical readout. Its main advantages are easy customization to different size and pitch of sensor array, and good immunity to electrical noise and magnetic interference as the photo detectors are located away from the electro-coil. The resonant frequency of the cantilever is tracked with a custom multi-channel lock-in amplifier implemented in software. The phase-based resonance tracking will be discussed in chapter 7.

The proposed method showed robust results with low laser power and very good noise immunity to interference signals and environmental vibrations. The sensor technology demonstrated here is very significant as it is scalable to larger arrays for simultaneous and real-time monitoring of multiple biological and chemical agents during fluid flow.

Simultaneous monitoring of cantilevers in an array has been demonstrated for atomic force microscopy operating in air. Those systems used electrical readout using fabricated piezo sensors [35,36], diffraction gratings with integrated photodiode array [37]. In these methods all the cantilever deflections are read at the same time using a dedicated electronics. This increases the number of electrical connections to the sensors and complicates the operation under water due to passivation requirements. Previously our group proposed a method that uses a single photodiode and frequency-multiplexing

for multi-analyte detection in air [43]. Similar frequency multiplexing approach was also reported for optical lever readout method using PSD and operating in vacuum [65]. It is also possible to employ time multiplexing, which reads one cantilever at a time using a single position sensitive detector (PSD), for static and dynamic mode measurements [38–42]. However, time multiplexing methods cannot provide real-time noise cancellation. The frequency-multiplexing methods are not suitable for cantilevers in fluids where the quality factors are low, resulting in large overlap in the frequency responses of the cantilevers.

For liquid operation, electrical readout methods are challenging due to required electrical connections. Applying optical lever readout method for array of cantilevers in parallel for simultaneous measurements requires complicated multiple PSD or quad detector fabrication with exact pitch of the cantilevers and also because of the noise and detection limits of the proposed methods, parallel measurements in liquids only reported in (i) Static mode by detecting the amount of bending of the cantilever using a single PSD and time multiplexing [41,66], (ii) Using commercial devices with multiple four-Quadrant photodiode readouts [67,68], (iii) White-light interferometry and imaging based parallel readout also reported for static mode operation in liquids [69,70] and (iv) Single cantilever interferometric readout [71,72].

As outlined above, simultaneous parallel measurements in liquids are challenging and there is no prior work in this area. In this work, we used cantilevers with the same dimensions, which have similar resonant frequencies. Cantilevers are driven open loop at the same drive frequency. The relative phase between the drive signal and the cantilevers are used to monitor the dynamic changes of all the cantilevers simultaneously in real-time with high precision. The measured phase shifts can be used to monitor analytes in liquids or liquid properties High precision measurements are obtained using a compact optical readout based on a fiber array and custom digital multi-channel lock-in amplifier for real-time monitoring.

6.2 Reflection Mode Optical Readout

Fig. 6-1 shows the optical path of the incoming and reflecting optical beam from the tip of the cantilever. According to the law of reflection, the rotation of the optical beam will be equal to twice of the mechanical rotation angle of the cantilever [64].

$$\theta_{opt} = 2\theta_m, \tag{6.1}$$

where, θ_m is the mechanical deflection angle of the tip of the cantilever and θ_{opt} is the angle of the reflected beam.

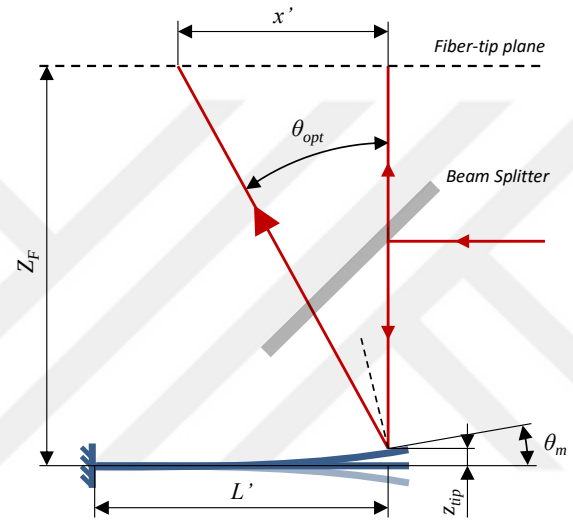

Figure 6-1 - Optical path of the incoming and reflected beam from the cantilever

Assuming small tip deflection amplitude for the cantilever, the mechanical rotation angle will be:

$$\theta_m(t) = \tan^{-1}\frac{z_{tip}\sin(\omega t)}{{}^{2}/_{3}L'} \cong \frac{3z_{tip}\sin(\omega t)}{2L'}. \tag{6.2}$$

Here, z_{tip} is the amplitude of the tip deflection, ω is the angular frequency of actuation and L' is the cantilever's effective length including the distance of the laser spot from the tip of the cantilever. And beam traveling distance on the fiber's tip plane will be:

$$x'(t) = Z_F \tan(\theta_{opt}(t)) \cong Z_F \theta_{opt}(t). \quad (6.3)$$

x' is the beam traveling distance and Z_F is the distance of fiber's tip plane to the cantilever. Combining equation (1), (2) and (3) we have:

$$x'(t) = \frac{3\, z_f\, z_{tip} \sin(\omega t)}{L'}. \quad (6.4)$$

6.3 Optical Fiber Modeling

Assuming a large core optical fiber as a circular aperture, coupled optical power to the fiber can be expressed as

$$P(x) = \iint A(x,y)G(x-x',y)dx'dy = \iint_A G(x-x',y)dx'dy. \quad (6.5)$$

A is the circular aperture's amplitude transfer function, with radius of w_{core} [64]:

$$A(x,y) = circ\left(\frac{\sqrt{x^2+y^2}}{w_{core}}\right), \quad (6.6)$$

and *G* is the Gaussian Laser beam intensity function of radius w and *x'* is the distance between fiber core center and the incident Laser beam:

$$G(x,y) = \frac{2P}{\pi w^2} e^{\frac{-2(x^2+y^2)}{w^2}}. \quad (6.7)$$

Fig. 6-2 shows 3D representations of the A and G functions, respectively for a core diameter of 486 µm, and beam diameter of 400 µm.

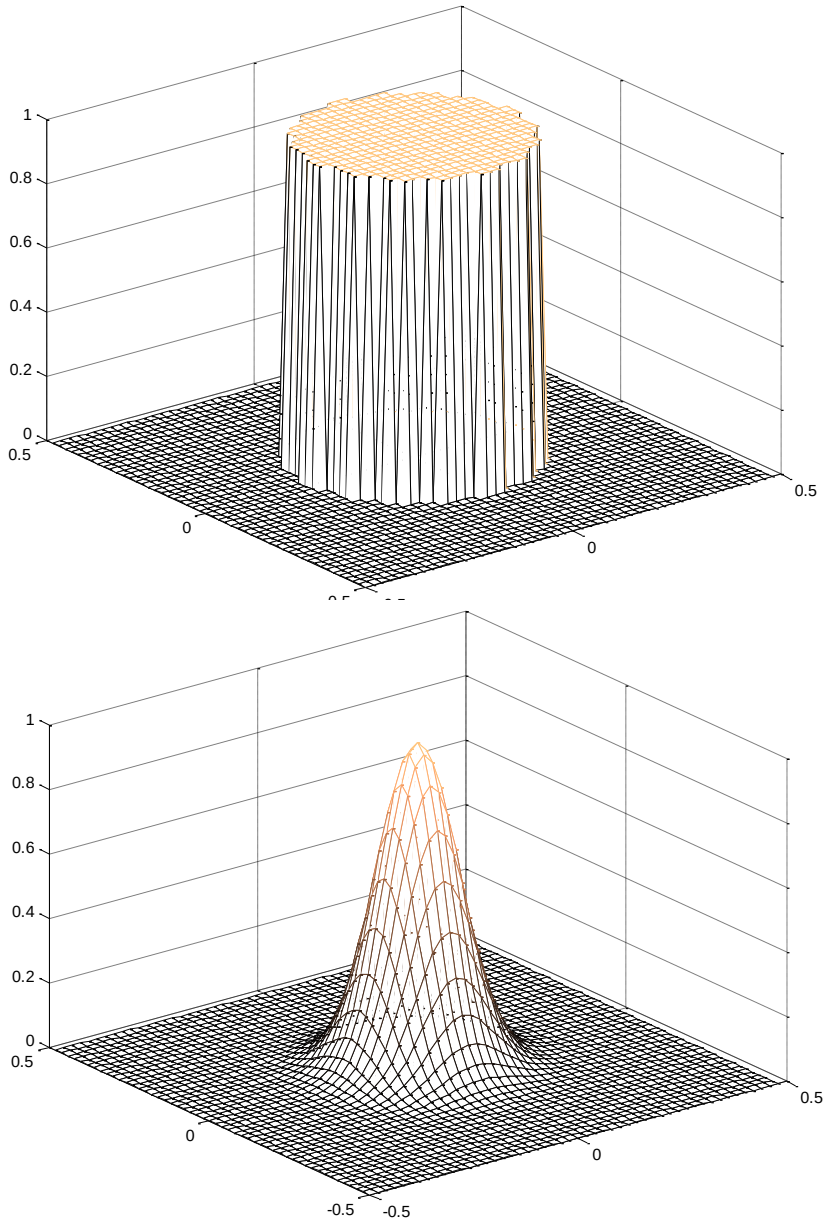

Figure 6-2 - 3D representations of the optical transfer function of the large core optical fiber *A(x,y)* (top) and optical intensity distribution of the Gaussian laser beam *G(x,y)* (bottom). X and Y axis unit are millimeters. Z axis is the normalized optical intensity or transfer rate.

Fig. 6-3 shows an illustration of the reflected beam coupling into the fiber and the coupled optical power to the photo diode and the modulation rate as a function of the distance between the beam and the center of the fiber.

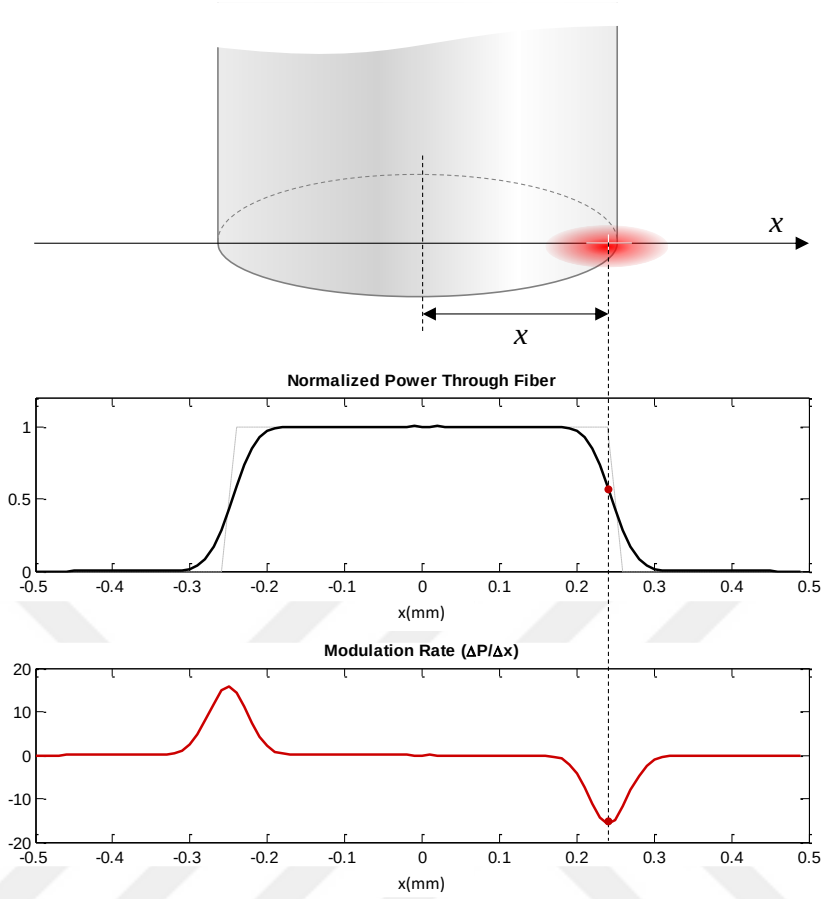

Figure 6-3 - Coupled optical power to the photo diode and the modulation rate

As shown in the Fig. 6-3, coupled optical power represents the DC component of the photo diode current and the modulation rate which is the derivative of the coupled power along the movement direction (x-axis) will be AC component of the photodiode current and could be written as follows:

$$p_{ac}(x) = \frac{\partial}{\partial x} P(x). \tag{6.8}$$

As seen in the Fig. 6-3, there are always two points corresponding to the two edges of optical fiber along x axis that gives the maximum AC signal. These points are symmetric with respect to the fiber center and are in the reverse phase response to each other.

The signal from the fiber is also highly dependent on the spot size on the fiber plane. Fig. 6-4, shows the modulation rate for different beam diameters from 100 to 500 µm.

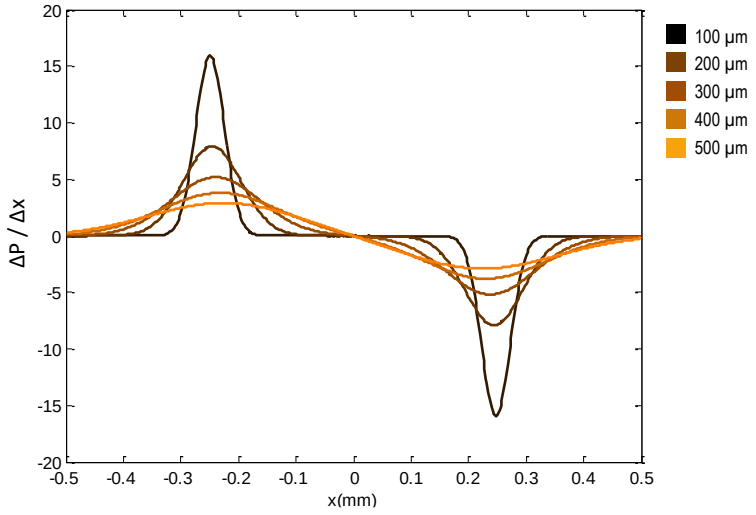

Figure 6-4 - Modulation rate for different beam diameters from 100 to 500µm on fiber.

As shown in the figure, the smaller spot size on the fiber, gives higher modulation rate. Based on the fact that the tighter focusing on the cantilever will cause larger beam divergence angles, gives the conclusion that the largest possible spot size on the cantilever has the lowest divergence angle, will produce smallest spot size on the fiber plane on a certain distance from the cantilever.

Using larger beam spot size on the cantilevers has three main disadvantages. The first one is the clipping effect on the cantilever which distorts the Gaussian shape of the beam and introduces side lobes on the fiber plane. The second problem is the reflected portion of the beam from the silicon surface of the substrate which introduces interfering signals couplings on top of the main signal. The third disadvantage of larger beam, is the higher clipping ratio of the reflected laser power which decreases the signal level on the photo diode. Therefore, the beam spot size on the cantilevers must be small enough with respect to the cantilever dimension to minimize these unwanted effects.

6.4 Multi-Spot Laser Beam Generator

A diffractive pattern generator was preferred to generate equally spaced Laser beams on the tip of the cantilevers. Fig. 6-5 shows a 3D illustration of the optical and mechanical design of the system, including the magnetic actuation coil and magnets, a

disposable cartridge contacting the MEMS sensor array, illumination engine and the parallel readout peak-up head using a fiber array.

Primarily, all the MEMS cantilevers were on a single chip in a single housing but a separated multi-channel cartridge design was also considered for future experiments with a channel pitch of 2mm. For such a large channel pitch, we selected a commercial 5 spot pattern generator DOE-263 by Laser Components Company with a diverging angle of 1.54°.

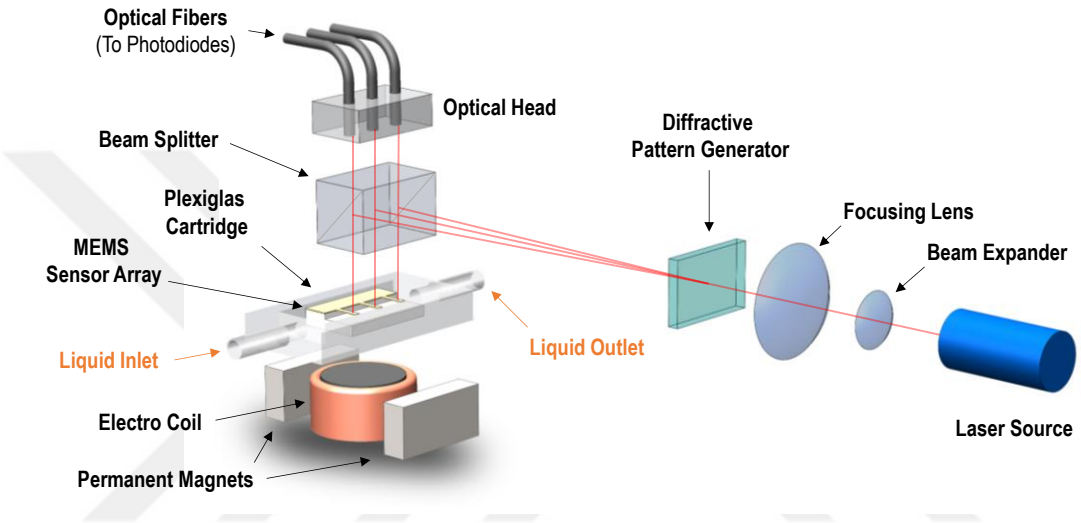

Figure 6-5 - 3D illustration of the optical and mechanical design of the system

For a diffractive pattern generator with a diffraction angle of β, placed at a distance of z from cantilevers, the spot pitch will be equal to:

$$d_{spots}(z) = \mathrm{z}\tan(\beta). \tag{6.9}$$

For a desired spot pitch, the required distance will be

$$\mathrm{z} = \frac{d_{spots}}{\tan(\beta)}. \tag{6.10}$$

For the mentioned pattern generator, required distance for 2mm spot pitches will be 74.4 mm. Since the focusing lens must be placed before the pattern generator in order to form similar spots on all of the cantilevers and considering enough space between the lens and pattern generator, the distance of the focusing lens to cantilevers will be around 100 mm.

Increasing the distance between the focusing lens and the focusing plane, increases the spot size. Assuming a collimated Laser source with wave length of λ and beam diameter of D on an ideal lens with focal length of f, the spot size at the focal point will be:

$$d = \frac{2 f \lambda}{D}. \tag{6.11}$$

For our setup, I preferred to use a He-Ne laser source for its perfect beam profile. The wavelength is 630 nm and the beam diameter was measured around 820 µm. Using a 100 mm focal length concave lens, the beam diameter will be around 154 µm. For our cantilevers of 20 to 50 µm width we need much smaller spot sizes.

Fig. 6-6, shows generated pattern aligned on 20 × 200 µm cantilevers using a single plano-convex lens with a focal length of 100 mm. A different pattern generator with smaller diffraction angle was used in this experiment to align the beams at a pitch of 600 µm.

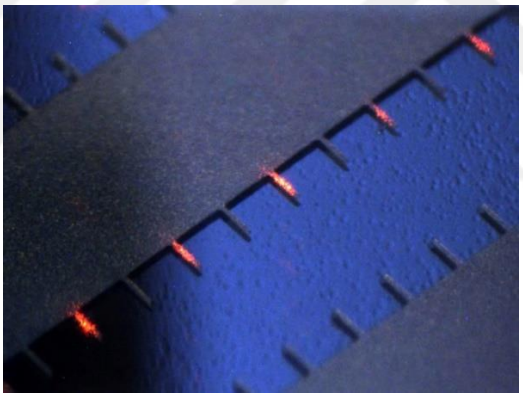

Figure 6-6 – Generated linear spot pattern aligned on 20×200 µm cantilevers.

As seen on the equation 6.11, to decrease the spot size, one could decrease the focal length of the lens or increase the beam diameter of the Laser source or both. As a solution, we added a high N.A. microscope lens before the focusing lens as a beam expander to increase the beam diameter on the lens and also due to large divergence angle of the incoming beam, we replaced the focusing lens with a smaller focal length one to maintain the focusing length. Fig. 6-7 shows the detailed optical design of the setup.

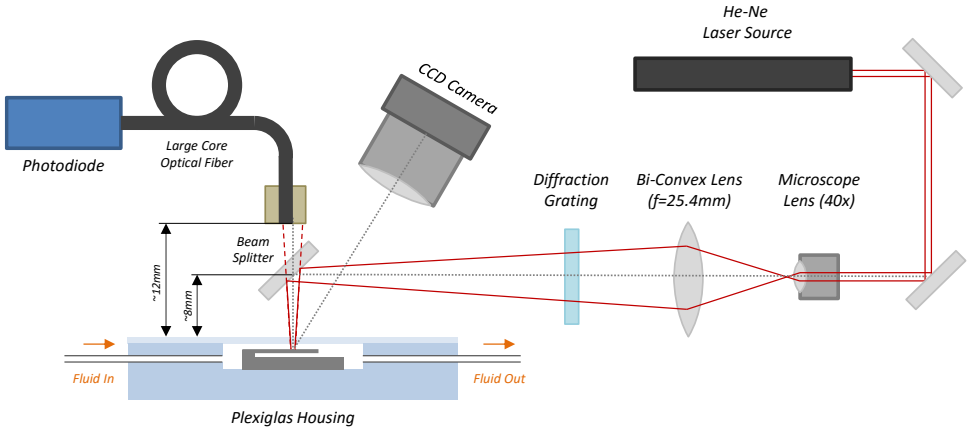

Figure 6-7 - Detailed optical design of the system

A 40× microscope objective with N.A. = 0.35 forms an 8 mm beam on the focusing lens. The focusing lens replaced with a 25.4 mm bi-convex lens. For a more precise estimation of the spot size on the focal plane and also to study the clipping effects, optical design simulated on the Zemax software using physical wave propagation method. Fig. 6-8 shows the Zemax model of the optical setup.

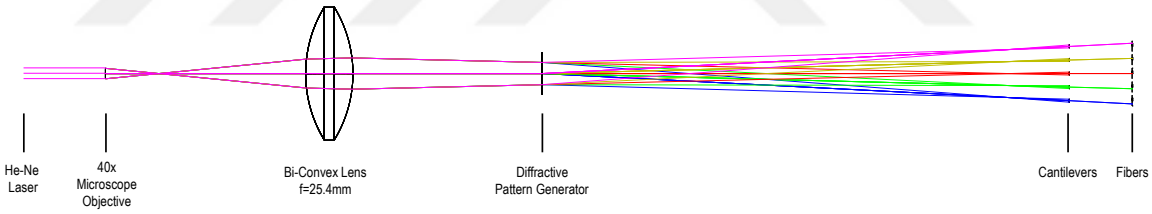

Figure 6-8 - Zemax model of the optical design

Cantilevers are modeled as rectangular mirrors, decentered to align the beams at a suitable distance from the edge of the cantilever tips. Although, the maximum displacement occurs at the tip of the cantilever, the Laser spot must be aligned at a minimum distance from the tip to preserve clipping of the spot at acceptable levels. Practically I observed the best results at a distance of 25 µm from the tip for our 200 µm cantilevers. Based on the simulations, with available optical elements, minimum achievable beam diameter was determined as 28 µm.

Cantilever width is also an important parameter which changes the shape of the reflected beam. Fig. 6-9, shows the reflected beam profile for 200 µm length cantilevers with different widths of 20 µm, 30 µm, 50 µm and 100 µm.

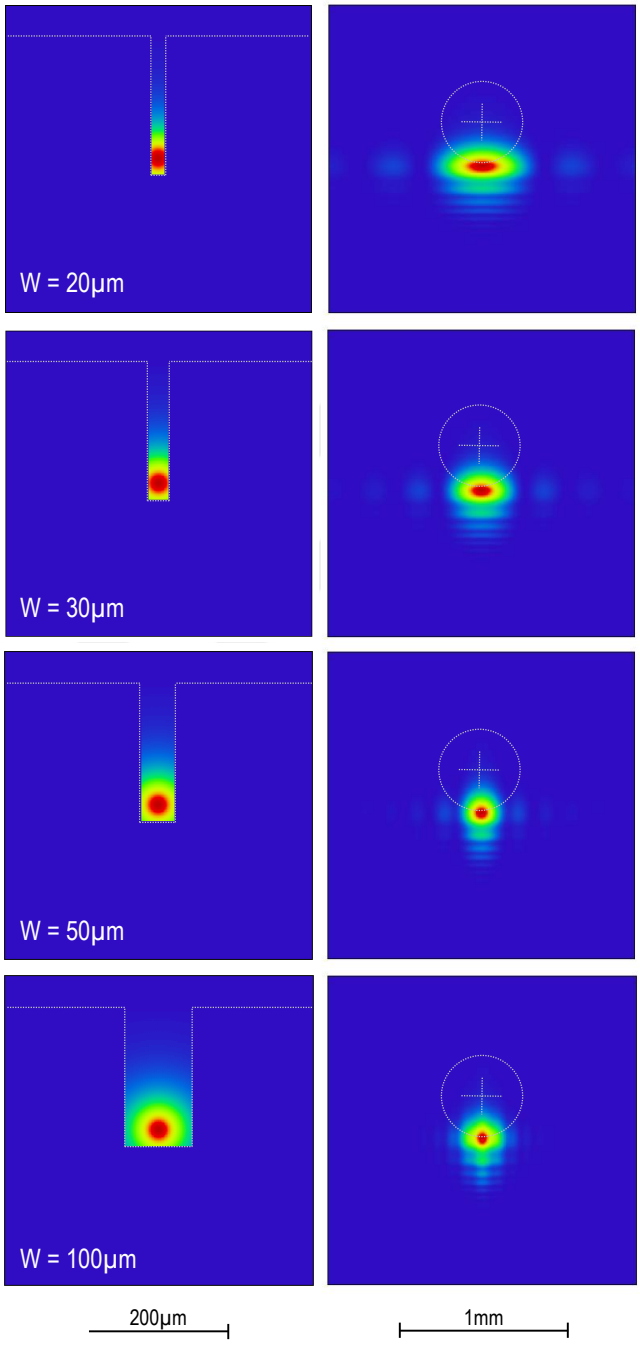

Figure 6-9 - Profile of the Laser beam on the cantilever and the reflected beam on the fiber plane for 200 µm length cantilevers with different widths of 20 µm, 30 µm, 50 µm and 100 µm. Dashed lines shows the edges of the cantilever and the location of the large core optical fiber (Ø = 486 µm).

I have also captured the intensity profile of the real reflected beam from 20×200 µm cantilever using a SLR camera and special perspective control macro lens. Fig. 6-10, shows the 3D representation of the captured photograph. Since there will be unwanted reflections in the optics, especially from the glass cover of the cartridge,

There is an important point to be considered here; the tall peak appeared in the intensity profile is the reflected portion of the laser beam from the glass cover of the cartridge. The real reflected beam from the cantilever are elliptic in shape as expected from the simulations.

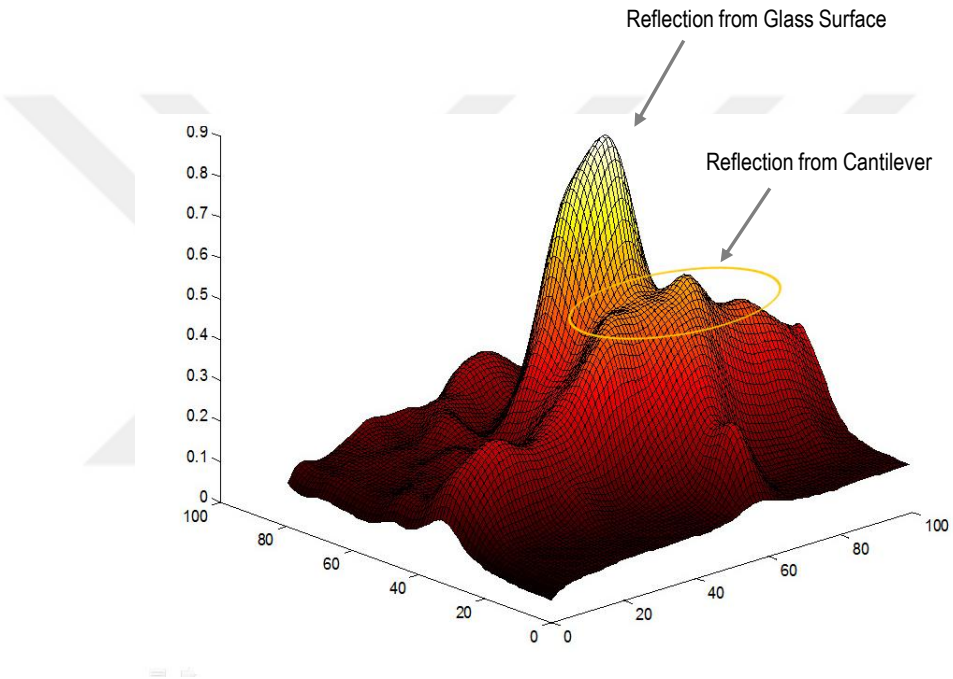

Figure 6-10 - 3D representation of the captured beam profile

The beam profile was captured by placing a very thin semitransparent tracing paper at the fiber plane and tacking the photograph of the beam on the paper. For minimizing the perspective distortions, a perspective control macro lens was preferred. As seen in the Fig. 6-10, shape of the reflected beam is very similar to the simulation results.

As well as distortions in the reflected beam, the beam diameter is also changes especially in 20 µm and 30 µm widths. And the intensity of the reflected beam will be

different. Fig. 6-11, shows the normalized intensity of the reflected beam along the beam movement axis (x-axis) for different cantilever widths.

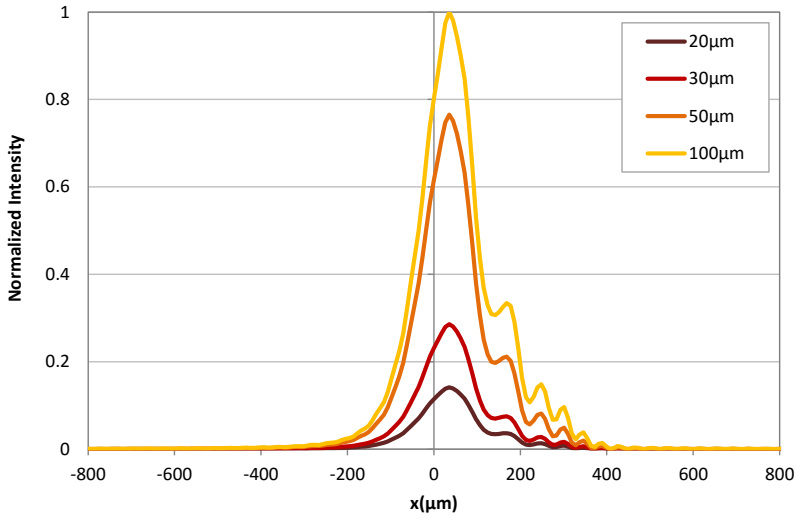

Figure 6-11 - Intensity of the reflected beam along the beam movement axis (x-axis) for different cantilever widths.

The origin in the Fig. 6-11, is the location of the ideal reflected beam without any clipping. The intensity is normalized based on the 100 µm cantilevers maximum reflected intensity. Based on the results, the reflected optical power from the cantilevers dramatically reduces in thin cantilevers. As will be discussed in the next chapter, the precision and the stability of the measurements are directly related to the strength of the readout signal, thus using thicker cantilevers will have higher SNR ratios and more precise measurement results.

The total optical power at the fiber plane is also dramatically decreases in thin cantilevers. In our optical setup, the total power of the Laser source is 5 mW. The optical power of each beam after the diffractive pattern generator will be 1mW per channel and the reflected power to the surface of the cantilevers after the beam splitter will be 500 µW per channel.

Taking the transmission properties of the optical elements into the account, the total transmission of the optical path was calculated around 91.59% without clipping effect of the cantilevers. Fig. 6-12, shows the total transmission of the optical path with

cantilever for different widths of 20, 30, 50 and 100 µm. The Laser beam is aligned at 25 µm distance from the cantilevers edge.

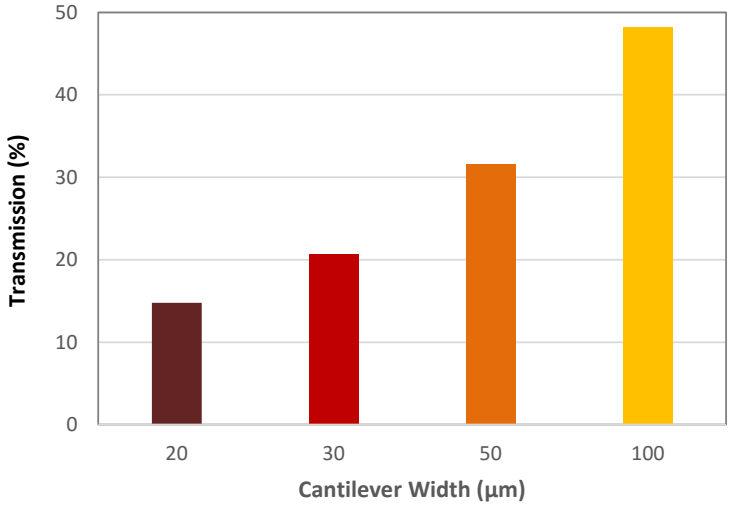

Figure 6-12 – Total optical transmission of each channel for different cantilever widths

Based on these simulation results, only 14.76% of the optical power will be reflected from 20 µm width cantilevers despite of the reflection coefficient of the cantilevers surface.

6.5 Fiber Array Optical Readout Head

I introduced the idea of using the optical fibers for optical readout, as an alternative method of putting photodiodes near the cantilevers. Using the optical fibers makes it possible to make pick-up heads with different pitches for matching to different MEMS chip designs easily. Another important advantage of using optical fibers is its electrical noise immunity. Since the modulated signals in the photodiodes are in orders of few millivolts, the magnetic field generated by the electro coil could easily be coupled to photodiode signals. Using optical fibers prevents these kind of electrical interferences by keeping the photodiodes far from the electro coil. I constructed the pick-up head using two FR4 pieces with carved parallel channels with proper fiber pitch. The optical fibers were sandwiched and glued between these two FR4 pieces. The other ends of the optical

fibers were connected to identical amplified photodiodes. Fig. 6-12, shows the five channel pick-up head with a channel pitch of 2.32 mm.

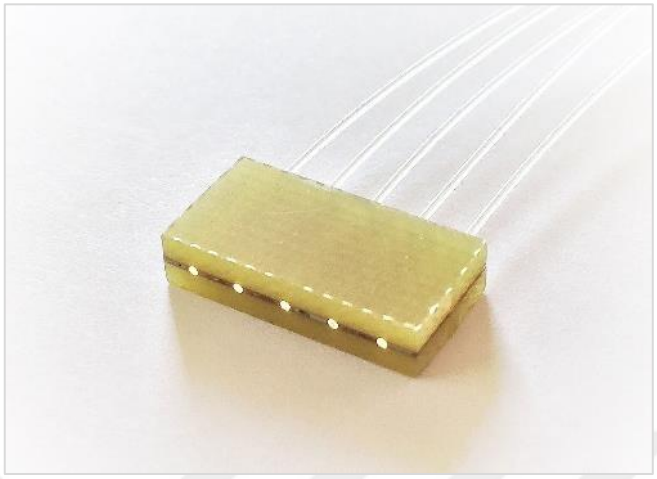

Figure 6-13 – Five channel home-made pick-up head (Channel pitch is 2.32 mm)

6.6 Optimum Fiber Distance

The beam traveling distance on the fiber plane has direct relation to the distance of the fiber. Since laser beam also grows linearly with z_f, the ac signal (v_{ac}) is expected to be remain constant. I performed simulations using MATLAB® to calculate the modulated signal on the photodiodes.

Developed simulation model, propagates the laser beam from the surface of the cantilever to the fibers and calculates the amount of the coupled optical power to the fiber. Then calculates the derivative of the coupled power with respect to the displacement in direction of the beam movement. Taking the electrical properties of the photodiode into the account, the code calculates the output current of the photodiode and resulting output voltage.

We used Thorlabs PDA36A-EC amplified photodiodes in our experimental setup. This amplified Si photodiode has an adjustable gain from 10 to 80 dB. For lowest noise performance the 40 dB gain was preferred, showing lowest NEP level of 5.93×10^{-13} W/$\sqrt{Hz}$. The peak response of the photodiode is 0.65 A/W at its peak sensitivity wavelength of 930nm. Based on the responsivity versus wavelength graph of the photodiode, the responsivity is around 0.32 A/W for λ=630 nm, the wavelength of our

He-Ne Laser. For the amplifier side, the transconductance gain of the photodiode for 40-dB gain was mentioned as 1.51×10^5 V/A. Therefore, the total gain of the amplified photodiode at its 40-dB gain, will be 4.832×10^5 V/W.

Taking these parameters into the account, I found that best sensitivity is obtained at distance of 10 ± 1 mm from the cantilevers. In these simulations, cantilever's tip vibration amplitude assumed to be 20 nm_{p-p} based on our experimental results in DI-water. Fig. 6-13, shows the simulation results.

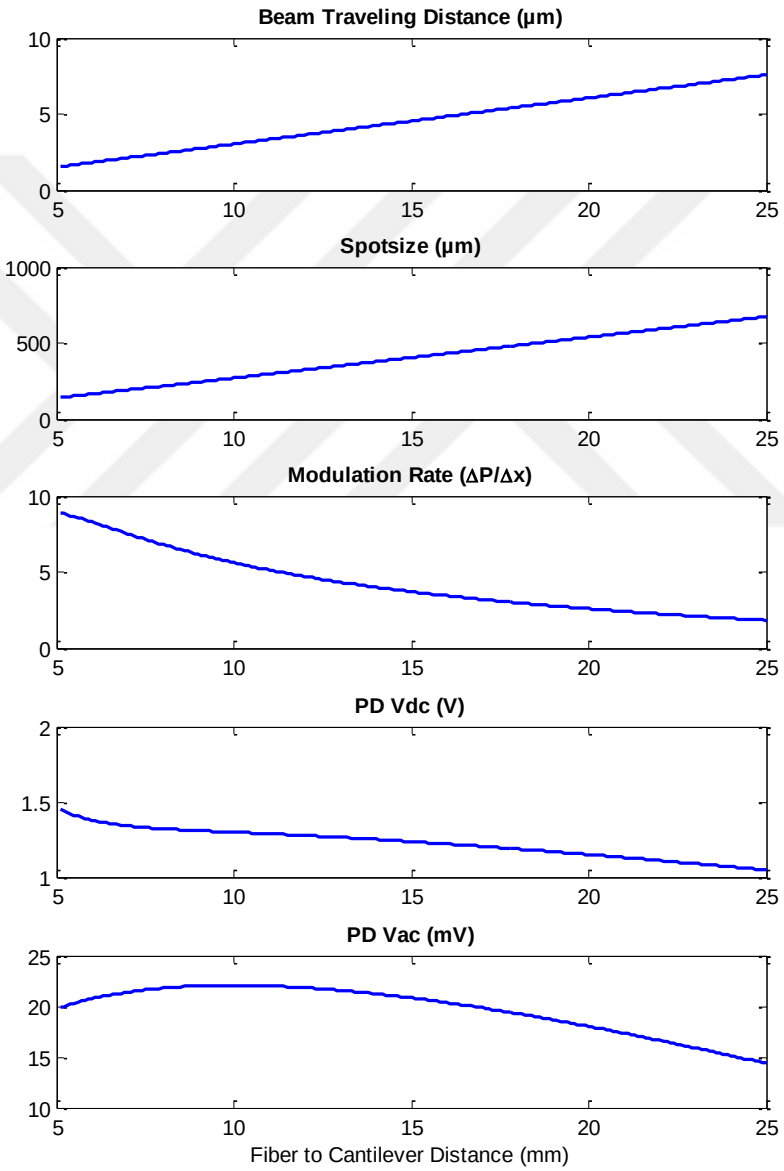

Figure 6-14 – Output signal optimization as a function of fiber distance

Since the generated laser beams, diverges with a fixed angle, the pitch of the fibers at the readout head is also depends to the distance of the fiber head. In our design, because of some physical limitations in the optical setup, the fibers placed around 12 mm from the cantilevers. At this distance, for 2 mm pitch of cantilevers, the fibers pitch will be 2.32 mm.

6.7 Optical Miss-Alignments

The simulations discussed in this chapter gives the optimum location of the optical fibers to get maximum signal from the vibration of the cantilevers. Another main problem in the alignment of the beams is the residual bending of the cantilevers.

With two cantilevers there is always possible to align the optical fiber for optimum beam locations by rotating the optical head. Fig. 6-15 shows a sketch of shifted beams from bended cantilevers and the rotated optical head to capture the optimum signal.

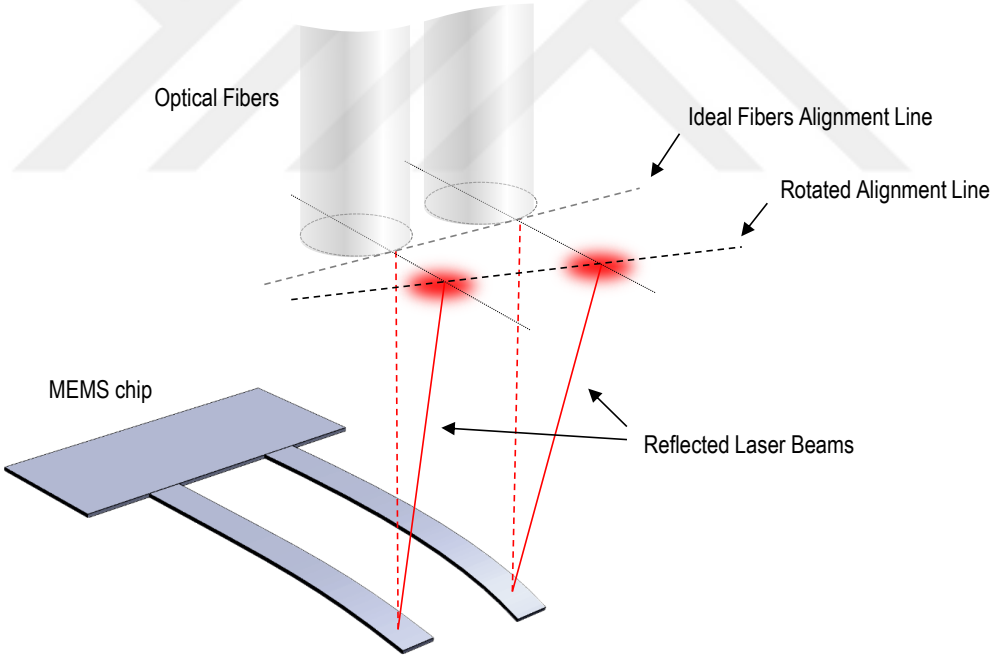

Figure 6-15 - Optical alignment of two channel optical readout with bended cantilevers

Unfortunately, with more than two cantilevers, the alignment for capturing maximum signal from all the cantilevers is not possible.

Based on the simulations of the modulation rate versus beam location, a maximum allowable tolerance for the beam deviation could be defined. Fig. 6-16, shows the modulation rate graph of our experimental system and the allowable deviation limit as the point where the modulation rate drops to half of its maximum value of full width at half maximum of the modulation rate. *x* is the distance of the beam from center of the optical fiber.

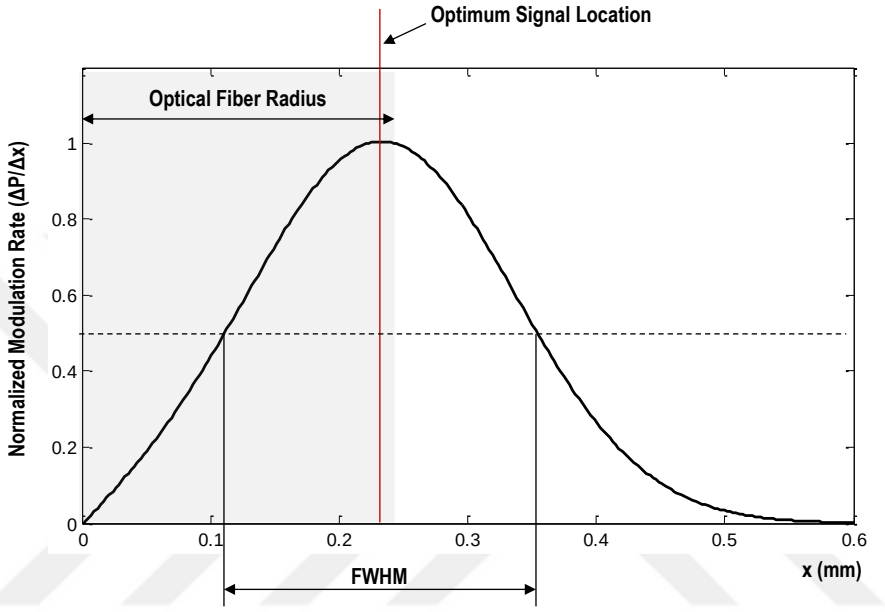

Figure 6-16 - Optimum beam location and FWHM of the modulation rate

FWHM of modulation rate for our system is about 220 µm. It means that a 110 µm deviation on the beam will reduce the AC signal to half of its maximum value.

From this deviation limit the maximum allowable bending for cantilevers could also be calculated. From equation 6-4, the maximum allowable beam bending could be calculated as follows:

$$z_b = \frac{x_b \cdot L}{3\, z_F}. \tag{6.12}$$

Here, z_b is the maximum allowable bending for cantilever measured at the tip of the cantilever. x_b is the maximum allowable beam deviation from its ideal location, L is the length of the cantilever and z_F is the cantilever for fiber plane distance.

For our experimental system, the maximum allowable bending for FWHM of the modulation rate will be around ±540 nm calculated based on the effective cantilever length and ±620 nm tip of cantilever.

Unfortunately, the bending of the fabricated cantilevers in our group is far below this bending limits. Fig. 6-17 shows 3D representation of white-light interferometric measurement results of the latest fabricated cantilevers for our experimental setup.

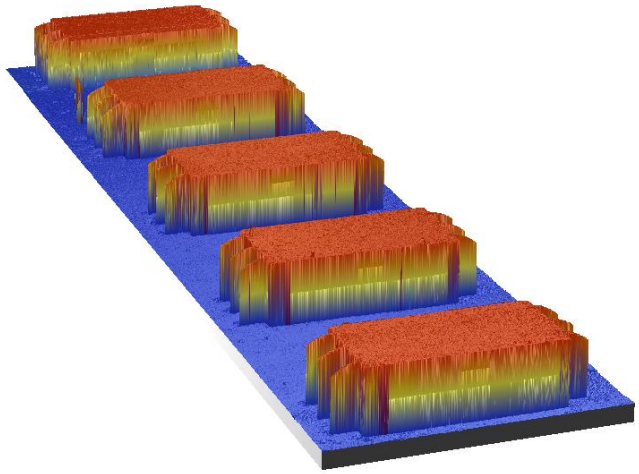

Figure 6-17 - 3D representation of white-light interferometric measurement results

Fig. 6-18, shows the height of the cantilevers along a straight line (shown as a thin red line) passing through the tip of cantilevers.

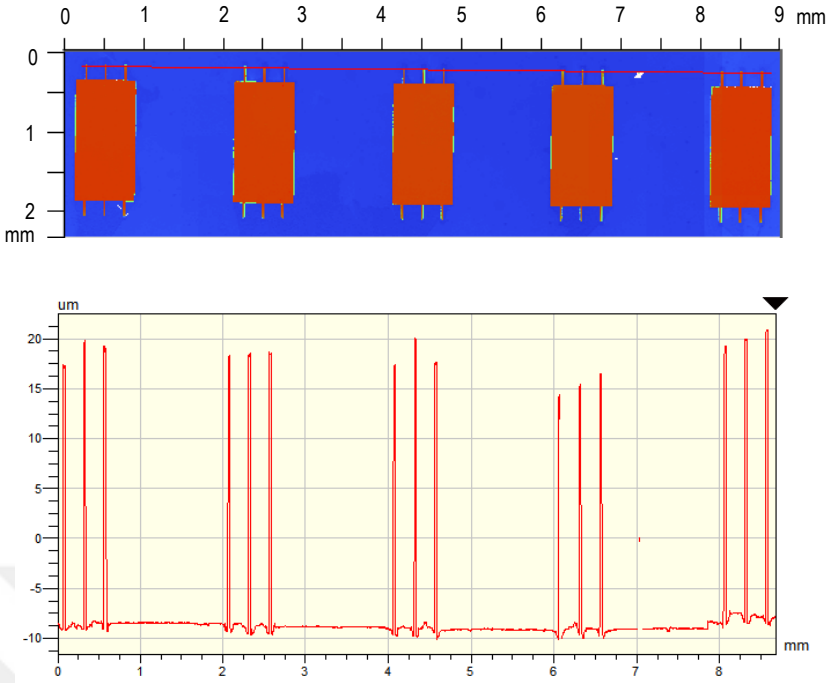

Figure 6-18 - Cantilever's tip height measurement results

White light interferometer measurement results, showed that the fabricated cantilevers are extensively bended in order of ±4µm with respect to average bending of all cantilevers. Based on the maximum allowable bending calculations, this cantilevers could not be used with the proposed optical readout method.

6.8 Conclusion

We developed a 5-spot Laser source for illuminating equally spaced cantilevers with pitch of 2 mm using a 5 mW He-Ne Laser. The minimum beam diameter of 28µm achieved using a focusing lens located at a distance of around 100 mm. A microscope objective used as beam expander prior to the focusing lens. With a total optical power of less than 500µW per channel, measurable ac signals observed at photodiodes.

A compact fiber array based pick-up was built for optical readout. Its main advantages are easy customization to different size and pitch, and good immunity to electrical noise and magnetic interference as the photo detectors are located away from the coil and electronics. The whole optical design was modeled in Zemax® and Matlab® and the optimum values for design parameters was discussed.

7 Phase Tracking Based Resonance Frequency Monitoring

7.1 Introduction

As discussed in chapter 3, we demonstrated parallel interferometric readout of MEMS cantilevers having different resonant frequencies operated in air allowing frequency multiplexing to separate the signal of each cantilever [43]. Similar frequency multiplexing approach was also reported for optical lever readout method using PSD and operating in vacuum [65]. However, the frequency-multiplexing method is not suitable for cantilevers in fluids where the quality factors are low, resulting in large overlap in the frequency responses of the cantilevers.

On order to use cantilever sensors with identical design, resulting similar resonant frequencies we employed phase-based measurement method. In this method, all of the cantilevers are driven open loop at the same excitation frequency. The relative phase between the drive signal and the cantilevers are used to monitor the dynamic changes of all the cantilevers simultaneously in real-time with high precision. The measured phase shifts are used to calculate the dynamic changes in resonant frequency, liquid viscosity, or mass accretion during the experiments. Fig. 7-1, shows block diagram of phase based measurement method.

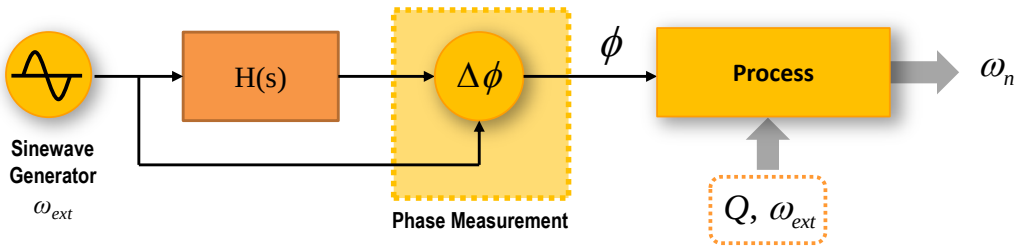

Figure 7-1 - Phase based natural frequency tracking method

Although the phase value directly could be used as the output parameter for most of the applications, but for applications where the resonant frequency value is needed,

one could calculate the resonant frequency of the cantilevers using the following equation:

$$\omega_n(\varphi) = \frac{2\omega_{ext}}{\frac{1}{Q\ tan(\varphi)} + \sqrt{\frac{1}{(Q\ tan(\varphi))^2} + 4}} \tag{7.1}$$

In this equation, ω_{ext} is the excitation or actuating angular frequency, ω_n is the angular natural frequency and Q is the quality factor. Fig. 7-2, shows the relative natural frequency vs. the measured phase, plotted for different quality factor resonators.

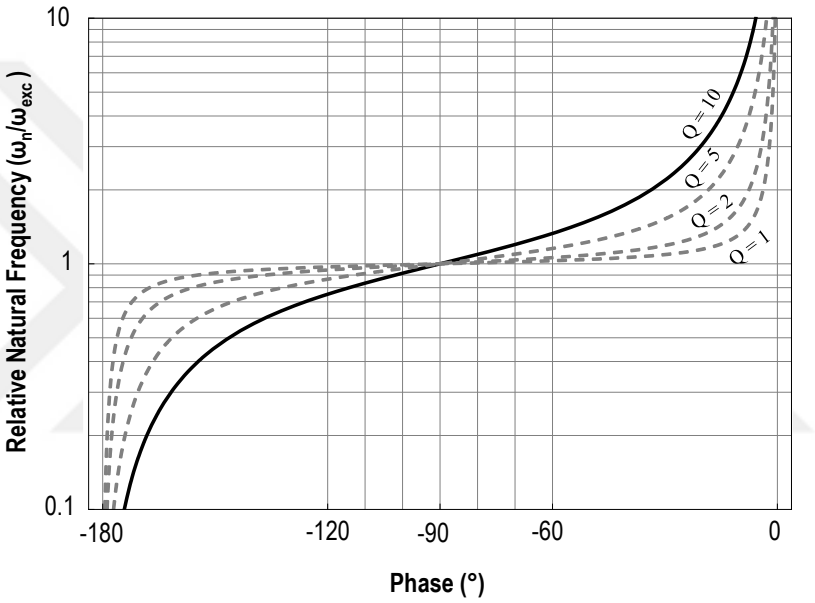

Figure 7-2 - Natural frequency vs. phase for different quality factor resonators

As seen on the Fig. 7-2, the sensitivity of the system directly depends on the quality factor. If we define the sensitivity of the system as the rate of the natural frequency to the phase of the system as follows:

$$S = \frac{d\omega_n}{d\varphi} \tag{7.2}$$

Calculating the derivative of the equation 7.1 with respect to phase and plotting versus the quality factor, shows a linear relationship between the sensitivity and the

quality factor. Fig. 7-3 shows the sensitivity of a system with natural frequency of 32 kHz excited at natural frequency, plotted as a function of the quality factor.

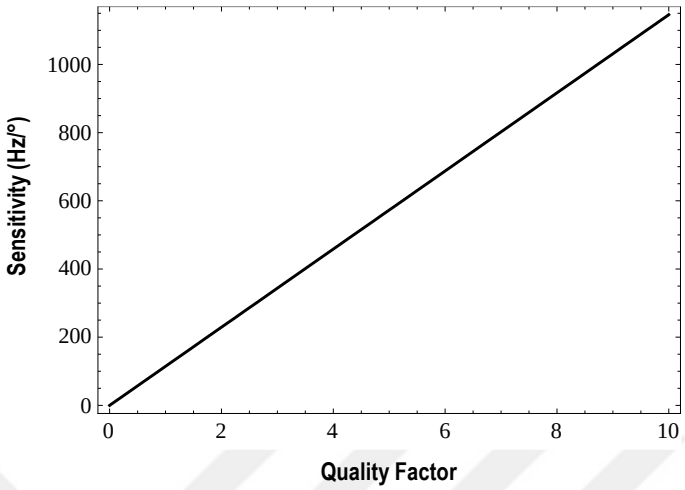

Figure 7-3 - Sensitivity vs. quality factor of a system with natural frequency of 32 kHz excited at its natural frequency.

For multi-channel resonance tracking systems, where we excite all the cantilevers with a fixed frequency, the sensitivity will depend on the frequency difference between the excitation frequency and the natural frequency of the cantilevers. Fig. 7-4, shows the sensitivity of the system as a function of the relative natural frequency.

The phase shift in our viscosity experiments, is a result of changes in both viscosity and density [31]. Viscosity of the liquids used in this experiment, changes from 0.95 cP for DI-water up to 4.10 cP for 50% Glycerol solution (measured using Anton Paar AMVn commercial viscometer at room temperature of 23°C), and the density change from 1.00 to 1.12 kg/m^3. The relative impact of viscosity and density on the phase shift depends of the cantilever geometry as well as other parameters [33], The resulting phase shifts in these experiments are mainly due to the viscosity changes, and the impact of the density change is small. Nevertheless, in our experiments we focused on the phase shift as a function of the Glycerol concentration in DI-water.

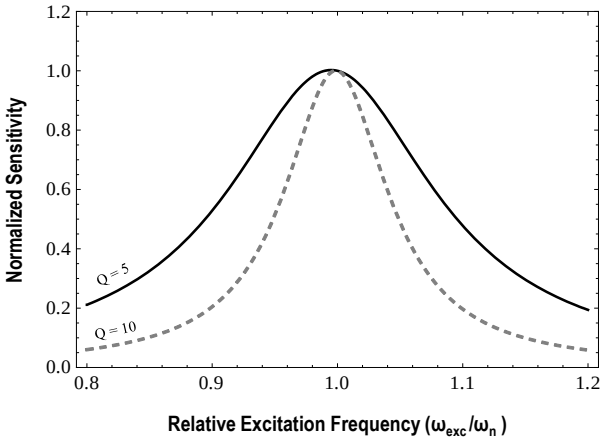

Figure 7-4 - Sensitivity versus relative natural frequency of the system

7.2 Principle of Lock-In Amplifiers

Lock-in amplifiers are very useful devices for detecting weak signals with a known frequency, buried in extremely high background noise. A Lock-in amplifiers consists of four main units, local quadrature oscillator, mixer, low-pass filter, and phase calculator. Fig. 7-5, shows the block diagram of a standard lock-in amplifier[1].

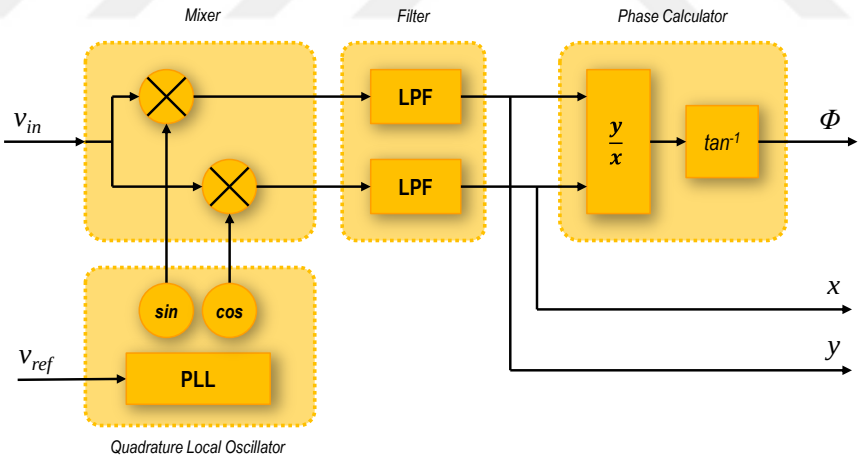

Figure 7-5 - Block diagram of a standard Lock-In amplifier

[1] This configuration also called as dual lock-in amplifier because of two channel mixer and filter.

The local quadrature oscillator mainly equipped with a PLL unit generates a sine and cosine waveform locked to a reference signal. Two mixer blocks multiplies the input signal to generated sine and cosine waves. Filtering the multiplied signals gives two low-frequency or dc signals called X and Y signals. The X and Y signals represents the amplitudes of the in-phase and quadrature components of the input signal, respectively. Dividing Y by X and taking the invert tangent of the Y/X gives the phase of the input signal with respect to the reference signal. For the input signal of v_{in} with known frequency of f_0, we have:

$$v_{in}(t) = Asin(2\pi f_0 + \phi_{in}). \tag{7.3}$$

And output of the quadrature oscillator (reference signals) are:

$$v_{rx}(t) = cos(2\pi f_0 + \phi_r), \tag{7.4}$$

$$v_{ry}(t) = sin(2\pi f_0 + \phi_r). \tag{7.5}$$

Here, Φ and Φr are the phases of the input and reference signals respectively. Now, the output of the mixers will be the multiplication of the input signal to reference signals:

$$v_x(t) = Asin(2\pi f_0 t + \phi_{in}) \cos(2\pi f_0 t + \phi_r) \tag{7.6}$$

$$= \frac{A}{2}[cos(\phi_{in} - \phi_r) + \cos(2\pi 2 f_0 t + \phi_{in} + \phi_r)] \tag{7.7}$$

$$v_y(t) = Asin(2\pi f_0 t + \phi_{in}) \, sin(2\pi f_0 t + \phi_r) \tag{7.8}$$

$$= \frac{A}{2}[sin(\phi_{in} - \phi_r) + \sin(2\pi 2 f_0 t + \phi_{in} + \phi_r)] \tag{7.9}$$

Assuming a low-pass filter with a cut-off frequency low enough from the f_0 ($f_c << f_0$), the second term with twice of the f0 will be cancelled and the outputs of the LPF, the X and Y signals will be:

$$X = \frac{A}{2} cos(\phi_{in} - \phi_r), \tag{7.10}$$

$$Y = \frac{A}{2} sin(\phi_{in} - \phi_r). \tag{7.11}$$

Here, the resulting signals are DC values, related to the amplitude of the input signal. The bandwidth of these signals is limited to the bandwidth of the low-pass filters. Lock-in amplifier usually have adjustable bandwidth from several kHz down to mHz levels. Using very narrow bandwidths will dramatically reduce the noise level by limiting the noise power from the whole spectrum to narrow bandwidth of the low-pass filter.

Also for measuring the phase of the input signal, defining the phase difference as:

$$\phi = \phi_{in} - \phi_r, \tag{7.12}$$

one could calculate the phase difference as follows:

$$\phi = tan^{-1}\left(\frac{Y}{X}\right). \tag{7.13}$$

The lock-in amplifiers could be implemented both with analog and digital electronics topologies. Modern digital lock-in amplifiers use high speed DSP processors for generating the sine and cosine waves and multiplication operations. I used similar methods to implement the multi-channel lock-in amplifier in LabVIEW.

7.3 Multi-Channel Phase Measurement

For our multi-channel phase measurement system first I used National Instruments two channel (two analog input) simultaneous sampling DAQ card PCI-6111 and implemented a code in LabVIEW® to generate the sine and cosine waveforms and calculate the multiplications, filtering and phase of the input signals in parallel. For two channel phase measurement, I used a digital input channel as the reference signal input. This reference signal triggers the generation of the sine and cosine waveforms. Fig. 7-6, shows the block diagram of the implemented method.

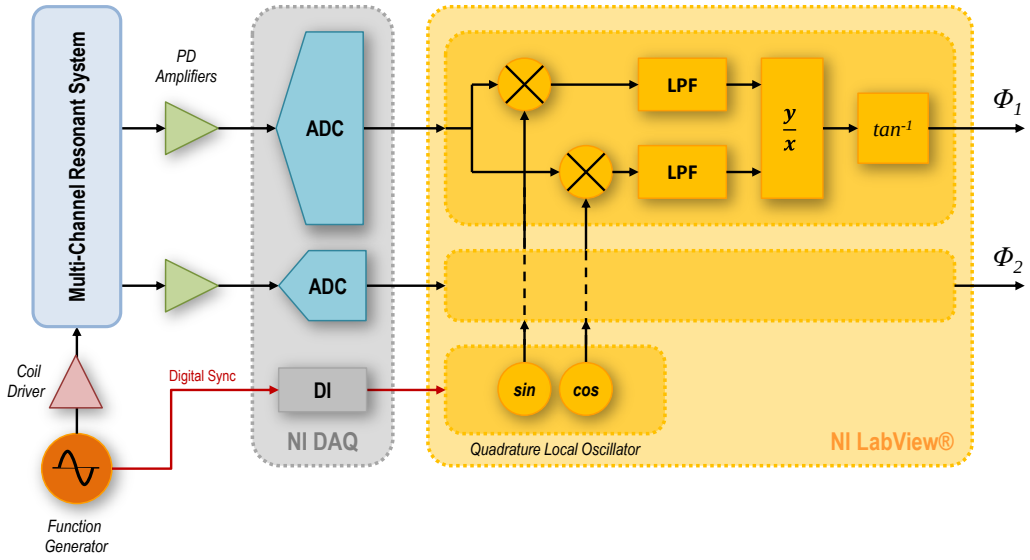

Figure 7-6 – Two channel phase measurement using two channel DAQ card

In this method with an N-Channel DAQ card it is possible to do N-channel measurement. But the phase noise of the measured signal is limited to the phase noise of the digital input signal. A phase measurement precision of < ±0.05° achieved with this method at sampling rate of 5MSps and averaging time of 10 seconds.

For higher channel count, we bought an 8-channel simultaneous sampling DAQ card PCI-6133 from National Instruments. Using this DAQ card, I developed a more precious topology by assigning one of the analog input channels for reference signal. Fig. 7-7 shows the block diagram of the implemented method.

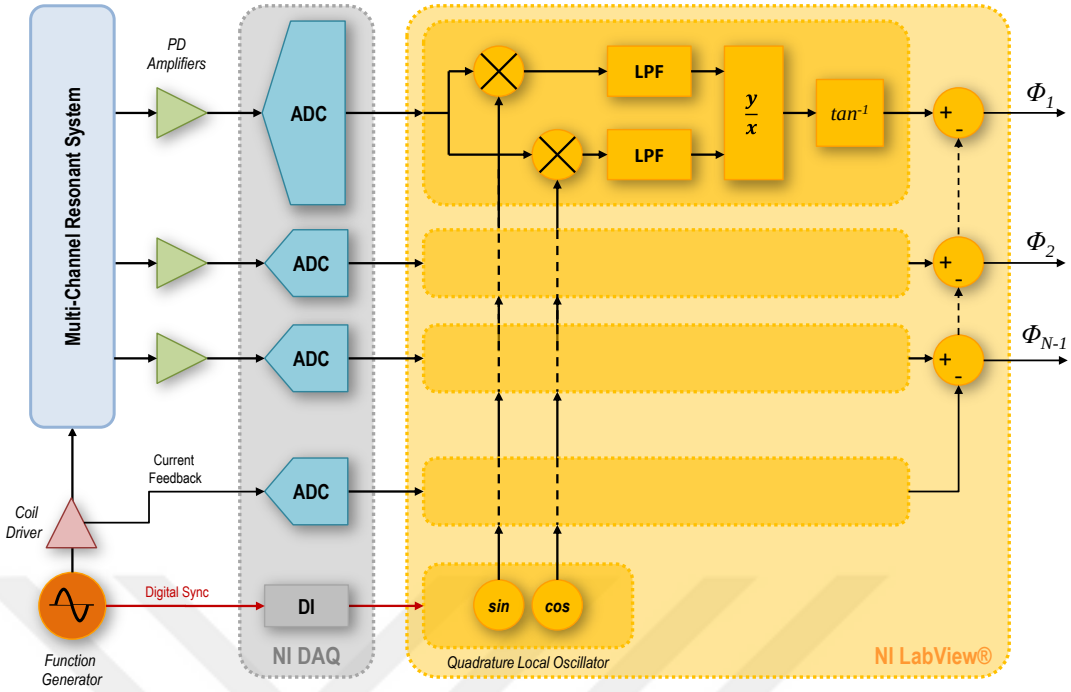

Figure 7-7 - N-1 channel phase measurement system using N-channel DAQ card

I implemented this method for 5-channel phase measurement in LabVIEW and absolute long-time phase precision of < ±0.0005° achieved at lower sampling rate of 2.5 MSps and averaging time of 2 seconds. Demonstrated precision level is comparable to commercial lock-in amplifiers available in the market. Fig. 7-8 shows the phase stability of this method implemented for 2 channel measurement.

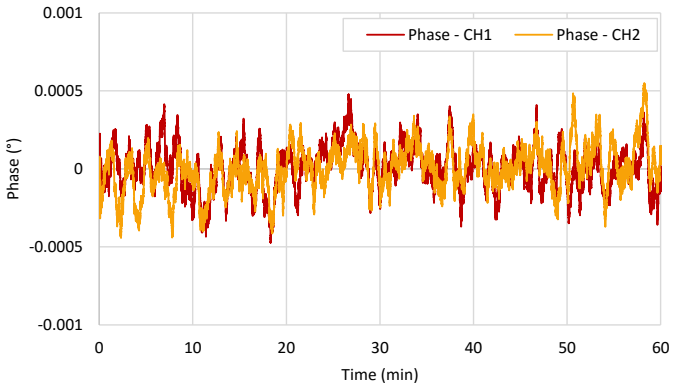

Figure 7-8 - Phase stability of the N-1 channel phase measurement method

The phase stability was measured by applying a 50 mVp-p sine wave to all three channels (two input channels + reference channel). The dynamic range of the ADCs are ±1.25 V. The noise performance of the system will be discussed in detail later in this chapter.

7.4 LabVIEW Implementation

Because of the limitations in the real-time data transfer between the DAQ card and PC, LabVIEW uses a block-wise data transfer method. In this method, sampled data of a certain sample size buffered in the DAQ card and then transfer to the PC. The block size and sample rates are defined and set at initialization of the code.

For continues stream of the sampled data, one could reconstruct the data by attaching the data blocks to each other. Fig. 7-9, shows block diagram of this approach.

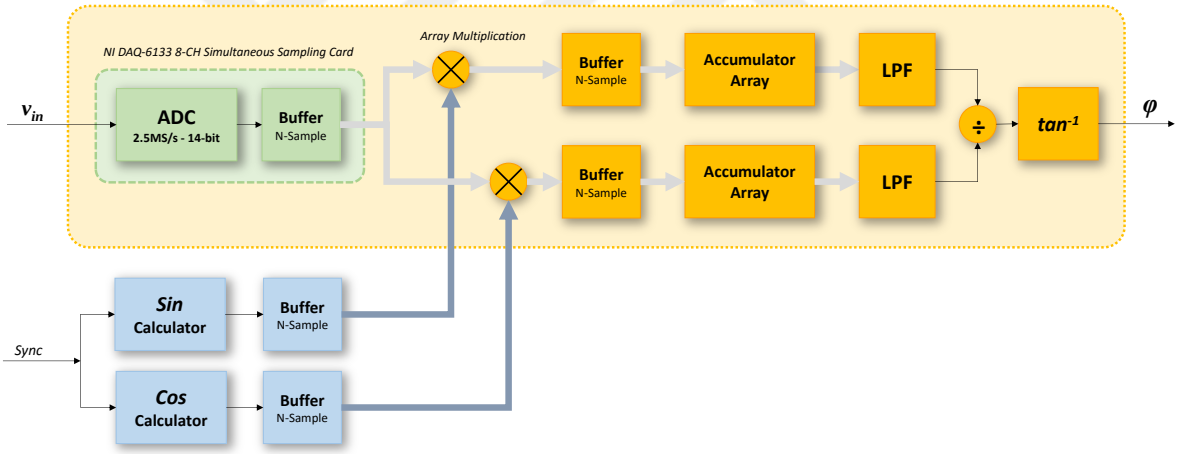

Figure 7-9 - LabVIEW implementation of the proposed phase measurement method

In this method, code calculates the sine and cosine waveforms also as N-sample blocks. Multiplies with N-sample data blocks from the DAQ card. Then calculated arrays are attached to each other in an accumulator array. Filtered value of the reconstructed array will be the X and Y signals. The phase of the signal will be inverse tangent of the Y/X as described before.

For filtering, I used a moving average filter with sample size of desired averaging time. For example, with a sampling rate of 5 MSps and averaging time of 2 seconds, the sample size will be $(5\times10^6) \times 2 = 10$ MS.

7.5 Phase Measurement Stability in Presence of Noise

The performance of the implemented method in the presence of noise is the main limiting factor of our measurement sensitivity. For determining the noise immunity performance of the implemented system, I developed a simulation model including the dominant noise mechanisms in our system. Fig. 7-10, shows the block diagram of the model showing main noise sources in our system before lock-in amplifier.

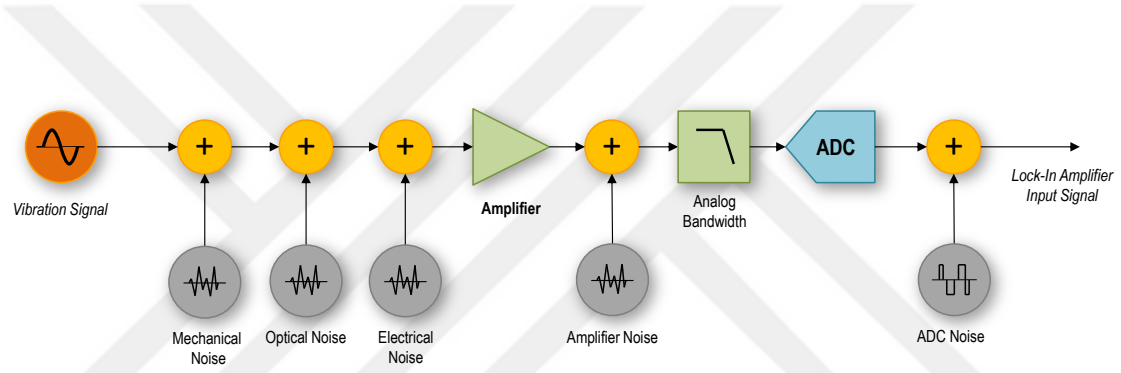

Figure 7-10 - Noise model showing main noise sources

Mechanical vibration of the cantilever induced by the Brownian motion of the liquid and all mechanical instabilities in optical system will introduce some noise into to system. The Laser beam used for optical readout has a lots of noise mechanisms such as Shot noise, Doppler noise and also some temperature dependent low frequency fluctuations. Electrical noise of the photo diode, amplifier and the signal conditioning circuits all had noises that will add up to the main signal.

For measuring the analog noises in our experimental setup separately, I measured the noise spectrum of out experimental system in different states. Table 7-1 shows the system configuration for each state and Fig. 7-11, shows the measurement results. Note that in this measurements the spectrum analyzer was used in AC mode with a low-pass filtering of around 30 Hz. The DC offset of the signals was not shown in this graph.

Table 7-1 - Differenet system configuration for measuring the noise spectrums

	Photo Diode	Laser Source	Actuation	Frequency Spectrum
A	OFF	OFF	OFF	Spectrum Analyzer's input stage noise
B	ON	OFF	OFF	Electrical noise (Dark noise)
C	ON	ON	OFF	Electrical + Optical noise
D	ON	ON	ON	Frequency sweep in DI-water + All noises

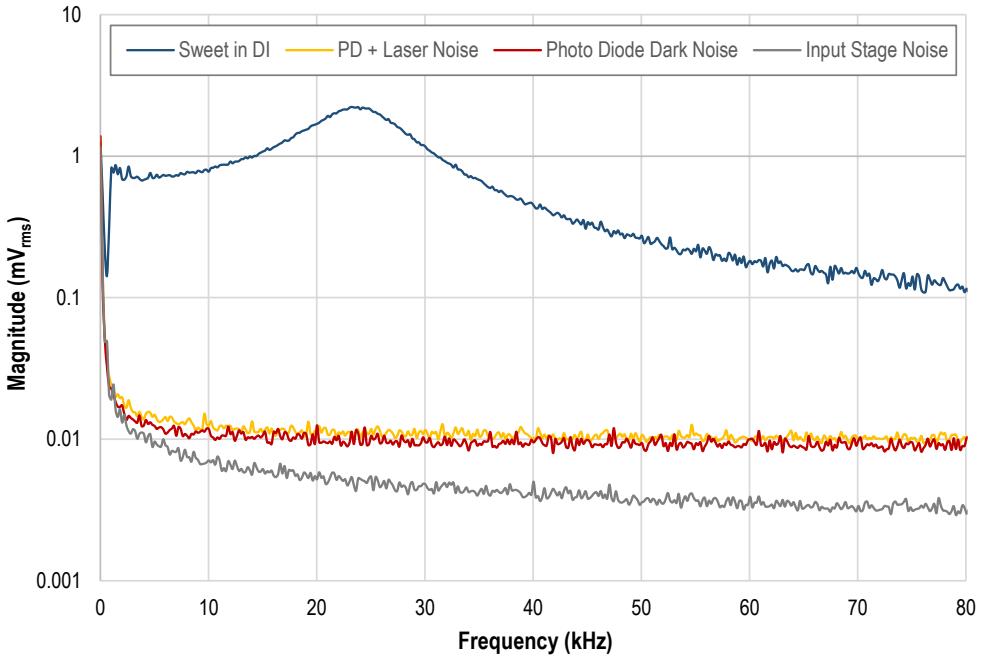

Figure 7-11 - Noise spectrum and frequency response of a 20×200 µm cantilever in DI-water

For determining the noise induced instabilities in the output of the system, I used a combined noise model to simulate the input signal. In this model, all the mechanical, electrical and optical noises are combined as analog noise source and the ADC and other numerical errors are represented as a digital noise source.

A DC source also added into the model representing the DC laser power coupled to the photodiode. In our optical system there is always a DC signal at the photodiode because of the reflections from the flat glass surface of the sensor housing. This dc signal will overflow the ADC input if there is no sufficient dynamic range and this is way we

need higher dynamic range in the ADC. Using an AC filter in the input stage could solve this but will introduce some phase delays and temperature depend analog instabilities which directly will appear as phase error in the measurements. Fig. 7-12 shows the block diagram of this input signal model.

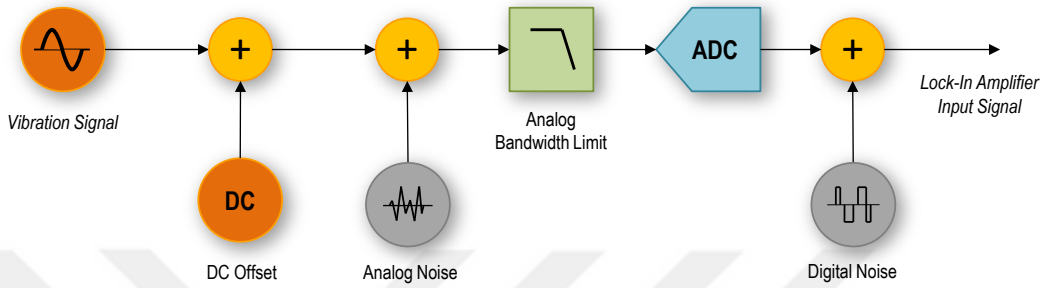

Figure 7-12 - Simplified noise model used in simulations

Analog noise source constructed with an inverse frequency noise source and a bandlimited white noise in LabVIEW. The digital noise was modeled as a 1-bit (LSB) uncertainty on the ADC output. Bit depth related quantization and dynamic range effects were also modeled in the ADC block. The ADCs in the DAQ card were 14-bit with input range of ±1.25 V and maximum sampling rate of 2.5 MSps. Fig. 7-13, shows the frequency spectrum of reconstructed input signal for a 32 kHz cantilever superimposed with analog and digital noise.

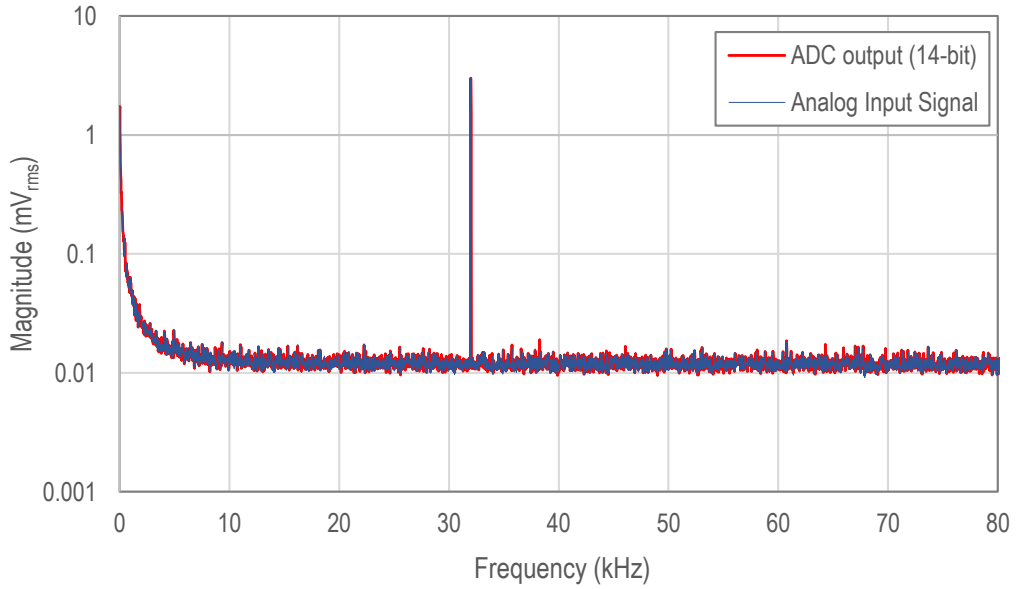

Figure 7-13 - Frequency spectrum of reconstructed input signal for a 32 kHz cantilever superimposed with analog and digital noise.

The parameters of the added analog noise were tuned to match the measured noise spectrum of our experimental setup. As seen in the Fig. 7-13, the digital noise has negligible effect on the noise spectrum for a bit depth of 14-bits in our system. Bit depth has an important impact on the digital noise. For detailed investigation on this effect I did a couple of simulation with various bit depths. Fig. 7-14, shows the noise spectrum for bit depths of 8, 10 and 12 bits. All with dynamic range of ±1.25 V.

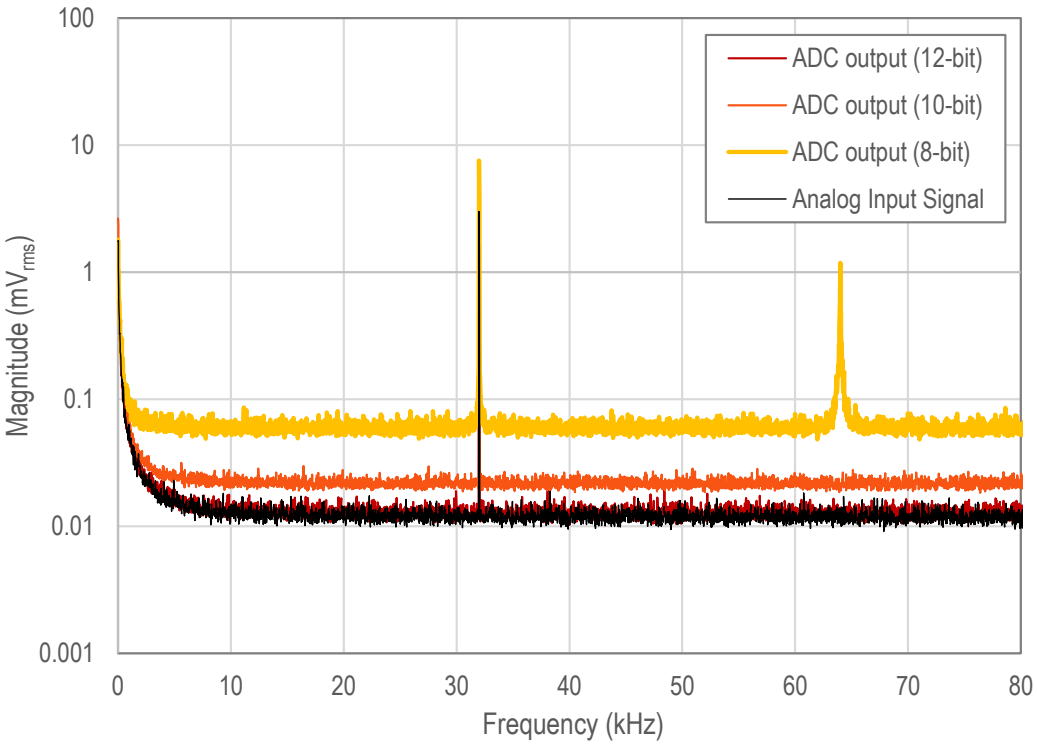

Figure 7-14 – The effect of ADC's bit-depth on noise spectrum of the system for bit depths of 8, 10 and 12 bits.

For very low bit depths considering the dynamic range of the ADC, the input signal's amplitude drops to levels comparable to the LSB. In this case, extensive digital noise appear as addition peaks in the frequency spectrum. The effect of sampling rate will be discussed later in the stability topic. Waveform of the analog input signal and ADC output samples for a 10-bit ADC with sampling rate of 2.5 MSps were shown in the Fig. 7-15.

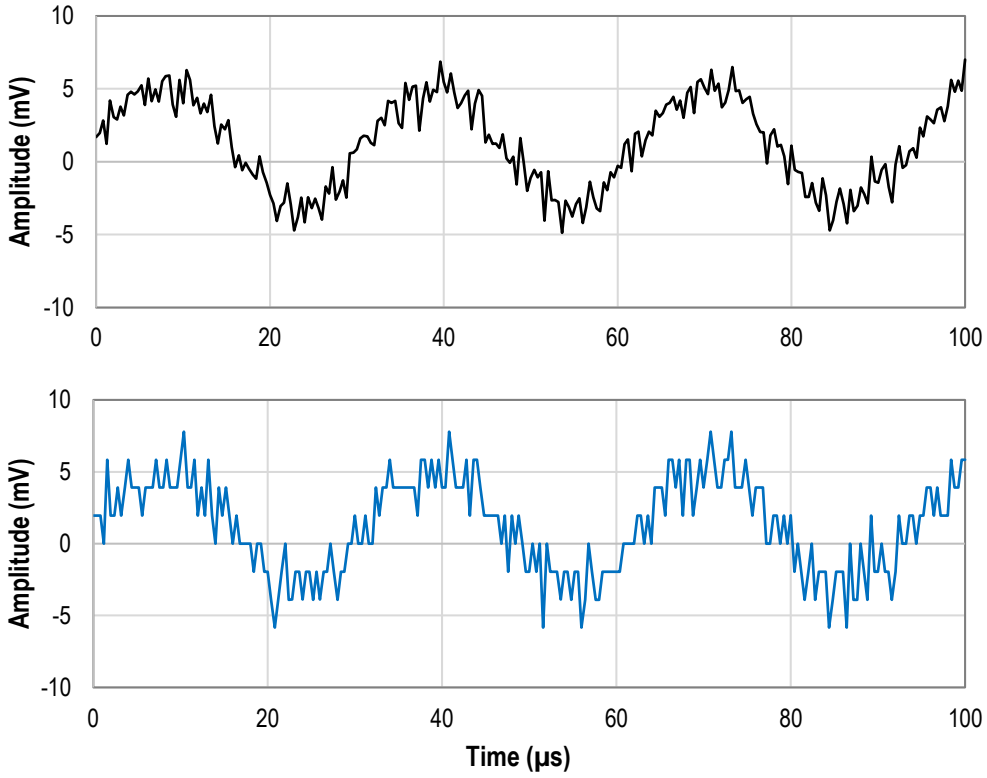

Figure 7-15 - Waveform of the analog input signal the ADC output samples for a 10-bit ADC.

Using the constructed input signal, the phase measurement stability of the system could be simulated. Fig. 7-16, shows the measurement stability of the system for 3 minutes.

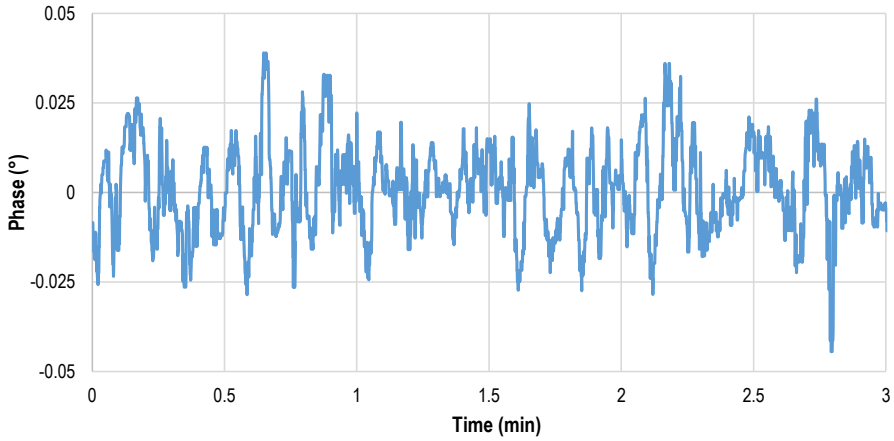

Figure 7-16 - Phase measurement stability of the system with simulated noise

The standard deviation of the measured phase was calculated around 12.5 m° with a peak to peak variation of < 0.085° with typical system parameters. Table 7-2, shows a summary of model parameters considered in this simulation.

Table 7-2 - Typical model parameters used in simulation

ADC Parameters	
Sampling Rate	2.5 MSps
Bit Depth	14 bit
Dynamic Range	±1.25 V
Lock-In Parameters	
Data Block Length	50 ms
Total Averaging Time	2 s
Input Signal Parameters	
Excitation Frequency	32 kHz
Signal Amplitude	3 mV_{rms}
DC Offset	300 mV
Photo Diode Bandwidth	150 kHz

7.6 Simulation of the System with Resonant Cantilever Model

For simulating the resonance frequency induced phase shifts in system, I added a second order resonator model representing the cantilever into the system. Fig. 7-17, shows the block diagram of the simulation model.

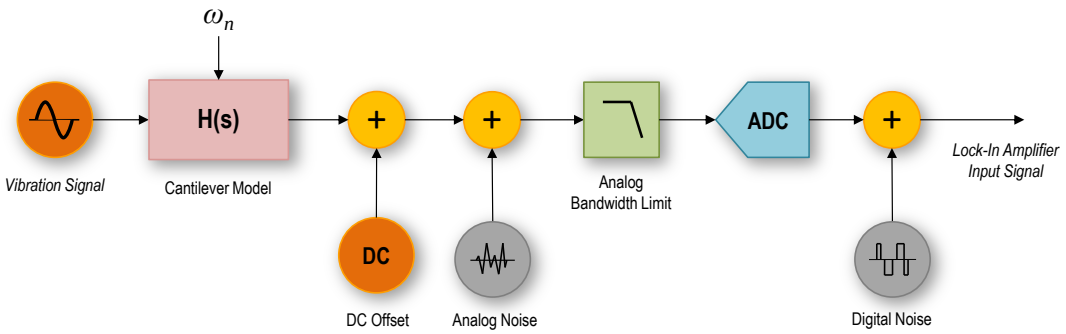

Figure 7-17 - Block diagram of the simulation model with cantilever model

Using this model, the phase shifts related to the resonance frequency shifts could be analyzed. A step function is used to apply desired frequency shift on the natural frequency of the cantilever at a certain time.

Based on the previous simulations, the standard deviation of the system was determined as 12.5 m°. From the analytical calculations described earlier in this chapter, the sensitivity of the simulated cantilevers, was calculated as 17.9 m°/Hz. Based on the sensitivity and stability values of the system, the equivalent detection limit at frequency domain could be calculated as follows:

$$\sigma_{f_n} = \frac{\sigma_\phi}{S} = \frac{12.5m^\circ}{17.9m^\circ} \cong 0.7\ Hz \tag{7.14}$$

Fig. 7-18, shows simulation results for frequency shifts at detection limit and twice of it for a cantilever with natural frequency of 32 kHz and quality factor of 5 excited at 32 kHz. The amplitude of the signal, analog noise and ADC parameters are matched to our experimental setup values. A step shifts in the natural frequency of the cantilever was applied at t = 25 s.

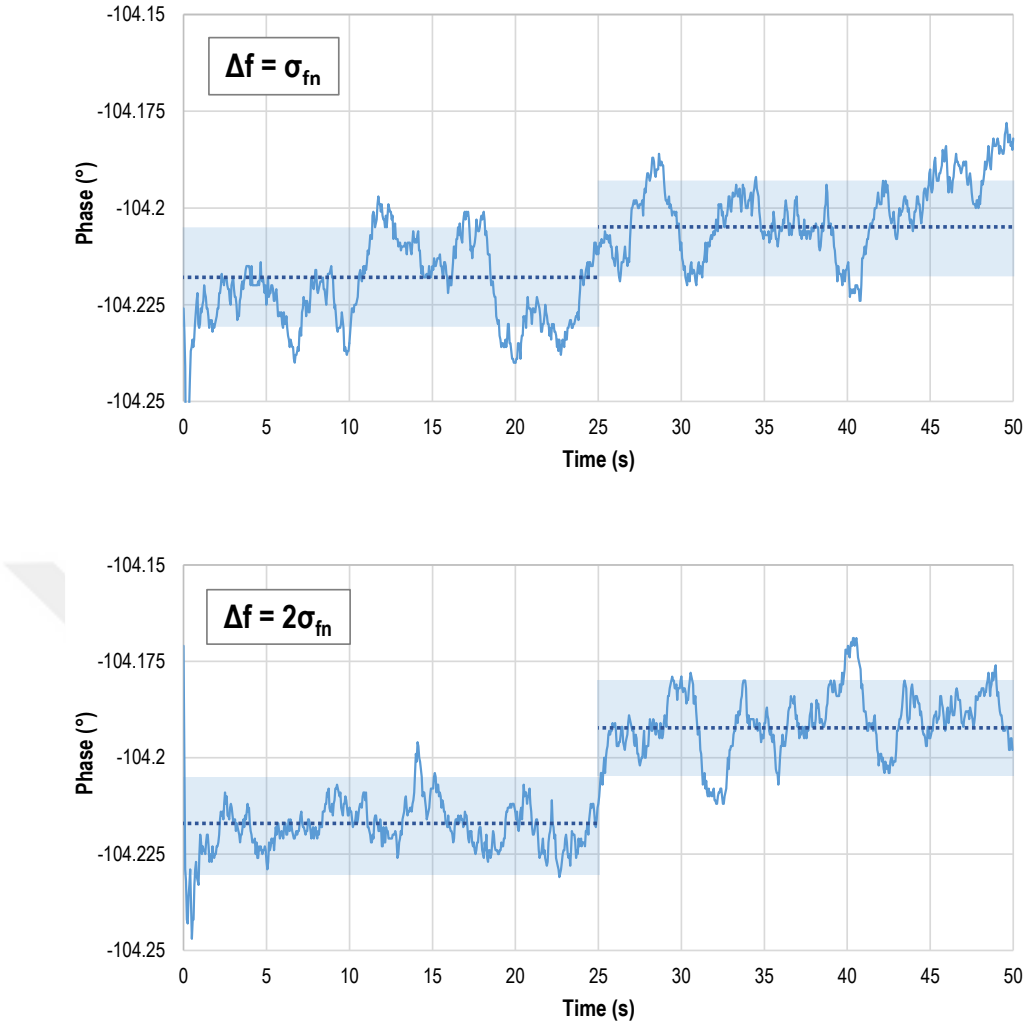

Figure 7-18 - Simulation results for detection limit σ_{fn} and $2\sigma_{fn}$ shift in natural frequency.

As appeared in the Fig. 7-18, the simulations showed very good agreement with the analytical estimated values for detection limit of the system.

7.7 Experimental Results

I did lots of experiments with different cantilever and housing designs during the development of the system. Here, I discuss the latest experimental results, a two-channel viscosity measurement experiment and longtime stability experiments in DI-water. For higher channel count I demonstrated a four channel stability measurement experiment.

7.8 Phase Stability with Digital Reference Channel

For measuring the stability and detection limit of the system in liquid, we performed long duration phase measurements with DI-water. The cantilevers were 20×200 µm and all were on the same chip. Fig. 7-19, shows the Plexiglas housing used in these experiments.

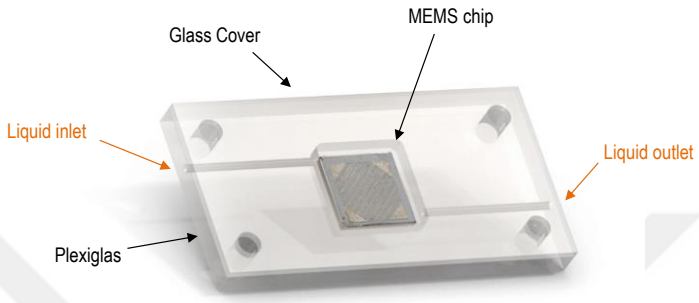

Figure 7-19 - Plexiglas housing design for in-liquid experiments

In this experiment we used a two channel DAQ card NI-6111 with digital reference input channel. This architecture was discussed in earlier in this chapter. The sampling rate was 5 MS/s and the ADCs are 12-bit.

Fig. 7-20, shows the longtime phase stability in the DI-water. The standard deviation of the measured phases for two channels was calculated as 0.88° and 0.57° for CH-1 and CH-2 respectively.

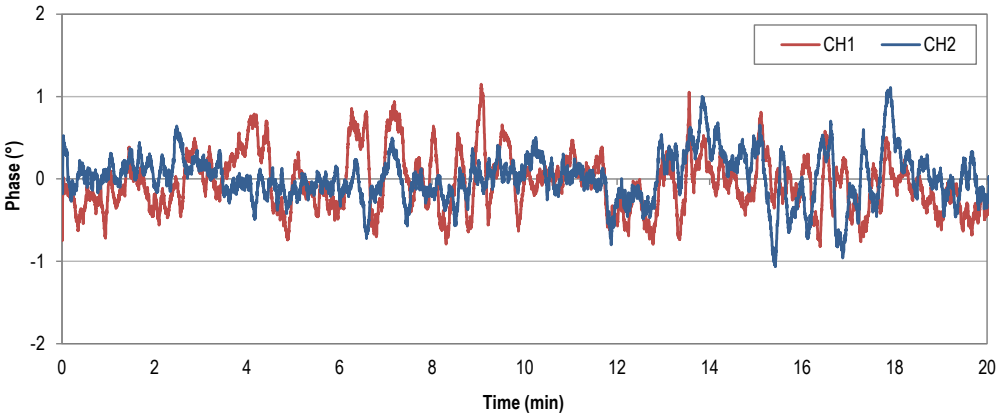

Figure 7-20 - Phase measurement stability in the DI-water using 2-CH DAQ

Fig. 7-21, shows the amplitude of the detected AC signals on photo diodes during the experiments.

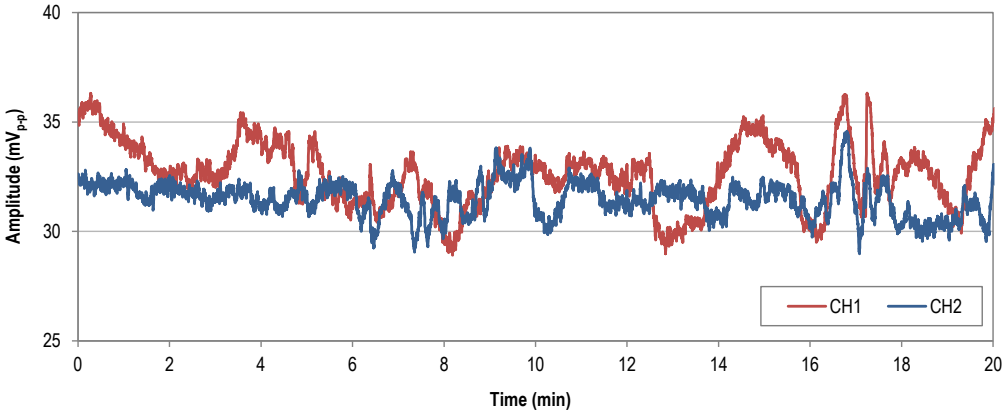

Figure 7-21 - Amplitude of the photo diode signals during the stability test

The scattered plot of the measured phase and amplitude values were also performed to observe dependences between the phase and amplitude values. Fig. 7-22, shows the scattered plot of the measured phase vs. the amplitude of the signals.

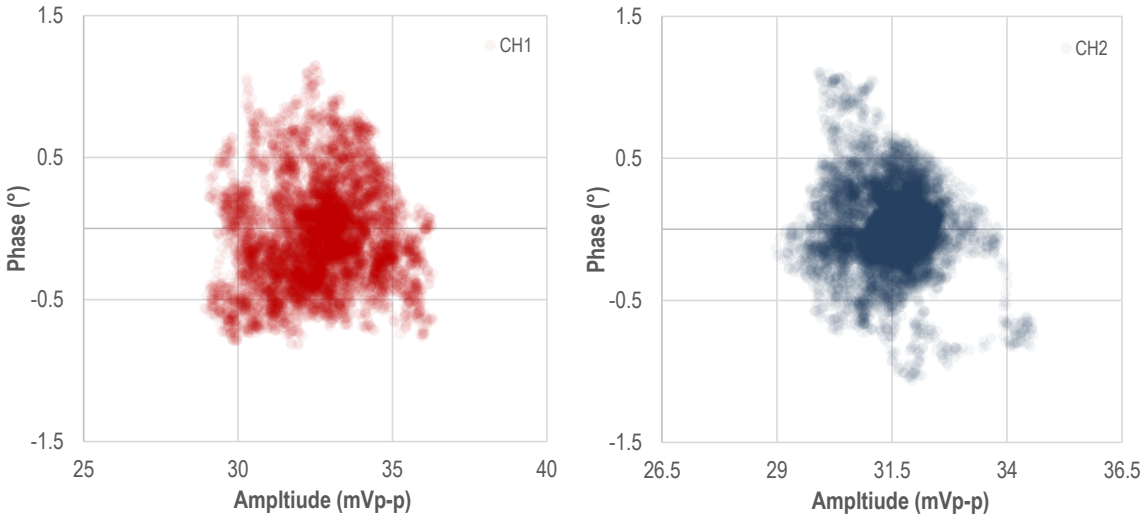

Figure 7-22 - Scattered plot of the measured phase vs. the amplitude of the signals

The scattered plots show no relationship between the instabilities in the phase and the amplitude values.

7.9 Two Channel Viscosity Measurement

For demonstrating the performance of the system, a viscosity experiment performed on two cantilevers using different glycerol solutions. The frequency response of the cantilevers was measured using a sweep generator and spectrum analyzer. The phase response was measured manually at certain frequencies. Fig. 7-23, shows the frequency and phase response of the cantilevers.

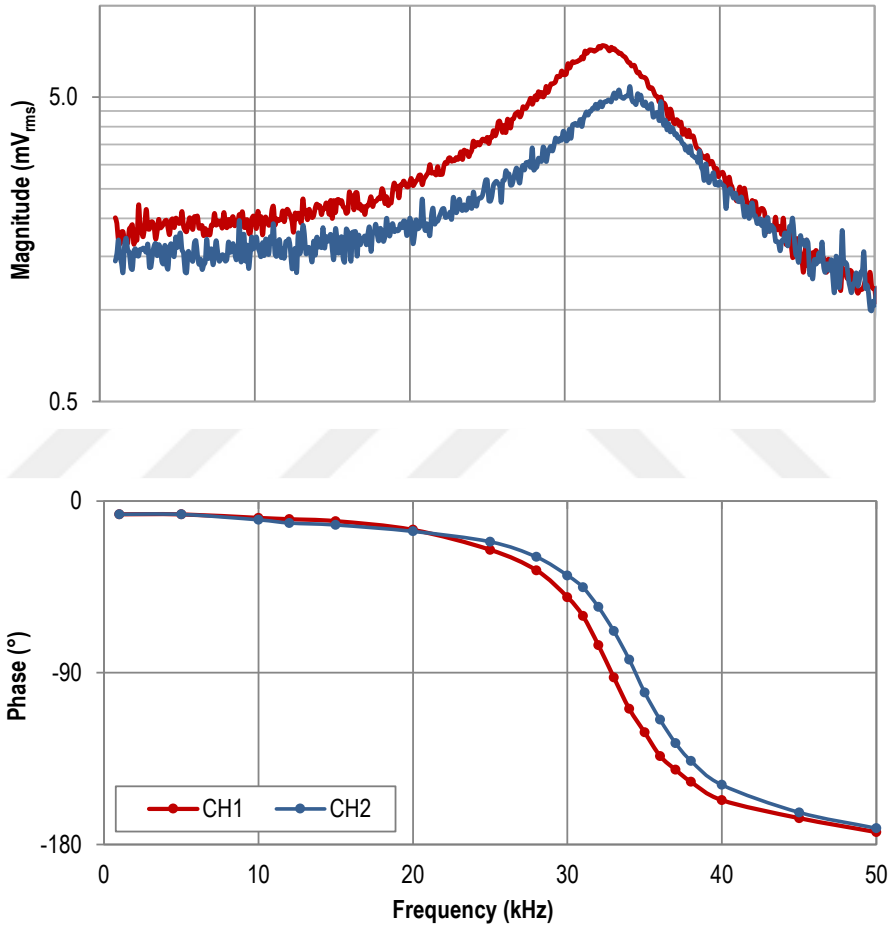

Figure 7-23 - Magnitude and phase response of the cantilevers used in viscosity experiment

The natural frequency and the quality factor of these cantilevers were calculated using the advanced Lorentzian method described earlier in previous chapter and the results were shown on Table 7-1. For equating the AC signals at photodiodes the excitation frequency was set to 34.3 kHz during the experiments.

For viscosity experiment, we used DI-water and Glycerol solutions in DI-water of 10%, 20%, 30%, 40% and 50% weight per volume. The demonstrated viscosity phase results are un-interrupted data and the system showed very robust results in terms of stability and repeatability even when the liquid flow occurred. Fig. 7-24. Shows the relative phase shift of each channel versus the Glycerol / DI-water weight percent.

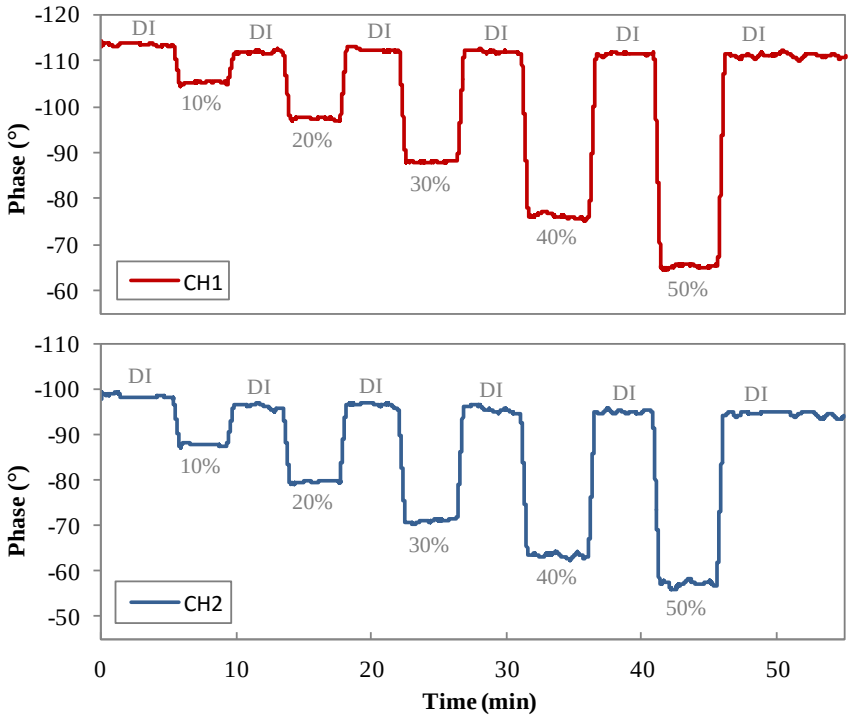

Figure 7-24 - Viscosity experiment result with DI water and Glycerol Solutions

The measured phase data is insensitive to amplitude changes and other disturbances in the fluid allowing measurements even during the fluid flows in the cell.

The measured phase shifts versus the viscosity change in term of weight percent per DI-water weight showed a linear relationship. Fig. 7-25 shows the viscosity sensitivity of the demonstrated system.

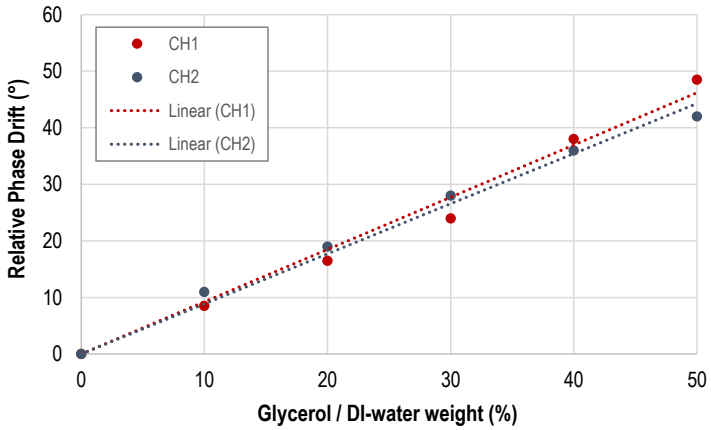

Figure 7-25 - Viscosity measurement sensitivity

The viscosity measurement sensitivity of two channels showed similar results and the slopes was calculated as 0.9236 and 0.8855 in terms of weight percent of Glycerol in DI-water per relative phase shift in degrees.

7.10 Phase Stability with Analog Reference Channel

Implementing the N-1 channel method with analog reference channel we achieved better stability results in the DI-water. In this experiment I used 8 analog input channel DAQ card NI PC-6133 from the National Instrument.

The longtime phase stability showed 10 order of magnitude improvement in respect with N-channel method using digital reference channel. Fig. 7-26 shows the phase stability and equivalent frequency stability results.

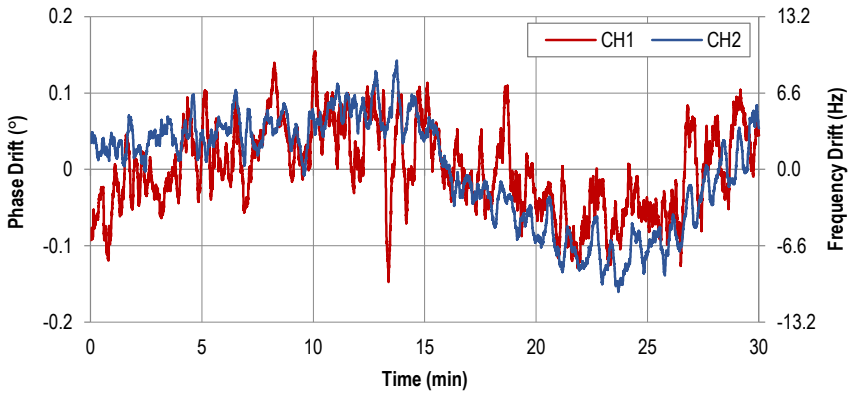

Figure 7-26 - Phase measurement stability using analog reference channel

The standard deviation of the measured phases was calculated around 25 m°. Using the stability achieved with this method, the best detection limit for Glycerol viscosity assuming an average sensitivity slope of two cantilevers will be around 280 ppm of Glycerol weight per DI-water weight.

7.11 Five Channel Phase Measurement Setup

Using the six analog input channels of the NI PC-6133 DAQ card, I expanded the phase measurement code to five simultaneous phase measurement channels. I used five identical Si amplified photo diodes PDA36A-EA from Thorlabs. For minimizing the phase delay variation in the cables, all are fixed to the optical table. I also constructed five channel fiber optic head for optical readout. Fig. 7-27 shows the cantilever design used for five channel measurements. Because of the limited angle of view only three of five cantilevers were shown in the image. Aligned Laser beams on tip of the cantilevers are also visible. This photograph was taken using the CCD camera established for optical alignment of the system.

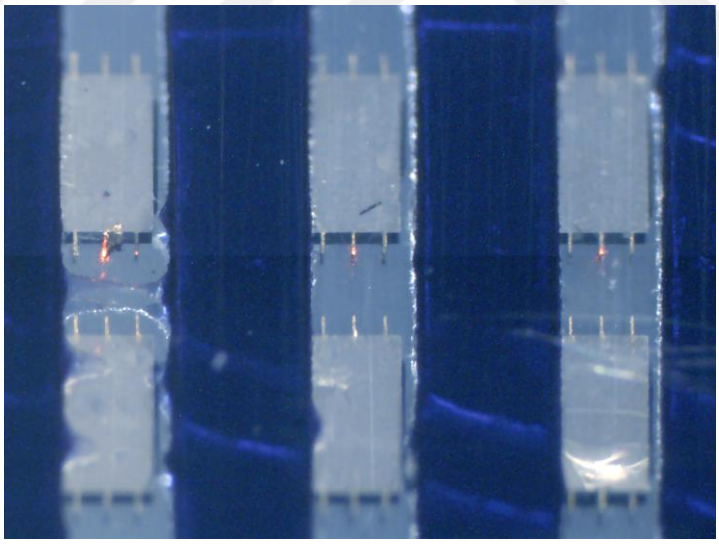

Figure 7-27 – Aligned Laser beams on tip of the cantilevers for five channel measurement setup

Because of the extensive bending in the fabricated cantilevers only four channel phase measurement achieved and due to the very low amplitude of the received signals

form the photodiodes the resulted stability increased to few degrees. Fig. 7-28 shows a screen shot of the developed five channel lock-in amplifier. Duration of the experiment was 15 min.

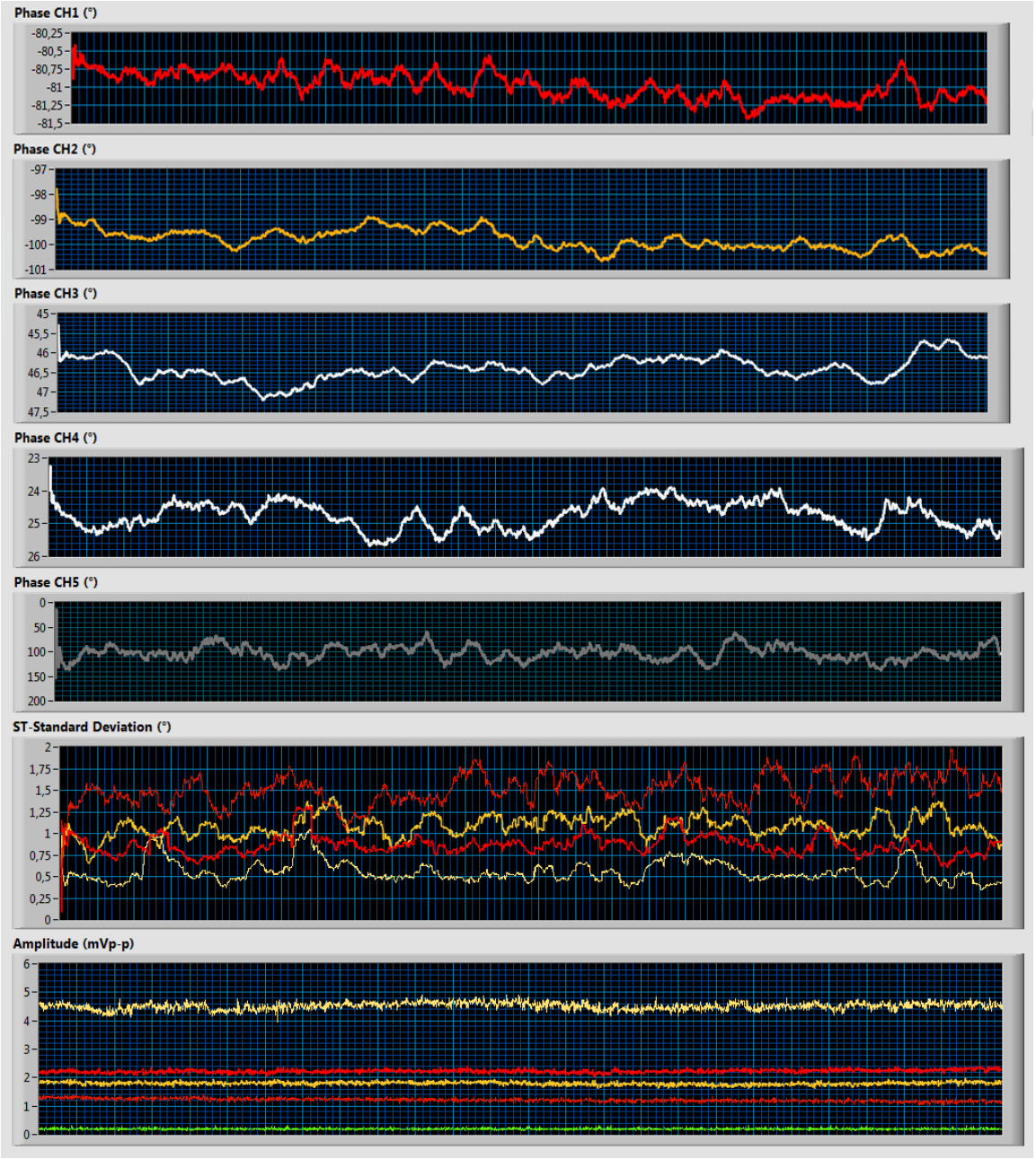

Figure 7-28 - Screenshot of the developed LabVIEW based five channel lock-in amplifier detecting four input signals.

The code calculates the phase of all channels with respect to the phase of analog reference channel. Input signals from all photodiodes were analyzed and the AC signal level of each channel and also the standard deviation of the measured phase values were shown on the screen.

I also equipped each channel with a spectrum analyzer for signal and noise level measurements. Fig. 7-29 shows the five channel spectrum analyzer unit of the code showing the AC signal levels form the photodiodes and the background noise strength.

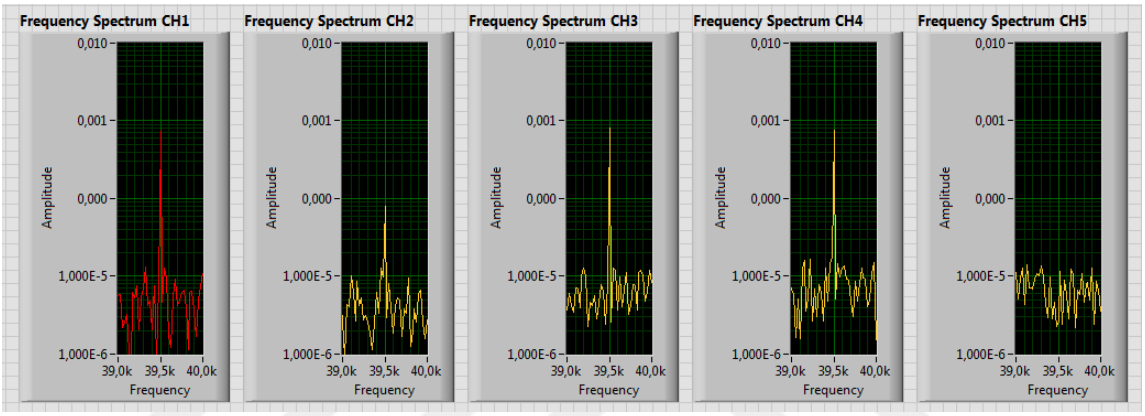

Figure 7-29 - Developed five channel spectrum analyzer for input signal strenght and noise level indication.

As discussed before in 6.5, because of the extensive residual bending of the manufactured cantilevers, acquired poor signal levels are as expected.

7.12 Conclusion

In this chapter, the phase based resonance frequency tracking method was discussed. Principle of lock-in amplifiers and developed multi-channel software lock-in amplifier for simultaneous phase measurement was discussed in detail. The stability and noise immunity of the phase detection method with noise was simulated under equivalent noise strength based on the experimental measurements. Cantilever model is also added to simulation model and the overall detection limit of the system was also calculated. The simulation results for detection limit showed perfect agreement with theoretically estimated values.

Experiments showed robust measurement results and very good noise immunity with two cantilevers. Developed five channel software was demonstrated but due to the extensive residual bending of the manufactured cantilevers, only four channel measurement achieved with very poor phase stability as expected and discussed in 6.5. Stable measurements was done with the two-channel system. We calculated detection limit of the proposed method based on the experimental results. The measured phase data is insensitive to cantilever displacement amplitude changes and other disturbances in the fluid allowing measurements even during the fluid flows in the cell. A viscosity experiment was done with different Glycerol in DI-water solutions. The sensitivity of the system was 0.9° phase shift per Glycerol/DI-water weight percent and the minimum detectable limit was 280 ppm.

8 Conclusion

In this thesis work, we focused on development of various resonance tracking and optical readout methods for magnetically actuated MEMS sensor arrays. For magnetic actuation of the mentioned sensors, we developed a dual-stage closed-loop a broadband coil driver with frequency range of DC-100 kHz at a nominal output current of 1 A_{p-p} for driving a single-layer air-core 40 turns solenoid coil with inductance of 18 µH. Control model of the driver was developed for design optimization. We achieved maximum phase error of 2° with total harmonic distortions of less than 1%.

Using the developed broadband magnetic actuator, simultaneous self-sustained operation of MEMS cantilever array is demonstrated. Microcantilevers are designed with different resonance frequencies and microfabrication was a simple one mask process. In order to perform parallel readout of the simultaneous oscillations, interferometric readout of 8 cantilevers through a single detector and a single electro-coil are used. One set of discrete feedback electronics is utilized to phase shift and amplify the photodetector signal and close the loop. Without any actuation, Brownian motion of the microcantilever array is observed clearly using a single photodetector and the interferometric setup. SSA oscillations are performed for seven microcantilevers with changing resonance frequencies in the 60-130 kHz range. Measurements are performed in air environment.

SSA method is suitable for high-quality factor resonators where most of the noise and harmonic distortions are filtered out in the resonator. As a more robust closed-loop method for low-quality factor resonators, we developed a broadband resonance tracking system that is based on CMOS digital PLLs. The method we propose provides a fixed-amplitude and frequency-independent +90° phase-shifted sinewave output for exciting resonant systems at their undamped resonance frequency that does not involve any initial tuning or calibration process. We employ an analog sinewave generation method with an acceptable THD of less than 2% and implement a passive second-order phase-lead filter in the input stage for compensating the propagation delays and achieving a maximum phase error of ±2.5° on the whole operating frequency range of 5 – 50 kHz. We discuss the advantages of this method over the conventional PLLs that use mixer-type phase detectors with limited frequency ranges and frequency-dependent phase errors. We

demonstrate the resonance tracking performance of the proposed system on a low-quality-factor series RLC resonator and also a high-quality-factor Quartz tuning fork crystal. We measure a long-term stability of 0.77 Hz with the RLC resonator locked at 20140.5 Hz and 0.19 mHz with a 32.768 kHz Quartz tuning fork with locking time of less than 5 ms. Wide operating frequency range, fast locking time, and tuningless operation of our system can make it into an attractive solution for driving MEMS sensors in integrated CMOS-MEMS designs and also parallel resonance tracking of MEMS sensor arrays in time multiplexed operation.

The PLL system we have developed shows extremely stable results with standard resonators, we have however experienced large frequency drifts originating from phase-detection errors in the interferometric optical readout. As a solution for interferometric optical readout problems, we developed a novel dual-edge detection method using two cascaded PLL stages. This method, shows extremely high immunity to drifts and asymmetry of the feedback signal as well as DC-offset drifts in front-end electronics. This method was used in a high sensitivity viscosity measurement system for measuring the viscosity of human blood plasma. In general case, this dual-edge phase detection method could be implemented in many digital PLL applications having asymmetrically distorted feedback signals. In this method, system detects both of the rising and falling edges of the input signal. A primary PLL locks into a pulse train generated by the dual-edge zero-crossing detector circuit and locks at twice of the input frequency. Then a divide by 2 circuit cascaded with a reverse phase detection circuit provides a square wave with a rising edge located exactly at the middle of the rising and falling edges of the input signal. This method, not only solves the phase errors due to the asymmetry of the input signal, but also solves for dc offset and low-frequency interferences on the input signal. Performance of this method was demonstrated on a RLC series resonator and MEMS cantilever sensors. With RLC resonator, sub PPM stability was achieved in long time experiments. This system was used to measure the viscosity of human blood plasma using MEMS cantilevers. Viscosity measurement sensitivity of 0.04 cP was achieved between 0.86 to 3.02 cP.

Since PLL systems could only lock into a single resonator at a time, for parallel measurements a time-multiplexing mechanism must be employed. As an alternative

method providing real-time simultaneous measurements, we developed a novel optical fiber-based readout method with phase-based resonance monitoring. We developed a 5-spot Laser source for illuminating equally spaced cantilevers with pitch of 2 mm using a 5 mW He-Ne Laser. The minimum beam diameter of 28 µm achieved using a focusing lens located at a distance of around 10 cm. A microscope objective used as beam expander prior to the focusing lens. With a total optical power of less than 500µW per channel, measurable ac signals observed at photodiodes. A compact fiber array based pick-up was built for optical readout. Its main advantages are easy customization to different size and pitch, and good immunity to electrical noise and magnetic interference as the photo detectors are located away from the coil and electronics. The whole optical design was modeled in Zemax® and Matlab® and the optimum values for design parameters was discussed.

For simultaneous parallel phase measurements we developed a software multi-channel lock-in amplifier. Stability of the developed phase measurement method was simulated under equivalent input noise strength, based on the experimental measurements. Cantilever model is also added to simulations and the overall detection limit of the system was calculated. The simulation results for detection limit showed perfect agreement with theoretically estimated values.

The detection limit of the proposed method was calculated based on the experimental results. The measured phase data is insensitive to cantilever displacement amplitude changes and other disturbances in the fluid allowing measurements even during the fluid flows in the cell. A viscosity experiment was done with different Glycerol in DI-water solutions. The sensitivity of the system was 0.9° phase shift per Glycerol/DI-water weight percent and the minimum detectable limit was 280 ppm. The sensor technology demonstrated here is very significant as it is scalable to larger arrays for simultaneous and real-time monitoring of multiple biological and chemical agents during fluid flow. To our knowledge this is the first demonstration of simultaneous parallel optical monitoring of dynamic mode micro-cantilever array in liquid environment.

9 Appendix I: Design and Characterization of Coils

Theoretically, generated magnetic field in electromagnetic coils linearly depends on the current passing through the coil. Fig. 2-1 shows the electric current direction and its relevant magnetic field in thin coils.

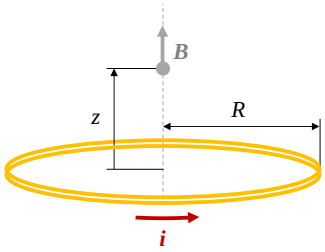

Figure 9-1 - Magnetic field of a thin coil

The intensity of the magnetic field in thin coils is similar to current loops. Equation 9-1 gives the generated magnetic field in any distance on the symmetric axis of a thin coil.

$$B = \frac{\mu_0 N i r^2}{2\sqrt{\left(r^2 + z^2\right)^3}} . \tag{9.1}$$

In these equations, μ_0 is the permeability constant (1.26×10^{-6} H/m), i is the current, r is the coil radius, z is the distance and N is the total number of turns [73].

In general case for thin shell solenoids with length Z the equation will be

$$B = \frac{\mu_0 N i}{2 Z}\left(\frac{z_2}{\sqrt{r^2 + z_2^2}} - \frac{z_1}{\sqrt{r^2 + z_1^2}}\right). \tag{9.2}$$

Here z_1 and z_2 are the distances from the ends of the solenoid on the symmetric axis of the solenoid [74,75]. Fig. 9-2 shows the thin shell solenoid case.

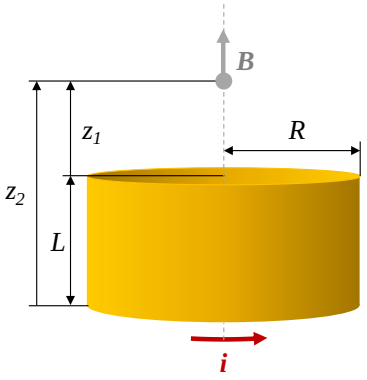

Figure 9-2 - Thin shell solenoid coil

In practical analog electronics, there is no ideal components in general and almost all of the analog components and circuit diagrams have parasitic and unwanted effects where must be carefully studied and took into account in precision applications.

Electromagnetic coils generally could not be model as simple inductors. In its simplest form the coil model consists of an ideal inductor in series with a resistor. The ideal inductor represents for the inductance of the coil and the resistor represents the resistance of the winding. Fig. 9-3 shows the simple coil model.

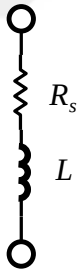

Figure 9-3 - Simple coil model consists of an inductor and a series resistor

This model might be sufficient for some simple applications but for precision applications, first of all one must check for the agreement of the model with experimental results.

In our experimental setup a 3.3 mH multi-layer, 640-turn coil was used in the setup. The outer diameter, inner diameter and the height of the coil are 14 mm, 8 mm and 6 mm. As the starting point for driver design, I started with measuring the coil parameters for modeling and simulations. Fig. 9-4 shows the mentioned coil.

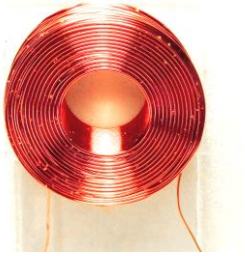

Figure 9-4 - 640 turn, multi-layer coil

For checking the validity of the coil model with the real coil, I setup an impedance measurement experiment for measuring the parameters of the coil. In this experiment, the coil under test in series with a reference resistor forms a first-order high-pass filter. Fig. 9-5 shows the experimental setup.

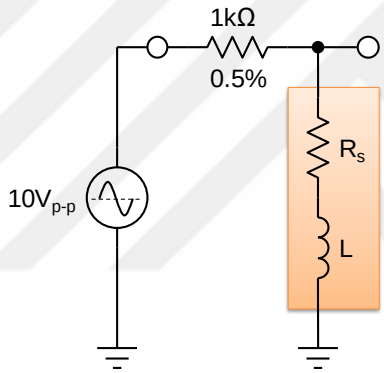

Figure 9-5 - Experimental setup for measuring the coil parameters

Using the output voltage amplitude and phase, one can calculate the impedance of the coil. Equations 9.3 to 9.5 shows the derivations.

$$V_{out} = V_{in} \frac{Z_{coil}}{\left(R_{in} + R_{ref}\right) + Z_{coil}}, \tag{9.3}$$

$$\left|Z_{coil}\right| = \frac{V_{out}}{V_{in}} \left(R_{in} + R_{ref}\right), \tag{9.4}$$

$$\angle Z_{coil} = \angle V_{out} - \angle V_{in}. \tag{9.5}$$

In these equations, R_{in} represents the output impedance of the signal generator (R_{in} = 50 Ω) and R_{ref} is the reference metal film precision resistor (R_{ref} = 1 kΩ, 0.05%). Fig. 9-6 shows the calculated magnitude and phase of the coil based on the experimental results measured from 0 to 2MHz.

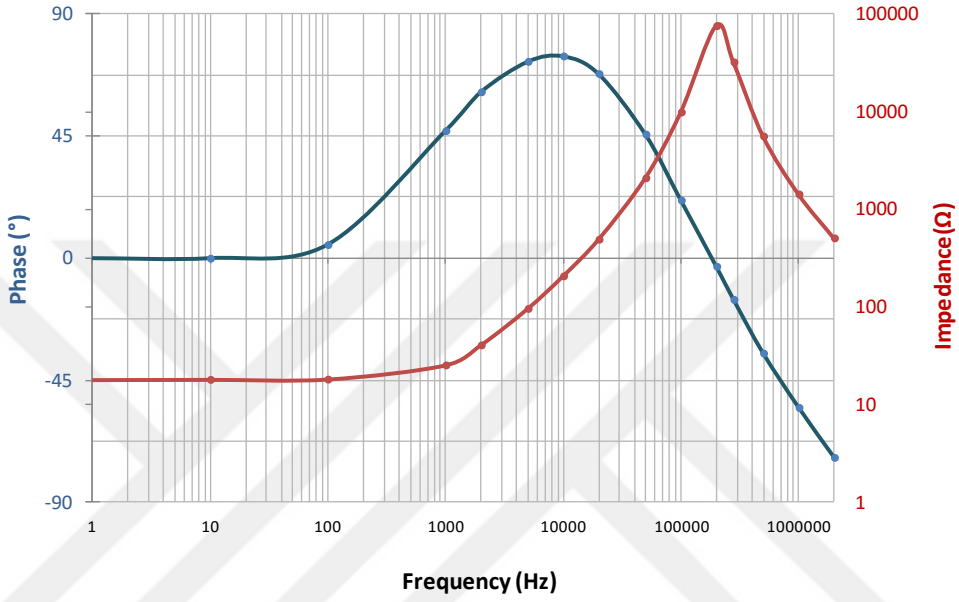

Figure 9-6 - Impedance measurement results for the multilayer 640-turn coil

As it appears clearly in the frequency response, the circuit shows a sharp resonant response around 200 kHz. The phase response also starts to deviate after 10 kHz. It means that there are highly dominant parasitic capacitance effects in the coil. As the result, the frequency response experiment showed that the simple coil model is not valid for this coil for frequencies higher than a few kHz.

In the next step, for modeling this coil, we studied more complicated coil models to match with experimental measurement results[76–78]. Fig. 9-7 shows a four element model for coils with parasitic capacitance effects.

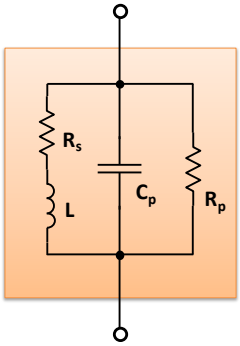

Figure 9-7 - Four-element coil model

In this model, additional parallel capacitor and resistor represent the parasitic capacitance and losses. These additional model parameters could be calculated from the resonance frequency and quality factor of the test circuit using the equations 9-6 and 9-7.

$$C_p = \frac{1}{(2\pi f_0)^2 L}, \tag{9.6}$$

$$R_p = 2\pi f_0 Q L, \tag{9.7}$$

where f_0 and Q respectively are the resonance frequency and quality factor of the test circuit [79]. Inductance and the series resistance are measured using an RLC meter. The measured values respectively are L = 3.32 mH and R_s = 18.2 Ω.

Based on the frequency response experiment the resonant frequency and quality factors of the test circuit calculated as f_0 = 204 kHz and Q = 10. Using the experimental data and the measured inductance and series resistor values we calculated the parallel capacitor and resistor values as C_p = 110 pF and R_p = 92 kΩ.

For checking the validity of the four-element coil model, we simulated the circuit using the calculated model parameters and compared to the measured frequency response. As shown in the Fig. 9-8, the simulation result for magnitude response shows little deviations from the experimental result, but the phase response shows huge differences for frequencies higher than 1 kHz.

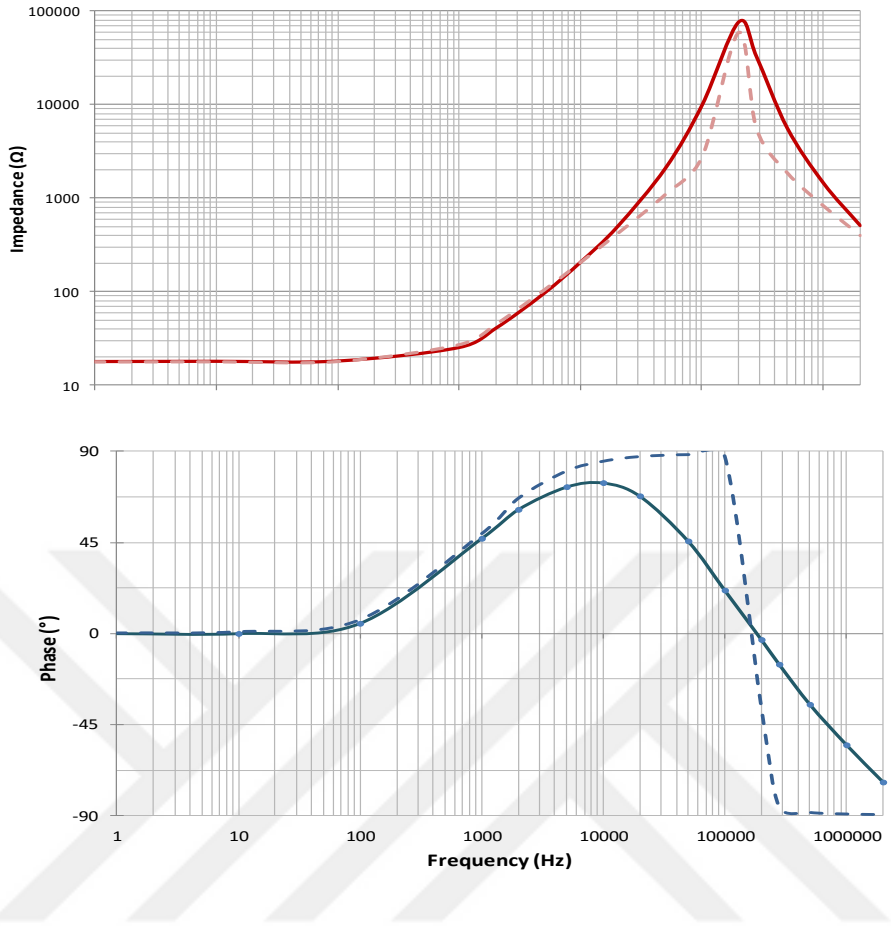

Figure 9-8 - Frequency response results for 640-turn multilayer coil

This comparison shows that, even the four-element coil model is not valid for our case for frequencies higher than 1 kHz. In the other side, as the resonance frequency of our MEMS devices are in the range of 10 to 70 kHz, these experiments clearly showed that this coil is not a suitable choice for broadband magnetic actuation.

The generated magnetic field inside the coil has a uniform distribution. In our project, the MEMS die containing the resonant cantilevers, placed in a few millimeter distances on top of the coil. In this case, the normal component of the magnetic field to the chip surface decreases from the center of symmetry to the corners. Fig. 9-9 shows the magnetic field generated by the coil and its normal component's distribution on the chip surface.

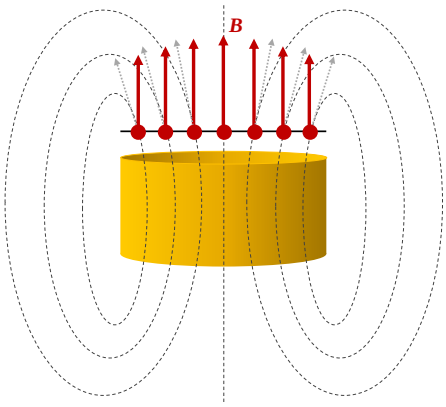

Figure 9-9 - Magnetic field distribution on the chip surface

For a maximum chip size of 10×10 mm^2, the coil's diameter assumed to be equal to the diameter of the chip. Therefore, d = $\sqrt{2}\ \times 10\ mm \cong 14\ mm$. Fig. 9-10 shows the chip and coils dimensions.

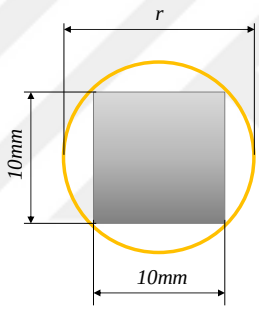

Figure 9-10 - Coil and MEMS die dimensions

From the driver design point of view, as the coil's impedance increases with frequency, for a fixed current operation we will need higher coil drive voltages for higher frequencies. In other words, for a certain maximum output voltage, higher inductance coils will restrict the bandwidth. Figure 9-11 shows the bandwidth of two coils L1 and L2 driven with fixed current, where L1 is greater than L2.

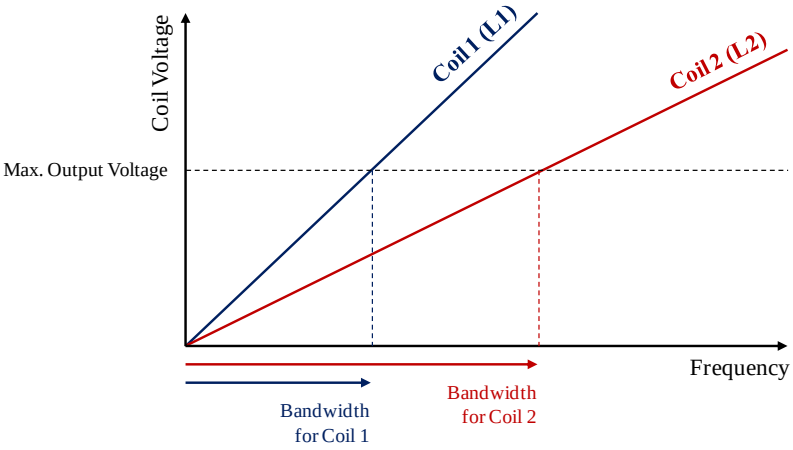

Figure 9-11 - Bandwidth vs. coil inductance (L1 > L2)

Assuming the simple coil model, we have

$$Z_L(j\omega) = j\omega L + R_s, \tag{9.8}$$

$$V_L(j\omega) = I_L\, Z_L(j\omega) = I_L(R_s + j\omega L). \tag{9.9}$$

As the coil impedance in high frequencies became very large with respect to the coil's resistive component,

$$I_L R_s << I_L\left|j\omega L\right|, \tag{9.10}$$

Then we can rewrite the equation as follows

$$\left|V_L\right| = I_L\left|j\omega L\right| < V_{max}, \tag{9.11}$$

Finally, the relation for maximum inductance versus maximum output voltage and maximum operating frequency or bandwidth of the driver could be written as

$$2\pi\, f_{max} L\, I_L < V_{max}, \tag{9.12}$$

$$L_{max} = \frac{V_{max}}{2\pi\, f_{max}\, I_L}. \tag{9.13}$$

V_{max} is the maximum output voltage for the driver, I_L is the coil current and L_{max} is the maximum allowable inductance for the coil.

On the other side, as the generated magnetic field relates linearly to the number of turns, as a result the maximum possible turn number with minimum inductance will be the key rule for broadband magnetic actuation coil design.

Approximate inductance of a single layer air core solenoid coil could be calculated using the simplified formula:

$$L = \frac{\alpha R^2 N^2}{9R + 10Z} \tag{9.14}$$

Here α is a numeric constant equal to 39.3700×10^{-6}. This approximation is close for solenoids with $Z \geq 0.8R$ [80]. As seen on equation 9.14, the inductance increases with second power of N, while the magnetic field increases linearly with N.

In the presence of the parasitic capacitances, a portion of electric current passes through the parallel capacitance branch and the magnitude of the generated magnetic field decreases in higher frequencies. For a broadband magnetic actuator, we need to minimize the parasitic capacitance effects in the coil. This makes it possible to maintain a fixed magnetic field in the case of fixed driving current.

One of the main sources of parasitic capacitance, is the formed capacitance between the coil layers in multilayer coils. For minimizing these effects, single layer coils are preferred.

For measuring this effect in single layer coils, I made a single layer coil with N = 12 and measured its parameters. Fig. 9-12, shows the measurement results for the handmade single layer coil.

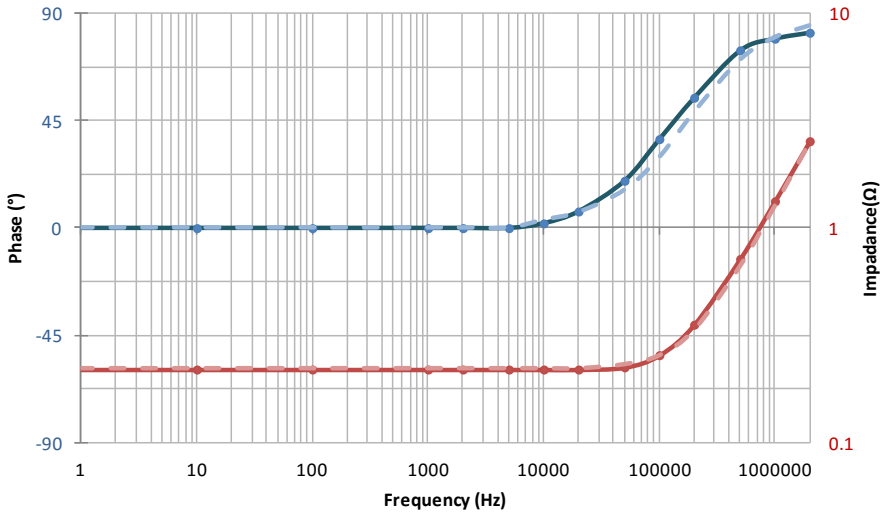

Figure 9-12 - Simulation and experimental results for handmade single layer coil

As predicted, comparing the simulation and measurement results shows no evidence of parasitic capacitance in that handmade single layer coil up to 2 MHz. For exact coil specification we also need to decide about the coil driver architecture and its limitations and then recalculate the optimum coil value.

10 Appendix II: RLC Resonator

For the equivalent series RLC circuit, the values for the desired natural frequency and quality factor could be derived as follows:

$$\omega_n = \frac{1}{\sqrt{LC}} \tag{10.1}$$

where, ω_n is the angular natural frequency of the resonator. In terms of frequency we have

$$f_n = \frac{2\pi}{\sqrt{LC}} \tag{10.2}$$

and

$$LC = \frac{4\pi^2}{{f_n}^2} \tag{10.3}$$

For the quality factor we have:

$$Q = \frac{1}{R}\sqrt{\frac{L}{C}} \tag{10.4}$$

then,

$$R = \frac{1}{Q}\sqrt{\frac{L}{C}} \tag{10.5}$$

Using the equation 10.3, one could calculate the value of LC then assuming a proper value for L, C could be calculated. Substuting the values of L and C in the equation 10.5, the value for R could be calculated for desired quality factor.

11 Appendix III: Analog Temperature Controller Design

For minimizing the temperature dependent drifts in the experimental setup, a temperature controlled housing for MEMS chip and a temperature controller was designed. Fig. 8-1 shows the housing design with heating resistors. In this design, two cupper plates were used in both sides of the cartridge. Each plate equipped with two 25 W Aluminum heating resistors. The resistors are connected in serious for equal heating of the plates and minimizing the heat graduations.

A temperature sensor was placed near the MEMS chip for temperature measurement. Rectangular openings were created on both of the cupper plates for optical readout on the top plate and for magnetic actuation on the bottom plate. A PCB for holding the electro-coil and permanent magnets was also designed. Fig. 8-2 shows the overall system schematics with temperature controller.

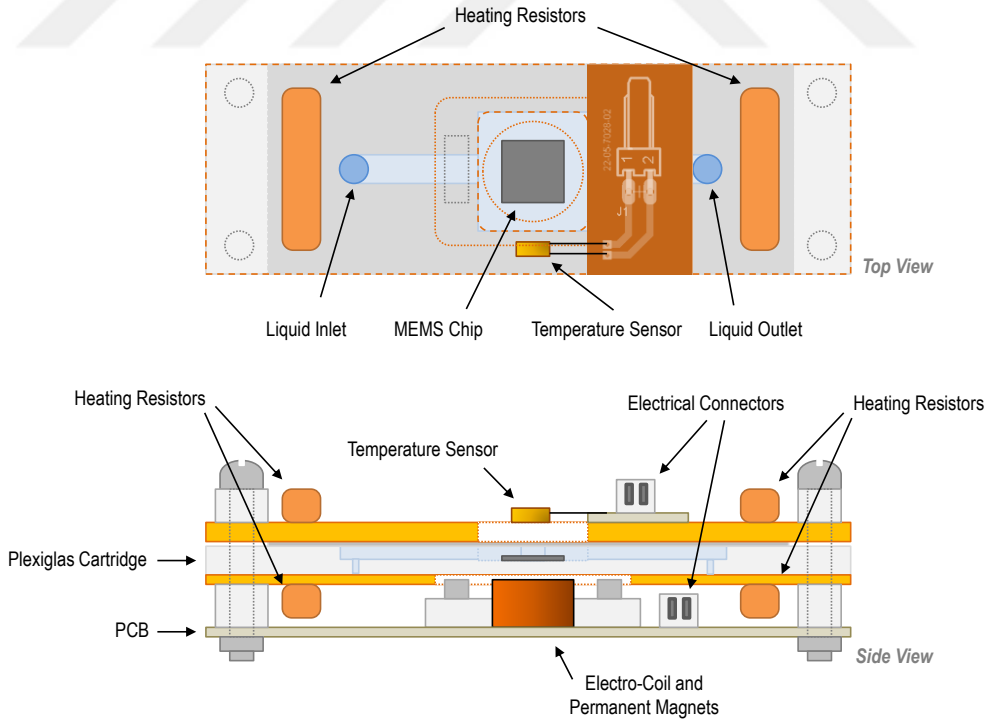

Figure 11-1 - Temperature controlled housing design

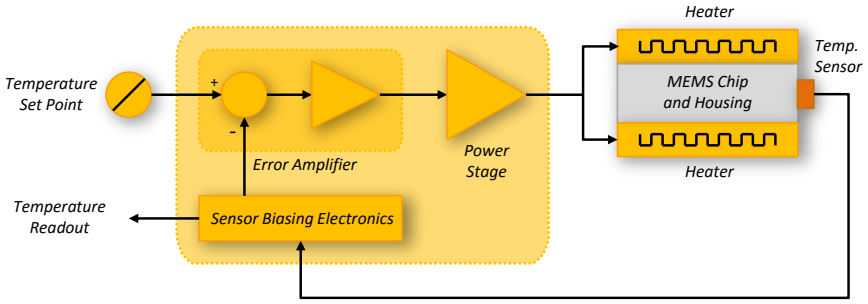

Figure 11-2 - Overall system schematics with temperature controller

For temperature control a proportional on-off control design implemented using a n-channel power MOSFET as switching element. An infinity gain op-amp circuit used as voltage comparator, controls the power MOSFET. For temperature measurement an AD590F sensor was used. This sensor has a 1 mA/°K current output. Using a series resistor of 1 kΩ, voltage output of 10 mV/°K could be measured across the resistor. For set point input, a voltage dividing network were implemented. Fig. 8-3, shows the temperature controller circuit.

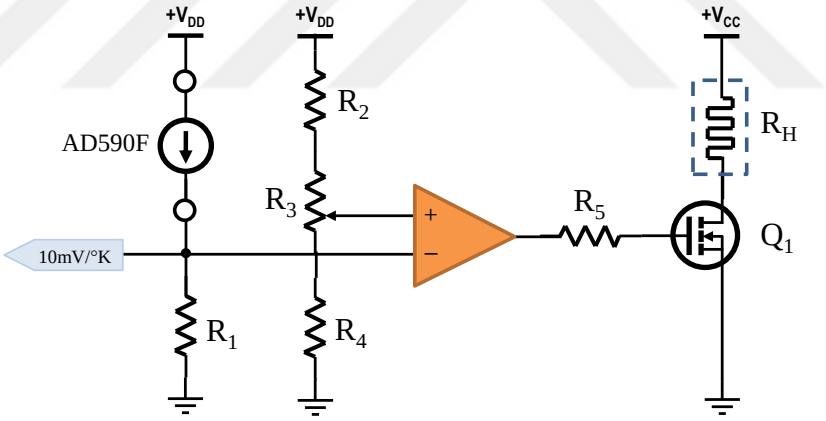

Figure 11-3 - Temperature Controller Circuit

R_H is the heater resistance. The positive input of the op-amp will be the set point voltage in 10 mV/°K scale. For temperature readout in Celsius degrees, the voltage at readout or set point must be subtracted by 2.7315 V to have a 10 mV/°C output. An extra voltage dividing network from a regulated reference voltage could be used for construct the analog offset voltage. For digital readout using a DAQ card, the subtraction may be done in software for higher stability.

I used a 30 A n-channel fast switching power MOSFET (IRF940) with very low R_{ON} of 44 mΩ as the R5 is the gate resistor of the Q1 and could be any value between 10 to 100 Ω to limit the charge currents in the gate.

Comparator op-amp LM308 was used instead of the op-amp, to keep the system working in switching mode. A +12 V supply voltage is used for heater resistance branch. For 15 Ω Aluminum resistors connected in series are used as heating resistance giving a total heating power of 2.4 W at 12 V supply voltage.

R_1 is 1 kΩ and must be a low-drift, low tolerance resistor. Set point voltage network could be implemented using a single potentiometer, but for more precious tenability two fixed resistors of R2 and R4 are used to constrict the tuning range to desired temperature range. 20 to 60°C temperature range corresponds to 2.93 to 3.33 V in the set point voltage. Using a 1 kΩ potentiometer as R3, the values of R2 and R4 will be 7.32 kΩ and 4.18 kΩ for a supply voltage of +5 V.

Because of the high gain of the op-amp, power MOSFET will work as a switch generally with a very low power dissipation on the transistor. But, as the frequency of the switching is not known, theoretically the switching mode power losses could not be calculated. Practically, a heat dissipation of e few watts was observed in prototype circuit. A medium size heat sink with a heat capacity of around 3°K/W was found sufficient to keep the power MOSFET cool. Fig. 8-4, shows the developed PCB of the temperature controller circuit.

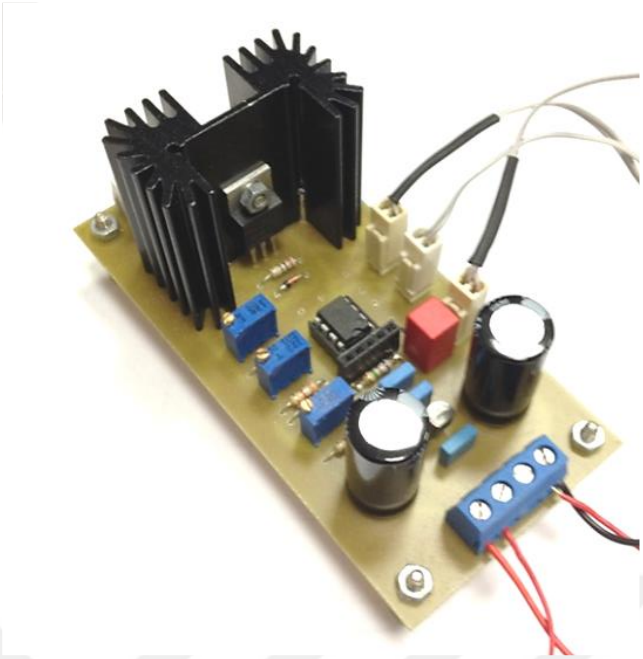

Figure 11-4 - Implemented Temperature Controller

For measuring the temperature, voltage at the readout output was measured used a DAQ card and a LabVIEW software. Fig. 8-5 shows the screenshot of the developed LabVIEW code.

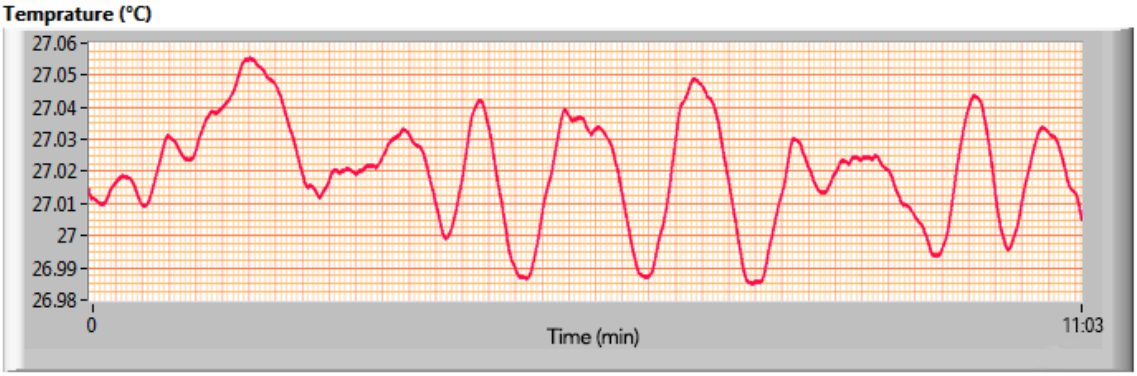

Figure 11-5 - Temperature stability at set point of 27°C

Experimentally, temperature stability of < ±50 m°K was achieved with the designed circuit in room temperature of 25°C for set points ranging from 26 to 40°C. Standard deviation of the measured temperature was 12 m°K at set point of 27°C.

12 Appendix IV: Advanced Lorentzian Fit Model

For calculating the resonance frequency of the cantilevers from the measured phase difference, precise value of the quality factor is necessary. Quality factor could be calculated from the frequency sweep results by fitting the measured amplitude values into a Lorentzian function. For scaling the amplitudes, a gain factor also must be added to the model or the amplitude values normalized. Equation 12.1, shows the standard Lorentzian function with scaling factor of g.

$$H(j\omega) = \frac{g}{1 + \frac{\omega}{\omega_n Q} j + \left(\frac{\omega}{\omega_n}\right)^2} \tag{12.1}$$

Fig. 12-1, shows the frequency response of two cantilevers measured in parallel and the corresponding fit results to the standard Lorentzian function with gain parameter.

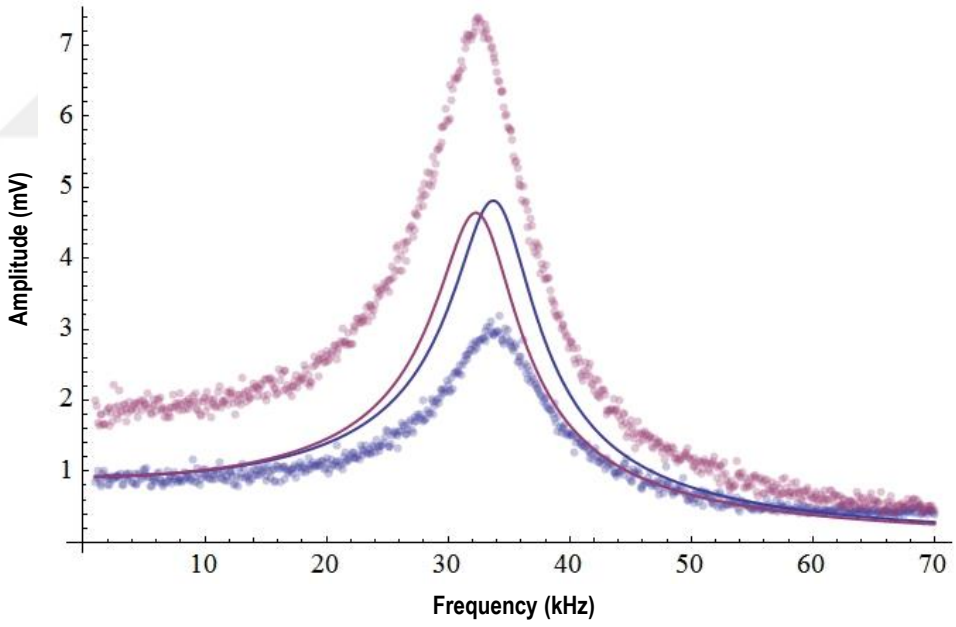

Figure 12-1 - Lorentzian function fit for the measured frequency responce of two cantilevers

Since the additional noise and the frequency response of the measurement circuits affects the measured values, direct fitting of values may not result good fits to standard Lorentzian function of equation 12.1.

For a more precise fitting, we developed a fit function by adding a noise floor parameter and also a linear frequency response model for the frequency response of the front end electronics and also the inverse frequency noise. Assuming the bandwidth of the electronics which are higher enough for desired frequency range, a first order linear approximation would be sufficient.

The advanced model could be represented as follows:

$$H(j\omega) = \frac{g}{1 + \frac{\omega}{\omega_n Q} j + \left(\frac{\omega}{\omega_n}\right)^2} + c_1\omega + c_0 \tag{12.2}$$

c_0 represents the effect of the additional noise floor and c_1 stands for the linear approximated frequency response of the front end electronics and also the additional inverse frequency or flicker noise. Fig. 12-2, shows the fit results with the advanced Lorentzian model.

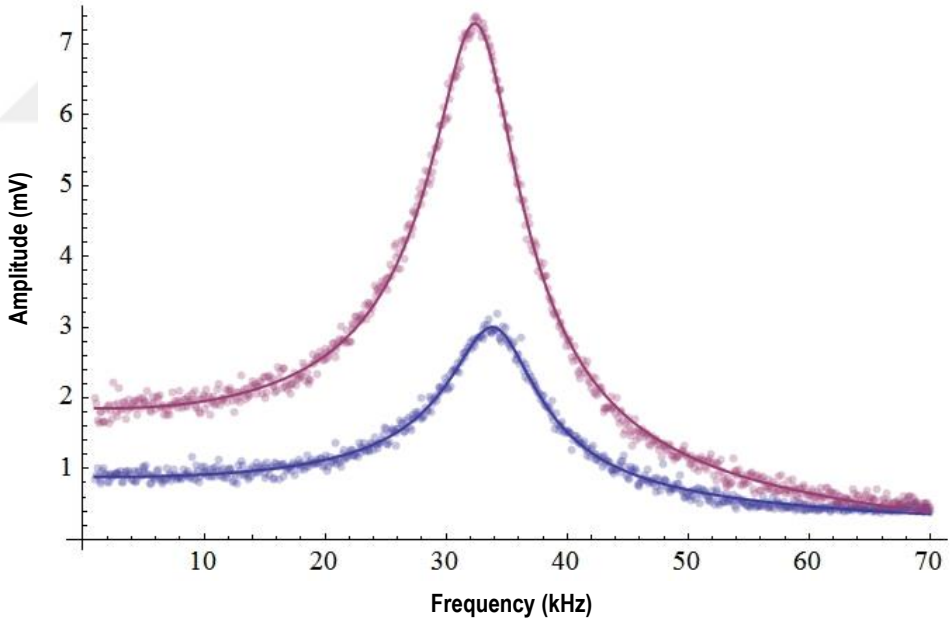

Figure 12-2 - Advanced Lorentzian function fit for the measured frequency responses

As seen in the Fig. 12-2, the advanced model perfectly fits on the experimental data. The resulting parameters for these two cantilevers are shown in Table 9-1.

Table 12-1 - Calculated parameters of the cantilever using advanced fit method

	CH-1	CH-2
Natural Frequency (kHz)	34.1812	32.7634
Quality Factor	4.852	4.675

Using the calculated correction coefficients from the advanced model, the unity gain frequency response of the cantilevers could also be reconstructed. Applying the inverse of the additional effects represented by coefficient g, c_0 and c_1 will give the unity gain frequency response of the cantilevers. Fig. 12-3, shows the resulting unity gain frequency response.

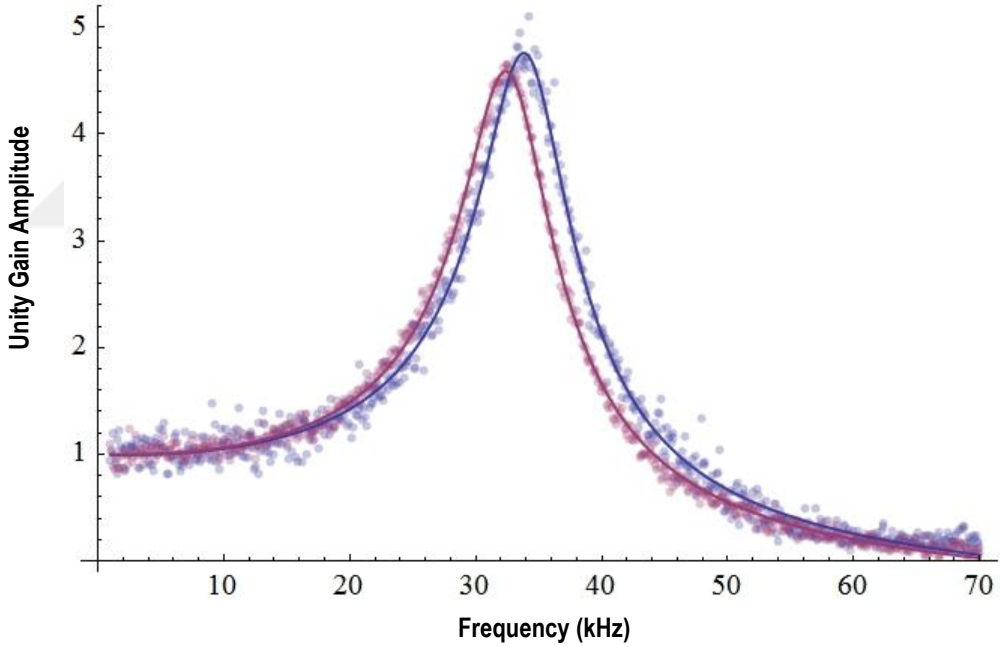

Figure 12-3 – Unity gain frequency response of the cantilevers using the correction coefficients

References

[1] E.A. Wachter, T. Thundat, Micromechanical sensors for chemical and physical measurements, Rev. Sci. Instrum. 66 (1995) 6. doi:10.1063/1.1145484.

[2] T. Thundat, P. I. Oden, and R. J. W, Microcantilever Sensors, Microscale Thermophys. Eng. 1 (1997) 185–199. doi:10.1080/108939597200214.

[3] J.K. Gimzewski, C. Gerber, E. Meyer, R.R. Schlittler, Observation of a chemical reaction using a micromechanical sensor, Chem. Phys. Lett. 217 (1994) 589–594. doi:10.1016/0009-2614(93)E1419-H.

[4] U. Dammer, M. Hegner, D. Anselmetti, P. Wagner, M. Dreier, W. Huber, H.J. Güntherodt, Specific antigen/antibody interactions measured by force microscopy, Biophys. J. 70 (1996) 2437–2441. doi:10.1016/S0006-3495(96)79814-4.

[5] P.K. Hansma, J.P. Cleveland, M. Radmacher, D.A. Walters, P.E. Hillner, M. Bezanilla, M. Fritz, D. Vie, H.G. Hansma, C.B. Prater, J. Massie, L. Fukunaga, J. Gurley, V. Elings, Tapping mode atomic force microscopy in liquids, Appl. Phys. Lett. 64 (1994) 1738–1740. doi:10.1063/1.111795.

[6] M. Su, S. Li, V.P. Dravida, Microcantilever resonance-based DNA detection with nanoparticle probes, Appl. Phys. Lett. 82 (2003) 3562–3564. doi:10.1063/1.1576915.

[7] L.A. Pinnaduwage, A. Wig, D.L. Hedden, A. Gehl, D. Yi, T. Thundat, R.T. Lareau, Detection of trinitrotoluene via deflagration on a microcantilever, J. Appl. Phys. 95 (2004) 5871–5875. doi:10.1063/1.1697619.

[8] J.L. Arlett, E.B. Myers, M.L. Roukes, Comparative advantages of mechanical biosensors., Nat. Nanotechnol. 6 (2011) 203–215. doi:10.1038/nnano.2011.44.

[9] D. Ham, A. Hajimiri, Virtual damping and Einstein relation in oscillators, IEEE J. Solid-State Circuits. 38 (2003) 407–418. doi:10.1109/JSSC.2002.808283.

[10] H. Urey, E. Timurdogan, E. Ermek, I.H. Kavakli, B.E. Alaca, MEMS biosensor for parallel and highly sensitive and specific detection of hepatitis, 2011 IEEE 24th Int. Conf. Micro Electro Mech. Syst. (2011) 920–923. doi:10.1109/MEMSYS.2011.5734576.

[11] E. Timurdogan, B.E. Alaca, I.H. Kavakli, H. Urey, MEMS biosensor for detection

of Hepatitis A and C viruses in serum, Biosens. Bioelectron. 28 (2011) 189–194. doi:10.1016/j.bios.2011.07.014.

[12] A. Ozturk, H.I. Ocakli, N. Ozber, H. Urey, I.H. Kavakli, B.E. Alaca, A magnetically actuated resonant mass sensor with integrated optical readout, IEEE Photonics Technol. Lett. 20 (2008) 1905–1907. doi:10.1109/LPT.2008.2005253.

[13] L. Vicci, A 3D magnetic force manipulator DC prototype, UNC Chapel Hill Dept. Comput. Sci. Tech. …. 031 (2001). http://citeseerx.ist.psu.edu/viewdoc/download?doi=10.1.1.21.6232&rep=rep1&type=pdf.

[14] S.P. Jarvis, A. Oral, T.P. Weihs, J.B. Pethica, A novel force microscope and point contact probe, Rev. Sci. Instrum. 64 (1993) 3515–3520. doi:10.1063/1.1144276.

[15] E.-L. Florin, M. Radmacher, B. Fleck, H.E. Gaub, Atomic force microscope with magnetic force modulation, Rev. Sci. Instrum. 65 (1994) 639. doi:10.1063/1.1145130.

[16] J.K. Fisher, J.R. Cummings, K. V. Desai, L. Vicci, B. Wilde, K. Keller, C. Weigle, G. Bishop, R.M. Taylor, C.W. Davis, R.C. Boucher, E.T. O'Brien, R. Superfine, Three-dimensional force microscope: A nanometric optical tracking and magnetic manipulation system for the biomedical sciences, Rev. Sci. Instrum. 76 (2005). doi:10.1063/1.1914777.

[17] L. Vicci, The 3DFM Magnet Drive Amplifier, UNCCH Dept Comput. Sci. Tech. Rep. TR05-002. TR05-002 (2005).

[18] M. Kageshima, T. Chikamoto, T. Ogawa, Y. Hirata, T. Inoue, Y. Naitoh, Y.J. Li, Y. Sugawara, Development of atomic force microscope with wide-band magnetic excitation for study of soft matter dynamics, Rev. Sci. Instrum. 80 (2009) 1–7. doi:10.1063/1.3080557.

[19] J. Tapson, J.R. Greene, Improved capacitance measurement by means of resonance locking, Meas. Sci. Technol. 5 (1994) 20–26. doi:10.1088/0957-0233/5/1/004.

[20] K. Kobayashi, H. Yamada, H. Itoh, T. Horiuchi, K. Matsushige, Analog frequency modulation detector for dynamic force microscopy, Rev. Sci. Instrum. 72 (2001) 4383–4387. doi:10.1063/1.1416104.

[21] H.S. Wasisto, Q. Zhang, S. Merzsch, A. Waag, E. Peiner, A phase-locked loop

frequency tracking system for portable microelectromechanical piezoresistive cantilever mass sensors, Microsyst. Technol. 20 (2014) 559–569. doi:10.1007/s00542-013-1991-9.

[22] S. Hayashi, On the Tracking of Resonance and Antiresonance of a Piezoelectric Resonator, IEEE Trans. Ultrason. Ferroelectr. Freq. Control. 38 (1991) 231–236. doi:10.1109/58.79607.

[23] H. Sheng, Y. Pei, X. Yang, F. Wang, C.W. Tipton, Frequency tracking control for a capacitor-charging parallel resonant converter with phase-locked loop, Conf. Proc. - IEEE Appl. Power Electron. Conf. Expo. - APEC. (2007) 1287–1292. doi:10.1109/APEX.2007.357681.

[24] P. Lin, Y. Ku, C. Lai, Y. Liao, Y. Huang, Implementation of a PLL-based High Frequency Resonant AC Power Supply, (2008) 1329–1334.

[25] W. Fu, B. Zhang, D. Qiu, Study on frequency-tracking wireless power transfer system by resonant coupling, 2009 IEEE 6th Int. Power Electron. Motion Control Conf. IPEMC ’09. 3 (2009) 2658–2663. doi:10.1109/IPEMC.2009.5157857.

[26] B.S. Chang, J.G. Lee, T. Kang, W.-T. Sung, Design and performance analysis of PLL based self oscillation loop in vibrating gyroscope, in: Proc. SPIE, ICMIT 2005 Mechatronics, MEMS, Smart Mater., 2005. doi:10.1117/12.664217.

[27] M. Bayindir, N. S., Kukrer, O., Yakup, Active power filter control using neural network technologies, IEE Proceedings-Electric Power Appl. 150 (2003) 139–145. doi:10.1049/ip-epa.

[28] C. Wang, H.H. Yu, M. Wu, W. Fang, Implementation of phase-locked loop control for MEMS scanning mirror using DSP, Sensors Actuators, A Phys. 133 (2007) 243–249. doi:10.1016/j.sna.2006.03.026.

[29] J.K. Sell, A.O. Niedermayer, B. Jakoby, A digital PLL circuit for resonator sensors, Sensors Actuators, A Phys. 172 (2011) 69–74. doi:10.1016/j.sna.2011.02.030.

[30] O. Cakmak, N. Kilinc, E. Ermek, A. Mostafazadeh, C. Elbuken, G.G.G. Yaralioglu, H. Urey, LoC sensor array platform for real-time coagulation measurements, in: Micro Electro Mech. Syst. (MEMS), 2014 IEEE 27th Int. Conf., 2014: pp. 330–333. doi:10.1109/MEMSYS.2014.6765643.

[31] O. Cakmak, C. Elbuken, E. Ermek, A. Mostafazadeh, I. Baris, B. Erdem Alaca, I.H.I.H. Kavakli, H. Urey, Microcantilever based disposable viscosity sensor for serum and blood plasma measurements., Methods. 63 (2013) 225–32. doi:10.1016/j.ymeth.2013.07.009.

[32] O. Cakmak, E. Ermek, N. Kilinc, S. Bulut, I. Baris, I.H. Kavakli, G.G. Yaralioglu, H. Urey, A cartridge based sensor array platform for multiple coagulation measurements from plasma, Lab Chip. 15 (2015) 113–120. doi:10.1039/C4LC00809J.

[33] O. Cakmak, E. Ermek, N. Kilinc, G.G. Yaralioglu, H. Urey, Precision density and viscosity measurement using two cantilevers with different widths, Sensors Actuators A Phys. 232 (2015) 141–147. doi:10.1016/j.sna.2015.05.024.

[34] A. Mostafazadeh, G.G.G. Yaralioglu, H. Urey, Optical fiber array based simultaneous parallel monitoring of resonant cantilever sensors in liquid, Sensors Actuators A Phys. 242 (2016) 132–139. doi:10.1016/j.sna.2016.03.004.

[35] S.C. Minne, S.R. Manalis, C.F. Quate, Parallel atomic force microscopy using cantilevers with integrated piezoresistive sensors and integrated piezoelectric actuators, Appl. Phys. Lett. 67 (1995) 3918. doi:10.1063/1.115317.

[36] S.C. Minne, G. Yaralioglu, S.R. Manalis, J.D. Adams, J. Zesch, a. Atalar, C.F. Quate, Automated parallel high-speed atomic force microscopy, Appl. Phys. Lett. 72 (1998) 2340–2342. doi:10.1063/1.121353.

[37] T. Sulchek, R.J. Grow, G.G. Yaralioglu, S.C. Minne, C.F. Quate, S.R. Manalis, A. Kiraz, A. Aydine, A. Atalar, Parallel atomic force microscopy with optical interferometric detection, Appl. Phys. Lett. 78 (2001) 1787–1789. doi:10.1063/1.1352697.

[38] H.P. Lang, R. Berger, C. Andreoli, J. Brugger, M. Despont, P. Vettiger, C. Gerber, J.K. Gimzewski, J.P. Ramseyer, E. Meyer, H.J. Güntherodt, Sequential position readout from arrays of micromechanical cantilever sensors, Appl. Phys. Lett. 72 (1998) 383–385. doi:10.1063/1.120749.

[39] M.K. Baller, H.P. Lang, J. Fritz, C. Gerber, J.K. Gimzewski, U. Drechsler, H. Rothuizen, M. Despont, P. Vettiger, F.M. Battiston, J.P. Ramseyer, P. Fornaro, E. Meyer, H.J. Güntherodt, A cantilever array-based artificial nose, Ultramicroscopy.

82 (2000) 1–9. doi:10.1016/S0304-3991(99)00123-0.

[40] F.M. Battiston, J.P. Ramseyer, H.P. Lang, M.K. Baller, C. Gerber, J.K. Gimzewski, E. Meyer, H.J. Güntherodt, A chemical sensor based on a microfabricated cantilever array with simultaneous resonance-frequency and bending readout, Sensors Actuators, B Chem. 77 (2001) 122–131. doi:10.1016/S0925-4005(01)00683-9.

[41] H. Lang, M. Hegner, C. Gerber, Cantilever array sensors, Mater. Today. 8 (2005) 30–36. doi:10.1016/S1369-7021(05)00792-3.

[42] N. Nugaeva, K.Y. Gfeller, N. Backmann, H.P. Lang, M. Düggelin, M. Hegner, Micromechanical cantilever array sensors for selective fungal immobilization and fast growth detection, Biosens. Bioelectron. 21 (2005) 849–856. doi:10.1016/j.bios.2005.02.004.

[43] S.Z.Z. Lulec, C. Sagiroglu, A. Mostafazadeh, E. Ermek, E. Timurdogan, Y. Leblebici, H. Urey, Simultaneous self-sustained actuation and parallel readout with MEMS cantilever sensor array, in: Micro Electro Mech. Syst. (MEMS), 2012 IEEE 25th Int. Conf., 2012: pp. 644–647. doi:10.1109/MEMSYS.2012.6170269.

[44] O. Cakmak, N. Kilinc, E. Ermek, A. Mostafazadeh, C. Elbuken, G.G. Yaralioglu, H. Urey, LoC sensor array platform for real-time coagulation measurements, in: Micro Electro Mech. Syst. (MEMS), 2014 IEEE 27th Int. Conf., 2014: pp. 330–333. doi:10.1109/MEMSYS.2014.6765643.

[45] A. Mostafazadeh, H. Urey, Broadband Resonance Tracking with Digital PLL and Analog Sinewave Generation for Resonant Sensors and Actuators, Sensors Actuators A Phys. (2016).

[46] A. Mostafazadeh, H. Urey, Dual-PLL Resonance Tracking for MEMS Sensors with Distorted Feedback Signals, Sensors Actuators A Phys. (2016).

[47] OPA544 High-Voltage, High-Current OPERATIONAL AMPLIFIER, 1997. http://www.ti.com/lit/ds/symlink/opa544.pdf.

[48] Texas Instruments, TL08xx JFET-Input Operational Amplifiers, 2015. http://www.ti.com/lit/ds/symlink/tl071.pdf.

[49] Texas Instruments, OPA55x High-Voltage , High-Current Operational Amplifiers, 2016. http://www.ti.com/lit/ds/symlink/opa551.pdf.

[50] N. Jalili, K. Laxminarayana, A review of atomic force microscopy imaging systems: Application to molecular metrology and biological sciences, Mechatronics. 14 (2004) 907–945. doi:10.1016/j.mechatronics.2004.04.005.

[51] M. Basso, P. Paoletti, B. Tiribilli, M. Vassalli, Modeling and analysis of auto-tapping AFM, in: Proc. IEEE Conf. Decis. Control, 2008: pp. 5188–5193. doi:10.1109/CDC.2008.4739214.

[52] M. Basso, P. Paoletti, B. Tiribilli, M. Vassalli, Modelling and analysis of autonomous micro-cantilever oscillations., Nanotechnology. 19 (2008) 475501. doi:10.1088/0957-4484/19/47/475501.

[53] J. Tamayo, M. Calleja, D. Ramos, J. Mertens, Underlying mechanisms of the self-sustained oscillation of a nanomechanical stochastic resonator in a liquid, Phys. Rev. B - Condens. Matter Mater. Phys. 76 (2007) 1–4. doi:10.1103/PhysRevB.76.180201.

[54] J.L. Pons, P. Ochoa, M. Villegas, J.F. Fern??ndez, E. Rocon, J. Moreno, Self-tuned driving of piezoelectric actuators. The case of ultrasonic motors, J. Eur. Ceram. Soc. 27 (2007) 4163–4167. doi:10.1016/j.jeurceramsoc.2007.02.130.

[55] A.A. Kuijpers, D. Lierop, R.H.M. Sanders, J. Tangenberg, H. Moddejonge, J.W.T. Eikenbroek, T.S.J. Lammerink, R.W. Wiegerink, Towards embedded control for resonant scanning MEMS micromirror, Procedia Chem. 1 (2009) 1307–1310. doi:10.1016/j.proche.2009.07.326.

[56] E. Kharrat, C., Colinet, Bias Voltage Control for Resonance Frequency Tracking in Electrostatic Mems Sensors, (2009) 5–9.

[57] H. Barkhausen, Lehrbuch der Elektronen-Röhren und ihrer technischen Anwendungen, S. Hirzel, Leipzig, 1935.

[58] B. Razavi, Design of Monolithic Phase-Locked Loops and Clock Recovery Circuits-A Tutorial, Monolith. Phase-Locked Loops Clock Recover. Circuits. (1996) 1–39. doi:10.1109/9780470545331.ch1.

[59] R. Best, Phase Locked Loops, 6th ed., McGraw-Hill, 2007. http://www.amazon.com/Phase-Locked-Loops-Simulation-Applications/dp/0071493751.

[60] R.G. Meyer, S. Lui, W.M. Sansen, S. Peeters, The Differential Pair as a Triangle-

Sine Wave Converter, IEEE J. Solid-State Circuits. 11 (1976) 418–420. doi:10.1109/JSSC.1976.1050748.

[61] Texas Instruments, Sine Approximation—Logarithmic Shaping, AN-263 Sine Wave Gener. Tech. (2013) 12–13. http://www.ti.com/lit/an/snoa665c/snoa665c.pdf.

[62] T. Henry, x-4046 VCO, (2010). http://www.birthofasynth.com/Thomas_Henry/Pages/X-4046.html.

[63] D.K. Morgan, CD4046B Phase-Locked Loop : A Versatile Building Block for Micropower Digital and Analog Applications, 2003.

[64] J.W. Goodman, Introduction to Fourier Optics, 2nd ed., McGraw-Hill, 1996.

[65] W.W. Koelmans, J. van Honschoten, J. de Vries, P. Vettiger, L. Abelmann, M.C. Elwenspoek, Parallel optical readout of cantilever arrays in dynamic mode., Nanotechnology. 21 (2010) 395503. doi:10.1088/0957-4484/21/39/395503.

[66] M. Toda, A.N. Itakura, S. Igarashi, K. Büscher, J.S. Gutmann, K. Graf, R. Berger, Surface stress, thickness, and mass of the first few layers of polyelectrolyte, Langmuir. 24 (2008) 3191–3198. doi:10.1021/la7028214.

[67] H. Hou, X. Bai, C. Xing, N. Gu, B. Zhang, J. Tang, Aptamer-based cantilever array sensors for oxytetracycline detection., Anal. Chem. 85 (2013) 2010–4. doi:10.1021/ac3037574.

[68] K. Gruber, T. Horlacher, R. Castelli, A. Mader, P.H. Seeberger, B. a. Hermann, Cantilever array sensors detect specific carbohydrate-protein interactions with picomolar sensitivity, ACS Nano. 5 (2011) 3670–3678. doi:10.1021/nn103626q.

[69] S. Kelling, F. Paoloni, J. Huang, V.P. Ostanin, S.R. Elliott, Simultaneous readout of multiple microcantilever arrays with phase-shifting interferometric microscopy, Rev. Sci. Instrum. 80 (2009) 093101. doi:10.1063/1.3212667.

[70] J. Polesel-Maris, L. Aeschimann, A. Meister, R. Ischer, E. Bernard, T. Akiyama, M. Giazzon, P. Niedermann, U. Staufer, R. Pugin, N.F. De Rooij, P. Vettiger, H. Heinzelmann, Piezoresistive cantilever array for life sciences applications, J. Phys. Conf. Ser. 61 (2007) 955–959. doi:10.1088/1742-6596/61/1/189.

[71] T. Sulchek, R. Hsieh, S.C. Minne, C.F. Quate, S.R. Manalis, Interdigital Cantilever as a Biological Sensor, (2001) 562–566.

[72] S.T. Koev, W.E. Bentley, R. Ghodssi, Interferometric readout of multiple cantilever sensors in liquid samples, Sensors Actuators, B Chem. 146 (2010) 245–252. doi:10.1016/j.snb.2010.02.038.

[73] D.J. Griffiths, Introduction to Electrodynamics, 3rd ed., Pearson Education, Inc., San Francisco, 2008.

[74] E. Denisson, Magnet Formulas, (2005). http://tiggerntatie.github.io/emagnet/solenoids/thinsolenoid.htm (accessed November 8, 2015).

[75] H.A. Haus, J.R. Melcher, Electromagnetic Fields and Energy, Prentice Hall, Inc., 1989.

[76] F.A. Kolster, The Effects of Distributed Capacity of Coils Used in Radio-Telegraphic Circuits, in: Inst. Radio Eng., 1913.

[77] R.G. Medhurst, H. F. Resistance and Self-Capacitance of Single-Layer Solenoids, Wirel. Eng. (1947) 35–43.

[78] L. Green, RF-inductor modeling for the 21st Century, EDN Mag. (2001) 67–74.

[79] M. O'Hara, Modeling Non-Ideal Inductors in SPICE, Milton Keynes, 1993.

[80] H.W. Silver, The ARRL Handbook for Radio Communications, ARRL, Newington, 2011.

Vita

Arif Mustafazade (Aref Mostafazadeh) was born in 1978 in Tabriz, Iran. He received the B.Sc. degree in electrical and electronics engineering from Tabriz Azad University (TAU), Tabriz-Iran, in 2001, M.A. degree in photography from Fine Arts Department of Marmara University, Istanbul-Turkey in 2008, and the M.Sc. degree in electrical and computer engineering from Koç University (KU), Istanbul-Turkey in 2010.

After graduation from TAU, he worked in a private research firm in Tabriz. In 2006, He moved to Istanbul to enroll in the M.A. program in Photography of Marmara University where he worked on the imaging optics and quality factors of imaging systems. From 2008 to 2010 he was research and teaching assistant in KU Laser Research Laboratory, and from 2010 to 2014 in KU Optical Microsystems Laboratory. In 2014, while pursuing his Ph.D., he founded the Electronics Research Laboratory in GAMAK Motors Company, the largest electric motor manufacturer in Turkey and started as project manager and chief design engineer.